Functionalization of Liposome with Organic Chromophore for Artificial Photosynthesis

Cumulative Dissertation

To obtain the academic degree

Doctor rerum naturalium (Dr. Rer. Nat.)

Submitted to the

Faculty of Natural Science of Ulm University

by

Novitasari Sinambela

born in Pematangsiantar

2025

Dean of the Faculty of Natural Science: Prof. Dr. Kay-E. Gottschalk

First Reviewer: Jun.-Prof. Dr. Andrea Pannwitz

Second Reviewer: Prof. Dr. Max Von Delius

Day of Promotion: 20 May 2025

Abstract

Photosynthesis starts by absorbing and transforming energy from solar photons into chemical energy, which is spatially collected and transported within the photosystems in the thylakoid membrane. The light-harvesting complexes in the thylakoid membrane absorb the energy and transfer it to the reaction center to ignite the electron transport chain. The biomimetic liposome membrane is used to mimic the thylakoid membrane. In this thesis, the functionalization of liposomes with organic chromophores is studied. The strategy and model system of how artificial photosynthesis could be built upon this biomimetic system are presented, including the examination and mechanistic investigation of photoinduced reactions in the liposome system.

In the first project, the liposome membrane is functionalized with perylene diimide. The electrostatic interaction between the negatively charged membrane and positively charged chromophore enables the photooxidation of perylene diimide in an aqueous system. The design principle of perylene diimide is being evaluated to propose an ultimate way of introducing organic chromophores in the complete water system. The liposome membrane is being used as the media for dissolving the organic chromophores in the aqueous system without significantly changing the properties of the chromophore. This finding applies to the molecular engineering of artificial cellular organelles and nano-reactors based on biomimetic vesicles and membranes.

In the second project, our attempt to mimic the actual photosynthesis system is achieved by the characteristics of the compartmentalization feature in the vesicle system together with the integrated organic chromophore as a molecular wire. Our model features a complementary redox reaction that is placed in the different compartments in the lipid bilayer system. The explored model is the combination of the oxidation of NADH and a reduction of XTT. The integrated organic molecular wire in the membrane was designed to align in the transmembrane position to be able to transfer electrons across the membrane. We evaluated the different combinations of placing XTT and NADH and observed fairly similar rates. The system was active in inert and in ambient air. This finding has opened another possibility of mimicking photosynthesis in the liposomal system with an abundant material such as organic molecular wire. This study showed the possibility of transferring multiple electrons across the membrane, which opens the possibility of having a total water splitting in this system.

In the final project, the same model reaction used in the second project was employed. The bridged bis(triarylamines) chromophores with intervalence charge transfer properties were examined. The focus was on the ability of these organic chromophores to facilitate photoinduced electron transfer in a lipid bilayer membrane. Two different derivatives of the bistriarylamine bridge were characterized, revealing their characteristic associated with the formation of mixed valence states that were demonstrated through UV-Vis/NIR spectroscopy and spectroelectrochemistry. The investigation assessed the ability of the bridged bis(triarylamines) to function as charge conduits, and their photoactivity was demonstrated in the oxidation of NADH and the reduction of XTT in the liposome system. The multielectron processes observed indicate that this system mimics the complexity of multielectron transfer in photosynthesis, suggesting its potential as a future model for achieving total water splitting and CO_2 reduction in a completely aqueous system.

Contents

Chapter 1 7
Introduction 7
Chapter 2 16
Recent Advances in Light Energy Conversion with Biomimetic Vesicle Membranes 16
Chapter 3 25
Alignment and Photooxidation Dynamics of a Perylene Diimide Chromophore in Lipid Bilayers 25
Chapter 4 51
Photoinduced Electron Transfer Across Phospholipid Bilayers in Anaerobic and Aerobic Atmospheres 51
Chapter 5 111
Recent Advances in Light Energy Conversion with Biomimetic Vesicle Membranes 111
Chapter 6 275
Summary, Conclusions, and Outlook 275
List of Publications 281
Curriculum Vitae 285
Acknowledgments 286
Declaration of Honesty in Academic Work 288

Chapter 1

Introduction

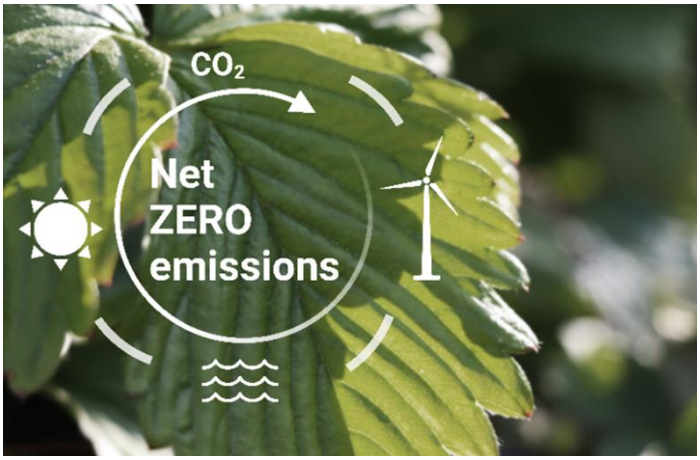

Figure 1.1 Outlined scenarios to achieve Net-ZERO CO_2 emission using renewable energy resources, including wind, wave, and solar energy.

The International Energy Agency (IEA) has outlined scenarios aimed at achieving Net-ZERO CO_2 emissions in the global energy sector by 2050 (Figure 1.1), a critical step is to limit the rise in global temperatures to no more than 1.5 °C. This transition necessitates a prioritization of clean energy technologies.[1] Recent advancements in government policies have significantly driven the reduction of carbon footprints, as evidenced by the substantial growth of wind and solar photovoltaic energy in regions such as Europe, the United States, India, and the People's Republic of China. From the late 1990s to 2019, global wind power capacity expanded by approximately 5%, while solar photovoltaic and biofuel production increased by 2.5% and 3%, respectively. Despite these advancements, the current pace of expansion remains insufficient to meet the Net-ZERO emissions target, which requires a 55% replacement of global energy sources with renewable alternatives. This underscores the urgent need to enhance the utilization of renewable energy sources, including wind, wave, and solar energy.[2]

Solar energy, in particular, stands out as one of the most abundant energy resources available globally. This fact reflected on the biological process of photosynthesis, the process of capturing and storing solar energy to produce chemical molecules to sustain life on Earth. The mimicry of the natural photosynthesis process can be one of the alternatives to essentially make use of solar energy. In the next section, the explanation of the light-dependent reactions of photosynthesis is presented.[3–5]

1.1 Natural Photosynthesis

The photosynthesis process involves a complex molecular system that converts light into energy. Green plants, cyanobacteria, and algae, called autotrophic organisms, can convert light through photosynthesis to produce energy.[6] Photosynthesis consists of two sets of reactions: the light-dependent reactions and the Calvin cycle.[3–5]

The light-dependent reactions are crucial to the context of this thesis and can be summarized as follows. These reactions occur within the thylakoid membrane, which creates a distinct compartment that separates oxidation and reduction processes. Within the chloroplast, the Z-scheme involves two main compartments: the thylakoid lumen and the stroma (Figure 1.2).

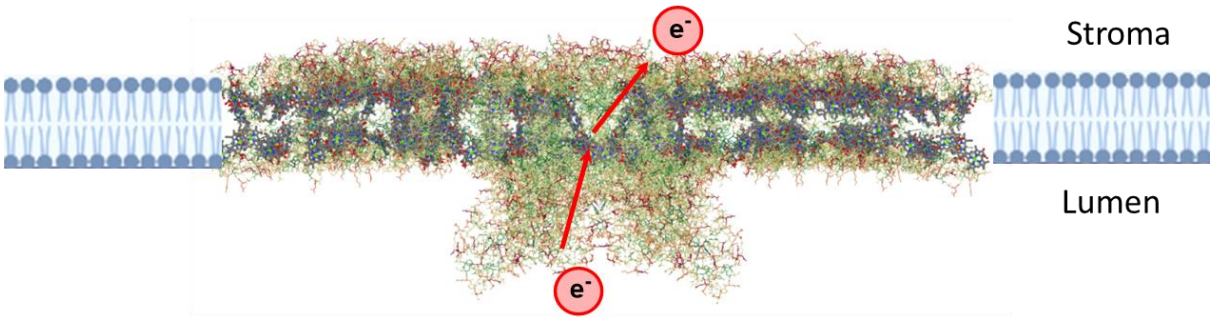

Figure 1.2 Two compartments in the thylakoid membrane: the lumen and the stroma. The electron transfer chain involves the PS I and PS II, which are embedded in the membrane.[4] The lipid bilayers created with BioRender.com.

The Z-scheme illustrates the flow of electrons from water to $NADP^+$ during the light-dependent reactions (Figure 1.3). The thylakoid lumen is the internal space enclosed by the thylakoid membranes, where water molecules are split, releasing electrons, protons, and oxygen. The process continues in the thylakoid membrane, where Photosystem I (PS I) and Photosystem II (PS II) operate in series. Light energy excites the central chlorophyll P680 in PS II, raising it to its excited state, P680*. The initial electron transfer begins when P680* donates an electron to pheophytin a (Pheo a). The electron transport chain then moves through a series of carriers, progressing from Pheo a to plastoquinone Qa, then to plastoquinone Qb, and finally to the cytochrome b6f complex (Cyt b6f). The Cyt b6f complex oxidizes plastoquinol and reduces plastocyanin, serving as a connector between the two photosystems. Simultaneously, light excites the reaction center chlorophyll P700 in PS I. The excited state P700* transfers an electron through a series of iron-sulfur centers to ferredoxin, which ultimately reduces $NADP^+$ to NADPH via the enzyme ferredoxin-$NADP^+$ reductase. In the stroma, the Calvin cycle (dark reactions) occurs, utilizing NADPH for carbon fixation to produce sugar.[4,6]

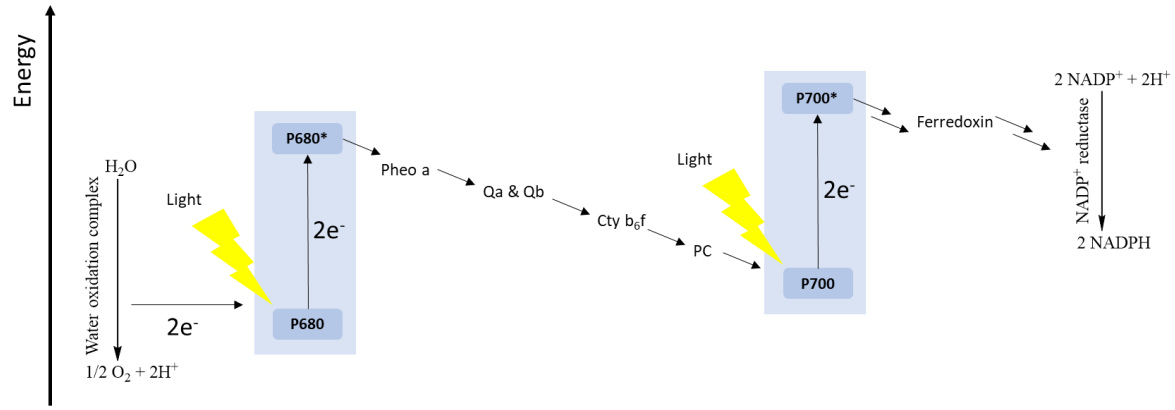

Figure 1.3 Simplified Z-scheme of photosynthesis system: illustrates the pathway of electron flow from water oxidation to $NADP^+$ reduction during the light-dependent reactions of photosynthesis.

In summary, the thylakoid membrane plays a crucial role in facilitating the light-dependent reactions by providing a medium for the active components of PS I and PS II. The compartmentalization properties of the membrane can effectively separate the water oxidation reaction and reduction reactions of $NADP^+$. These aspects are the key topics of this thesis.

1.2 Lipid Bilayers

The major part of this thesis deals with lipid bilayers. The relevant definitions, properties, and integration strategies are therefore summarized in this section.

Amphipathic lipids in an aqueous solution can self-assemble to form lipid bilayers. These amphipathic molecules consist of a hydrophilic polar head group that is covalently connected to hydrophobic hydrocarbon chains. Amphipathic phospholipids primarily contain a phosphate head group and two fatty acid chains that serve as hydrophobic tails (the examples are given in Chapter 2). The structure of lipid bilayers is formed by two sheets of lipid molecules arranged with their hydrophobic tails facing inward and their hydrophilic heads facing outward. The typical thickness of a lipid bilayer is about 3 to 5 nanometers (Figure 1.4).[7,8]

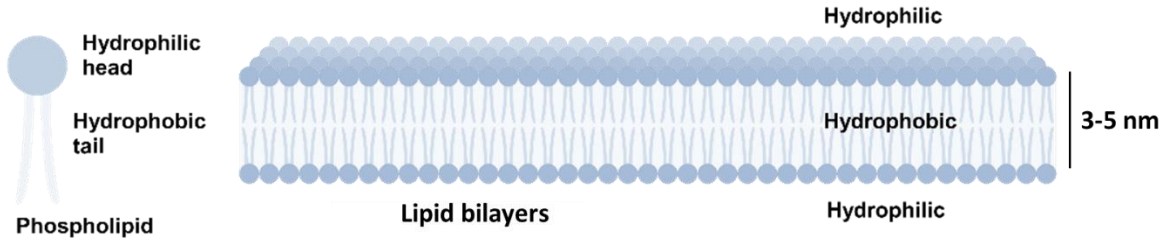

Figure 1.4 Structure of lipid bilayers, membrane, built from an amphipathic phospholipid. Created with BioRender.com.

The forces that hold amphipathic molecules together arise from weaker van der Waals forces, hydrophobic interactions, hydrogen bonding, and screened electrostatic interactions. These forces affect the interactions of the aggregates and the intermolecular forces within each aggregate based on different conditions, such as varying concentrations of electrolytes, lipids,

pH, or temperature. The hydrophobic attraction at the hydrocarbon-water interface and the hydrophilic head groups are the primary forces that govern the self-assembly of amphipathic into well-defined structures, such as bilayers. In the interfacial region, these two interactions compete as opposing forces; one tends to increase, while the other tends to decrease the interfacial area per molecule exposed to the aqueous phase. The most favored structure of the molecule can be measured or estimated based on its packing factor (χ), which is determined by the given optimal area a_0, the volume of their hydrocarbon v, and the critical chain length of the hydrophobic chain l_c, this data can be obtained from the crystallographic data of the amphipathic molecule. The value of χ corresponds to the favored structure, the spherical micelles ($\chi \leq \frac{1}{3}$) to non-spherical (ellipsoidal) micelles ($\frac{1}{3} < \chi < \frac{1}{2}$) to cylindrical or rod-like micelles ($\chi \approx \frac{1}{2}$) to various interconnected structures ($\frac{1}{2} < \chi < 1$) to vesicles and extended bilayers ($x \approx 1$) and finally to a family of "inverted" structures ($\chi > 1$) (Figure 1.5).[9]

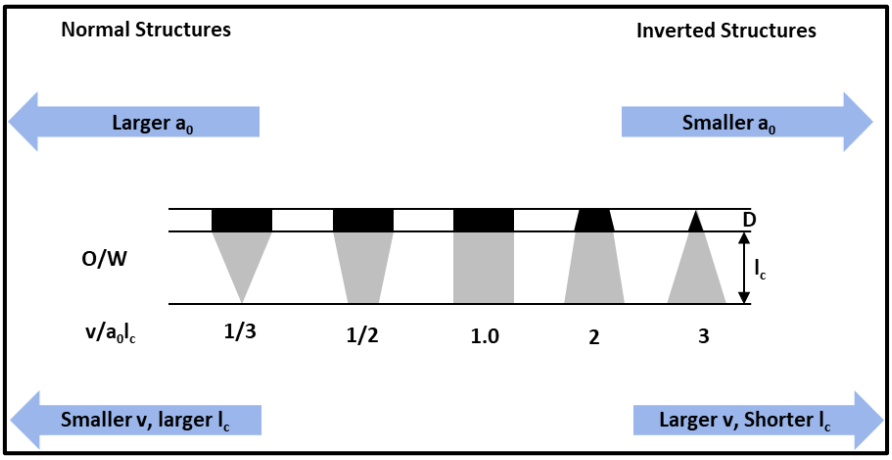

Figure 1.5 The packing factor χ, determines the most favored shapes of the self-assembled amphipathic molecules: estimated based on the optimal area (a_0), the volume of the hydrocarbon (v) and the length of the hydrophobic chain (l_c).

The formation of bilayers results from a χ value close to 1. If energetically favorable, the bilayers will close into spherical structures, forming vesicles or liposomes (spherical formations of bilayers with a diameter greater than 1000 nm are referred to as vesicles, while those with a diameter less than 1000 nm are called liposomes), rather than remaining as infinite planar bilayers. This curvature minimizes the surface area-to-volume ratio, reducing unfavorable interactions between the hydrophobic regions and water. Most biological lipid membranes form spherical bilayers or vesicles to ensure (1) that the bilayer membrane can compartmentalize different regions of cells; (2) that the membrane can remain intact even at low concentrations of lipids; and (3) that the membrane, when composed of unsaturated or branched lipids, remains in a fluid state at physiological temperatures. A critical aspect of the

fluidity of the lipid chain is that different lipid types can be packed together while maintaining a curved bilayer configuration.[9]

When using lipid bilayers as a medium for embedding the functional molecules four main strategies can be used: a) covalent attachment of the functional molecules to the lipid that is incorporated into the membrane, b) electrostatic interaction of charged functional molecules with the charged head groups of the lipids, c) integration of the functional molecules into the bilayer membranes, targeting the interface, the bulk phase, or the hydrophobic core of the membrane, and d) embedding the hydrophobic functional molecules that targets the hydrophobic core of the membrane (Figure 1.6).

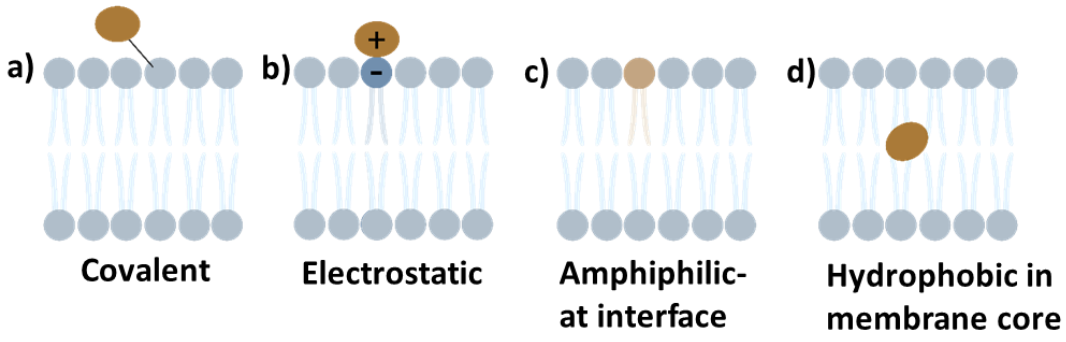

Figure 1.6 Strategies to integrate functional molecules in lipid bilayer membrane. Created with BioRender.com.

Covalent attachment strategies for lipid functionalization offer strong and stable connections between functional molecules and bilayer membranes, enabling precise control over modifications and allowing a wide range of molecules to be attached to the membrane.[10,11] The electrostatic strategies depend on the interactions between charged functional molecules and the oppositely charged lipid head groups.[12,13] For amphiphilic molecules at the interface, it is essential to design amphipathic functional molecules, as the alignment of the functional molecules within the membrane will depend on the structure of the functional molecules.[14–16] The hydrophobic in membrane core strategies focus on tethering the solubility of insoluble molecules in aqueous solutions, where the functional molecules remain soluble in the hydrophobic core of the membrane.[17]

1.3 Light Absorption and the Excited State

The major part of this thesis deals with light-driven reactions. The relevant definitions, light absorption, and excited state deactivation are therefore summarized in this section.

A light-driven reaction, also known as a photochemical reaction, is a chemical process that is initiated by the absorption of light energy. The photochemical reaction occurs when molecules can absorb the energy of light, followed by excitation. The molecules at the excited state will

have excess energy that usually leads to a different bond distance and angle than the ground state. The excited states have significantly higher vibrational and rotational energies. These differences in energy and structure result in different chemical properties.[18]

The Franck-Condon principle describes the behavior of electronic transitions in molecules, particularly in the context of the absorption of light. It is based on the disparity between the time scales of electronic and nuclear motions. According to the principle, electronic transitions occur so rapidly that the positions of nuclei remain essentially "frozen" during the process (Figure 1.7). Consequently, in photochemical reactions, the initial excited state is formed with the same nuclear geometry as the ground state. This principle explains the shape and intensity distribution of absorption bands in absorption spectra, as different vibrational levels have various probabilities determined by the overlap of the vibrational wavefunctions of the initial and final states.[18,19]

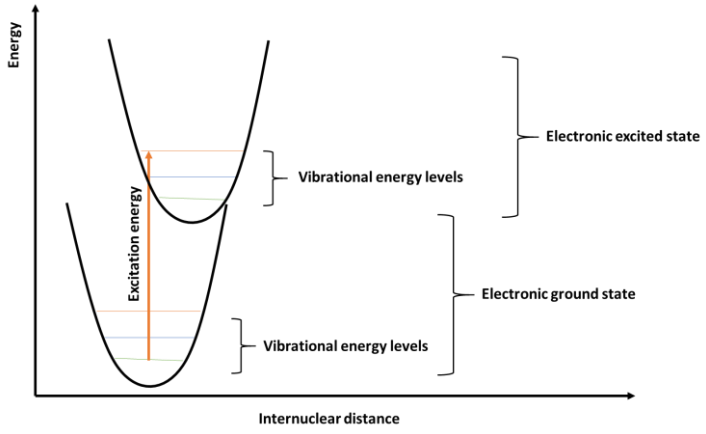

Figure 1. 7 In the Franck-Condon principle, electronic transitions occur very quickly compared to nuclear motions. Vibrational levels with minimal changes in the internuclear distance become favorable.

The deactivation processes of excited molecules that lead back to their ground state are known as relaxation processes, which can be graphically represented in the Jablonski diagram (see Figure 1.8). Relaxation can occur through multiple pathways, primarily categorized into two types: radiative and non-radiative processes. One specific non-radiative pathway is called internal conversion, which involves a transition from a higher electronic state to a lower electronic state, but not directly to the ground state; no radiation is emitted during this transition. Radiative processes occur through two mechanisms: fluorescence and phosphorescence. The relaxation from a singlet excited state occurs when an electron is excited without a spin flip, is known as fluorescence. Conversely, when an electron undergoes a spin flip during excitation, it is referred to as a triplet excited state. The transition associated with this spin flip is known as intersystem crossing, which is a non-radiative process that occurs between two isoenergetic vibrational levels belonging to electronic states of different

multiplicities. Excited state deactivation from a triplet excited state is known as phosphorescence.[20] The Jablonski diagram aids in understanding the photoluminescence lifetime by visually representing the processes that govern how long a molecule remains in an excited state before returning to the ground state. The photoluminescence lifetime refers to the average time a molecule spends in its excited state before emitting a photon (fluorescence or phosphorescence) or undergoing non-radiative relaxation. By linking energy transitions to time scales, the diagram provides a framework for interpreting time-resolved photoluminescence spectroscopy data. Fluorescence lifetimes typically occur on nanosecond scales, while phosphorescence lifetimes can extend to milliseconds or longer.[20]

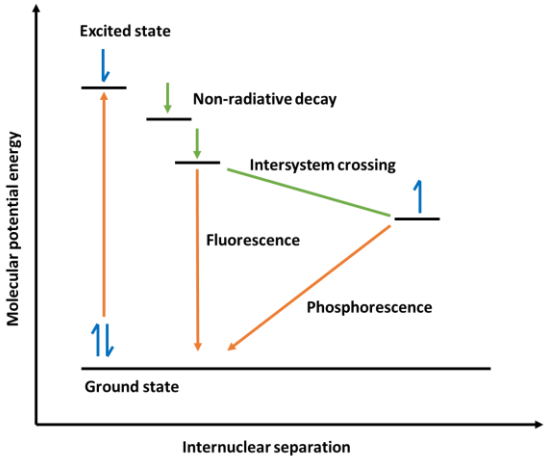

Figure 1.8 Simplified Jablonski diagram represents the dissipation of energy following light excitation, through different pathways: radiative emission, non-radiative dissipation, or rearrangement.

The lifetime and quantum yield of luminescence are two properties explicitly illustrated by the Jablonski diagram. The lifetime of luminescence is essential to determine the ability of the fluorophore to interact or diffuse in its environment. This information is available from its emission. The quantum yield is the ratio of the number of molecules reacted per photon absorbed. The reaction that obeys Einstein's law of photochemical equivalence will decompose one molecule per photon. When two or more molecules are decomposed per photon, the reaction has a high quantum yield. The reaction has a low quantum yield if the number of molecules decomposed is less than one per photon. The high quantum yield is when one photon decomposes or forms more than one molecule.[18]

Photoluminescence emission is a random process leading to relaxation to the ground state. The intensity of photoluminescence has a wide variety. Decreasing photoluminescence intensity is known as quenching. Quenching occurs when the excited state is deactivated by other molecules (quencher). The Stern-Volmer equation is well-known for describing quenching due to collisions with a quencher. Photoluminescence quantum yield F, the Stern-Volmer

quenching constant is K, k_q is the bimolecular quenching constant, τ_0 is the quenched lifetime, and Q is quencher concentration. The more significant value of K indicates that the fluorophore is free in the solution. If the fluorophore is inaccessible to the quenchers, it will find a low value of K.[21]

$$\frac{F_0}{F} = 1 + K\,[Q] = 1 + k_q\,\tau_0\,[Q] \qquad \text{Equation 1}$$

Photoluminescence quenching also occurs by various processes aside from collisional quenching with a quencher. Chromophores can weaken the incident light, or chromophores can form complexes with a quencher. When the emission has a more extended period, it allows the excited state to interact with other molecules.[21] Photoluminescence can be measured with two measurements: steady-state and time-resolved. Steady-state measurement observed the illuminated sample with a continuous beam of light and recorded the intensity of the emission spectrum. This measurement is an average of the time-resolved phenomena over the intensity decay of the sample. The time-resolved measurement is used to measure the sample's intensity decay or anisotropy decay. The intensity decays contain information about the presence of more than one conformational state. The time-resolved measurement also revealed the presence of transfer energy, and intensity decays how acceptors are distributed around the donors.[22]

1.4 Light-Driven Reactions in Lipid Bilayers

The upcoming chapters will explore various examples of utilizing lipid bilayer membranes for light-driven reactions. Chapter 2 provides a review of recent advancements in biomimetic and light-induced energy conversions involving liposomes and polymersomes, focusing on key areas such as energy transfer, electron transfer, photocatalysis, and artificial photosynthesis. Chapters 3, 4, and 5 will present specific case studies on the functionalization of liposomes with organic chromophores for artificial photosynthesis.

1.5 References

1. Net Zero Emissions by 2050 Scenario (NZE) – Global Energy and Climate Model – Analysis. *IEA* https://www.iea.org/reports/global-energy-and-climate-model/net-zero-emissions-by-2050-scenario-nze.
2. Clean energy technologies – the state of play – Energy Technology Perspectives 2020 – Analysis. *IEA* https://www.iea.org/reports/energy-technology-perspectives-2020/clean-energy-technologies-the-state-of-play.
3. Chow, W. S. Photosynthesis: From Natural Towards Artificial. *Journal of Biological Physics* **29**, 447–459 (2003).
4. Nelson, N. & Yocum, C. F. Structure and function of photosystems I and II. *Annual Review of Plant Biology* **57**, 521–565 (2006).

5. Ferreira, K. N., Iverson, T. M., Maghlaoui, K., Barber, J. & Iwata, S. Architecture of the Photosynthetic Oxygen-Evolving Center. *Science* **303**, 1831–1838 (2004).
6. Nelson, N. & Ben-Shem, A. The complex architecture of oxygenic photosynthesis. *Nat Rev Mol Cell Biol* **5**, 971–982 (2004).
7. Marsh, D. *Handbook of Lipid Bilayers*. (CRC Press, 2013). doi:10.1201/b11712.
8. Drabik, D., Chodaczek, G., Kraszewski, S. & Langner, M. Mechanical Properties Determination of DMPC, DPPC, DSPC, and HSPC Solid-Ordered Bilayers. *Langmuir* **36**, 3826–3835 (2020).
9. Israelachvili, J. N. Intermolecular and Surface Forces.
10. van Lengerich, B., Rawle, R. J. & Boxer, S. G. Covalent attachment of lipid vesicles to a fluid supported bilayer allows observation of DNA-mediated vesicle interactions. *Langmuir* **26**, 8666–8672 (2010).
11. Flores, J., White, B. M., Brea, R. J., Baskin, J. M. & Devaraj, N. K. Lipids: chemical tools for their synthesis, modification, and analysis. *Chem Soc Rev* **49**, 4602–4614 (2020).
12. Ramos, L., Schönhoff, M., Luan, Y., Möhwald, H. & Brezesinski, G. Electrostatic interactions between polyelectrolyte and amphiphiles in two- and three-dimensional systems. *Colloids and Surfaces A: Physicochemical and Engineering Aspects* **303**, 79–88 (2007).
13. Kundlacz, T. & Schmidt, C. Deciphering Solution and Gas-Phase Interactions between Peptides and Lipids by Native Mass Spectrometry. *Anal. Chem.* **95**, 17292–17299 (2023).
14. Nau, R. E. P., Bösking, J. & Pannwitz, A. Compartmentalization Accelerates Photosensitized NADH to NAD+ Conversion. *ChemPhotoChem* **6**, e202200158 (2022).
15. Casey, D., Charalambous, K., Gee, A., Law, R. V. & Ces, O. Amphiphilic drug interactions with model cellular membranes are influenced by lipid chain-melting temperature. *J R Soc Interface* **11**, 20131062 (2014).
16. Pannwitz, A. *et al.* Mimicking Photosystem I with a Transmembrane Light Harvester and Energy Transfer-Induced Photoreduction in Phospholipid Bilayers. *Chemistry – A European Journal* **27**, 3013–3018 (2021).
17. Kalipatnapu, S. & Chattopadhyay, A. Membrane Protein Solubilization: Recent Advances and Challenges in Solubilization of Serotonin1A Receptors. *IUBMB Life* **57**, 505–512 (2005).
18. Roundhill, D. M. *Photochemistry and Photophysics of Metal Complexes*. (Springer Science+Business Media, LLC, 1994).
19. Balzani, V., Ceroni, P. & Juris, A. *Photochemistry and Photophysics*. (Wiley-VCH Verlag, Weinheim, Germany, 2014).
20. *Principles of Fluorescence Spectroscopy*. (Springer US, Boston, MA, 2006). doi:10.1007/978-0-387-46312-4.
21. Gehlen, M. H. The centenary of the Stern-Volmer equation of fluorescence quenching: From the single line plot to the SV quenching map. *Journal of Photochemistry and Photobiology C: Photochemistry Reviews* **42**, 100338 (2020).
22. Munishkina, L. A. & Fink, A. L. Fluorescence as a method to reveal structures and membrane-interactions of amyloidogenic proteins. *Biochimica et Biophysica Acta (BBA) - Biomembranes* **1768**, 1862–1885 (2007).

Chapter 2

Recent Advances in Light Energy Conversion with Biomimetic Vesicle Membranes

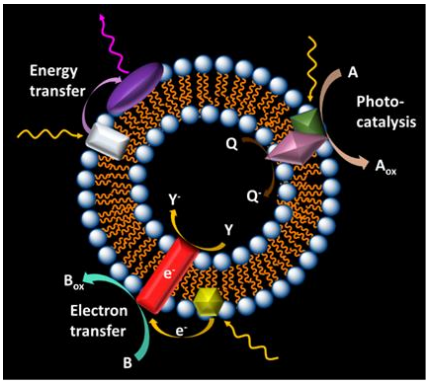

Vesicles can compartmentalize chemical reactions and provide possibilities for modifying the membrane with membrane-bound molecules. This mini-review highlights recent advances in biomimetic and light-induced energy conversions with liposomes and polymersomes, which are relevant to energy transfer, electron transfer, photocatalysis, and artificial photosynthesis. Lipid bilayer membranes are ubiquitous in natural chemical conversions. They enable self-assembly and compartmentalization of reaction partners, and it becomes increasingly evident that a thorough fundamental understanding of these concepts is highly desirable for chemical reactions and solar energy conversion with artificial systems. This mini-view focuses on selected case studies from recent years, most of which were inspired by either membrane-facilitated light harvesting or respective charge transfer. The main focus is on highly biomimetic liposomes with artificial chromophores, and some cases for polymer membranes will be made. Furthermore, we categorized these studies into energy transfer and electron transfer, with phospholipid vesicles and polymer membranes for light-driven reactions.

Author contributions:
Novitasari Sinambela: Outline and literature research on the chapter electron transfer at and across lipid bilayers, drawing of all illustrations, and manuscript revision.
Julian Bösking: Outline and literature research on the chapter energy transfer in the lipid bilayers part and manuscript revision.
Amir Abbas: Outline and literature research on the chapter light-energy conversion with the polymersomes part and manuscript revision.
Andrea Pannwitz: Paper writing and manuscript revision.

This chapter was published as a Minireview: Novitasari Sinambela, Julian Bösking, Amir Abbas, and Andrea Pannwitz*, Recent Advances in Light Energy Conversion with Biomimetic Vesicle Membranes, ChemBioChem **2021**, 22, 3140–3147. DOI: 10.1002/cbic.202100220. This article is licensed under CC BY 4.0 (https://creativecommons.org/licenses/by/4.0).

Check for updates

ChemBioChem

Minireviews
doi.org/10.1002/cbic.202100220

Chemistry Europe
European Chemical Societies Publishing

Recent Advances in Light Energy Conversion with Biomimetic Vesicle Membranes

Novitasari Sinambela,[a] Julian Bösking,[a] Amir Abbas,[a] and Andrea Pannwitz*[a]

Lipid bilayer membranes are ubiquitous in natural chemical conversions. They enable self-assembly and compartmentalization of reaction partners and it becomes increasingly evident that a thorough fundamental understanding of these concepts is highly desirable for chemical reactions and solar energy conversion with artificial systems. This minireview focusses on selected case studies from recent years, most of which were inspired by either membrane-facilitated light harvesting or respective charge transfer. The main focus is on highly biomimetic liposomes with artificial chromophores, and some cases for polymer-membranes will be made. Furthermore, we categorized these studies into energy transfer and electron transfer, with phospholipid vesicles, and polymer membranes for light-driven reactions.

1. Introduction

Chemical conversions associated to phospholipid bilayer membranes are ubiquitous in nature, and it becomes increasingly evident that a thorough fundamental understanding of this important class of self-assembly is highly desirable for chemical reactions and solar energy conversion, as it enables for compartmentalization of reactions and self-assembly of reaction partners.[1–3] Examples for compartmentalized chemical reactions were demonstrated using interfaces of two liquids, lipid bilayer membranes or similar soft materials.[3–7] The aspect of self-assembly was shown to be promising for the reduction of CO_2, proton reduction to produce H_2, and water oxidation.[8–13] In nature, the most relevant light-driven reactions are taking place during photosynthesis and in the thylakoid membrane of chloroplasts. Precisely oriented chromophores in transmembrane proteins are harvesting light and using it to induce a transmembrane charge transfer for compartmentalized water oxidation as well as nicotinamide adenine dinucleotide phosphate (NADP) reduction to NADPH and adenosine triphosphate (ATP) generation.[14–16] The most interesting transmembrane protein complexes for sunlight energy conversion are the light harvesting complexes (LHC) as well as photosystem I and II (PSI and PSII, see Figure 1). The LHC absorb light of various energies and transfer this energy to the central chromophores in PSII and PSI. Charge separation is induced and electrons are transferred between the photosystems, to finally provide electrons for NADP reduction on one side, while water is oxidized on the other side of the membrane. Both the protein scaffold and the membrane composition have an influence on the effectiveness of these processes in nature.[15,17] Inspired by nature, the concept of self-assembly and compartmentalization via lipid membranes is highly promising for synthetic chemical reactions. Examples of bilayer and vesicle forming molecules and polymers are depicted in Figure 2. The composition and properties of lipid bilayers can influence energy and electron transfer dynamics within lipid bilayers, as shown for the natural light harvesting complex,[17] as well as for artificial systems in this review.

This minireview focusses on selected case studies from recent years, most of which were inspired by either membrane-facilitated light harvesting or respective charge transfer. The main focus is on highly biomimetic liposomes with artificial chromophores, and some cases for polymer-membranes will be made. Furthermore, we categorized these studies into energy transfer and electron transfer, with phospholipid vesicles, and polymer membranes for light-driven reactions.

For a tutorial introduction, including detailed physicochemical aspects, the reader is referred to a recently published tutorial review,[18] and ion transfers,[19] and somewhat older studies were reviewed elsewhere.[20,21]

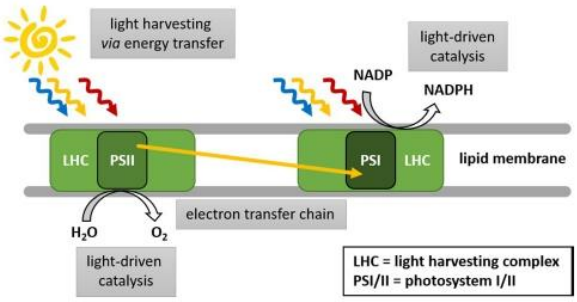

Figure 1. The LHCs as well as PSI and PSII play a central role in valorization of sunlight energy.

[a] N. Sinambela, J. Bösking, A. Abbas, Dr. A. Pannwitz
Institut für Anorganische Chemie I, Universität Ulm
Albert-Einstein-Allee 11, 89081 Ulm (Germany)
E-mail: andrea.pannwitz@uni-ulm.de

© 2021 The Authors. ChemBioChem published by Wiley-VCH GmbH. This is an open access article under the terms of the Creative Commons Attribution License, which permits use, distribution and reproduction in any medium, provided the original work is properly cited.

ChemBioChem
Minireviews
doi.org/10.1002/cbic.202100220
Chemistry Europe
European Chemical Societies Publishing

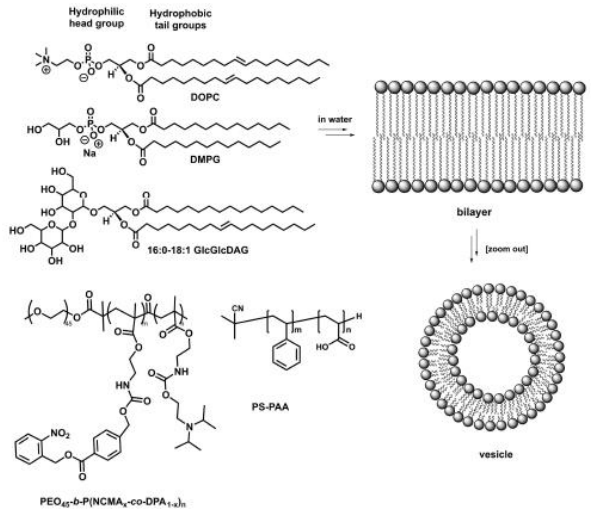

Figure 2. Examples for bilayer vesicle forming molecules: Phospholipids DOPC (1,2-dioleoyl-*sn*-glycero-3-phosphocholine) and DMPG (1,2-dimyristoyl-*sn*-glycero-3-phosphoglycerol), galactolipid 16:0–18:1 GlcGlcDAG (1-palmitoyl-2-oleoyl-3-bis(β-*d*-glucosyl)-*sn*-glycerol), and the block copolymers PEO_{45}-*b*-P($NCMA_x$-*co*-DPA_{1-x})$_n$ (PEO = polyethyleneoxide, NCMA = 2-nitrobenzyl ester-photocaged carboxyl monomer, DPA = tertiary amine-containing monomer with carbamiate side linkage) and PS-PAA (polystyrene-polyacrylic acid).

2. Energy Transfer in Lipid Bilayers

As described earlier, one of the key components in natural photosynthesis is the light harvesting complex which absorbs and transfer light energy. In the following, several studies of energy transfer in lipid membranes are reviewed. Most of these studies operate via Förster resonance energy transfer (FRET), while some energy transfer mechanisms rely on collision-induced energy transfers.

Depending on the composition, lipid bilayers can form different domains. Saturated phospholipid, such as 1,2-dipalmitoyl-*sn*-glycero-3-phosphocholine (DPPC), in combination with cholesterol form liquid ordered (Lo) domains, while unsaturated phospholipid, such as 1, 2-dioleoyl-*sn*-glycero-3-phosphocholine (DOPC) form liquid disordered (Ld) domains.[22] In order to generate a light harvesting system, efficient energy transfer, e.g. via Förster resonance energy transfer (FRET), is interesting. When constructing such a system, it must be kept in mind, that distance and distribution of donor and acceptor molecules are the main keys to achieve efficient FRET. Koshiyama and Ohba *et al.* have taken advantage of the domain specificity of selected energy donor and acceptor molecules within lipid bilayers.[23] Specifically, they showed that a maximum FRET rate could be achieved with the FRET pair of a modified fluorescein and hydrophobic zinc porphyrin (see Figure 3a). Both chromophores accumulate preferably in the liquid disordered Ld domain of lipid bilayers. By adjusting the lipid composition of the liposomes, via decreasing the DOPC:DPPC ratio to 1:3, the Ld domains decreased in size, which lead to a higher local concentration of the chromophores within these Ld domains. No energy transfer was observed in homogeneous solution and inefficient energy transfer was observed in vesicles with only Ld domain (1:0 DOPC:DPPC ratio). With this concept, the authors showed an efficient way of increasing light harvesting properties within lipid bilayers using modification of domain size.[23]

Light harvesting via energy transfer in lipid bilayers was used by Ikeda *et al.* to increase the amount of photogenerated singlet oxygen ($^1O_2$).[24] The hydrophobic oxygen sensitizer fullerene (C60) is a weak light absorber in the visible spectrum. Using lipid bilayer membranes, it was combined with the amphiphilic light harvester 1,10-dioctadecyl-3,3,30,30-tetramethylindodicarbocyanine (DiD) which strongly absorbs visible light between 600 and 700 nm (Figure 3b). Due to its positive charge, the latter molecule resides at the membrane-water interface, while the hydrophobic C60 resided in the hydrophobic region of the membrane. Adding a positive charge to the C60 via a quarternary ammonium group (C60-N^+, see Figure 3b) allowed for co-assembly of both chromophores at the membrane-water interface. Energy transfer from



Novitasari Sinambela studied chemistry at the Bandung Institute of Technology, Indonesia. She received her MSc degree in 2019. She is currently a PhD candidate in the laboratory of Andrea Pannwitz at Ulm University. Her work focusses on liposomes for artificial photosynthetic purposes, such as photocatalytic water splitting and transmembrane electron transfer.



Julian Bösking studied chemistry at Ulm University, Germany. After receiving his MSc degree in 2020 he started his PhD at Ulm University. His work focusses on energy transfer in vesicles.



Amir Abbas studied chemistry at the University of Sassari, Italy. He received his MSc degree in 2020 and is currently a PhD candidate in Andrea Pannwitz' research group at Ulm University on the functionalization of liposomes and polymersome vesicles.



Andrea Pannwitz obtained her PhD in 2017 at the University of Basel in Switzerland. After her Postdoc at Leiden University, The Netherlands, she started her independent career as junior professor for Inorganic Chemistry and Energy Conversion at Ulm University in Germany, with a major interest in photochemical conversions at membrane interfaces.

© 2021 The Authors. ChemBioChem published by Wiley-VCH GmbH

ChemBioChem
Minireviews
doi.org/10.1002/cbic.202100220
Chemistry Europe
European Chemical Societies Publishing

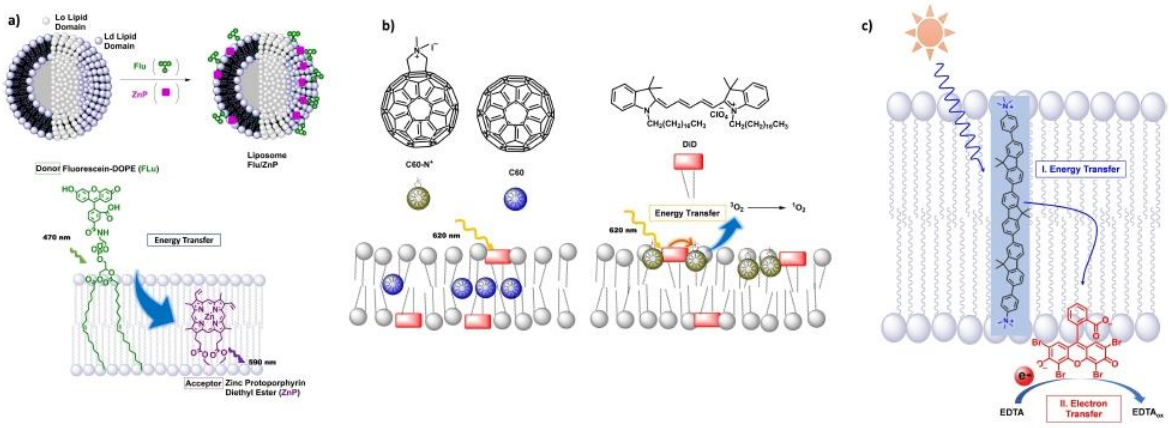

Figure 3. a) Accumulation of chromophores in Ld domains of liposomes for efficient energy transfer. Reproduced with permission from ref. [23]; Copyright: 2017, The Chemical Society of Japan. b) Light harvesting and energy transfer are enhanced at the membrane-water interface using amphiphilic, strongly at 620 nm absorbing DiD as energy donor and C60-N^+ as energy acceptor. Reproduced with permission from ref. [24]; Copyright: 2018, Wiley-VCH GmbH. c) Light-absorption by a transmembrane oligoaromatic chromophore, followed energy transfer to the acceptor, eosin Y and electron transfer at the membrane interface to water. Image reproduced from ref. [25]; published 2020 by Wiley-VCH GmbH, Creative Commons CC BY license.

photoexcited DiD to hydrophobic C60 and amphiphilic C60-N^+ was demonstrated via luminescence quenching. It was found that the assembly of energy donor and acceptor at the membrane-water interface strongly increased the energy transfer, from 55% to 87%. Likewise, the follow-up generation of singlet oxygen strongly increased upon co-assembling donor and acceptor at the membrane-water interface, as shown by bleaching of the singlet oxygen probe 1,10-anthracenediyl-bis(methylene)dimalonic acid (ABDA) at 400 nm. The same energy transfer effect was shown for other strongly absorbing light harvester when excitation occurred at their respective absorption maximum.[24] This study shows, liposomes are a powerful method to co-assemble energy transfer couples to increase quantum yields for follow-up reactions such as the generation of reactive oxygen species.

In another study, a biscationic oligofluorene dye with a hydrophobic core and charged headgroups was embedded into phospholipid bilayers (see Figure 3c). This dye acted as a light harvester for energy transfer. Addition of the energy acceptor eosin Y (EY^{2-}) to the phospholipid bilayer membrane induced energy transfer from the oligofluorene to EY^{2-} which was observed by luminescence quenching of the donor and lighting up of the acceptor emission. The acceptor's emission indicated that EY^{2-} was in its reactive electronic excited state. In their study, the authors used this energy for a follow-up electron transfer with the sacrificial electron donor ethylenediamine tetra acetic acid (EDTA) in solution.[25]

For some photochemical applications it is impossible to excite with high-energy light such as blue or UV-light, because light is absorbed by a thick layer of tissue or the solvent itself in a larger batch reactor. On the other hand, lower energy photons, such as green or red-light photons, can easily cross as they are poorly absorbed by the tissue or solvent. Sometimes, involving a photosensitizer absorbing at higher wavelength (lower energy) is sufficient to perform the desired photochemistry, as described earlier in this chapter.[24] However, some processes require the use of high energy photons for excitation.

Triplet-triplet annihilation upconversion is a method to generate high energy photons from low energy photons: The photosensitizer absorbs low energy photons and undergoes intersystem crossing to generate the excited triplet state of the photosensitizer. Upon collision with an annihilator molecule, this energy is transferred to generate the triplet excited state of the annihilator molecule and the ground state of the photosensitizer. Collision of two triplet annihilator molecules leads to triplet-triplet annihilation, whereby one molecule is promoted to the high-energy excited singlet state, and one molecule falls back into the ground state. The singlet excited state annihilator molecule then returns to the ground state by emitting a high energy photon.[27] As the annihilation process is collision based, the local concentration of the triplet excited state annihilator must be sufficiently high, which preferably happens when the triplet excited state lifetime of the annihilator molecules is long. Suitable photosensitizer-annihilator couples are platinum or palladium porphyrins in combination with 9,10-diphenylanthracene or perylene respectively (see Figure 4). In liposomes, these couples were shown to generate blue light from green, or red light respectively with a quantum yield of 2.3% and 0.5% respectively.[26] It is noted, that the fluidity of the membrane played an important role in achieving high quantum yields for triplet-triplet annihilation upconversion: By increasing the temperature above the gel-to-fluid phase transition temperature, the mobility within the membrane is significantly increased and blue light is generated with a high quantum yield.

Furthermore, these high energy photons were directly used in a productive ligand exchange reaction in neighboring liposomes functionalized with a cholesterol-sulfur-ruthenium-complex (Figure 4). Upon photoexcitation via in situ generated blue light the sulfur-ruthenium coordination bond is split via a

© 2021 The Authors. ChemBioChem published by Wiley-VCH GmbH

ChemBioChem
Minireviews
doi.org/10.1002/cbic.202100220
Chemistry Europe
European Chemical Societies Publishing

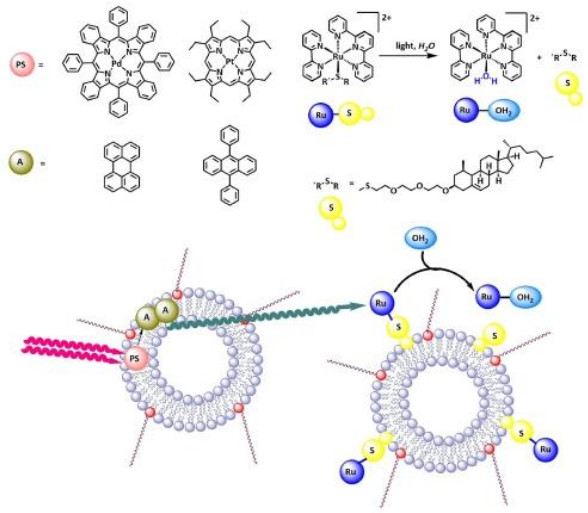

Figure 4. Triplet-triplet-annihilation-upconversion combined with a photochemical reaction. Reproduced with permission from ref. [26]; Copyright: 2013, Wiley-VCH GmbH. (PS = photosensitizer, A = annihilator).

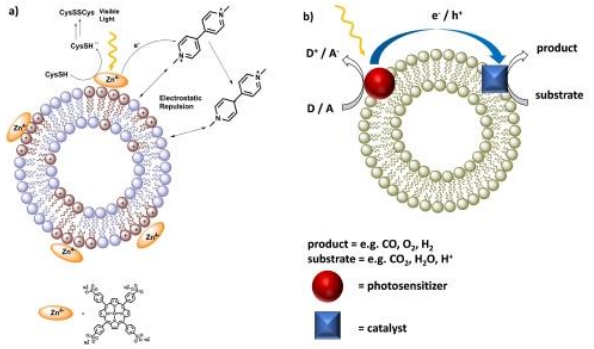

Figure 5. a) Light induced charge transfer from methyl viologen to photo-excited zinc porphyrin. Reproduced with permission from ref. [31]; Copyright: 2016, American Chemical Society. b) Charge transfer during photocatalysis. Upon photoexcitation the photosensitizer is oxidized or reduced by an acceptor (A) or donor (D) followed by electron (e^-) or hole (h^+) transfer to the active catalyst.

photochemical ligand exchange, and the $[Ru(tpy)(bpy)(OH_2)]^{2+}$ (tpy = terpyridine, bpy = bipyridine) complex is released into the surrounding aqueous bulk.[26] This principle could also be used with photosensitizer-annihilator pair and photoactivatable ruthenium complexes on the same liposomes,[28,29] and might be relevant for photochemical cancer therapy in deeper tissue,[26–30] and other photochemical conversions with liposomes.

3. Electron Transfer at and Across Lipid Bilayers

Light-induced charge separation is a challenge in solar energy conversion, including artificial photosynthesis and photoredox catalysis. Oftentimes, productive charge separation is in competition with unproductive charge recombination. The following three strategies ensure the forward reaction. I) Repulsion directly after the charge transfer,[31] II) rapid decomposition of one reactant by using sacrificial oxidants and reductants,[32] and III) kinetic control of the inherent electron transfer rate. The latter is taken into account by Markus' theory, which states, that there is an optimal driving force for an electron transfer as well as a reorganization barrier which play a major role in charge transfer.[33–37]

The repulsion strategy is especially easy to realize with liposomes. By choosing the lipid composition, the liposome surface charges can have positive, neutral or negative surface charges (for examples, see Figure 2 and Figure 5a). In one example, Bonnet *et al.* assembled positively charged liposome membrane surface with a negatively charged zinc porphyrin photosensitizer yielding an overall positively charged membrane surface.[31] Irradiation of these vesicles in presence of positively charged, water soluble methyl viologen lead to bimolecular oxidative quenching. The oxidized porphyrin was re-reduced by cysteine which acted as a sacrificial reductant. In the same experiment with all components present except for the liposomes, the forward reaction (oxidative quenching) was faster, but only little amounts of the final photoproducts were obtained, because the charge recombination within the porphyrin-methyl viologen ion pair was too fast and prevented charge separation. However, the overall positively charged membrane surface enabled for fast repulsion of the positively charged electron acceptor radical directly after the photo-induced electron transfer, and hence effective charge separation.

Taking advantage of the self-assembly and electron transfer dynamics between photosensitizers and catalysts at phospholipid bilayer surfaces, photocatalysis was successfully performed for water oxidation and reduction reactions, as well as CO_2 reduction, to assemble catalysts and photosensitizers in close proximity (Figure 5b).[10,11,38–40]

Key findings of these catalysis studies that the close embedment of photosensitizer and catalyst in the membrane changes the rate limiting step of catalysis, as it increases the electron transfer rate between photosensitizer and catalyst which was shown for water oxidation reactions.[10] The main reason for a fast electron transfer at liposome surfaces is attributed to the close proximity of the reactant. A potential disadvantage of the liposomal system can be, that the overall photooxidation of the photosensitizer at the membrane surface becomes rate limiting, which can be due to a limited access of the water-soluble reactant to the photosensitizer on the pseudo-2D-membrane surface.[10,41]

In catalysis with liposomes, temperature effects related to the transition temperature of the phospholipid mixture were observed. Very slow reaction rates and catalytic activity were observed at temperature below the gel-to-fluid phase transition temperature which is attributed to the higher mobility of the reactants in the membrane and hence increased diffusion rates.[18,38] On the other hand, clustering at lower mobility within the membrane can also increase the catalytic performance, as it

© 2021 The Authors. ChemBioChem published by Wiley-VCH GmbH

ChemBioChem
Minireviews
doi.org/10.1002/cbic.202100220
Chemistry Europe
European Chemical Societies Publishing

was shown for water oxidation in liposomes by König *et al.*[11] Furthermore, rigid hydrophobic environment within the membrane can also protect the individual species from side reactions and therefore increase the catalytic performance in lipid membranes in their more rigid gel phase.[45]

Vesicles have three distinguished compartments: the inner aqueous compartment, the hydrophobic membrane, and the aqueous bulk. Natural cell organelles, such as chloroplasts or mitochondria, take advantage of this compartmentalization for all sorts of biological functions, including cellular energy conversion. In the thylakoid membrane, upon photoinduced charge transfer across the membrane and a transmembrane pH gradient is established generating a proton-motif-force which provides energy for the ATP synthesis.

Transmembrane electron transfer and coupled pH-gradients have been realized in artificial liposomes with molecular systems by various research groups.[1,6] In the following we want to highlight some relatively recent examples which are depicted in Figure 6. Bhosale *et al.* have incorporated molecular dyads into the lipid bilayer of vesicles as schematized in Figure 6a.[42] A dyad typically consists of donor-spacer-acceptor-moieties. The authors have used naphthalene diimide as an acceptor and a zinc porphyrin as a donor. Upon usage of a dithiophene spacer, the length of the molecule spanned 3.5 nm and matched the thickness of an egg yolk phosphatidylcholine-bilayer. Such vesicles were loaded with in the inner compartment with the water-soluble sulfonato naphthoquinone as electron acceptor, and 8-hydroxypyrene-1,3,6-trisulfonate (HPTS) as spectroscopic pH sensor and proton donor. Upon photoexcitation in presence of the sacrificial reductant EDTA in the bulk, the pH in the inner aqueous compartment increased, because of the following process: Photoexcitation of the dyad was followed by (photo-) reduction of the dyad by EDTA. The reduced dyad transferred the electrons intramolecularly across the membrane, and the quinone was reduced. The reduced quinone in the inner compartment took up the surrounding protons and basifies the inner compartment. It was furthermore shown that this transmembrane electron transfer only took place if the length of the dyad matched the bilayer thickness.[42]

Electron transfer across the lipid bilayer membrane can be performed with membrane-soluble electron relays such as hydrophobic quinones, 1-methoxy-*N*-methylphenazium (MMP^+) and tetracyanoquinodimethane (TCNQ).[43,44] Sundmacher *et al.* mimicked mitochondrial transmembrane electron transport with liposomes containing reduced nicotinamide adenine dinucleotide (NADH) in their inner aqueous compartment. The encapsulated NADH was then oxidized by the membrane soluble TCNQ and in turn reduced ferricyanide located outside of liposomes.[44] In this study, the simple molecule TCNQ could be used to replace the natural transmembrane enzymes NADH-ubiquinone oxidoreductase (I) and quinol-cytochrome-c oxidoreductase (II) as well as Fe ions in the heme group of cytochrome C (see Figure 6b).

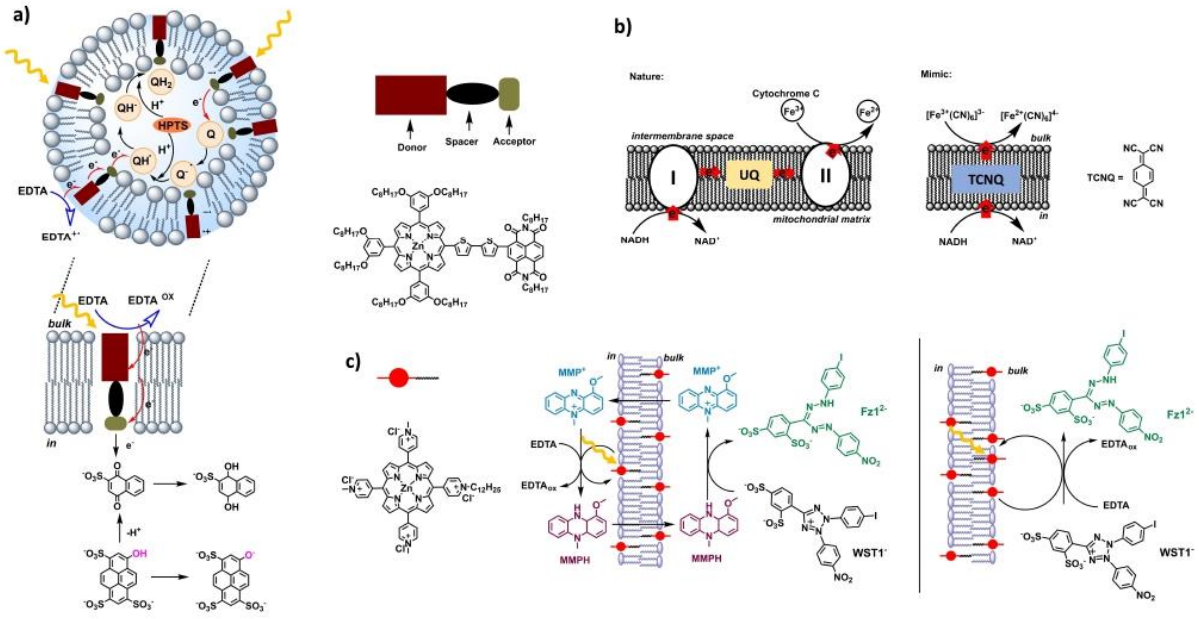

Figure 6. a) Charge separation, transmembrane electron transfer and a proton gradient were achieved with zinc-porphyrin-NDI dyads with suitable spacer length matching the length of lipid bilayer membrane. Reproduced with permission from ref. [42]; Copyright: 2015, Elsevier. b) TCNQ acting as electron relay across lipid bilayer membrane replacing transmembrane electron transfer proteins I and II as well as membrane soluble ubiquinone (UQ). Reproduced with permission from ref. [43]; Copyright: 2018, American Chemical Society. c) An amphiphilic, membrane embedded zinc porphyrin is photoreduced by the sacrificial electron donor EDTA in the inner aqueous compartment of liposomes. The membrane soluble electron relay, MMPH, catalytically transports the electrons across the membrane to reduce the $WST1^-$ dye in the bulk to generate the strongly colored $Fz1^{2-}$. In another scenario, the photoreduction took place at the membrane-bulk interface in absence of the transmembrane electron relay. Reproduced from ref. [44]; published 2015 by Royal Society of Chemistry, Creative Commons Attribution 3.0 Unported Licence.

© 2021 The Authors. ChemBioChem published by Wiley-VCH GmbH

ChemBioChem
Minireviews
doi.org/10.1002/cbic.202100220
Chemistry Europe
European Chemical Societies Publishing

In another system, *light-induced* transmembrane electron transfer was achieved using DPPC phospholipid bilayer vesicles, functionalized with amphiphilic zinc porphyrins. The sacrificial hydrophilic electron donor EDTA was encapsulated within these vesicles, and upon irradiation with visible light the photoreduction of the porphyrin took place. Electron transfer across the membrane only took place when the electron relay 1-methoxy-*N*-methylphenazium (MMP^+) was added as methyl sulfate salt: reduction of MMP^+ yielded the neutrally charged MMPH which is hydrophobic enough to cross the hydrophobic membrane. The water soluble 2-(4-iodophenyl)-3-(4-nitrophenyl)-5-(2,4-disulfophenyl)-2*H*-tetrazolium anion ($WST1^-$) was added to the bulk and was reduced to the strongly colored formazan dye $Fz1^{2-}$. Interestingly, the quantum yield for $Fz1^{2-}$ generation was 2.7 times higher when the direct photoreduction was physically separated from the $Fz1^{2-}$ generation by the vesicle membrane (Figure 6c). The authors attribute this separation of photosensitizer and photoproduct through the membrane leads to prevents recombination reactions in the photoexcited state.[43]

4. Light-Energy Conversion with Polymersomes

In order to produce robust material at a large scale for large scale solar fuels production, a more robust material is needed. The discussed lipid vesicle membranes are good and excellent material for biomimetic construction of processes, but their dynamic and relatively labile molecular and material properties might be disadvantageous for large scale solar fuel production. Polymer based vesicles (so called polymersomes) have proven to be very versatile in properties[46,47,56,48–55] as well as opportunities for functionalization with proteins such as transmembrane proteins.[57]

Polymersome membranes are generally constructed by self-assembly of individual AB or ABC linear, branched or dendritic copolymers (examples for linear copolymers see Figure 2). Oftentimes, A describes the hydrophilic part, B the hydrophobic part, and C is an optional hydrophilic part. In general, a molecular weight ration of A/B of 1/3 to 1/2 enables for bilayer formation in water, whereas an A/B ration of $\leq$ 1/3 favors the formation of micelles. This behavior is similar to lipids and based on the packing parameters that govern the geometry of their packing behavior.[58]

While lipid-based vesicles are very well studies for photochemical and artificial photosynthetic reactions, polymersomes are so far much less investigated. It might be the availability of the material, or the specific properties: The rigidity and mechanical robustness of polymer type materials might affect the reaction rates at the membrane surface, as well as in transmembrane processes such as permeation or transmembrane mass transport.

In the following, several studies on light induced/light driven processes will be presented, including selected studies which propose avenues to overcome permeability challenges for light induced processes to in these artificial vesicles.

Zheng, Zhou *et al.* have constructed a light-harvesting polymeric vesicles with spatially separated donors and acceptors, based on hyperbranched polymers (branched polymersomes, Figure 7).[59] With their system the authors mimicked the natural photosynthetic light harvesting systems, by encapsulating the energy donors 4-chlor-7-nitro-2,1,3-benzodiazole (NBD-Cl) in the hyperbranched cores of the vesicles and anchoring the hydrophilic rhodamine R energy acceptors to the surface of the vesicles via host guest interactions with cyclodextrins. Due to the encapsulation and host-guest interactions of energy donor and acceptor detrimental self-quenching is avoided, and the energy transfer efficiency is 80%.[59]

Thordarsen *et al.* have self-assembled the transmembrane electron transfer protein cytochrome c oxidase of the natural mitochondrial electron transport chain within the hydrophobic part of the polymersome membrane of polystyrene-polyacrylic acid block copolymer bilayers (see Figure 2).[61] In addition to this natural protein, a semi-artificial protein complex was associated via self-assembly: The natural cytochrome c was covalently functionalized at CYS102 with a photoredox active ruthenium terpyridine complex, which was positively charged and situated in the negatively charged, hydrophilic polyacrylic acid layer of the copolymer bilayers. Light irradiation in presence of sacrificial electron donating EDTA enabled for photoreduction of the transmembrane protein, followed by oxygen reduction in the inner compartment of the polymersome and proton translocation from inside to outside of the vesicle, as it is the function of cytochrome oxidase. As a consequence, a basification of the inner compartment was observed via a fluorescent pH marker.[60] This pH gradient is highly biomimetic and indicates the storage of light energy in form of an electrochemical transmembrane potential. It might be used for the driving of ATP synthase.

As described earlier, polymersomes can be constructed of hydrophobic-hydrophilic block-copolymers. Typically, the A-part composes of the hydrophilic part while the B-part of the copolymers consists of the hydrophobic tail. An additional hydrophobic or hydrophilic C-block-copolymer might be added as

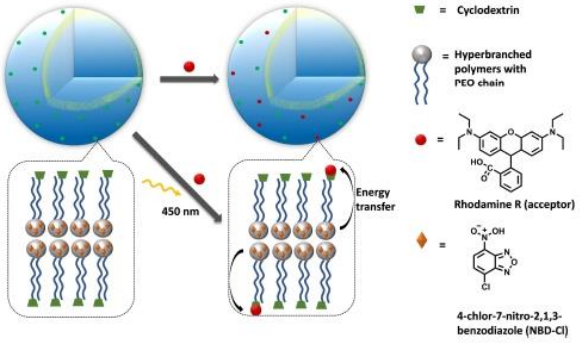

Figure 7. Energy transfer mediated by hyperbranched polymers with NBD-Cl as energy donor encapsulated inside hyperbranched cores and rhodamine B as energy acceptors incorporated on the surface of vesicle with cyclodextrin as host (PEO = polyethyleneoxide) Reproduced with permission from ref. [59]; Copyright: 2017, John Wiley and Sons.

© 2021 The Authors. ChemBioChem published by Wiley-VCH GmbH

ChemBioChem
Minireviews
doi.org/10.1002/cbic.202100220
Chemistry Europe
European Chemical Societies Publishing

well. To address the issue of mass transport from the inside to the outside of the polymersome, several approaches have been proposed. They include integration of transmembrane proteins,[61,62] and reaction-induced triggering of the permeability properties of the membrane.[46,47] The latter is especially interesting in the context of artificial photosynthesis, as the reactions can directly be triggered by light irradiation. Liu *et al.* have applied this context to achieve a transition from typical polymersomes to so called polyion complex vesicles (PICsomes).[63] They incorporated light-cleavable ester groups, as well as tertiary amine functions into the B and C co-block polymers. Upon ester cleavage, the carboxylic acid function can be deprotonated by the neighboring tertiary amine an generate ion pairs. In synergy with other hydrogen bonding interactions within the copolymer framework, the ion pair formed a stable membrane that was permeable to water soluble substances. Furthermore, the authors demonstrated that by selectively choosing the composition of the B and C co-block polymers, the size selectivity could be achieved, which demonstrated, that the challenge of mass transport can be solved with polymeric vesicles.[63]

In summary, we have presented several recent studies on light induced electron and energy transfer within liposomal and polymer membranes that will be highly relevant for the construction of artificial photosynthetic membrane systems. We believe that the aspect of compartmentalization of reactions and self-assembly of reactants will become more and more important for chemistry in general, and light energy conversion in particular. Using vesicles based on biomimetic lipids or artificial polymers will enable various strategies in this regard.

Acknowledgements

The authors are grateful to the Vector Stiftung (project number P2019-0110) and the Deutsche Forschungsgemeinschaft (DFG, project TRR234 "CataLight" project number 364549901, project B8) for financial support. Open Access funding enabled and organized by Projekt DEAL.

Conflict of Interest

The authors declare no conflict of interest.

Keywords: energy transfer · liposomes · luminescence · photocatalysis · vesicles

[1] G. Steinberg-Yfrach, P. A. Liddell, S.-C. Hung, A. L. Moore, D. Gust, T. A. Moore, *Nature* **1997**, *385*, 239–241.
[2] P. Seta, E. Bienvenue, A. L. Moore, P. Mathis, R. V. Bensasson, P. Liddell, P. J. Pessiki, A. Joy, T. A. Moore, D. Gust, *Nature* **1985**, *316*, 653–655.
[3] D. Gust, T. A. Moore, *Science* **1989**, *244*, 35–41.
[4] T. E. Miller, T. Beneyton, T. Schwander, C. Diehl, M. Girault, R. McLean, T. Chotel, P. Claus, N. S. Cortina, J. Baret, T. J. Erb, *Science* **2020**, *368*, 649–654.
[5] M. Morasch, J. Liu, C. F. Dirscherl, A. Ianeselli, A. Kühnlein, K. Le Vay, P. Schwintek, S. Islam, M. K. Corpinot, B. Scheu, D. B. Dingwell, P. Schwille, H. Mutschler, M. W. Powner, C. B. Mast, D. Braun, *Nat. Chem.* **2019**, *11*, 779–788.
[6] S. Bhosale, A. L. Sisson, P. Talukdar, A. Fürstenberg, N. Banerji, E. Vauthey, G. Bollot, J. Mareda, C. Röger, F. Würthner, N. Sakai, S. Matile, *Science* **2006**, *313*, 84–86.
[7] W. E. Ford, J. W. Otvos, M. Calvin, *Nature* **1978**, *274*, 507–508.
[8] N. Ikuta, S. Takizawa, S. Murata, *Photochem. Photobiol. Sci.* **2014**, *13*, 691–702.
[9] M. Hansen, F. Li, L. Sun, B. König, *Chem. Sci.* **2014**, *5*, 2683–2687.
[10] B. Limburg, J. Wermink, S. S. van Nielen, R. Kortlever, M. T. M. Koper, E. Bouwman, S. Bonnet, *ACS Catal.* **2016**, *6*, 5968–5977.
[11] M. Hansen, F. Li, L. Sun, B. König, *Chem. Sci.* **2014**, *5*, 2683–2687.
[12] M. Hansen, S. Troppmann, B. König, *Chem. Eur. J.* **2016**, *22*, 58–72.
[13] B. Limburg, J. Wermink, S. S. Van Nielen, R. Kortlever, M. T. M. Koper, E. Bouwman, S. Bonnet, *ACS Catal.* **2016**, *6*, 5968–5977.
[14] A. Ben-Shem, F. Frolow, N. Nelson, *Nature* **2003**, *426*, 630–635.
[15] N. Nelson, C. F. Yocum, *Annu. Rev. Plant Biol.* **2006**, *57*, 521–565.
[16] R. E. Blankenship, *Molecular Mechanisms of Photosynthesis*, Wiley Blackwell, **2014**.
[17] S. Tietz, M. Leuenberger, R. Höhner, A. H. Olson, G. R. Fleming, H. Kirchhoff, *J. Biol. Chem.* **2020**, *295*, 1857–1866.
[18] A. Pannwitz, D. M. Klein, S. Rodríguez-Jiménez, C. Casadevall, H. Song, E. Reisner, L. Hammarström, S. Bonnet, *Chem. Soc. Rev.* **2021**, *50*, 4833–4855.
[19] F. De Riccardis, I. Izzo, D. Montesarchio, P. Tecilla, *Acc. Chem. Res.* **2013**, *46*, 2781–2790.
[20] J. N. Robinson, D. J. Cole-Hamilton, *Chem. Soc. Rev.* **1991**, *20*, 49–94.
[21] X. Xie, E. Bakker, *Phys. Chem. Chem. Phys.* **2014**, *16*, 19781–19789.
[22] P. Husen, L. R. Arriaga, F. Monroy, J. H. Ipsen, L. A. Bagatolli, *Biophys. J.* **2012**, *103*, 2304–2310.
[23] T. Hatae, T. Koshiyama, M. Ohba, *Chem. Lett.* **2017**, *46*, 756–759.
[24] D. Antoku, S. Satake, T. Mae, K. Sugikawa, H. Funabashi, A. Kuroda, A. Ikeda, *Chem. Eur. J.* **2018**, *24*, 7335–7339.
[25] A. Pannwitz, H. Saaring, N. Beztsinna, X. Li, M. A. Siegler, S. Bonnet, *Chem. Eur. J.* **2021**, *27*, 3013–3018.
[26] S. H. C. Askes, A. Bahreman, S. Bonnet, *Angew. Chem. Int. Ed.* **2014**, *53*, 1029–1033; *Angew. Chem.* **2014**, *126*, 1047–1051.
[27] V. Balzani, P. Ceroni, A. Juris, *Photochemistry and Photophysics*, Wiley-VCH, Weinheim, **2014**.
[28] S. H. C. Askes, M. Kloz, G. Bruylants, J. T. M. Kennis, S. Bonnet, *Phys. Chem. Chem. Phys.* **2015**, *17*, 27380–27390.
[29] S. H. C. Askes, M. S. Meijer, T. Bouwens, I. Landman, S. Bonnet, *Molecules* **2016**, *21*, 1460.
[30] S. H. C. Askes, S. Bonnet, *Nat. Chem. Rev.* **2018**, *2*, 437–452.
[31] B. Limburg, E. Bouwman, S. Bonnet, *J. Phys. Chem. B* **2016**, *120*, 6969–6975.
[32] Y. Pellegrin, F. Odobel, *Comptes Rendus Chim.* **2017**, *20*, 283–295.
[33] T. Higashino, T. Yamada, M. Yamamoto, A. Furube, N. V. Tkachenko, T. Miura, Y. Kobori, R. Jono, K. Yamashita, H. Imahori, *Angew. Chem. Int. Ed.* **2016**, *55*, 629–633; *Angew. Chem.* **2016**, *128*, 639–643.
[34] R. A. Marcus, N. Sutin, *Biochim. Biophys. Acta* **1985**, *811*, 265–322.
[35] R. A. Marcus, *Phys. Chem. Chem. Phys.* **2012**, *14*, 13729–30.
[36] M. Kuss-Petermann, O. S. Wenger, *Angew. Chem. Int. Ed.* **2016**, *55*, 815–819; *Angew. Chem.* **2016**, *128*, 826–830.
[37] M. Kuss-Petermann, O. S. Wenger, *J. Am. Chem. Soc.* **2016**, *138*, 1349–1358.
[38] S. Troppmann, B. König, *Chem. Eur. J.* **2014**, *20*, 14570–14574.
[39] N. Ikuta, S. Y. Takizawa, S. Murata, *Photochem. Photobiol. Sci.* **2014**, *13*, 691–702.
[40] Y. Sato, S. Takizawa, S. Murata, *J. Photochem. Photobiol. A* **2016**, *321*, 151–160.
[41] B. Limburg, E. Bouwman, S. Bonnet, *ACS Catal.* **2016**, *6*, 5273–5284.
[42] M. M. A. Kelson, R. S. Bhosale, K. Ohkubo, L. A. Jones, S. V. Bhosale, A. Gupta, S. Fukuzumi, S. V. Bhosale, *Dyes Pigm.* **2015**, *120*, 340–346.
[43] B. Limburg, E. Bouwman, S. Bonnet, *Chem. Commun.* **2015**, *51*, 17128–17131.
[44] M. Wang, C. Wölfer, L. Otrin, I. Ivanov, T. Vidaković-Koch, K. Sundmacher, *Langmuir* **2018**, *34*, 5435–5443.
[45] S. Troppmann, B. König, *ChemistrySelect* **2016**, *1*, 1405–1409.
[46] J. Gaitzsch, X. Huang, B. Voit, *Chem. Rev.* **2016**, *116*, 1053–1093.
[47] H. Gumz, T. H. Lai, B. Voit, D. Appelhans, *Polym. Chem.* **2017**, *8*, 2904–2908.
[48] X. Liu, P. Formanek, B. Voit, D. Appelhans, *Angew. Chem. Int. Ed.* **2017**, *56*, 16233–16238; *Angew. Chem.* **2017**, *129*, 16451–16456.
[49] S. E. Sherman, Q. Xiao, V. Percec, *Chem. Rev.* **2017**, *117*, 6538–6631.

© 2021 The Authors. ChemBioChem published by Wiley-VCH GmbH

ChemBioChem
Minireviews
doi.org/10.1002/cbic.202100220
Chemistry Europe
European Chemical Societies Publishing

[50] W. Jiang, Y. Zhou, D. Yan, *Chem. Soc. Rev.* **2015**, *44*, 3874–3889.
[51] Q. Shao, S. Zhang, Z. Hu, Y. Zhou, *Angew. Chem. Int. Ed.* **2020**, *59*, 17125–17129; *Angew. Chem.* **2020**, *132*, 17273–17277.
[52] J. C. M. Va Hest, D. A. P. Delnoye, M. W. P. L. Baars, M. H. P. Van Genderen, E. W. Meijer, *Science* **1995**, *268*, 1592–1595.
[53] L. Zhang, A. Eisenberg, *Science* **1995**, *268*, 1728–1731.
[54] L. Zhang, K. Yu, A. Eisenberg, *Science* **1996**, *272*, 1777–1779.
[55] B. M. Discher, Y. Y. Won, D. S. Ege, J. C. M. Lee, F. S. Bates, D. E. Discher, D. A. Hammer, *Science* **1999**, *284*, 1143–1146.
[56] V. Percec, D. A. Wilson, P. Leowanawat, C. J. Wilson, A. D. Hughes, M. S. Kaucher, D. A. Hammer, D. H. Levine, A. J. Kim, F. S. Bates, K. P. Davis, T. P. Lodge, M. L. Klein, R. H. Devane, E. Aqad, B. M. Rosen, A. O. Argintaru, M. J. Sienkowska, K. Rissanen, S. Nummelin, J. Ropponen, *Science* **2010**, *328*, 1009–1014.
[57] M. Garni, S. Thamboo, C. A. Schoenenberger, C. G. Palivan, *Biochim. Biophys. Acta Biomembr.* **2017**, *1859*, 619–638.
[58] J. N. Israelachvili, D. J. Mitchell, B. W. Ninham, *J. Chem. Soc. Faraday Trans. 2* **1976**, *72*, 1525–1568.
[59] H. Li, Y. Liu, T. Huang, M. Qi, Y. Ni, J. Wang, Y. Zheng, Y. Zhou, D. Yan, *Macromol. Rapid Commun.* **2017**, *38*, 1600818.
[60] D. Hvasanov, J. R. Peterson, P. Thordarson, *Chem. Sci.* **2013**, *4*, 3833–3838.
[61] C. G. Palivan, R. Goers, A. Najer, X. Zhang, A. Car, W. Meier, *Chem. Soc. Rev.* **2016**, *45*, 377–411.
[62] C. Kleineberg, C. Wölfer, A. Abbasnia, D. Pischel, C. Bednarz, I. Ivanov, T. Heitkamp, M. Börsch, K. Sundmacher, T. Vidaković-Koch, *ChemBioChem* **2020**, *21*, 2149–2160.
[63] X. Wang, C. Yao, G. Zhang, S. Liu, *Nat. Commun.* **2020**, *11*, 1524.

Manuscript received: May 6, 2021
Revised manuscript received: June 28, 2021
Accepted manuscript online: July 5, 2021
Version of record online: July 14, 2021

© 2021 The Authors. ChemBioChem published by Wiley-VCH GmbH

Chapter 3

Alignment and Photooxidation Dynamics of a Perylene Diimide Chromophore in Lipid Bilayers

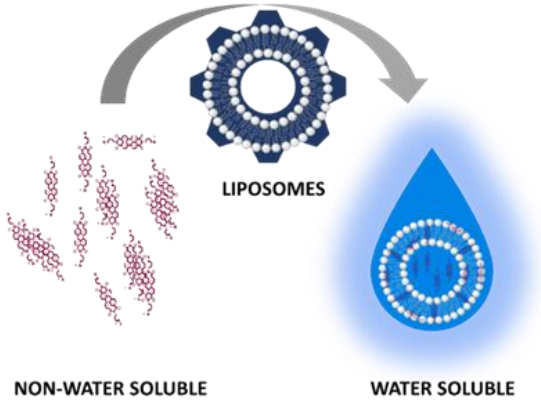

This chapter presents a method for enabling photochemical reactions using biomimetic membranes in a fully aqueous system. The design principle of organic dyes being integrated into the membrane is studied. Perylene diimide (PDI) is a metal-free chromophore that is highly abundant, photochemically active, easy to modify, and strongly absorbs visible light. These reasons lead to a significant interest in studying the alternative system for water-splitting reactions based on perylene diimide. In this study, we synthesized an amphiphilic perylene diimide, which enables the dye to be incorporated into the membrane and drives a photo-induced photooxidation reaction. This approach opens the possibility of using biomimetic membranes as the media for introducing non-water-soluble organic compounds in a fully aqueous system.

Author contributions:
Novitasari Sinambela: Performed the chemical synthesis and liposome assemblies, steady-state and time-resolved spectroscopy characterization, confocal imaging measurement, photooxidation experiments, paper writing, and manuscript revision.
Richard Jacobi + David Hernández-Castillo + Leticia González: Design of the computational protocols, and analysis of all calculations, paper writing, and manuscript revision.
Elisabeth Hofmeister + Nina Hagmeyer + Benjamin Dietzek-Ivanšić: EPR spectroscopy investigations.
Benjamin Dietzek-Ivanšić + Andrea Pannwitz: Design of the study.
Andrea Pannwitz: Paper writing and manuscript revision.

This chapter has been published as a full paper: Novitasari Sinambela, Richard Jacobi, David Hernández-Castillo, Elisabeth Hofmeister, Nina Hagmeyer, Benjamin Dietzek-Ivanšić, Leticia González, and Andrea Pannwitz,*, Alignment and Photooxidation Dynamics of a Perylene Diimide Chromophore in Lipid Bilayers. Mol. Syst. Des. Eng. **2023**. DOI: 10.1039/D2ME00243D. This article is licensed under CC BY 3.0 (https://creativecommons.org/licenses/by/3.0).

MSDE

ROYAL SOCIETY OF CHEMISTRY

PAPER

View Article Online
View Journal | View Issue

Check for updates

Cite this: *Mol. Syst. Des. Eng.*, 2023, **8**, 842

Alignment and photooxidation dynamics of a perylene diimide chromophore in lipid bilayers†

Novitasari Sinambela,[a] Richard Jacobi,[bc] David Hernández-Castillo,[bc] Elisabeth Hofmeister,[f] Nina Hagmeyer,[ef] Benjamin Dietzek-Ivanšić,[ef] Leticia González *[bd] and Andrea Pannwitz *[a]

Received 11th November 2022,
Accepted 20th February 2023

DOI: 10.1039/d2me00243d

rsc.li/molecular-engineering

We present a method of enabling photochemical reactions in water by using biomimetic, water-soluble liposomes and a specifically functionalized perylene diimide chromophore. Linking two flexible saturated C4-alkyl chains with terminal positively charged trimethylammonium groups to the rigid perylene diimide core yielded $[1]^{2+}$ allowing for its co-assembly at the lipid bilayer interface of DOPG liposomes (DOPG = 1,2-dioleoyl-*sn*-*glycero*-3-phospho-(1′-*rac*-glycerol)) with a preferred orientation and in close proximity to the water interface. According to molecular dynamics simulations the chromophore aligns preferably parallel to the membrane surface which is supported by confocal microscopy. Irradiation experiments with visible light and in the presence of a negatively charged, water-soluble oxidant were slower in the DOPG-membrane than under acetonitrile–water reaction conditions. The generated radical species was characterized by EPR spectroscopy in an acetonitrile–water mixture and associated to the DOPG-membrane. Time-resolved emission studies revealed a static quenching process for the initial electron transfer from photoexcited $[1]^{2+}$ to the water soluble oxidant. The findings presented in this study yield design principles for the functionalization of lipid bilayer membranes which will be relevant for the molecular engineering of artificial cellular organelles and nano-reactors based on biomimetic vesicles and membranes.

Design, System, Application

The system presented here demonstrates a design principle of how molecular species such as perylene diimides can be incorporated into lipid bilayer membranes in a preferred orientation and parallel to the membrane surface. Specifically, the functionalization of a rigid perylene diimide core with two flexible saturated C4-alkyl chains and terminal positively charged trimethylammonium groups leads to membrane anchorage on negatively charged membrane surfaces. This methodology is relevant for the design of molecular lipid bilayer hybrid materials and provides an underexplored opportunity to enable (photo-)chemical reactions with high spatial control which enables reaction confinement at the lipid bilayer membrane and for compartmentalization within the inner aqueous compartment of water-soluble vesicles. The findings presented here are relevant within the context of artificial cellular organelles and nano-reactor design.

Introduction

In the context of solar light energy conversion including light-driven water splitting to form oxygen and hydrogen, as well as enzymatic catalysis, photoredox catalysis and water detoxification, it is oftentimes essential to be able to use water as solvent or co-solvent. However, water solubility for a given light active molecule or material typically requires synthetic efforts or adapted material or molecular systems design strategies.[1–3]

In nature, the challenge of chemical reactions in water with partly or fully water insoluble reaction partners is solved by the compartmentalization of reaction spaces using lipid bilayer membranes which span cells, vesicles and cellular compartments. Especially interesting for light energy

[a] *Institute of Inorganic Chemistry I, Ulm University, Albert-Einstein-Allee 11, 89081 Ulm, Germany. E-mail: andrea.pannwitz@uni-ulm.de*
[b] *Institute of Theoretical Chemistry, Faculty of Chemistry, University of Vienna, Währinger Straße 17, 1090 Vienna, Austria. E-mail: leticia.gonzalez@univie.ac.at*
[c] *Doctoral School in Chemistry (DoSChem), University of Vienna, Währinger Straße 42, 1090 Vienna, Austria*
[d] *Vienna Research Platform on Accelerating Photoreaction Discovery, University of Vienna, Währinger Straße 17, 1090 Vienna, Austria*
[e] *Institute of Physical Chemistry and Abbe Center of Photonics, Friedrich Schiller University Jena, Helmholtzweg 4, Jena 07743, Germany*
[f] *Leibniz Institute of Photonic Technology (IPHT), Research Department Functional Interfaces, Albert-Einstein-Straße 9, Jena 07745, Germany*
† Electronic supplementary information (ESI) available. See DOI: **https://doi.org/10.1039/d2me00243d**

This journal is © The Royal Society of Chemistry and IChemE 2023

conversion are the processes in natural photosynthesis, where solar energy conversion is enabled within hydrophobic membranes and their interface towards aqueous compartments. The most essential photochemical reaction step in photosynthesis is light-driven charge transfer from the photoexcited light-absorbing molecule towards an electron acceptor or an electron donor. An important aspect here is the precise orientation of the chromophores within the membrane.[4]

By mimicking nature, we are here exploring a method for photochemical redox processes to be performed in water and at the interface of biomimetic phospholipid bilayers using an organic, molecular chromophore embedded with the membrane and at the interface with water. In this case the lipid bilayer membrane builds up vesicles which can be varied in size and shape[5] and can prospectively act as nano-photoreactors.[6] Successful light-driven CO_2 reduction, hydrogen evolution, water oxidation and NADH oxidation at biomimetic lipid bilayer vesicles (liposomes) have previously been reported using metal based photosensitizers based on ruthenium polypyridyl complexes.[5–12] Our motivation to investigate an organic chromophore is to enable light-driven chemical transformations with photosensitizers from more abundant resources. By constructing a photoactive molecular system with lipid bilayers, the microenvironment of the individual chromophore is altered from a typical solution environment which can change and oftentimes improves the reaction dynamics or chromophore stability.[5,11] We therefore characterized the light driven oxidation dynamics between an organic chromophore and a water soluble oxidant.

The organic chromophore investigated here is a substituted version of perylene diimide (PDI). PDIs are known for their activity as photosensitizers in photoredox catalysis in organic solution and their aggregation behavior in solution.[13–16] Typically, PDIs absorb light in the visible region of the solar spectrum, and therefore they enable low-energy photon emission compared to UV light which might be relevant in the technological context using LED light sources for photochemical reactions. In this study, PDI has been substituted with two butyl trimethyl ammonium alkyl chains at the imine-nitrogens, forming *N*,*N*′-di(butylenetrimethylammonium)-3,4,9,10-perylenediimide $[\mathbf{1}]^{2+}$ as PF_6 salt ($[\mathbf{1}]^{2+}$, see Fig. 1). In principle, the length of the molecule matches the thickness of the phospholipid bilayers of around 2.4 nm, potentially enabling preferred orientations at artificial lipid bilayers, such as 1,2-dioleoyl-*sn*-*glycero*-3-phospho-(1′-*rac*-glycerol) (DOPG) bilayers.[5,17,18] Here, the specific orientation of $[\mathbf{1}]^{2+}$ within the lipid bilayer was investigated explicitly using all-atom molecular dynamics (MD) simulations. Light-driven electron transfer to an oxidant in solution generates a PDI based radical which was studied by EPR spectroscopy in homogeneous solution and at DOPG liposomes, while the detailed difference of the reaction dynamics of the homogeneous solution and at DOPG liposomes was resolved using time resolved fluorescence spectroscopy, giving insights into the reaction dynamics at the biomimetic membrane–water interface.

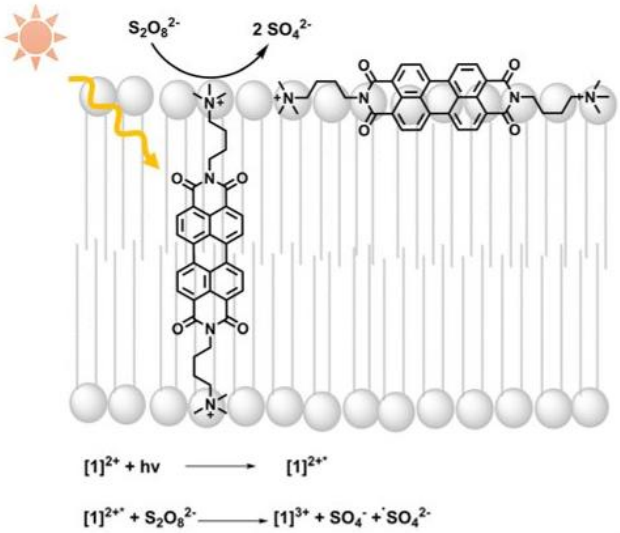

Fig. 1 Light absorption by $[\mathbf{1}]^{2+}$ is followed by photooxidation of $[\mathbf{1}]^{2+}$ by persulfate; equations of initial light-driven reactions are included.

Results

Synthesis of $[\mathbf{1}]^{2+}$ and lipid bilayer integration

The substituted PDI $[\mathbf{1}]^{2+}$ was synthesized from perylene-3,4,9,10-tetracarboxylic dianhydride as described in the ESI:† a condensation reaction with (4-aminobutyl) dimethylamine yielded an uncharged PDI which was then methylated with CH_3I to introduce charged trimethyl amine groups. After salt exchange using an aqueous solution of NH_4PF_6, the PF_6-salt of $[\mathbf{1}]^{2+}$ was isolated with an overall yield of 76% over two chemical reactions and one salt exchange.

Integration of $[\mathbf{1}]^{2+}$ into liposomes was only possible when using the negatively charged 1,2-dioleoyl-*sn*-*glycero*-3-phospho-*rac*-(1-glycerol) sodium salt (DOPG) as the phospholipid. Neutrally charged lipids such as DMPC (1,2-dimyristoyl-*sn*-*glycero*-3-phosphocholine) did not take up $[\mathbf{1}]^{2+}$, indicating a benefit of the electrostatic attraction between $[\mathbf{1}]^{2+}$ and the lipid. For liposome preparation, DOPG as the main lipid, $[\mathbf{1}]^{2+}$ and the PEGylated lipid 1,2-dimyristoyl-*sn*-*glycero*-3-phosphoethanolamine-*N*-[methoxy(polyethylene glycol)-2000] (ammonium salt) (14 : 0 PEG2000 PE) for steric stabilization of the vesicles were combined in the desired molar ratio in a chloroform–acetonitrile mixture (here: 100 : 1 : 1). Solvent evaporation yielded a lipid film which was hydrated with an aqueous buffer to yield giant vesicles for confocal microscopy, and additional extrusion yielded small vesicles (liposomes) with typical hydrodynamic diameters of 110–120 nm indicating stability of vesicles containing $[\mathbf{1}]^{2+}$. In some cases, size exclusion chromatography was performed additionally to remove $[\mathbf{1}]^{2+}$ outside of the liposomes (Fig. 2). More details

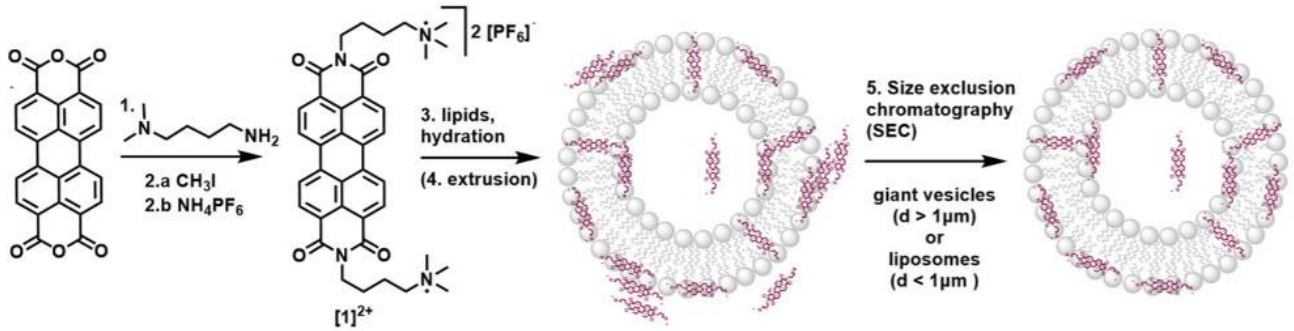

Fig. 2 Synthesis of $[1]^{2+}$ starting from perylene-3,4,9,10-tetracarboxylic dianhydride and incorporation of $[1]^{2+}$ into vesicle membranes. Reaction conditions and yields: 1.) 4 eq. (4-aminobutyl)dimethylamine, i-butanol, 90 °C, 24 h, 95%; 2.a) 3 eq. CH_3I, toluene, reflux, 3 h; 2.b) excess NH_4PF_6, H_2O, 65 °C, 76%; 3.) phosphate buffer, 100 : 1 : 1 (*n*/*n*/*n*) DOPG lipids/14 : 0 PEG2000 PE/ $[1]^{2+}$; 4.) extrusion; 5.) size exclusion chromatography (SEC).

on the vesicle preparation are described in the experimental part.

Spectroscopic characterization

Similar to other substituted PDIs, $[1]^{2+}$ is soluble in organic solvents and strongly absorbs visible light in the region between 400 nm and 550 nm with three characteristic absorption bands, indicating the dominance of monomeric species of $[1]^{2+}$ over aggregation.[14,19] In acetonitrile, these absorption bands are at 453, 484 and 520 nm with extinction coefficients ranging between 14 000 and 61 000 M^{-1} cm^{-1}. In a 1 : 1 (V : V) mixture of acetonitrile and water, the absorption peaks are shifted to lower energy by 7 to 10 nm indicating an impact of the solvent environment on the electronic levels of the chromophore. Such bathochromic shifts in the PDI spectra were previously observed with protic solvents and are probably due to stabilization of the more polarizable excited states upon hydrogen bonding with the solvent and the formation of J-aggregates.[13,20–22] In the emission spectra, three maxima and a similar red-shift were observed when going from acetonitrile (531, 571 and 620 nm) to the acetonitrile/water 1 : 1 (V : V) mixture (540, 580 and 630 nm) (see Fig. 3). The fluorescence lifetime determination yielded mono-exponential decays in acetonitrile and in acetonitrile/water 1 : 1 (V : V) with a lifetime of (4.1 ± 0.1) ns or (4.2 ± 0.1) ns, respectively (see Table 1). In other PDI-based chromophores, similar fluorescence lifetimes of around 4 ns were reported.[23–25]

Fig. 3 shows the absorption and emission spectra of $[1]^{2+}$ in DOPG-liposomes. Upon manual baseline correction of the Tyndall scattering in the absorption spectrum (the dotted line in Fig. 3), the similarity between the absorption spectra in solution and in liposomes becomes evident. In DOPG liposomes the three absorption and emission bands of $[1]^{2+}$ are at similar wavelengths to those in acetonitrile/water 1 : 1 (V : V); however, the vibrational bands at 460 nm and 640 nm respectively appear as a shoulder instead of distinct peaks, indicating some level of aggregation within the lipid bilayers. Typically, the assembling chromophores within hydrophobic lipid bilayers would yield hypsochromic spectral shifts, as the more hydrophobic environment typically destabilizes the more polar or more polarizable excited states.[26] However, the incorporation into lipid membranes shows a bathochromic shift with respect to the organic solvent and only a minor shift by one to two nanometers compared to acetonitrile/water 1 : 1 (V : V), which indicates that the chromophore is exposed to hydrogen bonding water molecules when embedded within the lipid bilayer. In terms of fluorescence lifetime, embedding $[1]^{2+}$ into the lipid bilayer of DOPG liposomes slightly reduced the excited state lifetime to around 4.0 ns.

Size exclusion chromatography after vesicle preparation typically removes water soluble and smaller aggregates from the bulk solution around the vesicles. Doing so here had no effect on the spectral data, but confocal microscopy of giant

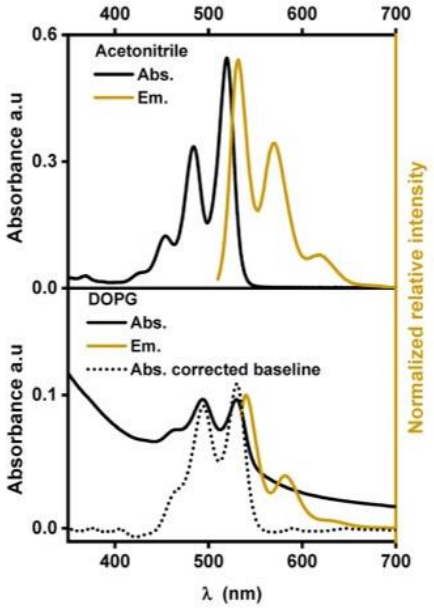

Fig. 3 Absorption and emission spectra of $[1]^{2+}$ in various environments.

This journal is © The Royal Society of Chemistry and IChemE 2023

Table 1 Spectroscopic data for $[1]^{2+}$

Solvent or lipid	λ_{Abs} (nm) (ε [M^{-1} cm^{-1}])	λ_{em} (nm)	τ (ns)
Acetonitrile	453 (14000), 484 (38000), 520 (61000)	531, 571, 620	4.1 ± 0.1
Acetonitrile/water (1 : 1)	461(18700), 490 (49000), 527 (76000)	540, 580, 630	4.2 ± 0.1
DOPG liposomes[a]	460, 494, 530	540, 582, 630	4.1 ± 0.1
DOPG liposomes[b]	460, 494, 530	540, 582, 630	4.0 ± 0.1

[a] DOPG : (14 : 0 PEG2000 PE) : $[1]^{2+}$ = 100 : 1 : 1; in phosphate buffer (10 mM, pH 7.0). [b] DOPG : (14 : 0 PEG2000 PE) : $[1]^{2+}$ = 100 : 1 : 1; in phosphate buffer (10 mM, pH 7.0) after size exclusion.

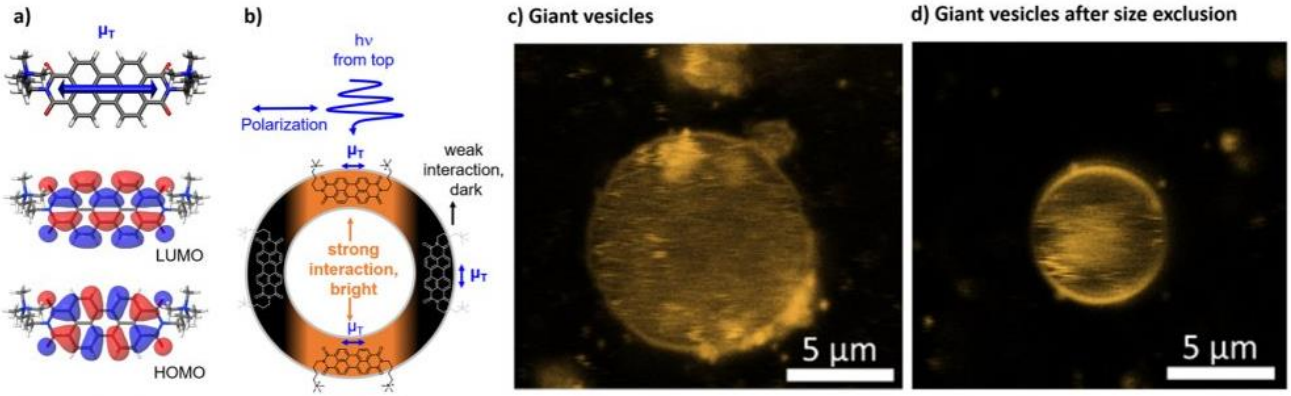

Fig. 4 a) DFT optimized structures of $[1]^{2+}$ including the shape of the HOMO and LUMO and the directionality of the calculated transition dipole moment (μ_T). b) Illustration of the interactions of a polarized light source with the transition dipole moment of $[1]^{2+}$ in the lipid bilayer. c and d) Confocal images of giant vesicles with DOPG : (14 : 0 PEG2000 PE) : $[1]^{2+}$ = 100 : 1 : 1; in phosphate buffer (10 mM, pH 7.0) upon fixation in an agarose hydrogel d) without size exclusion chromatography and e) after size exclusion chromatography.

vesicles showed that, clearly, some aggregates could be removed from the bulk around the vesicles (Fig. 4c and d).

Confocal microscopy and the preferred orientation

The integration into the lipid bilayer was proven by confocal fluorescence microscopy as depicted in Fig. 4c and d showing typical giant vesicles loaded with around 1 mol% $[1]^{2+}$. In these confocal microscopy images, the sample is irradiated with a polarized laser source at 488 nm and the microscopy image is collected in the range of emission of $[1]^{2+}$, at 503–750 nm. As seen in Fig. 4c and d, the shape of a round vesicle is emissive, which indicates targeted incorporation of the fluorescent $[1]^{2+}$ into the lipid bilayer of these vesicles. It was observed that size exclusion chromatography could remove some aggregated $[1]^{2+}$ from the bulk around the giant vesicle but that some aggregates have been enclosed within the vesicle. The latter is shown by the fluorescent matter in the inner volume of the vesicle in Fig. 4c and d. As the giant vesicles are fixated within the agarose hydrogel, the vesicle itself can be resolved well, but the inner aqueous compartment of the vesicle contains a highly mobile aqueous buffer, so that the fluorescent matter in the inner compartment cannot be resolved well with a microscope and appears to be rather diffuse. Furthermore, a double half-moon effect is seen within this image, where the equatorial region of the vesicle remains dark while the north and south poles are brightly emissive. This double half-moon effect is typical for chromophores with one main transition dipole moment at the excitation wavelength and a preferred orientation within the relatively rigid matrix of the lipid bilayer.[18,26] As revealed by time-dependent density functional theory (TD-DFT), the transition of $[1]^{2+}$ associated with emission, *i.e.*, between the first excited singlet state and the ground state, is of ππ*-character, as indicated by the HOMO and LUMO (see Fig. 4a). The corresponding transition dipole moment oscillates along the main molecular axis between the two imine-nitrogens (see Fig. 4b) which enables orientation dependent interaction with the polarized incident laser light source and selective excitation (and emission) of the well-aligned chromophores with respect to the incident polarized laser. As schematized in Fig. 4b, the alignment of the molecules of $[1]^{2+}$ parallel to the membrane surface leads to the observed half-moon effect as this requires a preferred orientation of $[1]^{2+}$ with respect to the membrane surface. This would enable easy access of water-soluble reactants to the chromophore $[1]^{2+}$ which is therefore close to the membrane–water interface. However, in previous work, luminescent chromophores with rigid backbones in a vesicle membrane showed the double halfmoon effect as well but most likely due to a preference for a transmembrane alignment.[18,26] Using MD simulation, we have elucidated the orientation preference of $[1]^{2+}$ within the lipid double layer.

MD simulations and orientation

We performed 50 MD simulations in total, where $[1]^{2+}$ was put into a cubic box of 90 Å side length. In 20 of these 50

trajectories, 150 DOPG molecules were randomly distributed in an aqueous solution alongside $[1]^{2+}$. In the remaining 30 trajectories, 170 DOPG molecules were placed into the box to simulate the assembly of the lipid bilayer and the alignment of $[1]^{2+}$ within it. Two different lipid concentrations were used to investigate the influence of lipid concentration on the outcome; as in the experimental preparation of the giant vesicles and liposomes, the solvent was evaporated and therefore the lipid concentration was not constant. The stages, which the MD simulations underwent, were similar throughout all the trajectories and have been previously reported for the self-assembly of lipid bilayer membranes.[27,28] These are exemplarily represented in Fig. 5 for $[1]^{2+}$ that inserts parallel to the assembled membrane (-Fig. 5a–d) and for one inserting transmembrane (e–h). At first, all molecular components are randomly distributed in the simulation box (a and e). Usually within the first 10 ns, the phospholipids aggregate, with $[1]^{2+}$ bound to the aggregates (b and f). The aggregates assemble in one plane, forming a membrane, which is penetrated by water pores (c and g). As is apparent from our simulations, the configuration of $[1]^{2+}$ relative to the water pores is impacting the final insertion. In the final stage, the water pores disappear and a fully assembled bilayer is formed. This vanishing of the pores can take a couple of hundred of nanoseconds, especially in the trajectories with a higher number of lipid molecules. If $[1]^{2+}$ is in the pore when the water molecules leave the hydrophobic area of the membrane, $[1]^{2+}$ assembles the transmembrane. This does not happen if $[1]^{2+}$ does not penetrate through one of the pores. As there appears to be some chance of whether $[1]^{2+}$ penetrates a pore when the pore disappears, there is also a statistical distribution between parallel and transmembrane insertions over the trajectories. The results of the assembly simulations are presented in Table 2.

The MD simulations predict a preference for the parallel insertion mode of $[1]^{2+}$ into the membrane. This trend is particularly clear from the simulations with 150 DOPG molecules with *ca.* 80% of the trajectories displaying parallel insertions (Fig. 5a–d) but also evident in the simulations using more DOPG molecules, with the parallel insertion mode still amounting to over 60% of the completed trajectories. We therefore conclude that the parallel $[1]^{2+}$ should be the dominant species responsible for the double half-moon effect exhibited in the confocal microscopy images. However, an important finding of the simulations is that in both sets there are non-negligible amounts of transmembrane $[1]^{2+}$ (Fig. 5e–h), indicating that both insertion modes occur in the membrane, and any subsequent analysis cannot be limited to a single orientation. In both orientations, $[1]^{2+}$ is partially exposed to hydrogen bonding water molecules from the aqueous phase and can potentially engage in light-driven oxidation reactions with water soluble reactants.

Photooxidation

To see if the membrane-associated $[1]^{2+}$ could engage in light-driven reactions with reactants in the aqueous bulk, the respective DOPG liposomes were exposed to the water-soluble oxidant sodium peroxydisulfate ($Na_2S_2O_8$) and a 470 nm light source. To exclude effects of vesicle size and surface curvature on the reaction dynamics,[6,29] unilamellar, monodisperse vesicles with an average hydrodynamic diameter of around 120 nm were prepared, providing a high surface area compared to giant multilamellar vesicles. The reaction progress was monitored using time resolved and steady state UV-vis absorption spectroscopy and emission spectroscopy and the radical generation was additionally characterized using electron paramagnetic resonance spectroscopy (EPR).

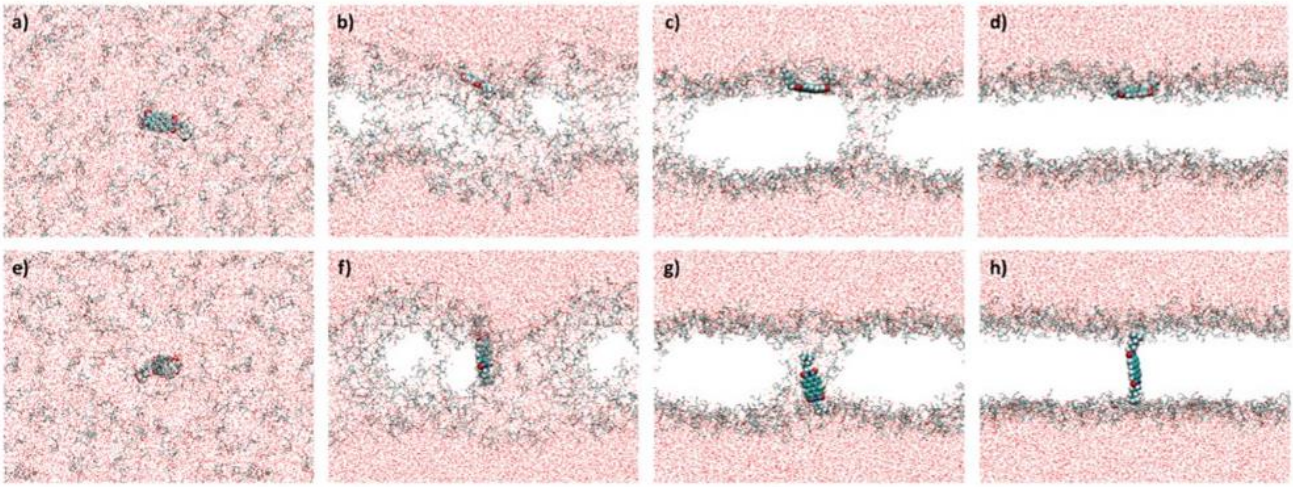

Fig. 5 Stages of the membrane assembly in the simulations. a–d) Parallel insertion of $[1]^{2+}$ (62–81%, see Table 3); e–h) transmembrane insertion of $[1]^{2+}$ (19–38%, see Table 3). Color code: red = oxygen, white = hydrogen, blue = nitrogen, yellow = phosphorus, and turquois = carbon. The alkyl tails of the lipid bilayer are omitted for clarity.

This journal is © The Royal Society of Chemistry and IChemE 2023

Table 2 Results of the assembly simulations of $[1]^{2+}$

DOPG molecules	Trajectories with $[1]^{2+}$ assembled in the membrane	Parallel insertions	Transmembrane insertions
150	16	13 (81%)	3 (19%)
170	21	13 (62%)	8 (38%)

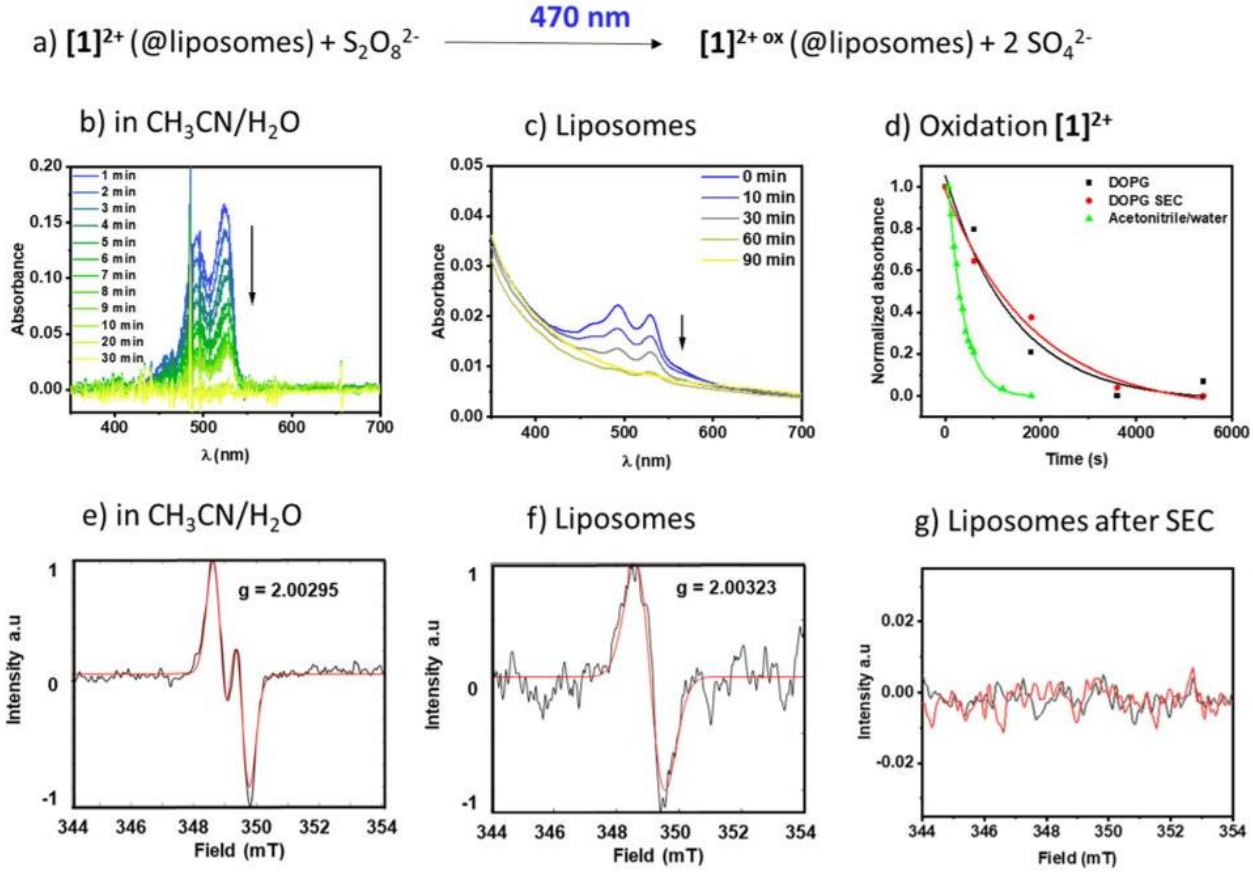

Fig. 6 a) Photooxidation of $[1]^{2+}$ and temporally resolved UV-vis spectra in b) acetonitrile/water 1 : 1 (V : V) and c) DOPG : (14 : 0 PEG2000 PE) : $[1]^{2+}$ = 100 : 1 : 1 liposomes in phosphate buffer (10 mM, pH 7.0) after size exclusion. d) Temporal evolution of the PDI absorbance at 527 nm (acetonitrile/water) and 530 nm (DOPG) in different environments. e–g) EPR spectra of the photooxidized PDI after 18 h irradiation at 455 nm in e) acetonitrile/water and f and g) liposomes with DOPG : (14 : 0 PEG2000 PE) : $[1]^{2+}$ = 100 : 1 : 1 in phosphate buffer (10 mM, pH 7.0) f) without size exclusion and g) after chromatography (SEC).

In pure water $[1]^{2+}$ was insufficiently soluble and therefore we added acetonitrile to generate a 1 : 1 (V : V) mixture of acetonitrile and water to solubilize both $[1]^{2+}$ and the oxidant sodium persulfate in a homogenous solution. Fig. 6b shows the respective time-dependent spectra under homogeneous conditions, and Fig. 6d shows the absorbance *vs.* time profiles, demonstrating a fast consumption of $[1]^{2+}$ with a rate constant of $(3.04 \pm 0.1)\ 10^{-3}\ s^{-1}$. The photogenerated radical $[1]^{3+\bullet}$ was characterized under comparable homogeneous conditions using EPR (Fig. 6e) and shows a signal with A_1 = 59 MHz and A_2 = 7 MHz and a *g*-factor of g = 2.00295 compatible with a radical centered on one carbon and one hydrogen, which is in agreement with the formation of *J*-aggregates of $[1]^{2+}$ in aqueous solution.

Upon incorporation of $[1]^{2+}$ into the membrane of DOPG liposomes, the rate of oxidation becomes slower, as seen in the time-dependent evolution of the spectra in Fig. 6c and in 6d. Furthermore, the kinetics of the photooxidation in liposomes do not depend on the purification of the liposomes ($(0.70 \pm 0.3)\ 10^{-3}\ s^{-1}$ *vs.* $(0.55 \pm 0.1)\ 10^{-3}\ s^{-1}$ without or with size exclusion chromatography purification, respectively). However, the EPR signal of only the non-size excluded liposomes could be detected under the measurement conditions applied here. It shows a singlet at g = 2.00323, compatible with an unpaired electron localized on a carbon. It is expected that upon inclusion of a radical into a solid-state matrix, it is difficult for the radicalized molecule to align within the magnetic field of the resonator, resulting

in line broadening due to anisotropic effects. As a radical signal is visible in the non-size excluded samples, we assume that there are small amounts of mobile $[\mathbf{1}]^{2+}$ molecules that can rotate and align to some extent in the magnetic field and this appears as a broad signal in the EPR spectrum. Size exclusion seems to remove this fraction of mobile molecules and thereby removes the signature of a radical at the applied resolution, which might be due to strong band broadening due to the solid-like state matrix of the lipid bilayer.[30] Removal of $[\mathbf{1}]^{2+}$ from the bulk aqueous solution *via* size exclusion is supported by a diminished absorption of the PDI signal at 527 nm (see Fig. 6c *vs.* Fig. S2.1†). Based on the extinction coefficient in acetonitrile/water and neglecting the scattering effect we estimate that the overall concentration of $[\mathbf{1}]^{2+}$ in the sample is reduced from around 1.3 μM to around 0.3 μM, which indicates that a large portion of the chromophore in solution could be removed. As the UV-vis spectroscopic signatures and conversion rates in liposomes are practically identical, we conclude that the radical species oxidized $[\mathbf{1}]^{2+}$ is formed nevertheless.

In an emission quenching assay, the so-called Stern–Volmer plot, we observed that the photoexcited state of $[\mathbf{1}]^{2+}$ is quenched at various concentrations of the oxidant $Na_2S_2O_8$. Quenching of homogeneously dissolved $[\mathbf{1}]^{2+}$ in 1 : 1 (V : V) acetonitrile–water mixture occurred with a Stern–Volmer constant with different values for the quenching of the emission spectrum's intensity and lifetime with $K_{SV}(I_0/I)$ = 17.0 ± 2.9 and $K_{SV}(\tau_0/\tau)$ = 0.04 ± 0.02, respectively, which indicates a static quenching process as the intensity-based Stern–Volmer constant is positive and the lifetime-based Stern–Volmer constant is close to zero.[7,31,32] Upon incorporation of $[\mathbf{1}]^{2+}$ into liposomes the intensity and lifetime-based Stern-Volmer constants differ from each other with $K_{SV}(I_0/I)$ = 20.9 ± 1.9 and $K_{SV}(\tau_0/\tau)$ = −0.17 ± 0.02, respectively. The lifetime-based Stern–Volmer constant appears to be slightly negative, however, when comparing the actual lifetimes, no significant effect is observed, as the lifetimes stay constant within the experimental error of the lifetime measurements. Comparing it to the intensity-based Stern–Volmer constant, it is close to zero, indicating static quenching. Within liposomes after size exclusion, the intensity-based lifetime Stern–Volmer constant is $K_{SV}(I_0/I)$ = 14.2 ± 1.9 while the lifetime-based Stern–Volmer constant approaches zero $K_{SV}(\tau_0/\tau)$ = −0.17 ± 0.02 which strongly indicates a static quenching process (Fig. 7).[7,31,32] Such static quenching processes are typical for singlet emitters with short excited state lifetimes where a pre-associated chromophore–quencher adduct needs to be formed for the quenching process to take place (Table 3).[31]

From the Stern–Volmer constants and the lifetime of the chromophore in the absence of a quencher, the quenching constant k_q can be calculated as follows:[31,33] $k_q = K_{SV} \cdot \tau_0$. Interestingly, all quenching constants k_q are very similar for all the investigated environments of $[\mathbf{1}]^{2+}$, however, the rate of photooxidation to complete oxidation of $[\mathbf{1}]^{2+}$ differs by around a factor of two between the homogeneous solution and liposomes (Table 3). We propose that these differences in the kinetics are due to the differences in the diffusion behavior of the water-soluble persulfate anions through the membrane, which access the chromophores at the inner membrane surface and aqueous compartment more slowly than in the homogenous environment (Fig. 8). This explanation is in line with reported transmembrane diffusion coefficients for ionic species of around 10^{-3} to 10^{-8} cm s^{-1} and reported cases of transmembrane diffusion of smaller ions.[34–36]

Conclusions and outlook

In summary, $[\mathbf{1}]^{2+}$ forms *J*-aggregates in the presence of water and can be incorporated into negatively charged lipid bilayers of DOPG. According to results obtained from MD simulations, it preferably aligns parallel to the membrane surface although transmembrane orientations are also possible to a minor extent. Light-driven oxidation by the water-soluble, negatively charged oxidant persulfate takes place *via* a static quenching mechanism both in liposomes and in homogeneous solution due to electrostatic pre-association of both reactants. Despite similar excited state quenching dynamics, the photooxidation of $[\mathbf{1}]^{2+}$ is two factors faster in homogeneous solution compared to the lipid bilayer environment, which is attributed to the relatively slow

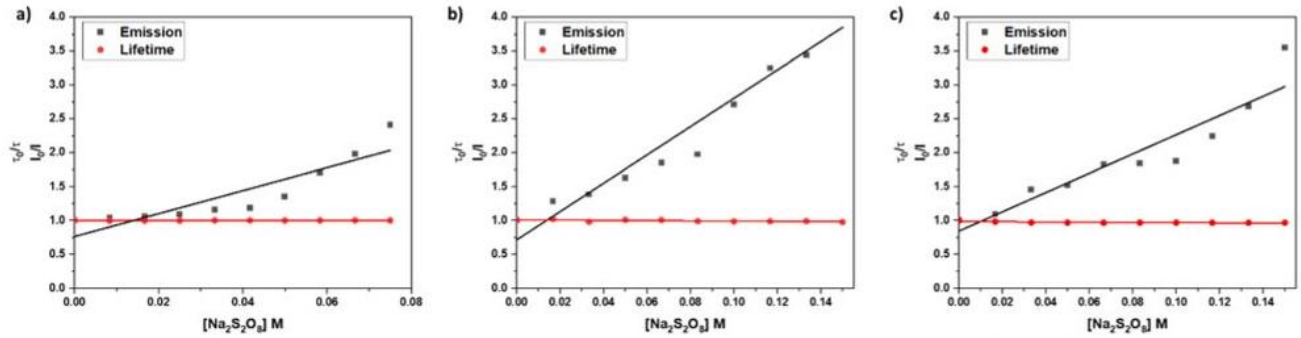

Fig. 7 Stern–Volmer quenching experiments for different systems: a) acetonitrile/water 1 : 1 (V : V), b) DOPG : (14 : 0 PEG2000 PE) : $[\mathbf{1}]^{2+}$ = 100 : 1 : 1 liposomes in phosphate buffer (10 mM, pH 7.0) without size exclusion chromatography, c) DOPG : (14 : 0 PEG2000 PE) : $[\mathbf{1}]^{2+}$ = 100 : 1 : 1 liposomes in phosphate buffer (10 mM, pH 7.0) after size exclusion chromatography.

This journal is © The Royal Society of Chemistry and IChemE 2023

Table 3 Oxidation rate constants, Stern–Volmer quenching constants and quenching constants of $[1]^{2+}$ in acetonitrile/water and DOPG membranes, monitored at the absorption maximum

Solvent or lipid	k_{ox} (10^{-3} s^{-1})	K_{SV} from I_0/I (M^{-1})	K_{SV} from τ_0/τ (M^{-1})	k_q (10^{-9} M^{-1} s^{-1}) from I_0/I
Acetonitrile/water	3.04 ± 0.1	17.0 ± 2.9	0.04 ± 0.02	70.9 ± 0.03
DOPG liposomes[a]	0.70 ± 0.3	20.9 ± 1.9	−0.17 ± 0.02	85.9 ± 0.02
DOPG liposomes[a,b]	0.55 ± 0.1	14.2 ± 1.9	−0.17 ± 0.02	56.8 ± 0.04

[a] DOPG : (14 : 0 PEG2000 PE) : $[1]^{2+}$ = 100 : 1 : 1; in phosphate buffer (10 mM, pH 7.0). [b] After size exclusion.

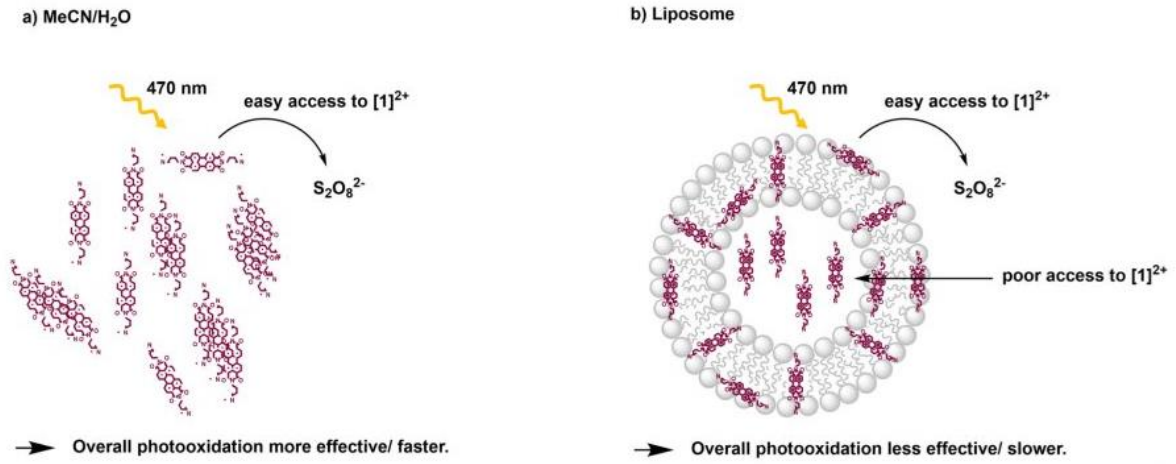

Fig. 8 Illustration of photooxidation experiments for different systems: a) acetonitrile/water 1 : 1 (V:V); b) DOPG : (14 : 0 PEG2000 PE) : $[1]^{2+}$ = 100 : 1 : 1 liposomes in phosphate buffer (10 mM, pH 7.0).

diffusion of the oxidant through the lipid bilayer membrane to photooxidize the chromophore within the aqueous interior of the liposomes. These findings will be important for the design and engineering of molecular systems in the context of light-driven catalysis involving amphiphilic membrane materials and abundant organic photosensitizers.

Experimental and methods part

All reagents were commercially available. Perylene tetracarboxylic dianhydride and methyl iodide were purchased from Merck. (4-Aminobutyl)dimethylamine was purchased from Enamine. The synthesis of $[1]^{2+}$ was adapted from a previously reported procedure (ESI,† S1). All synthesis reactions were carried out under an inert atmosphere using standard Schlenk-techniques and argon gas. A Bruker DRX 400 spectrometer was used to obtain nuclear magnetic resonance (NMR) spectra recorded at 298 K. MestReNova was used for the evaluation of the spectra. The mass spectra of the compounds were obtained using a matrix assisted laser desorption ionization (MALDI) Bruker Reflex III mass spectrometer. *trans*-2-[3-(4-*tert*-Butylphenyl)-2-methyl-2-propenylidene]malononitrile was used as the matrix. Elemental analysis was performed by Mikroanalytisches Laboratorium Kolbe in Oberhausen, Germany. The elemental content of the molecules was reported as the element's mass fraction percentage. Absorption spectra were recorded on a JASCO V760 spectrometer or an Avantes AvaSpec. Starna fluorescence quartz cuvettes with a path length of 1 cm were used. Luminescence was recorded using a Horiba Jobin Yvon FluoroMax4 Plus C spectrophotometer equipped with a 150 W xenon lamp. The error of the lifetime was estimated to be 0.1 ns. The errors given in Table 3 are based on the error derived from the data fitting. In the case of the K_{SV} constants from τ_0/τ, the slope value was very small, and we report the standard deviation of the slope fitting or 10% if the standard deviation was smaller than 10%. The size distribution of the hydrodynamic diameter (Z_{Avg}) was measured at 20 °C with a Zetasizer Pro from Malvern operating at 633 nm with a scattering angle of 173°. Confocal microscopy images were obtained using a Leica TCS SP8 confocal microscope equipped with a 488 nm laser as the excitation source and detected in the range of 503–750 nm. Images were processed with LasX. Luminescence lifetimes were recorded with a DeltaPro system from Horiba Scientific using a 451 nm pulsed laser source and a 495 nm long pass filter; the instrument response function was measured with LUDOX silica nanoparticles.

Preparation and characterization of giant vesicles and liposomes

Giant vesicles and liposomes were prepared as follows. The lipids 1,2-dioleoyl-*sn-glycero*-3-phospho-(1′-*rac*-glycerol) (DOPG) and 1,2-dimyristoyl-*sn-glycero*-3-phosphoethanolamine-*N*-[methoxy(polyethylene glycol)-2000]

(ammonium salt) (14 : 0 PEG2000 PE) were prepared as stock solutions in $CHCl_3$. To prepare a lipid film in a 5 mL round-bottom flask, a 1 mL stock solution of DOPG (5.0 mM) and 1 mL 14 : 0 PEG2000 PE (0.05 mM) in $CHCl_3$ and 1 mL $[\mathbf{1}]^{2+}$ (0.05) in acetonitrile were combined. The organic solvents were evaporated under vacuum leading to deposition of the lipid on the flask wall. The film was dried under high vacuum for at least one hour and hydrated with 10 mM buffer phosphate (KH_2PO_4 (626 mg, 4.6 mmol), $K_2HPO_4{\cdot}3H_2O$ (1.186 g, 5.2 mmol), and K_2SO_4 (1.70 g, 9.74 mmol) in Milli-Q water (1 L) to reach a final pH of 7.0). The dispersed lipid film was repeatedly freeze-thawed using liquid N_2 and a water bath at room temperature yielding giant vesicles. To obtain liposomes of uniform size, the dispersion was extruded at room temperature through 200 nm cellulose membrane filters 11 times with an Avanti Polar Lipids mini-extruder. If applicable, the liposome mixture was subjected to a Sephadex G-25 size exclusion chromatography (SEC) column (6 cm length, 2 cm diameter) using phosphate buffer pH 7.0 as the eluent. Dynamic light scattering (DLS) on liposomes with and without SEC typically yielded a Z_{Avg}-diameter of around 110–120 nm and a PDI of around 0.1. Confocal microscopy with a Leica TCS SP8 and sample wells (μ-Slide 8 Well ibiTreat) was used to characterize giant vesicles. Prior to microscopy, and if applicable, giant vesicles were subjected to SEC as described above. 100 μL of the giant vesicle sample was loaded to a well, and then 200 μl of a freshly prepared, air-cooled agarose solution (1 weight% in water) was added and mixed. Confocal microscopy measurements were conducted after the mixed solutions had settled at room temperature.

Photoirradiation

The typical reactions were carried out with 5 μM of $[\mathbf{1}]^{2+}$ and 50 mM sodium persulfate mixed in a quartz cuvette with a total volume of 3 mL. The mixtures were stirred at room temperature and illuminated with a LED-stick (Nichia Corporation; NSPB500AS) (λ = 470 nm, 27 mW measured with a Hioki 3664 optical power meter set to 470 nm) which consisted of a custom-made reactor equipped with four ventilators to exclude heating of the samples.[37] The samples were monitored *via* UV-vis spectroscopy after 0, 10, 30, 60, and 90 minutes.

EPR measurements

Samples with a concentration of 10–4 mM $[\mathbf{1}]^{2+}$ and 50 eq. of $Na_2S_2O_8$ in acetonitrile/water (V : V = 1 : 1) were prepared. For the measurements of $[\mathbf{1}]^{2+}$ integrated into DOPG liposomes, samples with a concentration of 10–4 mM $[\mathbf{1}]^{2+}$ and 10 mM DOPG and 50 eq. of $Na_2S_2O_8$ were prepared in phosphate buffer pH 7.0. All sample solutions were transferred into a flat cell with a volume of approximately 200 μL under ambient conditions. CW EPR spectroscopic measurements were carried out at the X-Band using a Bruker ELEXSYS E500 spectrometer equipped with an SHQE resonator. Measurements were performed at room temperature with microwave powers of 5–6 mW and modulation amplitudes of 0.1 mT (without liposomes), 0.5 mT (with liposomes) and 0.3 mT (with liposomes SEC). A fiber-coupled LED (455 nm, Thorlabs M455F3) was installed for continuous irradiation of the samples in the resonator for up to 20 h. Simulation of experimental data was carried out with EasySpin.[38]

Computational details

The transition dipole moment (μ_T) of $[\mathbf{1}]^{2+}$ was computed using time-dependent density functional theory (TD-DFT) at the RB3LYP/def2-SVP level of theory,[39–42] as implemented in the program package Gaussian16, revision C.01,[43] using the optimized first excited singlet structure. Solvent effects for acetonitrile were included implicitly using the polarizable conductor-like calculation model (CPCM) by placing the solute in a cavity within the solvent reaction field.[44,45] Dispersion interaction effects were corrected empirically using the Grimme D3 model with Becke–Johnson damping.[46,47]

Classical force field MD simulations of the lipid bilayer assembly were carried out to elucidate the orientation and alignment of $[\mathbf{1}]^{2+}$. To this aim, we randomly distributed 150 and 170 DOPG lipids (20 and 30 trajectories, respectively) and one molecule of $[\mathbf{1}]^{2+}$ in a cubic box of 90 Å side length. The remaining box volume was then filled with water molecules and KCl ions to ensure charge neutrality and attain a salt concentration of 0.15 mol l^{-1}. The starting systems were assembled with the input generator CHARMM-GUI.[48]

All the MD simulations were performed with the program packages Amber20 and AmberTools21.[49] $[\mathbf{1}]^{2+}$ was described using the generalized Amber force field included in AmberTools21, with ground state point charges computed within the restrained electrostatic potential atomic partial charge (RESP) scheme in Gaussian16 on the RB3LYP/def2-SVP level of theory (see above). The lipids were described using the Lipid17 force field, while water and the atomic ions were described using the "optimal" point charge model[50] implemented in AmberTools21. After a 10 000 step minimization with 5000 steps employing the steepest gradient algorithm and another 5000 steps using a conjugate gradient algorithm, the systems were heated using a Langevin thermostat at a collision frequency of 1.0 ps^{-1} to 100 K in 2500 time steps (5 ps), followed by heating to 300 K in 50 000 steps (100 ps). Finally, the systems were propagated until the membrane was assembled and all water pores had disappeared. The insertion mode of $[\mathbf{1}]^{2+}$ was then investigated by eye.

For all simulations, a time step of 2 fs was used with the SHAKE algorithm[51] applied to freeze hydrogen bonds at a relative geometric tolerance of 1.10^{-7}, thus enabling large time steps. Constant pressure periodic boundary conditions were superimposed with anisotropic pressure scaling at a pressure relaxation time of 1 ps, which was increased to 2 ps for the second heating phase only. The cutoff for non-bonded

This journal is © The Royal Society of Chemistry and IChemE 2023

interaction terms was set to 10 Å. The simulations were performed using the GPU (CUDA) version of pmemd.[52–54]

In general, simulations with fewer (150) DOPG molecules ran more stably and were more likely to assemble a membrane. By contrast, the higher number of DOPG molecules (170) led to more simulations crashing due to distortion of the rectangular periodic box and lipid molecules clump together more often, not forming a membrane. Additionally, the CHARMM-GUI input generator with which we obtained the systems prompted a warning in the 170 DOPG simulations, claiming that too little volume of solvent is left after the placement of $[\mathbf{1}]^{2+}$ and the lipid molecules. As a result, more trajectories with 170 DOPG molecules needed to be executed to compensate for the crashing trajectories. This also allowed us to obtain more solid statistics in the latter case, as here the difference in parallel and transmembrane insertion modes was smaller compared to the 150 DOPG simulations.

Conflicts of interest

There are no conflicts to declare.

Acknowledgements

The authors thank the Deutsche Forschungsgemeinschaft (DFG, project TRR234 "CataLight" project number 364549901, projects B8, C3 and A1), the Austrian Science Fund (FWF project no. I3987-N28 and I6116) and the Vector Stiftung (project number P2019-0110) for financial support. The confocal images were recorded at the Core Facility for Confocal and Multiphoton Microscopy at Ulm University which is supported by the DFG through project number 91BGG INST 381/39-1. We thank Dr. Sviatlana Kalinina and Dr. Christian Bökel for their support during confocal microscopy.

References

1 J. Volarić, W. Szymanski, N. A. Simeth and B. L. Feringa, *Chem. Soc. Rev.*, 2021, **50**, 12377–12449.
2 L. Zhou, F. Lv, L. Liu and S. Wang, *Acc. Chem. Res.*, 2019, **52**, 3211–3222.
3 A. Call, M. Cibian, K. Yamamoto, T. Nakazono, K. Yamauchi and K. Sakai, *ACS Catal.*, 2019, **9**, 4867–4874.
4 N. Nelson and C. F. Yocum, *Annu. Rev. Plant Biol.*, 2006, **57**, 521–565.
5 A. Pannwitz, D. M. Klein, S. Rodríguez-Jiménez, C. Casadevall, H. Song, E. Reisner, L. Hammarström and S. Bonnet, *Chem. Soc. Rev.*, 2021, **50**, 4833–4855.
6 R. E. P. Nau, J. Bösking and A. Pannwitz, *ChemPhotoChem*, 2022, **6**, e202200158.
7 S. Rodríguez-Jiménez, H. Song, E. Lam, D. Wright, A. Pannwitz, S. A. Bonke, J. J. Baumberg, S. Bonnet, L. Hammarström and E. Reisner, *J. Am. Chem. Soc.*, 2022, **23**, 50.
8 D. M. Klein, S. Rodríguez-Jiménez, M. E. Hoefnagel, A. Pannwitz, A. Prabhakaran, M. A. Siegler, T. E. Keyes, E. Reisner, A. M. Brouwer and S. Bonnet, *Chem. – Eur. J.*, 2021, **27**, 17203–17212.
9 S. Troppmann and B. König, *Chem. – Eur. J.*, 2014, **20**, 14570–14574.
10 M. Hansen, F. Li, L. Sun and B. König, *Chem. Sci.*, 2014, **5**, 2683–2687.
11 B. Limburg, J. Wermink, S. S. Van Nielen, R. Kortlever, M. T. M. Koper, E. Bouwman and S. Bonnet, *ACS Catal.*, 2016, **6**, 5968–5977.
12 N. Ikuta, S. Takizawa and S. Murata, *Photochem. Photobiol. Sci.*, 2014, **13**, 691–702.
13 N. Kihal, A. Nazemi and S. Bourgault, *Nanomaterials*, 2022, **12**, 1223.
14 F. Würthner, *Chem. Commun.*, 2004, 1564–1579.
15 B. Wang and C. Yu, *Angew. Chem.*, 2010, **122**, 1527–1530.
16 D. Costabel, A. Skabeev, A. Nabiyan, Y. Luo, J. B. Max, A. Rajagopal, D. Kowalczyk, B. Dietzek, M. Wächtler, H. Görls, D. Ziegenbalg, Y. Zagranyarski, C. Streb, F. H. Schacher and K. Peneva, *Chem. – Eur. J.*, 2021, **27**, 4081–4088.
17 D. Marsh, *Handbook of Lipid Bilayers*, CRC Press, 2013.
18 A. Pannwitz, H. Saaring, N. Beztsinna, X. Li, M. A. Siegler and S. Bonnet, *Chem. – Eur. J.*, 2021, **27**, 3013–3018.
19 M. Hariharan, Y. Zheng, H. Long, T. A. Zeidan, G. C. Schatz, J. Vura-Weis, M. R. Wasielewski, X. Zuo, D. M. Tiede and F. D. Lewis, *J. Am. Chem. Soc.*, 2009, **131**, 5920–5929.
20 H. Dincalp, N. Avcibasi and S. Icli, *J. Photochem. Photobiol., A*, 2007, **185**, 1–12.
21 S. Ghosh, X.-Q. Li, V. Stepanenko and F. Würthner, *Chem. – Eur. J.*, 2008, **14**, 11343–11357.
22 F. C. Spano and C. Silva, *Annu. Rev. Phys. Chem.*, 2014, **65**, 477–500.
23 W. E. Ford and P. V. Kamat, *J. Phys. Chem.*, 1987, **91**, 6373–6380.
24 H. Langhals, J. Karolin and L. B. Johansson, *J. Chem. Soc., Faraday Trans.*, 1998, **94**, 2919–2922.
25 S. Berardi, V. Cristino, M. Canton, R. Boaretto, R. Argazzi, E. Benazzi, L. Ganzer, R. Borrego Varillas, G. Cerullo, Z. Syrgiannis, F. Rigodanza, M. Prato, C. A. Bignozzi and S. Caramori, *J. Phys. Chem. C*, 2017, **121**, 17737–17745.
26 L. E. Garner, J. Park, S. M. Dyar, A. Chworos, J. J. Sumner and G. C. Bazan, *J. Am. Chem. Soc.*, 2010, **132**, 10042–10052.
27 Å. A. Skjevik, B. D. Madej, C. J. Dickson, K. Teigen, R. C. Walker and I. R. Gould, *Chem. Commun.*, 2015, **51**, 4402–4405.
28 Å. A. Skjevik, B. D. Madej, C. J. Dickson, C. Lin, K. Teigen, R. C. Walker and I. R. Gould, *Phys. Chem. Chem. Phys.*, 2016, **18**, 10573–10584.
29 J. N. Robinson and D. J. Cole-Hamilton, *Chem. Soc. Rev.*, 1991, **20**, 49–94.
30 P. Gast and E. J. J. Groenen, in *eMagRes*, John Wiley & Sons, Ltd, Chichester, UK, 2016, pp. 1435–1444.
31 V. Balzani, P. Ceroni and A. Juris, *Photochemistry and Photophysics*, Wiley-VCH Verlag, Weinheim, Germany, 2014.
32 H. Song, A. Amati, A. Pannwitz, S. Bonnet and L. Hammarström, *J. Am. Chem. Soc.*, 2022, **144**, 19353–19364.
33 M. H. Gehlen, *J. Photochem. Photobiol., C*, 2020, **42**, 100338.

34 D. W. Deamer and J. Bramhall, *Chem. Phys. Lipids*, 1986, **40**, 167–188.
35 J. de Gier, *Chem. Phys. Lipids*, 1993, **64**, 187–196.
36 J. Wu, R. M. Crist, S. E. McNeil and J. D. Clogston, *J. Pharm. Biomed. Anal.*, 2019, **165**, 41–46.
37 S. Tschierlei, M. Karnahl, M. Presselt, B. Dietzek, J. Guthmuller, L. González, M. Schmitt, S. Rau and J. Popp, *Angew. Chem.*, 2010, **122**, 4073–4076.
38 S. Stoll and A. Schweiger, *J. Magn. Reson.*, 2006, **178**, 42–55.
39 J. P. Perdew, *Phys. Rev. B: Condens. Matter Mater. Phys.*, 1986, **33**, 8822.
40 C. Lee, W. Yang and R. G. Parr, *Phys. Rev. B: Condens. Matter Mater. Phys.*, 1988, **37**, 785–789.
41 F. Weigend and R. Ahlrichs, *Phys. Chem. Chem. Phys.*, 2005, **7**, 3297.
42 F. Weigend, *Phys. Chem. Chem. Phys.*, 2006, **8**, 1057.
43 M. J. Frisch, G. W. Trucks, H. B. Schlegel, G. E. Scuseria, M. A. Robb, J. R. Cheeseman, G. Scalmani, V. Barone, G. A. Petersson, H. Nakatsuji, X. Li, M. Caricato, A. V. Marenich, J. Bloino, B. G. Janesko, R. Gomperts, B. Mennucci, H. P. Hratchian, J. V. Ortiz, A. F. Izmaylov, J. L. Sonnenberg, F. Ding Williams, F. Lipparini, F. Egidi, J. Goings, B. Peng, A. Petrone, T. Henderson, D. Ranasinghe, V. G. Zakrzewski, J. Gao, N. Rega, G. Zheng, W. Liang, M. Hada, M. Ehara, K. Toyota, R. Fukuda, J. Hasegawa, M. Ishida, T. Nakajima, Y. Honda, O. Kitao, H. Nakai, T. Vreven, K. Throssell, J. A. Montgomery Jr., J. E. Peralta, F. Ogliaro, M. J. Bearpark, J. J. Heyd, E. N. Brothers, K. N. Kudin, V. N. Staroverov, T. A. Keith, R. Kobayashi, J. Normand, K. Raghavachari, A. P. Rendell, J. C. Burant, S. S. Iyengar, J. Tomasi, M. Cossi, J. M. Millam, M. Klene, C. Adamo, R. Cammi, J. W. Ochterski, R. L. Martin, K. Morokuma, O. Farkas, J. B. Foresman and D. J. Fox, *Gaussian 16, Revision C.01*, Gaussian, Inc., Wallingford, CT, 2016.
44 V. Barone and M. Cossi, *J. Phys. Chem. A*, 1998, **102**, 1995–2001.
45 M. Cossi, N. Rega, G. Scalmani and V. Barone, *J. Comput. Chem.*, 2003, **24**, 669–681.
46 S. Grimme, J. Antony, S. Ehrlich and H. Krieg, *J. Chem. Phys.*, 2010, **132**, 154104.
47 S. Grimme, S. Ehrlich and L. Goerigk, *J. Comput. Chem.*, 2011, **32**, 1456–1465.
48 S. Jo, T. Kim, V. G. Iyer and W. Im, *J. Comput. Chem.*, 2008, **29**, 1859–1865.
49 D. A. Case, K. Belfon, I. Y. Ben-Shalom, S. R. Brozell, D. S. Cerutti, T. E. Cheatham, III, V. W. D. Cruzeiro, T. A. Darden, R. E. Duke, G. Giambasu, M. K. Gilson, H. Gohlke, A. W. Goetz, R. Harris, S. Izadi, S. A. Izmailov, K. Kasavajhala, A. Kovalenko, R. Krasny, T. Kurtzman, T. S. Lee, S. LeGrand, P. Li, C. Lin, J. Liu, T. Luchko, R. Luo, V. Man, K. M. Merz, Y. Miao, O. Mikhailovskii, G. Monard, H. Nguyen, A. Onufriev, F. Pan, S. Pantano, R. Qi, D. R. Roe, A. Roitberg, C. Sagui, S. Schott-Verdugo, J. Shen, C. L. Simmerling, N. R. Skrynnikov, J. Smith, J. Swails, R. C. Walker, J. Wang, L. Wilson, R. M. Wolf, X. Wu, Y. Xiong, Y. Xue, D. M. York and P. A. Kollman, *AMBER 2020*, University of California, San Francisco, 2020.
50 S. Izadi, R. Anandakrishnan and A. V. Onufriev, *J. Phys. Chem. Lett.*, 2014, **5**, 3863–3871.
51 J.-P. Ryckaert, G. Ciccotti and H. J. C. Berendsen, *J. Comput. Phys.*, 1977, **23**, 327–341.
52 R. Salomon-Ferrer, A. W. Götz, D. Poole, S. Le Grand and R. C. Walker, *J. Chem. Theory Comput.*, 2013, **9**, 3878–3888.
53 A. W. Götz, M. J. Williamson, D. Xu, D. Poole, S. Le Grand and R. C. Walker, *J. Chem. Theory Comput.*, 2012, **8**, 1542–1555.
54 S. Le Grand, A. W. Götz and R. C. Walker, *Comput. Phys. Commun.*, 2013, **184**, 374–380.

This journal is © The Royal Society of Chemistry and IChemE 2023

Electronic Supplementary Material (ESI) for Molecular Systems Design & Engineering.
This journal is © The Royal Society of Chemistry 2023

Supporting Information

Alignment and photooxidation dynamics of a perylene diimide chromophore in lipid bilayers

Authors:

Novitasari Sinambela,[a] Richard Jacobi,[b,c] David Hernández-Castillo,[b,c] Elisabeth Hofmeister,[f] Nina Hagmeyer,[e,f] Benjamin Dietzek-Ivanšić,[e,f] Leticia González,[b,d] and Andrea Pannwitz[a]

[a]Institute of Inorganic Chemistry I, Ulm University, Albert-Einstein-Allee 11, 89081 Ulm, Germany

[b]Institute of Theoretical Chemistry, Faculty of Chemistry, University of Vienna, Währinger Straße 17, 1090 Vienna, Austria

[c]Doctoral School in Chemistry (DoSChem), University of Vienna, Währinger Straße 42, 1090 Vienna, Austria

[d]Vienna Research Platform on Accelerating Photoreaction Discovery, University of Vienna, Vienna, Austria, Währinger Straße 17, 1090 Vienna

[e]Institute of Physical Chemistry and Abbe Center of Photonics, Friedrich Schiller University Jena, Helmholtzweg 4, Jena 07743, Germany

[f]Leibniz Institute of Photonic Technology (IPHT), Research Department Functional Interfaces, Albert-Einstein-Straβe 9, Jena 07745, Germany

Contents

S1. Synthesis and characterization of 2 and $[1]^{2+}$ 3

Synthesis of N,N'-di(butylenedimethylamine)-3,4,9,10-perylenediimide (2) 3

Synthesis of N,N'-di(butylenetrimethylammonium)-3,4,9,10-perylenediimide $[1]^{2+}$ as PF_6 salt 4

S2. Photooxidation of $[1]^{2+}$ and temporally resolved UV-vis spectra in DOPG 6

S3. Stern-Volmer quenching experiment 7

S4. Typical hydrodynamic diameter of DOPG liposome containing $[1]^{2+}$ 11

S5. Coordinates of $[1]^{2+}$ 11

References 14

S1. Synthesis and characterization of 2 and $[1]^{2+}$

Synthesis of N,N'-di(butylenedimethylamine)-3,4,9,10-perylenediimide (2)

In 20 mL of isobutanol perylene tetracarboxylic dianhydride (0.100 g, 0.255 mmol, 1.00 eq.) and (4-aminobutyl) dimethylamine (0.14 mL, 1.02 mmol, 4.00 eq.) were combined, stirred and heated at 90 °C for 24 h under argon atmosphere. After the mixture was cooled to room temperature, the crude product was collected by filtration. To remove unreacted PTCDA, to the mixture was added 5% aqueous NaOH solution and stirred at 90 °C for 30 minutes. The product was separated from solvent by filtration and washed with water and ethanol. The red solid powder then dried under vacuum to give 0.14 g (0.238 mmol, 95% yield) product.

^{1}H NMR (400 MHz, $CDCl_3$) δ 8.61 (d, *J* = 8.0 Hz, 4H), 8.53 (d, *J* = 8.1 Hz, 4H), 4.20 (t, 4H), 2.45 – 2.23 (m, 4H), 2.22 (s, 12H), 1.86 – 1.67 (m, 4H), 1.61 – 1.39 (m, 4H).

MALDI-MS: calcd. for $[C_{36}H_{36}N_4O_4]^+$ (m/z): 588.27, found: 588.27

Anal. calcd. for $C_{36}H_{36}N_4O_4$: C, 73.45; H, 6.16; N, 9.52; O, 10.87, found C, 73.16; H, 6.15; N, 9.49; O, 10.96.

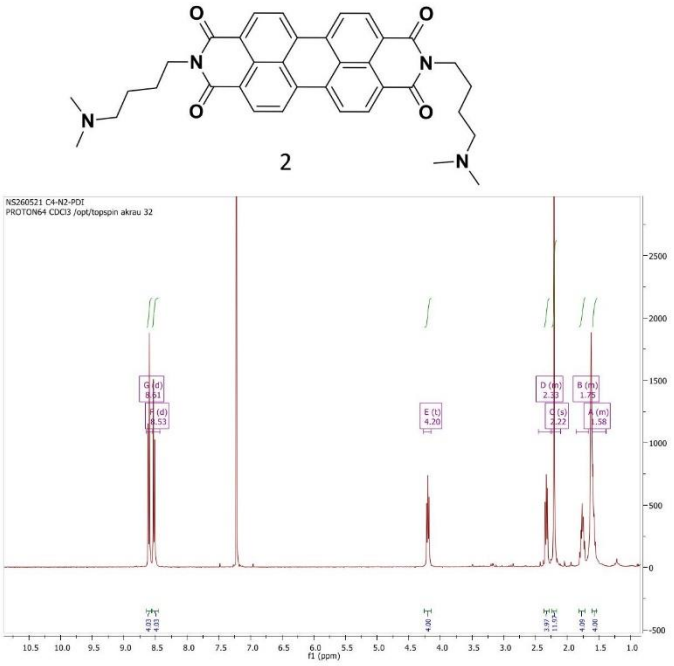

Figure S1.1: ^{1}H NMR spectrum of 2 in $CDCl_3$.

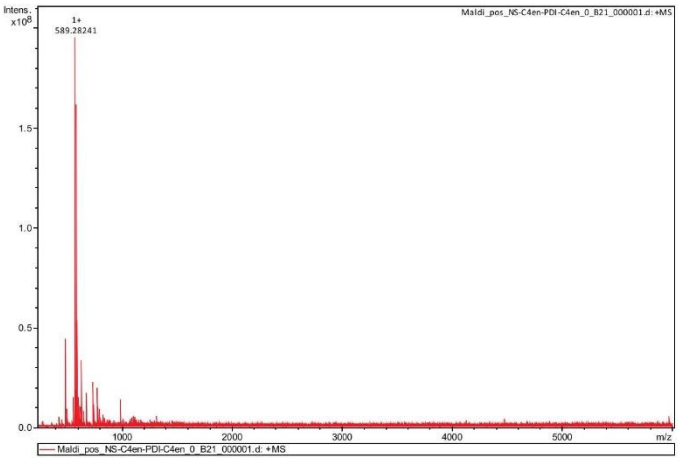

Figure S1.2: mass spectrum of 2.

Synthesis of N,N'-di(butylenetrimethylammonium)-3,4,9,10-perylenediimide $[1]^{2+}$ as PF_6 salt

A degassed solution of N,N'-di(butylenedimethylamine)-3,4,9,10-perylenediimide (0.100 g, 0.170 mmol, 1 eq.) and methyl iodide (0.287 mL, 1.70 mmol, 10 eq.) in 10 mL of toluene was refluxed for 3 h under argon atmosphere. The suspended mixture was collected by filtration, washed with ether and dried under vacuum. To the aqueous solution of the obtained compound was added dropwise to an aqueous solution of NH_4PF_6. After stirring of the solution at 65 °C for 1 h, the precipitate was centrifugated, washed with water to remove produced exchanged salts and dried under vacuum to give 0.12 g (0.130 mmol, 76 % yield) of the desired product.

^{1}H NMR (400 MHz, CD_3CN) δ 8.47 – 8.30 (m, 8H), 4.18 (t, *J* = 6.7 Hz, 4H), 3.39 – 3.29 (m, 4H), 3.04 (s, 18H), 1.85 – 1.70 (m, 8H).

MALDI-MS: calcd. for $[C_{38}H_{42}F_6N_4O_4P]^{2+}$(m/z): 763.28, found: 763.28

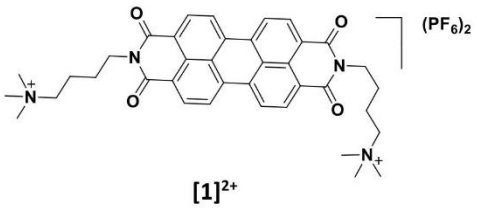

$[1]^{2+}$

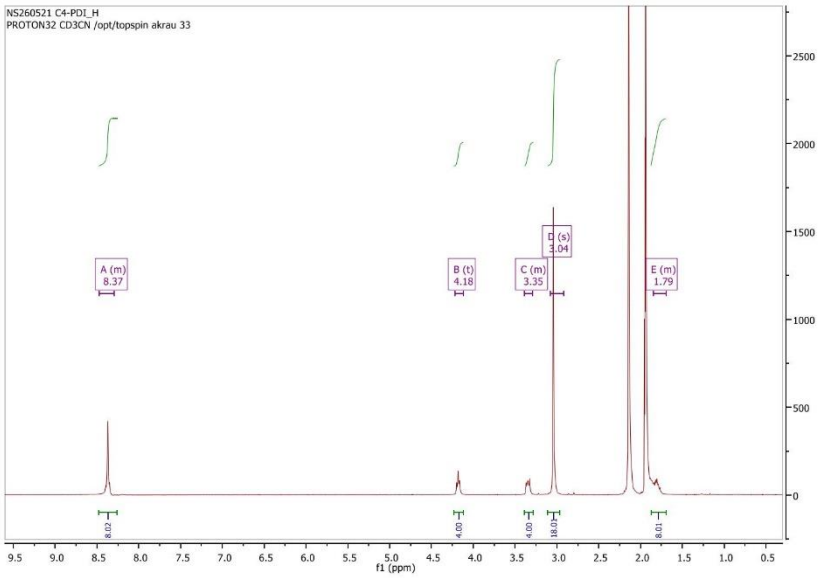

Figure S1.3: ^{1}H NMR spectrum of **[1]$^{2+}$**.

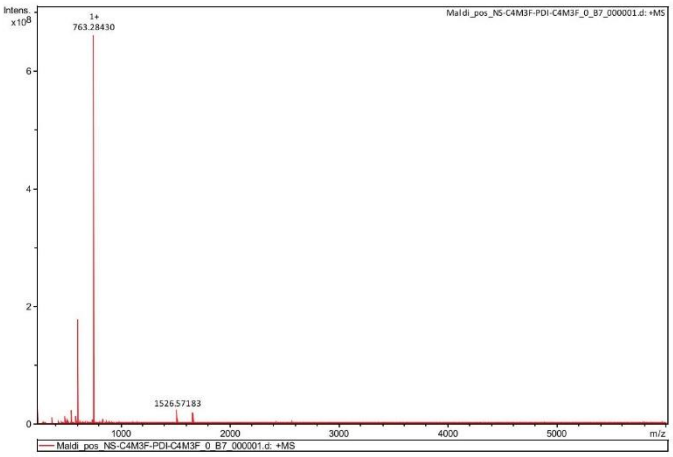

Figure S1.4: mass spectrum of **[1]$^{2+}$**.

Anal. calcd. for $C_{38}H_{42}F_{12}N_4O_4P_2 \cdot 0.1\ NH_4PF_6$: C, 49.34; H, 4.62; N, 6.21; found C, 49.53; H, 4.81; N, 6.07.

S2. Photooxidation of $[1]^{2+}$ and temporally resolved UV-vis spectra in DOPG

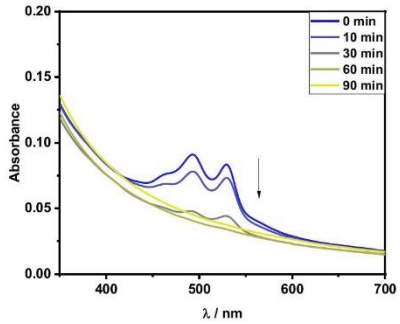

Figure S2.1. Photooxidation of $[1]^{2+}$ and temporally resolved UV-vis spectra in DOPG:(14:0 PEG2000 PE):$[1]^{2+}$ = 100:1:1 liposomes in phosphate buffer (10 mM, pH 7.0) without size exclusion.

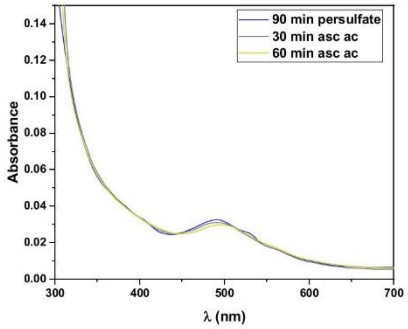

Figure S2.2. UV-vis spectra of Addition of photooxidized $[1]^{2+}$ upon addition of 100 mM of ascorbic acid. Experimental conditions: DOPG:(14:0 PEG2000 PE):$[1]^{2+}$ = 100:1:1 liposomes in phosphate buffer (10 mM, pH 7.0) without size exclusion with 50 mM of sodium persulfate after irradiation of 90 min and afterward additional 100 mM of ascorbic acid.

S3. Stern-Volmer quenching experiment

Solutions were prepared as described in main pages.

In cuvette:

V = 3 mL

[1]$^{2+}$ = 1 uM

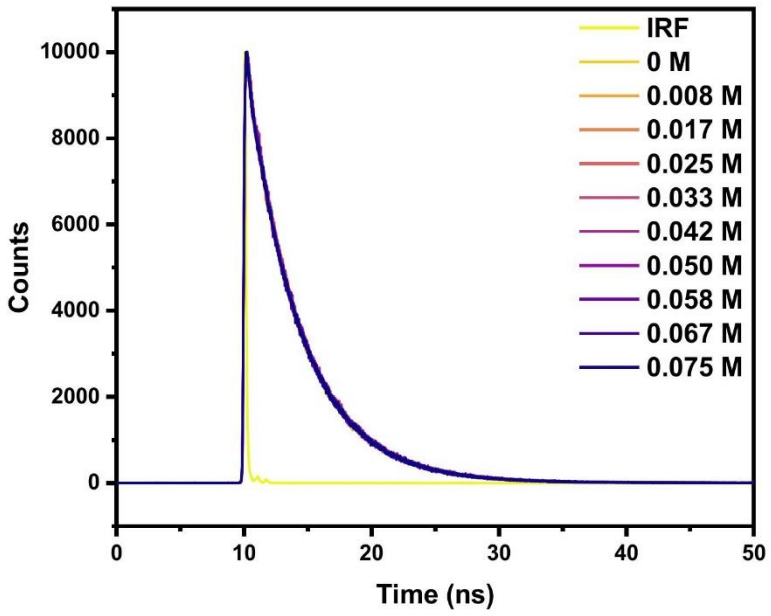

Figure S3.1. Kinetic traces of luminescence decay upon excitation at 450 nm in acetonitrile/water 1:1 (V/V) and 1 μM **[1]**$^{2+}$ and various concentrations of $Na_2S_2O_8$ as quencher.

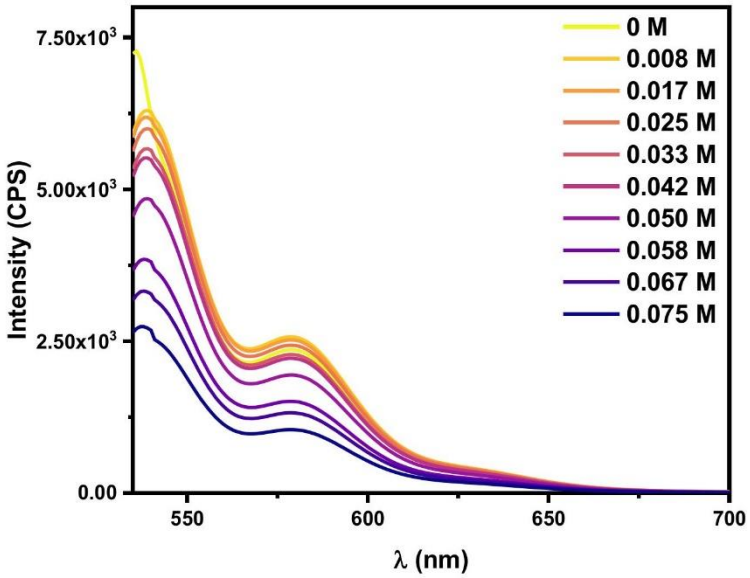

Figure S3.2. Luminescence quenching upon addition various concentrations of $Na_2S_2O_8$ in acetonitrile/water 1:1 (V/V) and 1 μM **[1]**$^{2+}$.

Liposomes were prepared as described in methods section.

In cuvette:

V = 3 mL

[1]$^{2+}$= 1.67 μM

[DOPG] = 167 μM

[14:0 PEG2000 PE] = 0.17 μM

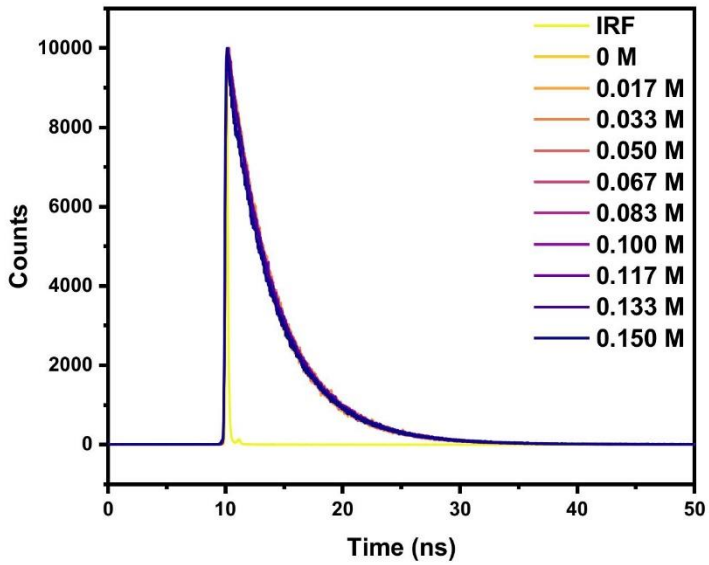

Figure S3.3. Kinetic traces of luminescence decay upon excitation at 450 nm at pH 7.0 of DOPG liposomes without size exclusion chromatography with 1% (14:0 PEG2000 PE), 1% **[1]**$^{2+}$ and various concentrations of $Na_2S_2O_8$ as quencher.

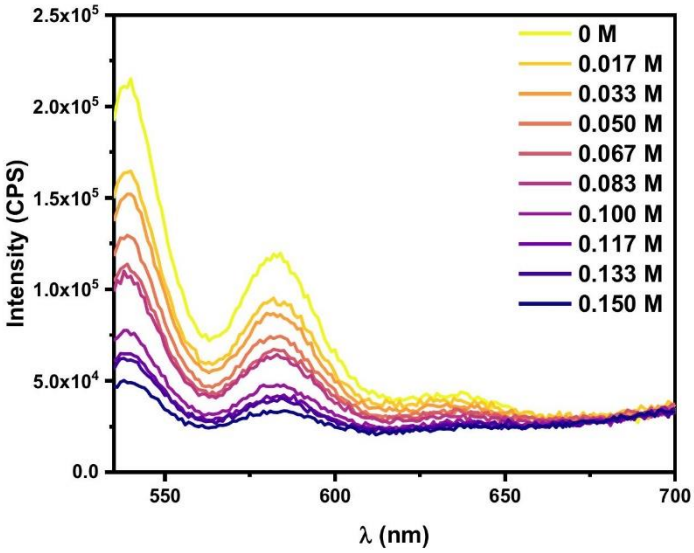

Figure S3.4. Luminescence quenching upon addition various concentrations of $Na_2S_2O_8$ in DOPG liposomes without size exclusion chromatography with 1% (14:0 PEG2000 PE), 1% **[1]**$^{2+}$.

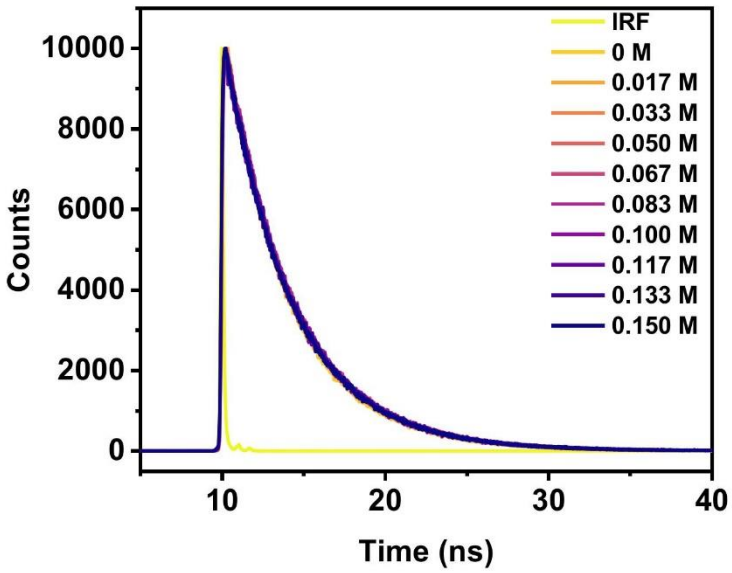

Figure S3.5. Kinetic traces of luminescence decay upon excitation at 450 nm at pH 7.0 of DOPG liposomes with size exclusion chromatography with 1% (14:0 PEG2000 PE), 1% **[1]**$^{2+}$ and various concentrations of $Na_2S_2O_8$ as quencher.

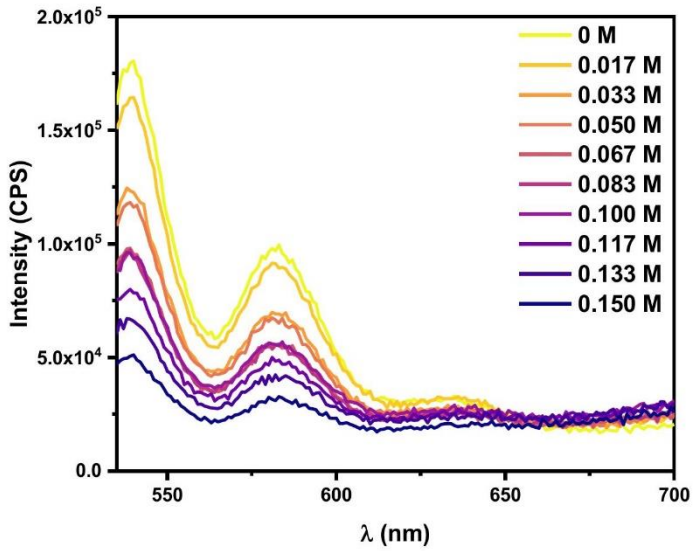

Figure S3.6. Luminescence quenching upon addition various concentrations of $Na_2S_2O_8$ in DOPG liposomes with size exclusion chromatography with 1% (14:0 PEG2000 PE), 1% **[1]**$^{2+}$.

S4. Typical hydrodynamic diameter of DOPG liposome containing $[1]^{2+}$

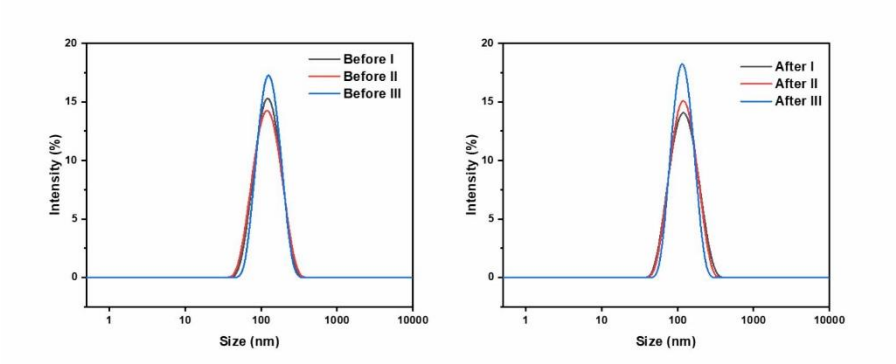

Figure S4.1. DLS measurements of DOPG liposomes with size exclusion chromatography with 1% (14:0 PEG2000 PE), 1% **$[1]^{2+}$,** before (left) and after (right) photooxidation reaction.

Table S1. DLS data: average size and polydispersity index, before and after photooxidation reaction.

Parameters	Before	After
	Mean	Mean
Z-average (nm)	117	111
Polydispersity index	0.11	0.07

S5. Coordinates of $[1]^{2+}$

88

N-substituted perylene diimide

C	-2.87525	0.33453	-2.20917
C	-1.47598	0.33312	-2.22232
C	-0.73452	-0.46864	-1.34924
C	-1.43165	-1.31061	-0.42502
C	-2.86098	-1.30408	-0.41931
C	-3.57197	-0.46982	-1.31791
C	0.73451	-0.46862	-1.34924
C	-0.73462	-2.15708	0.49533
C	0.73464	-2.15708	0.49532
C	1.43166	-1.31061	-0.42504
C	1.47747	-2.95501	1.37056

C	-1.47744	-2.95499	1.37060
C	-2.87715	-2.94018	1.37093
C	-3.57316	-2.12443	0.49022
H	-3.43712	-3.56719	2.06556
H	-3.43370	0.96855	-2.89845
C	1.47596	0.33316	-2.22231
C	2.87523	0.33458	-2.20917
C	3.57196	-0.46978	-1.31792
C	2.86099	-1.30406	-0.41934
H	3.43368	0.96862	-2.89844
C	2.87718	-2.94020	1.37088
H	3.43716	-3.56722	2.06548
C	3.57318	-2.12442	0.49017
H	-0.97164	0.98102	-2.93676
H	0.97162	0.98107	-2.93673
H	0.97373	-3.60899	2.08003
H	-0.97368	-3.60896	2.08008
C	-5.04956	-0.43312	-1.30725
C	-5.05192	-2.11493	0.51782
N	-5.69935	-1.25468	-0.38311
O	-5.69000	0.31268	-2.03849
O	-5.70382	-2.80106	1.28843
C	5.04955	-0.43307	-1.30728
C	5.05195	-2.11492	0.51775
N	5.69936	-1.25465	-0.38317
O	5.68999	0.31274	-2.03851
O	5.70385	-2.80107	1.28834
C	7.17126	-1.23607	-0.34782
H	7.49511	-2.26562	-0.15655
H	7.50873	-0.93520	-1.34588
C	7.77571	-0.31772	0.71914

H	8.86068	-0.50404	0.70476
H	7.42635	-0.63122	1.71627
C	7.54817	1.19116	0.51366
H	8.35409	1.74123	1.02110
H	7.62013	1.41482	-0.55943
C	6.20222	1.63437	1.07170
H	6.18316	1.52365	2.16409
H	5.38163	1.03334	0.67076
C	4.40618	3.26992	1.28716
C	6.71981	4.02413	1.51548
C	5.84735	3.37232	-0.68138
N	5.81032	3.07731	0.79141
C	-7.17125	-1.23611	-0.34775
H	-7.49509	-2.26566	-0.15645
H	-7.50873	-0.93526	-1.34581
C	-7.77569	-0.31774	0.71921
H	-8.86066	-0.50407	0.70485
H	-7.42630	-0.63121	1.71633
C	-7.54817	1.19114	0.51368
H	-8.35408	1.74122	1.02113
H	-7.62017	1.41477	-0.55941
C	-6.20221	1.63439	1.07167
H	-6.18312	1.52370	2.16406
H	-5.38162	1.03336	0.67072
C	-6.71983	4.02415	1.51539
C	-4.40620	3.26999	1.28702
C	-5.84743	3.37229	-0.68148
N	-5.81034	3.07733	0.79132
H	3.73695	2.62275	0.70905
H	4.12458	4.31999	1.15234
H	4.36511	3.00154	2.34872

H	7.74546	3.88133	1.16150
H	6.65893	3.82105	2.59060
H	6.39493	5.04953	1.30641
H	6.88824	3.40953	-1.01599
H	5.37154	4.34450	-0.85021
H	5.31473	2.57963	-1.21833
H	-6.39497	5.04955	1.30629
H	-6.65892	3.82110	2.59052
H	-7.74549	3.88133	1.16144
H	-4.36509	3.00163	2.34859
H	-4.12463	4.32006	1.15217
H	-3.73697	2.62281	0.70891
H	-5.31481	2.57960	-1.21841
H	-5.37164	4.34448	-0.85035
H	-6.88832	3.40948	-1.01606

References

[1] B. Limburg, E. Bouwman, S. Bonnet, *Chem. Commun* **2015**, *51*, 17128.

Chapter 4

Photoinduced Electron Transfer Across Phospholipid Bilayers in Anaerobic and Aerobic Atmospheres

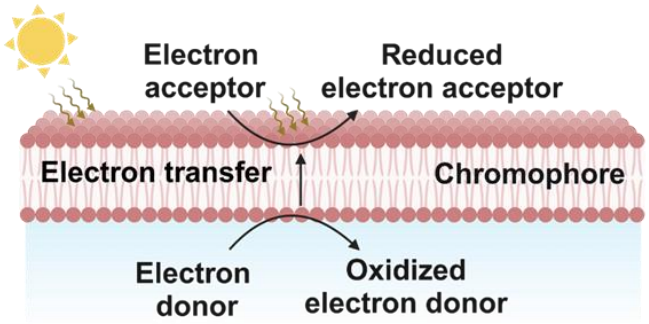

Nature performs most reactions under compartmentalized, aqueous conditions in cells and cellular compartments. Specifically, in natural photosynthesis, chromophores are precisely aligned within the membrane to trigger photoinduced electron transfer reactions. This study will demonstrate how liposomes can easily organize molecular components in space through their self-assembly and compartmentalization ability. We designed and synthesized an amphiphilic organic chromophore substituted with positively charged that can be integrated into phospholipid bilayers. Integration of this chromophore in the phospholipid bilayer enables electron transfer across the lipid bilayers, where a photooxidation reaction of NADH (nicotinamide adenine dinucleotide hydrogen) and photoreduction of XTT (4-methoxy-5-[3-(2-methoxy-4-nitro-5-sulfonatophenyl)-5-(phenylcarbamoyl)tetrazol-3-ium-2-yl]-2-nitrobenzenesulfonate) takes place at the same time by compartmentalization in the liposome. Compartmentalized, light-driven redox reactions and transmembrane electron transfer are proven with dynamic light scattering, absorption and fluorescence spectroscopy, and confocal microscopy.

Author contributions:
Novitasari Sinambela: Performed the chemical synthesis and liposome assemblies, steady-state and time-resolved spectroscopy characterization, confocal imaging measurement, spectroelectrochemistry measurements with data analysis, transmembrane electron transfer experiments, paper writing, and manuscript revision.
Richard Jacobi + Leticia González: Design of the computational protocols, and analysis of all calculations, paper writing, and manuscript revision.
Dieter Sorsche: Structure determination with single crystal X-ray diffraction.
Andrea Pannwitz: Paper writing and manuscript revision.

This chapter was published as a full paper: Novitasari Sinambela, Richard Jacobi, Dieter Sorsche, Leticia González,* and Andrea Pannwitz,* Photoinduced Electron Transfer Across Phospholipid Bilayers in Anaerobic and Aerobic Atmospheres, Angew. Chem. Int. Ed. 2025, e202423393. DOI: 10.1002/anie.202423393. This article is licensed under CC BY 4.0 (https://creativecommons.org/licenses/by/4.0).

GDCh Research Article Angewandte International Edition Chemie www.angewandte.org

How to cite: *Angew. Chem. Int. Ed.* **2025**, e202423393
doi.org/10.1002/anie.202423393

Artificial Photosynthesis

Photoinduced Electron Transfer Across Phospholipid Bilayers in Anaerobic and Aerobic Atmospheres

Novitasari Sinambela[+], Richard Jacobi[+], Dieter Sorsche, Leticia González, and Andrea Pannwitz**

Abstract: In natural photosynthesis, light-driven electron transfer across the thylakoid membrane enables efficient charge separation and the confinement of reaction spaces for generating NADPH and CO_2 and oxidation of water. These reactions are complementary redox reactions and require different reaction conditions for optimal performance. However, current artificial photosynthesis studies only take place in the bulk and are sensitive toward oxygen and air, which limits their applicability under aerated and water-splitting conditions. Herein, we report light-driven electron transfer across a lipid bilayer membrane of liposome vesicles via a rigid oligoaromatic molecular wire that allows to electronically connect an oxidation and reduction reaction which are spatially separated by the membrane. The molecular wire has a simple, symmetric, easy-to-synthesize design based on benzothiadiazole and fluorene units and absorbs in the visible spectrum which makes it suitable for solar energy conversion. The model reactions in this study are light-driven NADH oxidation on one side of the membrane and light-driven reduction of an organic water-soluble dye in the bulk phase of liposomes. Additionally, the system is active in both aerobic and anaerobic atmospheres, rendering it ideal for aerobic conditions or reactions that produce oxygen such as solar-driven water splitting and artificial photosynthesis applications.

Introduction

The most relevant process of light-energy conversion in nature is photosynthesis, which takes place within the thylakoid membrane of cyanobacteria and chloroplasts. The thylakoid membrane is a lipid bilayer that assembles multiple protein supercomplexes in a transmembrane fashion to absorb light and transfer electrons across the membrane to generate high-energy products such as NADPH (nicotinamide adenine dinucleotide phosphate hydrogen) and carbohydrates as well as oxygen as a side product.[1] The benefit of transmembrane electron transfer is that the oxidation site is physically separated from the reduction site and that such compartmentalization can fine-tune local reaction conditions to prevent detrimental recombination.[2,3] Additionally, the transmembrane charge transfer generates a proton gradient which fuels the ATP synthase (ATP = adenosine triphosphate, see Figure 1a).[4,5]

Current artificial photosynthetic systems mostly investigate either an individual catalytic light-driven reduction (e.g., H_2 evolution,[6] CO_2 reduction[7]) or an individual oxidation reaction (e.g., water oxidation),[8,9] both of which are still relying on the use of sacrificial reagents. A useful oxidation and reduction reaction combination is challenging due to their typically different reaction conditions and reported examples also rely on sacrificial reagents.[10] For instance, reduction reactions such as H_2 evolution perform best under acidic conditions due to a favorable thermodynamic redox potential

[*] N. Sinambela[+], D. Sorsche, A. Pannwitz
Institute of Inorganic Chemistry I, Ulm University, Albert-Einstein-Allee 11, 89081 Ulm, Germany
E-mail: andrea.pannwitz@uni-jena.de

R. Jacobi[+], L. González
Institute of Theoretical Chemistry, Faculty of Chemistry, University of Vienna, Währinger Straße 17, 1090 Vienna, Austria
E-mail: leticia.gonzalez@univie.ac.at

R. Jacobi[+]
Doctoral School in Chemistry (DoSChem), University of Vienna, Währinger Straße 42, 1090 Vienna, Austria

L. González
Vienna Research Platform on Accelerating Photoreaction Discovery, University of Vienna, Währinger Straße 17, 1090 Vienna, Austria

A. Pannwitz
Institute for Inorganic and Analytical Chemistry (IAAC), Chemisch-Geowissenschaftliche Fakultät, Friedrich Schiller University Jena, Humboldtstraße 8, 07743 Jena, Germany

A. Pannwitz
Center for Energy and Environmental Chemistry Jena (CEEC), Friedrich Schiller University Jena, Philosophenweg 7a, 07743 Jena, Germany

A. Pannwitz
Helmholtz Institute for Polymers in Energy Applications Jena (HIPOLE Jena), Lessingstraße 12–14, 07743 Jena, Germany

[+] Both authors contributed equally to this work.

Additional supporting information can be found online in the Supporting Information section

© 2025 The Author(s). Angewandte Chemie International Edition published by Wiley-VCH GmbH. This is an open access article under the terms of the Creative Commons Attribution License, which permits use, distribution and reproduction in any medium, provided the original work is properly cited.

© 2025 The Author(s). Angewandte Chemie International Edition published by Wiley-VCH GmbH

GDCh Research Article Angewandte International Edition Chemie

15213773, 0, Downloaded from https://onlinelibrary.wiley.com/doi/10.1002/anie.202423393 by KIZ der Universitat Ulm, Wiley Online Library on [22/05/2025]. See the Terms and Conditions (https://onlinelibrary.wiley.com/terms-and-conditions) on Wiley Online Library for rules of use; OA articles are governed by the applicable Creative Commons License

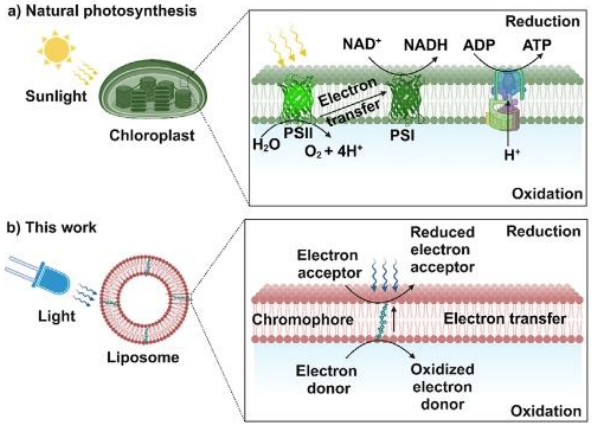

Figure 1. Light-driven transmembrane in electron transfer. a) In natural photosynthesis, the light is absorbed by multiple protein supercomplexes to convert solar energy and produce NADPH and ATP (PSI = photosystem I, PSII = photosystem II). b) This work integrates a light-active molecule for photoinduced transmembrane electron transfer in a liposome membrane to connect two spatially separated oxidation and reduction reactions. Created in https://BioRender.com.

connected to proton uptake. In contrast, oxidation reactions such as water oxidation are thermodynamically optimal at basic pH as they typically involve proton release. Therefore, it is desirable to perform the reduction and oxidation reaction in different compartments while connecting the compartments electronically.

The system we report here uses a very simple, symmetric oligoaromatic molecular wire $\mathbf{[1]^{2+}}$ that spans across the lipid bilayer membrane of artificial vesicles and effectively transfers electrons across the membrane under both inert and aerated conditions (Figures 1b and 2a). The aim is to give proof of multielectron transfer that resembles the complexity of multielectron transformation like water splitting and CO_2 reduction. The design principle of $\mathbf{[1]^{2+}}$ matches the one for membrane-spanning molecules, having a central hydrophobic region and two terminal hydrophilic groups.[15,16] The distance between the terminal hydrophilic trimethylammonium groups is 3 nm and matches the thickness of the membrane to avoid destabilization of the membrane. Interaction with visible light is ensured via the benzothiadiazole at its center. Hydrophobicity is maintained by adding fluorene to its core. The symmetric design of $\mathbf{[1]^{2+}}$ ensures a very easy chemical synthesis and a very defined membrane insertion. The rigid oligoaromatic design of the transmembrane molecular wire $\mathbf{[1]^{2+}}$ has the potential for light-driven electron transfer in a more rigid polymer-based material, which will be relevant for the technological scale-up process. As electron transfer does not rely on diffusion within the membrane, it will be possible to transfer electrons in an environment like a polymer-based membrane.

Pioneering work on light-driven transmembrane electron transport across vesicle bilayers was previously reported with a photosensitizer within the membrane combined with molecular electron shuttles resulting in diffusion-based transmembrane electron transfer. A prominent example of the pioneering work is shown in Figure 2b.[17–19] There are more diffusion-based systems, which are reported for inert conditions.[2,11,20–26] Diffusion-independent light-driven electron transfer has been reported for photoelectrochemical studies with *planar* lipid bilayers using the type of photosensitizer shown in Figure 2b.[27,28] A few elegant, but synthetically demanding rigid transmembrane molecular wires and supramolecular barrel were reported for light-driven transmembrane electron transfer, shown in Figure 2c,d.[12,13] As opposed to our molecular wire $\mathbf{[1]^{2+}}$ the reported asymmetric systems can insert from both sides with no preference. Apart from vesicle lipid bilayer membranes, the transmembrane design is also interesting for photoelectrochemical electron transfer and catalysis at electrode surfaces covered with an inorganic SiO_2 membrane coating (Figure 2e).[14] The function of these transmembrane electron transfer systems was to protect and connect the photo- and electrochemical components.[29,30]

Results and Discussion

Synthesis and Characterization

The oligoaromatic light active molecule $\mathbf{[1]^{2+}}$ was synthesized starting from benzothiadiazole, which was functionalized via bromination and successive two-fold Suzuki-cross-coupling with dimethyl fluorene boronic acid, yielding the unpolar core **fbf** (4,7-bis[9,9-dimethylfluoren2-yl]-2,1,3-benzothiadiazole). Subsequent bromination, Suzuki-cross-coupling with a boronic acid of *N*,*N*-dimethyl aniline, followed by methylation of the nitrogen groups and ion exchange yielded the final product as PF_6-salt as a yellow solid in overall five steps and an overall yield of 18% (Figure 3a). The crystal structure can be found in the CCDC database with the identifier 2376492. The detailed synthesis and characterization can be found in the Supporting Information (Section S1).

For liposome preparation, DPPC (dipalmitoylphosphatidylcholin) as the main lipid, $\mathbf{[1]^{2+}}$ and the PEGylated lipid 14:0 PEG2000 PE were combined in the desired molar ratio of 100:1:1. DPPC liposomes were chosen because they are not permeable for larger water-soluble molecules at room temperature, which is the operating temperature during the experiments.[17,31,32] In addition to DPPC, 1 mol% of 14:0 PEG2000 PE was added to the lipid mixture to increase stability and to prevent aggregation of the liposome via steric repulsion by the PEG chains on the liposome surface.[22,33,34] Membrane integration of $\mathbf{[1]^{2+}}$ into DPPC lipid bilayer was achieved via lipid film hydration, as described in detail in Section S2. Lipid film hydration yielded giant vesicles. When lipid film hydration was followed by extrusion, it yielded unilamellar vesicles with a typical diameter of 110 for empty liposomes and 140 nm average with encapsulated NADH according to dynamic light scattering (DLS). The size of the liposomes remained the same before and after irradiation for both cases, implying that the liposomes could retain their structure under irradiation (Section S3).

To characterize the photophysical properties and membrane integration of $\mathbf{[1]^{2+}}$, UV–vis absorption and emission spectra were recorded, and emission lifetime measurements

© 2025 The Author(s). Angewandte Chemie International Edition published by Wiley-VCH GmbH

GDCh Research Article Angewandte International Edition Chemie

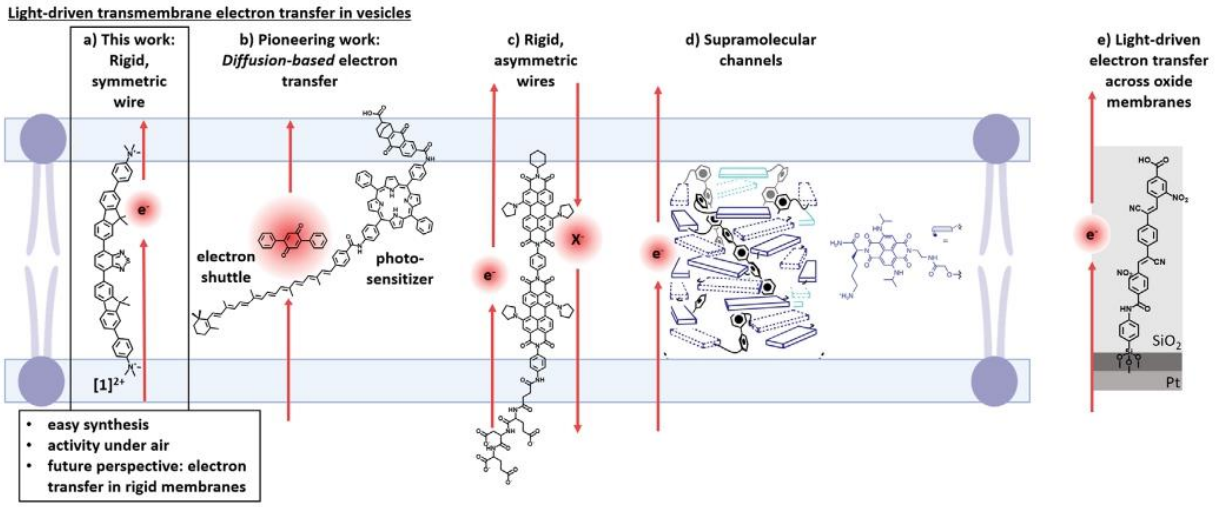

Figure 2. Reported systems for artificial photosynthesis: a) This work with molecular wire ($[\mathbf{1}]^{2+}$) to transfer electrons across the membrane, b) diffusion-based light-driven electron transfer via electron shuttle with triad harvesting complex,[11] c) passive anion transport with indirect proof of the electron transfer via pH change,[12] d) light-driven electron transfer through complex supramolecular barrel like assembly, (reproduced from Ref. [13] under license number 5 911 880 595 918 from The American Association for the Advancement of Science),[13] and e) molecular wire embedded in a 2-nm-thick SiO_2 membrane enables electron flow from microbial catalysts to the inorganic anode.[14]

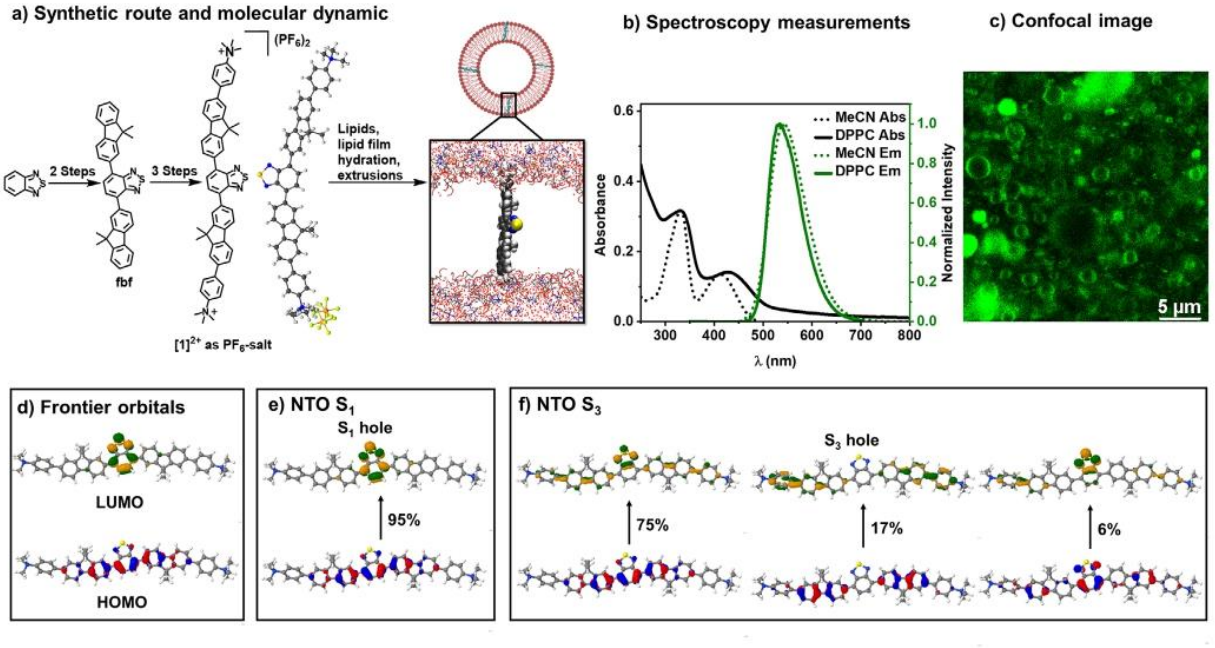

Figure 3. Characterization of the molecular wire $[\mathbf{1}]^{2+}$. a) Synthetic route of $[\mathbf{1}]^{2+}$ as PF_6-salt, solid-state structure of $[\mathbf{1}](\mathbf{PF_6})_2$ (cocrystallized solvent molecule acetonitrile omitted for clarity), and a snapshot of the molecular dynamic simulation of $[\mathbf{1}]^{2+}$ in the DPPC membrane, showing how $[\mathbf{1}]^{2+}$ orients within the membrane. Color code: red = oxygen, white = hydrogen, blue = nitrogen, yellow = sulfur, golden = phosphorus, and grey = carbon. The alkyl tails of the lipid bilayer are omitted for clarity. b) UV–vis absorption (Abs, in black) + emission (Em, in green) spectra of $[\mathbf{1}]^{2+}$ with a ratio of DPPC:$[\mathbf{1}]^{2+}$:(14:0 PEG2000 PE) = 100:1:1; in phosphate buffer 10 mM pH 7.0 (solid line) and MeCN (acetonitrile, dot line). c) Confocal microscopy image of giant vesicles with DPPC:$[\mathbf{1}]^{2+}$:(14:0 PEG2000 PE) = 100:1:1; in phosphate buffer 10 mM, pH 7.0 after size exclusion chromatography, upon fixation in agarose hydrogel. d) Visualization of the frontier orbitals HOMO and LUMO. e), f) Natural transition orbitals (NTOs) for the S_1 and S_3 excitations.

© 2025 The Author(s). Angewandte Chemie International Edition published by Wiley-VCH GmbH

15213773, 0, Downloaded from https://onlinelibrary.wiley.com/doi/10.1002/anie.202423393 by KIZ der Universitat Ulm, Wiley Online Library on [22/05/2025]. See the Terms and Conditions (https://onlinelibrary.wiley.com/terms-and-conditions) on Wiley Online Library for rules of use; OA articles are governed by the applicable Creative Commons License

15213773, 0, Downloaded from https://onlinelibrary.wiley.com/doi/10.1002/anie.202423393 by KIZ der Universitat Ulm, Wiley Online Library on [22/05/2025]. See the Terms and Conditions (https://onlinelibrary.wiley.com/terms-and-conditions) on Wiley Online Library for rules of use; OA articles are governed by the applicable Creative Commons License

Table 1: Spectroscopic data of $[\mathbf{1}]^{2+}$.

Solvent or lipid	λ_{Abs} (nm)	λ_{em} (nm)	τ (ns) Ar	τ (ns) air
Acetonitrile	330, 410	540	5.6 ± 0.04	5.4 ± 0.04
DPPC[a)]	330, 430	535	5.2 ± 0.1	5.2 ± 0.1

[a)] DPPC:$[\mathbf{1}]^{2+}$:(14:0 PEG2000 PE) = 100:1:1 in phosphate buffer (10 mM, pH 7.0).

were performed (see Figure 3b and Table 1). It was observed that $[\mathbf{1}]^{2+}$ has two absorption bands in polar organic solvent (acetonitrile) at 330 and 410 nm, respectively, and one emission band at 540 nm, which decays with a lifetime of $\tau = 5.4 \pm 0.5$ ns, indicating a spin-allowed fluorescence from a singlet excited state. In DPPC liposomes, the high-energy absorption band has the same shift as in the organic solvent. By contrast, the lower-energy band in the visible region shifts slightly bathochromically to 430 nm (Figure 3d), indicating a stabilization of the respective LUMO (lowest unoccupied molecular orbital) or destabilization of the respective HOMO (highest occupied molecular orbital), in the nonpolar membrane environment, in line with similar dyes in unpolar solvents.[35] The weak tail in the red region of the liposome absorption spectrum is due to light scattering and the Tyndall effect.[36,37] In the emission spectra, a small hypsochromic shift toward higher energy of the emission band by 5 to 535 nm was observed, suggesting that the lowest excited state of $[\mathbf{1}]^{2+}$ resides within the hydrophobic membrane core. The emission lifetime within the membrane remained similar with $\tau = 5.2 \pm 0.2$ ns; which is a low environmental influence and was also observed for other singlet emitters in solvents versus membrane (Supporting Information Section S4).[34]

Upon incorporation into the DPPC liposomes, which are less polar compared to acetonitrile,[38] the absorption band at lower energies at around 410 nm undergoes a bathochromic shift to 430 nm, while the higher energy band remains at 330 nm as in acetonitrile. To rationalize why one of the bands shifts to lower energies while the other is barely affected, we resort to time-dependent density functional theory calculations. We used the CAM-B3LYP[39] functional and def2-SVP[40,41] basis set, as implemented in Gaussian 16,[42] whereby the amount of HF exchange is reduced to reproduce the experimental absorption energies.[43] Further details are presented in the Supporting Information Section S5. The calculations evidence that the two absorption bands should be assigned to the S_1 and S_3 singlet electronic excitations, respectively, while the transition to the S_2 is dark. The hole and electron of the excitation to the S_1 closely resemble the shape of the HOMO and LUMO (Figure 3d). During the excitation to the S_1 (Figure 3e), the electron density is transferred from the fluorene units to the benzothiadiazole unit. By contrast, in the S_3 (Figure 3f), both the hole and the excited state electron are similarly delocalized over large parts of the molecule, making the S_3 comparable in electronic properties to the ground state. Further discussion of the electronic structures in the ground and excited states can be found in the Supporting Information Section S6.

How these excited states are influenced by the environment requires elucidating the alignment of $[\mathbf{1}]^{2+}$ within DPPC liposomes to judge which part of the molecule is exposed to which electrostatic environment. As the DPPC liposome is too small for confocal microscopy, we prepared giant vesicles functionalized with $[\mathbf{1}]^{2+}$, shown in Figure 3c. The fact that the membrane is selectively stained confirms that $[\mathbf{1}]^{2+}$ preferably binds to the membrane. Additionally, the luminescence reveals a double-half moon-shaped vesicle membrane, indicating that $[\mathbf{1}]^{2+}$ adopts a preferred orientation within the membrane.[15,16,34] Furthermore, we also measure the integration of the hydrophobic chromophore core (**fbf**) in the DPPC membrane with confocal microscopy, which does not show a half-moon shape, presumably due to a random orientation of **fbf** within the lipophilic part of the membrane. Further exploration of the alignment of $[\mathbf{1}]^{2+}$ in the membrane can be found in the Supporting Information Section S7. The transmembrane alignment of $[\mathbf{1}]^{2+}$ is ensured by its geometry matching with the geometry of the membrane. $[\mathbf{1}]^{2+}$ has a hydrophobic core and two charged, hydrophilic $N(CH_3)_3$-groups at a distance of 2.99 nm from one another based on crystal structure; in the structure optimized with DFT calculation the distance is 3.1 nm, and in the MD-simulations, the distance varies between 2.8 and 3.1 nm. As the membrane thickness is typically between 3 and 5 nm, the molecule can span across lipid bilayer as the thickness of the membrane, which is also demonstrated by MD-simulations, see a snapshot in Figure 3a and other trajectories in the Supporting Information Section S7.[44] The nature of this preferred orientation is unraveled with molecular dynamics (MD) simulations (see computational setup in Section S8). In those, the photoactive molecule $[\mathbf{1}]^{2+}$ is placed randomly within a simulation box together with 128 DPPC molecules solvated in water. During the simulation, the lipid bilayer self-assembles, usually within 1–3 μs, and due to its hydrophobicity, $[\mathbf{1}]^{2+}$ assembles in the newly formed membrane. The orientation of $[\mathbf{1}]^{2+}$ with respect to the membrane could occur in different ways, such as in a transmembrane fashion, or parallel to the surface of the membrane as we previously found for a different chromophore in a lipid bilayer.[34] However, in our simulations $[\mathbf{1}]^{2+}$ aligns transmembrane, as shown in the representative MD snapshot in Figure 2a (and others in Section S8). We therefore conclude that the transmembrane configuration is the preferred alignment of $[\mathbf{1}]^{2+}$ and thus responsible for the experimental signature. In detail, the ends of the molecular rod, i.e., the two trimethylammonium groups, are embedded in the opposite head group layers, which are zwitterionic and thus can be regarded as polar. The parts closer to the center of the molecule are embedded between the hydrophobic tails. As a result, the central rings of $[\mathbf{1}]^{2+}$ are most exposed to the change in polarity between the polar acetonitrile and the unpolar membrane. Incidentally, this is exactly the region where both the excitations to S_1 and S_3 are located. As outlined above, the S_1 exhibits a different electronic structure compared to the S_0, and because the polar solvent will adjust to the ground state, it will stabilize the S_0 more than an excited state of different electronic structure. When this stabilization is removed upon incorporation into the liposomes, the S_0 will be more destabilized than the S_1, resulting in the excitation redshift evidenced in the absorption

© 2025 The Author(s). Angewandte Chemie International Edition published by Wiley-VCH GmbH

15213773, 0, Downloaded from https://onlinelibrary.wiley.com/doi/10.1002/anie.202423393 by KIZ der Universitat Ulm, Wiley Online Library on [22/05/2025]. See the Terms and Conditions (https://onlinelibrary.wiley.com/terms-and-conditions) on Wiley Online Library for rules of use; OA articles are governed by the applicable Creative Commons License

spectra. The S_3, by contrast, is similar to the S_0 in electronic structure and will thus be similarly stabilized, explaining why it is much less affected by the environmental change and thus the excitation is not shifted noticeably.

Transmembrane Electron Transfer

As a model reaction, we investigated the light-driven oxidation of NADH within the inner aqueous compartment of the liposome vesicles and the light-driven reduction of XTT (2,3-bis(2-methoxy-4-nitro-5-sulfophenyl)-2*H*-tetrazolium-5-carboxanilide sodium salt) in the outer aqueous bulk compartment. XTT is a well-known chemical reagent in a biological assay to prove the presence of cellular reducing equivalents such as NADH, forming a strongly colored formazan dye upon reduction.[45] XTT and NADH were chosen because their conversion can easily be monitored by UV–vis absorption spectroscopy,[45,46] as opposed to weakly absorbing Co or Fe species,[47,48] which would be difficult to quantify given the Tyndall scattering of the liposomes and the absorption of $\mathbf{[1]}^{2+}$ itself. NADH and XTT and their oxidized and reduced products are water-soluble and are anticipated to stay within their respective aqueous compartment in the inside or outside of the vesicel respectively, as opposed to, e.g., methyl viologen which comproportionates and diffuses across the membrane.[49]

To enable transmembrane electron transfer across a lipid bilayer, we prepared DPPC liposomes that are impermeable to larger water-soluble molecules[17,31,32] and integrated 1 mol% of the amphiphilic transmembrane chromophore $\mathbf{[1]}^{2+}$, as described above. The water-soluble electron donor NADH was added to the inner compartment of the liposome, while the water-soluble electron acceptor XTT was placed in the bulk or on the outer part of the liposome, forming so-called NADH/$\mathbf{[1]}^{2+}$/XTT liposomes (Figure 5a). Upon light irradiation, the absorption band at $\lambda_{max} = 470$ nm gradually increased, corresponding to the electron uptake of XTT to generate its reduced form formazan (Fz),[45] indicating that photoinduced electron transfer had occurred (Figure 5b). Simultaneously, the NADH absorption band at 340 nm is diminished, indicating oxidation of the electron donor. However, the quantification based on the decrease of NADH absorption is not used, as the onefold oxidized NADH tends to form a dimer which also absorbs at 340 nm.[50,51] Leakage through the membrane was excluded through various reference experiments (Section S9), leading to the conclusion that, indeed, transmembrane electron transfer takes place. Based on the analysis of the thermodynamic properties, the excited state of $\mathbf{[1]}^{2+}$ is reduced by NADH with a driving force of −0.37 eV and a driving force of −0.69 eV to oxidize by XTT. These values show that it is easier to oxidize $\mathbf{[1]}^{2+}$ than to reduce it (Figure 4, the details can be found in the Supporting Information Section S10).

It was furthermore confirmed that the original NADH/$\mathbf{[1]}^{2+}$/XTT liposomes perform light-driven transmembrane electron transfer under inert conditions with a rate constant of $k_{Ar} = (1.76 \pm 0.09)\ 10^{-12} s^{-1}$ for Fz formation during the first 10 min of irradiation, and a quantum yield of $Qy = 0.045\%$. The rate constant of Fz was determined by fitting the first 10 min of data with a linear function, and the Qy was determined by the number of Fz formed divided by the number of absorbed photons as described in Section S11. Interestingly, we found that the presence of oxygen only reduced the reaction rate and Qy by around factor 2 and the by a factor of 0.45 to $Qy = 0.020\%$, as reported in Table 2. This observation is very promising, as oxygen normally inhibits electron transfer reactions when performed with a diffusion-based electron shuttle.[2,22,26,52] It seems that the transmembrane molecular wire approach provides robustness, potentially enabling the investigation of transmembrane water-splitting reactions in the future as well as reactions under aerobic conditions. Performing light-driven electron transfer under noncompartmentalized conditions, with electron donor and acceptor in the outer bulk ($\mathbf{[1]}^{2+}$/NADH, XTT in Figure 5c and Table 2 entry 2), significantly reduced the overall electron transfer efficiency, especially under aerated conditions. This suggests that the transmembrane electron transfer is indeed more efficient than a liposome-bulk system, and that compartmentalization might play a large role in accelerating the desired reactions, thereby minimizing the detrimental effect of oxygen. There are several reasons for such an improvement under compartmentalization conditions: (i) It enables stepwise reactions at different compartments, (ii) it allows for high local concentration of NADH in the inner part of the liposome, allowing for effective oxidation, and (iii) it prevents recombination.[46]

Reference measurements for the stability of $\mathbf{[1]}^{2+}$ during 2 h of irradiation, oxidation of encapsulated NADH, bulk oxidation of NADH, bulk reduction of XTT with and without $\mathbf{[1]}^{2+}$, and bulk oxidation and reduction of XTT and NADH, as well as measurements of NADH/$\mathbf{[1]}^{2+}$/XTT and the opposite combination XTT/$\mathbf{[1]}^{2+}$/NADH, the core of dye **fbf** with a combination of NADH/**fbf**/XTT and NADH/$\mathbf{[1]}^{2+}$/XTT under aerobic and anaerobic atmosphere at an elevated temperature close to the transition temperature and experiments with different loading of $\mathbf{[1]}^{2+}$ can be found in Section S11. The reverse combination, XTT/$\mathbf{[1]}^{2+}$/NADH, showed that the photoinduced transmembrane electron transfer across the membrane can also occur in the reverse configuration. The respective data are shown in Supporting Information Figures S33 and S39, showing comparable Fz formation compared to the normal system (2.53 nmol (XTT/$\mathbf{[1]}^{2+}$/NADH) vs. 2.68 nmol (NADH/$\mathbf{[1]}^{2+}$/XTT)), which highlights the adaptability of the system. An inherent limitation of our transmembrane electron transfer design is that a transmembrane potential can build up, which ultimately stops the transmembrane electron transfer. To balance the buildup of charges across the membrane, we tested two transmembrane ion transporters, gramicidin A and 18-crown-6 ether (also see Table 2, entries 3,4). Gramicidin A is an ion-channel-forming peptide, selective for small ions, such as protons.[53] Under ambient aerated conditions, the initial quantum yield of gramicidin A was reduced and performed better in an inert atmosphere compared to the same system without gramicidin A. It was observed that gramicidin A played a role as an ion balancer, leading to an increase in initial quantum yield and an improvement in reaction rate. Gramicidin A

© 2025 The Author(s). Angewandte Chemie International Edition published by Wiley-VCH GmbH

15213773, 0, Downloaded from https://onlinelibrary.wiley.com/doi/10.1002/anie.202423393 by KIZ der Universitat Ulm, Wiley Online Library on [22/05/2025]. See the Terms and Conditions (https://onlinelibrary.wiley.com/terms-and-conditions) on Wiley Online Library for rules of use; OA articles are governed by the applicable Creative Commons License

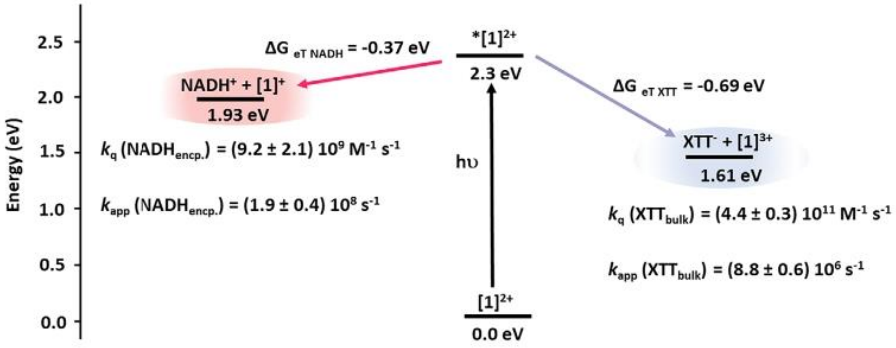

Figure 4. Energy profile of the redox reactions between photoexcited $[\mathbf{1}]^{2+}$ and NADH or XTT, respectively, including the quenching constants k_q from the Stern–Volmer quenching studies. The apparent quenching konstants k_{app} quantify the quenching at the experimental conditions for transmembrane electron transfer, namely at 0.021 M encapsulated NADH and at 2×10^{-5} M XTT in the bulk, respectively.

Table 2: Different systems of light-driven electron transfer in inert and ambient air; reaction rates of Fz formation at initial $t = 10$ min and initial quantum yield ($Q\gamma$).

Entry	Conditions	k_{air} Fz air (10^{-12} s^{-1})	k_{Ar} Fz Ar (10^{-12} s^{-1})	$Q\gamma$ air (%)	$Q\gamma$ Ar (%)
1	NADH/$[\mathbf{1}]^{2+}$/XTT	1.18 ± 0.01	1.76 ± 0.09	0.020	0.044
2	$[\mathbf{1}]^{2+}$/NADH, XTT	0.13 ± 0.01	0.50 ± 0.02	0.001	0.012
3	NADH/$[\mathbf{1}]^{2+}$, 1% gramicidin A/XTT	1.50 ± 0.02	1.95 ± 0.04	0.030	0.053
4	NADH/$[\mathbf{1}]^{2+}$, 4.2% 18-crown-6/XTT	0.60 ± 0.01	0.63 ± 0.02	0.011	0.014

accelerated the electron transfer rate constant by 11% under Ar and 27% under air. The quantum yield in the first 10 min is increased by 20% under Ar and by 50% under air. Another transmembrane ion transfer reagent 18-crown-6 ether was incorporated into the membrane. This transporter is selective only to K^+ cations.[54] Adding 18-crown-6 to the phosphate buffer in the experiment enables the transport of K^+ cations to compensate for the charge imbalance in both compartments. It was observed that the addition of 18-crown-6 did not result in a better rate or quantum yield of transmembrane transfer compared to the addition of gramicidin A.

Upon photoexcitation of $[\mathbf{1}]^{2+}$, the photoredox reactions take place from the excited state of $[\mathbf{1}]^{2+}$.

To explore the photoinduced electron transfer in DPPC liposomes, the prepared samples of integrated $[\mathbf{1}]^{2+}$ in DPPC, $[\mathbf{1}]^{2+}$ in DPPC with encapsulated NADH (NADH/$[\mathbf{1}]^{2+}$), and $[\mathbf{1}]^{2+}$ in DPPC with XTT placed at the bulk ($[\mathbf{1}]^{2+}$/XTT), and the combination of encapsulated NADH and XTT in bulk (NADH/$[\mathbf{1}]^{2+}$/XTT) respectively, were excited at 420 nm with ~10 ns laser pulses (all the temporal spectra in different timescales and temporal kinetics can be found in the Supporting Information Section S12). According to the transient absorption (TA) spectra, both the reduction and the oxidation of $[\mathbf{1}]^{2+}$ are happening: The spectral features of reduced $[\mathbf{1}]^{2+}$ can be found in the transient absorption spectrum of NADH/$[\mathbf{1}]^{2+}$ as well as in the spectroelectrochemical UV–vis spectrum of reduced $[\mathbf{1}]^{2+}$ as a broad absorption band between 500 and 700 nm (see Figure 5g). Under oxidative conditions and upon photoirradiation, the formazan photoproduct Fz accumulates and obstructs the transient absorption measurements as it creates a bleach at the Fz absorption wavelength at 500 nm. The same artifact was also observed in the sample composition of NADH/$[\mathbf{1}]^{2+}$/XTT, making it challenging to evaluate the photoexcited species in this composition (see Supporting Information Figure S40).

To elucidate the electron transfer dynamics of $[\mathbf{1}]^{2+}$, we conducted time-resolved and steady-state emission spectroscopy. In an emission quenching assay, known as the Stern–Volmer plot,[55] it was observed that the photoexcited state of $[\mathbf{1}]^{2+}$ was quenched at varying concentrations of NADH and XTT (Table 3, spectra and kinetic traces can be found in Section S13). NADH, acting as a reductive quencher, showed a Stern–Volmer constant with different values for quenching of the emission spectrum's intensity and lifetime, with $K_{SV}(I_0/I) = 47.8 \pm 11$ M^{-1} and K_{SV} $(\tau_0/\tau) = -2.2 \pm 0.8$ M^{-1}, respectively. As the lifetime-based K_{SV} (τ_0/τ) is close to zero, a static quenching process is active, indicating the association of cationic membrane-bound photosensitizer and anionic NADH through electrostatic attraction at the ground state (Figure 5d). The same behavior was also observed in the bulk experiment with NADH as a quencher with $K_{SV}(I_0/I) = 7.3 \pm 1.0$ $M^{-1}$and K_{SV} $(\tau_0/\tau) = 0.6 \pm 0.4$ M^{-1}, the lifetime based on K_{SV} (τ_0/τ) is close to zero (the Stern–Volmer plot this experiment can be found in Supporting Information Section S13). On the other hand, XTT, acting as an oxidative quencher, showed a mixture of dynamic and static quenching processes, with the intensity-based and lifetime-based Stern–Volmer constants being positive, with $K_{SV}(I_0/I) = (2.2 \pm 0.2)$ 10^3 $M^{-1}$and K_{SV} $(\tau_0/\tau) = (3.0 \pm 1.1)$ 10^2 M^{-1}, respectively. These constants indicate excited state electron transfer upon the diffusional encounter

© 2025 The Author(s). Angewandte Chemie International Edition published by Wiley-VCH GmbH

15213773, 0, Downloaded from https://onlinelibrary.wiley.com/doi/10.1002/anie.202423393 by KIZ der Universitat Ulm, Wiley Online Library on [22/05/2025]. See the Terms and Conditions (https://onlinelibrary.wiley.com/terms-and-conditions) on Wiley Online Library for rules of use; OA articles are governed by the applicable Creative Commons License

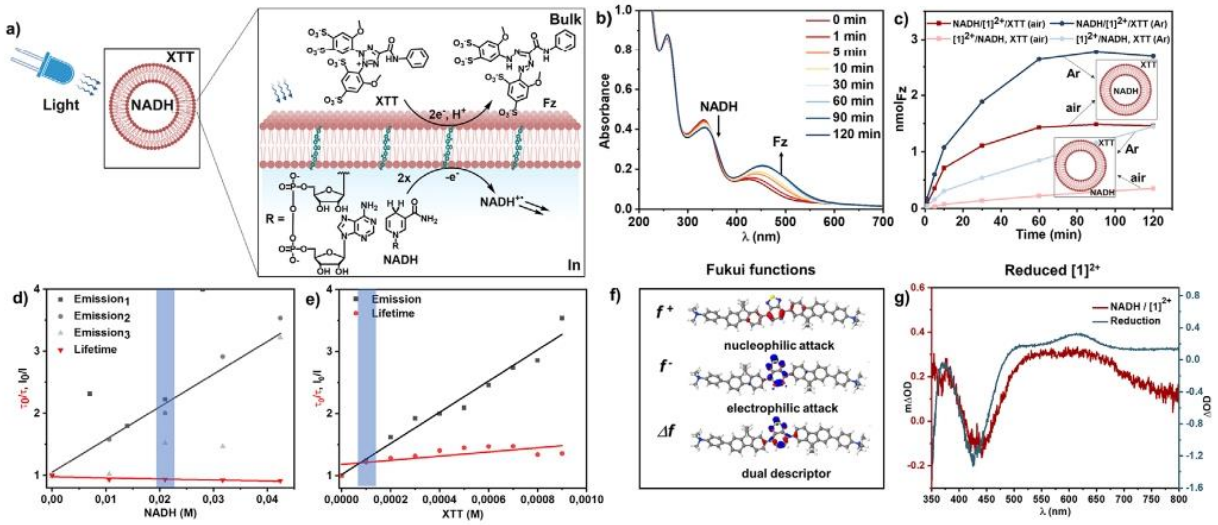

Figure 5. Transmembrane electron transfer. a) Schematic illustration of electron transfer across lipid bilayer with encapsulation of NADH, integration of **[1]**$^{2+}$ and XTT at the bulk solution of the liposome (anaerobic atmosphere). b) Evolution of the UV–vis absorption spectrum of DPPC:(14:0 PEG2000 PE):**[1]**$^{2+}$ = 100:1:1 with a composition of NADH/**[1]**$^{2+}$/XTT upon irradiation with 470 nm LED light. c) Number of Fz formation under irradiation with 470 nm LED light over time for NADH/**[1]**$^{2+}$/XTT (bold lines) and **[1]**$^{2+}$/NADH, XTT (lighter lines) under inert and ambient atmospheres. d) Stern–Volmer quenching experiments of DPPC:(14:0 PEG2000 PE):**[1]**$^{2+}$ = 100:1:1 liposomes in phosphate buffer (10 mM, pH 7.0) with different concentrations of encapsulated NADH inside the liposome. e) Stern–Volmer quenching experiments of DPPC:(14:0 PEG2000 PE):**[1]**$^{2+}$ = 100:1:1 liposomes in phosphate buffer (10 mM, pH 7.0) with XTT as the quencher at the bulk solution of liposome. f) Fukui functions of **[1]**$^{2+}$ in the S_1. g) Transient absorption (TA) spectra of reduce **[1]**$^{2+}$ in DPPC liposome (red line) and spectroelectrochemistry (blue line).

Table 3: Stern–Volmer quenching constants of **[1]**$^{2+}$ in DPPC membrane with NADH and XTT as quenchers.

Quencher	K_{SV} from I_0/I (M^{-1})	K_{SV} from τ_0/τ (M^{-1})	k_q from I_0/I ($M^{-1}s^{-1}$)	k_q from τ_0/τ ($M^{-1}s^{-1}$)	Quenching Mechanism
$NADH_{encp.}$	47.8 ± 11	-2.2 ± 0.8	$(9.2 \pm 2.1)\ 10^9$	$(-4.2 \pm 1.6)\ 10^8$	Static
$NADH_{bulk}$	7.3 ± 1.0	0.6 ± 0.4	$(1.4 \pm 0.2)\ 10^9$	$(1.1 \pm 8.0)\ 10^8$	Static
XTT_{bulk}	$(2.2 \pm 0.2)\ 10^3$	$(3.0 \pm 1.1)\ 10^2$	$(4.4 \pm 0.3)\ 10^{11}$	$(5.8 \pm 2.1)\ 10^{10}$	Dynamic/static

between the liposome-bound **[1]**$^{2+}$ and XTT and also through the association of the anionic XTT with membrane-bound photosensitizer at the ground state (Figure 5e).[7,33,34] The quenching constants k_q were calculated from the Stern–Volmer constants K_{SV} via the relationship $K_{SV} = k_q \cdot \tau_0$.[55] The intensity-based values yield very hiqh quenching constants on the order of 10^9–10^{11} M^{-1} s^{-1}, probably due to the ground-state association. Interestingly, the quenching constant k_q by XTT in the bulk is more efficient than by encapsulated NADH, in line with the 0.32 eV higher driving force for oxidative versus reductive quenching (Figure 4). However, under the experimental conditions of transmembrane electron transfer with 0.021 M encapsulated NADH and 2×10^{-5} M XTT in the bulk, the apparent quenching constant k_{app} is much lower for quenching by XTT compared to quenching by encapsulated NADH k_{app} ($NADH_{encp.}$) = $(1.9 \pm 0.4)\ 10^8$ s^{-1} and k_{app} (XTT_{bulk}) = $(8.8 \pm 0.6)\ 10^6$ s^{-1}.

To elucidate further on what causes these different quenching constants and which molecule parts of **[1]**$^{2+}$ are involved in the charge transfer, we computed Fukui functions in the S_1 excited state (Section S5). The Fukui descriptor is a spatially resolved measure of the interaction between a molecule and either a nucleophile or an electrophile. It thus describes the change in the electronic wave function upon oxidation or reduction. Upon photoexcitation of **[1]**$^{2+}$, the photo redox reactions take place from the excited state of **[1]**$^{2+}$. The Fukui function for a nucleophilic attack is defined as the difference between the electron density of the molecule in the initial state with N electrons and the electron density after reduction with an additional electron: $f^+ = \rho_{N+1} - \rho_N$. Analogously, the Fukui function for an electrophilic attack is the difference in density before and after oxidation: $f^- = \rho_N - \rho_{N-1}$. The Fukui functions for **[1]**$^{2+}$ are shown in Figure 5f. In blue, f^- shows the areas where **[1]**$^{2+}$ would donate an electron, and thus be oxidized (by XTT), while f^+ shows those where it would accept an electron to be reduced (by NADH). According to these Fukui functions, **[1]**$^{2+}$ would be oxidized in the central moiety with the electron mostly stemming from the sulfur atom, and it would be reduced mostly into the six-membered ring of the central moiety. To weigh the oxidative and reductive properties of **[1]**$^{2+}$, we also compute the so-called dual descriptor, which is the difference between the Fukui functions of an oxidation and a reduction: $\Delta f = f^+ - f^-$, also shown in Figure 5f. It prominently exhibits the character

© 2025 The Author(s). Angewandte Chemie International Edition published by Wiley-VCH GmbH

15213773, 0, Downloaded from https://onlinelibrary.wiley.com/doi/10.1002/anie.202423393 by KIZ der Universitat Ulm, Wiley Online Library on [22/05/2025]. See the Terms and Conditions (https://onlinelibrary.wiley.com/terms-and-conditions) on Wiley Online Library for rules of use; OA articles are governed by the applicable Creative Commons License

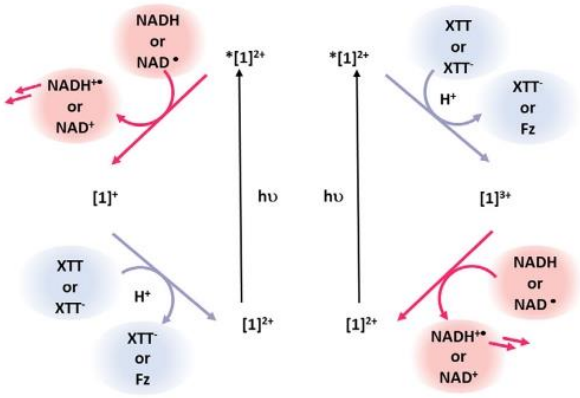

Figure 6. Proposed mechanism of electron transfer under inert conditions. Potential comproportionation of $[\mathbf{1}]^{3+}$ with $[\mathbf{1}]^{+}$ to $[\mathbf{1}]^{2+}$ is omitted for clarity.

of f^{-}, which means that the electron donating properties of the central moiety overweigh the electron accepting character. In other words, it is easier to oxidize $\mathbf{[1]}^{2+}$ than to reduce it which is in line with the experimentally determined redox potentials (E_{ox} = 1.0 V vs. Fc/Fc^{+} and E_{red} = −1.7 V vs. Fc/Fc^{+} in acetonitrile, see Table S2 and Figure S20). It is also in line with the Stern–Volmer constants being so much larger for quenching by XTT compared to quenchning by NADH, which is also in line with the respective driving force for (see Figure 4).

We propose the following overall mechanism, also schematized in Figure 6: Upon photoexcitation to generate $*\mathbf{[1]}^{2+}$ excited state charge transfer takes place with NADH as well with XTT in individual subsets of $*\mathbf{[1]}^{2+}$, generating the oxidized and reduced $\mathbf{[1]}^{2+}$ within the membrane. Although the excited state electron transfer to XTT might be dominant, we cannot rule out excited sate electron transfer from NADH, as both processes are very fast based on the Stern–Volmer data and the transient absorption spectrum shown in Figure 5. The oxidized and reduced versions of $\mathbf{[1]}^{2+}$ might then comproportionate yielding two equivalents of $\mathbf{[1]}^{2+}$, or react further with the substrates in the aqueous phases. $\mathbf{[1]}^{3+}$ can oxidize a second equivalent of NADH, and $\mathbf{[1]}^{+}$ can reduce the photogenerated XTT^{-} a second time. The generated $NADH^{+\cdot}$ is known to quickly loose its proton and dimerize.[50,51] Unreacted $NAD^{\cdot}$ can undergo a second electron donation to either $\mathbf{[1]}^{3+}$ or $*\mathbf{[1]}^{2+}$. In the presence of oxygen, photo-oxidation or photoreduction may be mediated by photogenerated singlet oxygen (Supporting Information, Figure S55).[45,56]

Conclusions and Outlook

In summary, we report a very simple and novel design of a photoactive molecular wire for transmembrane electron transfer using visible light under inert and aerated conditions. We demonstrate, with confocal spectroscopy and molecular dynamic simulations, that $\mathbf{[1]}^{2+}$ integrates with transmembrane orientation in the lipid bilayer. Light-driven electron transfer dynamics across the membrane were verified with two model redox reactions, and the excited state, photoreduced, and photooxidized products were characterized, along with the static and dynamic/static character of the initial photoinduced electron transfer. Overall, the liposomal system allowed us to electronically connect two complementary redox reactions through visible light-driven electron transfer. This process is crucial for solar energy conversion and the development of more advanced systems with robust and sturdy membranes. Additionally, it is important for the design of artificial cells and cellular compartments. Although the challenge of resupplying the inner aqueous compartment with substrate still needs to be solved, the here presented findings on nanoreactors and transmembrane electron transfer are valuable for designing chemical synthetic methodologies involving compartmentalization. To create a larger photoreactor, the same approach can be applied to polymer-based vesicles or larger planar membranes. The biorelated nature of the lipid bilayer membrane also offers opportunities for incorporating enzymatic catalysis, as the lipid membrane's complex units can be organized to carry out specific functions.

Methods

The General Procedure of Liposome Preparation

To a 5 mL round bottom flask was added 1 mL of DPPC (5 mM in $CHCl_3$), 1 mL of 14:0 PEG2000 PE (0.05 mM in $CHCl_3$), and 1 mL of $\mathbf{[1]}^{2+}(PF_6)_2$ (0.05 mM in acetonitrile). The organic solvents were evaporated under vacuum leading to deposition of lipids on the flask wall. The film was dried under high vacuum for at least 1 h and hydrated with phosphate buffer pH of 7.0 and added 15 mg of NADH. The dispersed lipid film was repeatedly freeze-thawing, using liquid N_2 and a water bath at 52 °C, forming the giant vesicles. To obtain liposomes of uniform size, the dispersion was extruded at 52 °C through 200 nm cellulose membrane filters 11 times with an Avanti Polar Lipids mini-extruder. The liposome mixture was subjected to a Sephadex G-25 size exclusion chromatography (SEC) column (6 cm length, 2 cm diameter) using phosphate buffer pH 7.0 as eluent; the liposome loaded with NADH was collected as the first band.

The General Procedure of Photoirradiation

The typical reactions were carried out within quartz cuvettes where 300 µL of liposome solution, 10 µL of 1 mM XTT, and 190 µL phosphate buffer pH 7.0 were added. The mixtures were illuminated within a custom-made reactor equipped with four ventilators to exclude heating of the samples and an LED-stick (Nichia Corporation; NSPB500AS) (λ = 470 ± 10 nm, 15.7 mW measured with a Hioki 3664 optical power meter set to 470 nm).[57] The samples were monitored via UV–vis spectroscopy after 0, 1, 5, 10, 30, 60, 90, and 120 min.

© 2025 The Author(s). Angewandte Chemie International Edition published by Wiley-VCH GmbH

15213773, 0, Downloaded from https://onlinelibrary.wiley.com/doi/10.1002/anie.202423393 by KIZ der Universitat Ulm, Wiley Online Library on [22/05/2025]. See the Terms and Conditions (https://onlinelibrary.wiley.com/terms-and-conditions) on Wiley Online Library for rules of use; OA articles are governed by the applicable Creative Commons License

Acknowledgements

The authors thank the Deutsche Forschungsgemeinschaft (DFG, project TRR234 "CataLight" project number 364549901, projects B8 and C3) and the Austrian Science Fund (FWF project No. I6116). A.P. gratefully acknowledges the Vector Stiftung (project number P2019-0110) and the Carl-Zeiss-Stiftung for financial support. The confocal images were recorded at the Core Facility for Confocal and Multiphoton Microscopy at Ulm University which is supported by the DFG through project number 91BGG INST 381/39-1. The authors thank Dr. Sviatlana Kalinina and Dr. Christian Bökel for their support during confocal microscopy. Some figures were prepared using a license from https://BioRender.com/. The Vienna Scientific Cluster (VSC) is acknowledged for the generous allocation of computational resources.

Open access funding enabled and organized by Projekt DEAL.

Conflict of Interests

The authors declare no conflict of interest.

Data Availability Statement

The data that support the findings of this study are available in the Supporting Information of this article.

Keywords: Artificial photosynthesis · Compartmentalization · Electron transfer · Lipid bilayer

[1] N. Nelson, A. Ben-Shem, *Nat. Rev. Mol. Cell Biol.* **2004**, *5*, 971–982.
[2] G. Steinberg-Yfrach, P. A. Liddell, S.-C. Hung, A. L. Moore, D. Gust, T. A. Moore, *Nature* **1997**, *385*, 239–241.
[3] H. Hu, Z. Wang, L. Cao, L. Zeng, C. Zhang, W. Lin, C. Wang, *Nat. Chem.* **2021**, *13*, 358–366.
[4] J. B. Arc, *Plant, Cell and Environment* **1983**, *6*, 311–322.
[5] A. Trebst, *Annu. Rev. Plant Physiol.* **1974**, *25*, 423–458.
[6] S. Troppmann, B. König, *Chem. A Eur. J.* **2014**, *20*, 14570–14574.
[7] S. Rodríguez-Jiménez, H. Song, E. Lam, D. Wright, A. Pannwitz, S. A. Bonke, J. J. Baumberg, S. Bonnet, L. Hammarström, E. Reisner, *J. Am. Chem. Soc.* **2022**, *144*, 9399–9412.
[8] M. Hansen, F. Li, L. Sun, B. König, *Chem. Sci.* **2014**, *5*, 2683–2687.
[9] H. Song, A. Amati, A. Pannwitz, S. Bonnet, L. Hammarström, *J. Am. Chem. Soc.* **2022**, *144*, 19353–19364.
[10] C. Zhu, Z. Gao, W. Yu, S. Xia, W. Chen, G. Song, Y. Huang, F. Lv, H. Bai, S. Wang, *Small* **2024**, *20*, 2306440.
[11] B. C. Patterson, D. H. Thompson, J. K. Hurst, *J. Am. Chem. Soc.* **1988**, *110*, 3656–3657.
[12] A. Perez-Velasco, V. Gorteau, S. Matile, *Angew. Chem. Int. Ed.* **2008**, *47*, 921–923.
[13] S. Bhosale, A. L. Sisson, P. Talukdar, A. Fürstanberg, N. Banetji, E. Vauthey, G. Bollot, J. Mareda, C. Röger, F. Würthner, N. Sakai, S. Matile, *Science* **2006**, *313*, 84–86.
[14] J. A. Cornejo, H. Sheng, E. Edri, M. Ajo-Franklin, C. H. Frei, *Nat. Commun.* **2018**, *9*, 2263.
[15] A. Pannwitz, H. Saaring, N. Beztsinna, X. Li, M. A. Siegler, S. Bonnet, *Chem. Eur. J.* **2021**, *27*, 3013–3018.
[16] L. E. Garner, J. Park, S. M. Dyar, A. Chworos, J. J. Sumner, G. C. Bazan, *J. Am. Chem. Soc.* **2010**, *132*, 10042–10052.
[17] K. Watanabe, K. Moriya, T. Kouyama, A. Onoda, T. Minatani, S. Y. Takizawa, S. Murata, *J. Photochem. Photobiol. A: Chem.* **2011**, *221*, 113–122.
[18] J. N. Robinson, D. J. Cole-Hamilton, *Chem. Soc. Rev.* **1991**, *20*, 49.
[19] D. Gust, T. A. Moore, A. L. Moore, *Acc. Chem. Res. 34*, 40–48.
[20] M. S. Tunuli, J. H. Fendler, *J. Am. Chem. Soc.* **1981**, *103*, 2507–2513.
[21] P. P. Infelta, M. Graetzel, J. H. Fendler, *J. Am. Chem. Soc.* **1980**, *102*, 1479–1483.
[22] B. Limburg, E. Bouwman, S. Bonnet, *Chem. Commun.* **2015**, *51*, 17128–17131.
[23] C. Laane, W. E. Ford, J. W. Otvos, M. Calvin, *Proc. Natl. Acad. Sci. USA* **1981**, *78*, 2017–2020.
[24] W. E. Ford, J. W. Otvos, M. Calvin, *Proc. Natl. Acad. Sci. USA* **1979**, *76*, 3590–3593.
[25] K. C. Hwang, D. Mauzerall, Photoinduced Electron Transport across a Lipid Bilayer Mediated by C7o **1993**, 361.
[26] G. Steinberg-Yfrach, J.-L. Rigaud, E. N. Durantini, A. L. Moore, D. Gust, T. A. Moore, *Nature* **1998**, *392*, 479–482.
[27] P. Seta, E. Bienvenue, A. L. Moore, T. A. Moore, D. Gust, *Electrochim. Acta* **1989**, *34*, 1723–1727.
[28] P. Seta, E. Bienvenue, A. L. Moore, P. Mathis, R. V. Bensasson, P. Liddell, P. J. Pessiki, A. Joy, T. A. Moore, D. Gust, *Nature* **1985**, *316*, 653–655.
[29] H. Frei, *Photosynth. Res.* **2024**, *162*, 473–495.
[30] W. Kim, B. A. McClure, E. Edri, H. Frei, *Chem. Soc. Rev.* **2016**, *45*, 3221–3243.
[31] E. Wu, K. Jacobson, D. Papahadjopoulos, *Biochemistry* **1977**, *16*, 3936–3941.
[32] J. R. Sheats, H. M. McConnell, *Proc. Natl. Acad. Sci. USA* **1978**, *75*, 4661–4663.
[33] H. Song, A. Amati, A. Pannwitz, S. Bonnet, L. Hammarström, *J. Am. Chem. Soc.* **2022**, *144*, 19353–19364.
[34] N. Sinambela, R. Jacobi, D. Hernández-Castillo, E. Hofmeister, N. Hagmeyer, B. Dietzek, L. González, A. Pannwitz, *Mol. Syst. Des. Eng.* **2023**, *8*, 842–852.
[35] K. Susumu, J. A. N. Fisher, J. Zheng, D. N. Beratan, A. G. Yodh, M. J. Therien, *J. Phys. Chem. A.* **2011**, *115*, 5525–5539.
[36] T. A. Nguyen, Q. D. Tang, D. C. T. Doan, M. C. Dang, *Adv. Nat. Sci: Nanosci. Nanotechnol.* **2016**, *7*, 035003.
[37] K. Bruun, C. Hille, *Sci. Rep.* **2019**, *9*, 10504.
[38] G. Gramse, A. Dols-Perez, M. A. Edwards, L. Fumagalli, G. Gomila, *Biophys. J.* **2013**, *104*, 1257–1262.
[39] T. Yanai, D. P. Tew, N. C. Handy, *Chem. Phys. Lett.* **2004**, *393*, 51–57.
[40] F. Weigend, R. Ahlrichs, *Phys. Chem. Chem. Phys.* **2005**, *7*, 3297.
[41] F. Weigend, *Phys. Chem. Chem. Phys.* **2006**, *8*, 1057.
[42] M. J. Frisch, G. W. Trucks, H. B. Schlegel, G. E. Scuseria, M. A. Robb, J. R. Cheeseman, G. Scalmani, V. Barone, G. A. Petersson, H. Nakatsuji, X. Li, M. Caricato, A. V. Marenich, J. Bloino, B. G. Janesko, R. Gomperts, B. Mennucci, H. P. Hratchian, J. V. Ortiz, A. F. Izmaylov, J. L. Sonnenberg, F. DingWilliams, F. Lipparini, F. Egidi, J. Goings, B. Peng, A. Petrone, T. Henderson, D. Ranasinghe, V. G. Zakrzewski, et al., Gaussian 16, Revision C.01, Gaussian, Inc., Wallingford, CT **2016**. *Citation | Gaussian.com*, https://gaussian.com/citation/ (accessed: December 2023).
[43] K. Okuno, Y. Shigeta, R. Kishi, H. Miyasaka, M. Nakano, *J. Photochem. Photobiol. A Chem.* **2012**, *235*, 29–34.

© 2025 The Author(s). Angewandte Chemie International Edition published by Wiley-VCH GmbH

[44] D. Marsh, *Handbook of Lipid Bilayers* 0 ed., CRC Press, Boca Raton, Florida, USA **2013**, https://doi.org/10.1201/b11712.
[45] M. W. Sutherland, B. A. Learmonth, *Free Radical Res.* **1997**, *27*, 283–289.
[46] R. E. P. Nau, J. Bösking, A. Pannwitz, *ChemPhotoChem* **2022**, *6*, e202200158.
[47] S. A. Sapp, C. M. Elliott, C. Contado, S. Caramori, C. A. Bignozzi, *J. Am. Chem. Soc.* **2002**, *124*, 11215–11222.
[48] G. H. Rizvi, *J. Radioanal. Nucl. Chem.* **1988**, *125*, 333–339.
[49] L. Hammarstroem, M. Almgren, J. Lind, G. Merenyi, T. Norrby, B. Aakermark, *J. Phys. Chem.* **1993**, *97*, 10083–10091.
[50] J. Kiwi, *J. Photochem.* **1981**, *16*, 193–202.
[51] B. Czochralska, W. Kawczynski, G. Bartosz, D. Shugar, *Bioch. Biophys. Acta (BBA) – General Subjects* **1984**, *801*, 403–409.
[52] M. M. A. Kelson, R. S. Bhosale, K. Ohkubo, L. A. Jones, S. V. Bhosale, A. Gupta, S. Fukuzumi, S. V. Bhosale, *Dyes Pigm.* **2015**, *120*, 340–346.
[53] D. W. Urry, M. C. Goodall, J. D. Glickson, D. F. Mayers, *Proc. Natl. Acad. Sci. USA* **1971**, *68*, 1907–1911.
[54] R. N. Greene, *Tetrahedron Lett.* **1972**, *13*, 1793–1796.
[55] V. Balzani, P. Ceroni, A. Juris, *Photochemistry and Photophysics: Concepts, Research, Applications*, John Wiley & Sons, Weinheim, Germany **2014**.
[56] K. Hirakawa, M. Mori, *ACS Omega* **2021**, *6*, 8630–8636.
[57] S. Tschierlei, M. Karnahl, M. Presselt, B. Dietzek, J. Guthmuller, L. González, M. Schmitt, S. Rau, J. Popp, *Angew. Chem.* **2010**, *122*, 4073–4076.

Manuscript received: November 30, 2024
Revised manuscript received: February 10, 2025
Accepted manuscript online: February 22, 2025
Version of record online: ■■, ■■

© 2025 The Author(s). Angewandte Chemie International Edition published by Wiley-VCH GmbH

15213773, 0, Downloaded from https://onlinelibrary.wiley.com/doi/10.1002/anie.202423393 by KIZ der Universitat Ulm, Wiley Online Library on [22/05/2025]. See the Terms and Conditions (https://onlinelibrary.wiley.com/terms-and-conditions) on Wiley Online Library for rules of use; OA articles are governed by the applicable Creative Commons License

Supporting Information

Photoinduced Electron Transfer across Phospholipid Bilayers in Anaerobic and Aerobic Atmospheres

Authors:

Novitasari Sinambela[+,a] Richard Jacobi[+,b,c] Dieter Sorsche,[a] Leticia González*,[b,d] Andrea Pannwitz* [a,e,f,g]

[a] Institute of Inorganic Chemistry I, Ulm University, Albert-Einstein-Allee 11, 89081 Ulm, Germany

[b] Institute of Theoretical Chemistry, Faculty of Chemistry, University of Vienna, Währinger Straße 17, 1090 Vienna, Austria

[c] Doctoral School in Chemistry (DoSChem), University of Vienna, Währinger Straße 42, 1090 Vienna, Austria

[d] Vienna Research Platform on Accelerating Photoreaction Discovery, University of Vienna, Vienna, Austria, Währinger Straße 17, 1090 Vienna

[e] Institut für Anorganische und Analytische Chemie (IAAC), Chemisch-Geowissenschaftliche Fakultät, Friedrich-Schiller-Universität Jena, Humboldtstraße 8, 07743 Jena

[f] Center for Energy and Environmental Chemistry Jena (CEEC), Friedrich-Schiller-Universität Jena, Philisophenweg 7a, 07743 Jena

[g] Helmholtz Institute for Polymers in Energy Applications Jena (HIPOLE Jena), Lessingstraße 12–14, 07743 Jena, Germany

[+] These authors contributed equally

Table of Contents

S1. Experimental details..... 3
S2. Liposome preparation..... 12
S3. The typical hydrodynamic diameter of DPPC liposome containing $[1]^{2+}$..... 13
S4. Lifetime of $[1]^{2+}$ in different environments..... 14
S5. Computational details for the computation of electronic excited states and Fukui functions..... 14
S6. Characterization of the excited states..... 17
S7. Confocal microscopy..... 19
S8. Computational details on the membrane assembly simulations..... 20
S9. Calceine-luminescence leakage test..... 22
S10. Electrochemical and Spectroelectrochemical characterization..... 24
S11. Photoirradiation..... 29
S12. Nanosecond transient absorption spectra..... 36
S13. Stern-Volmer quenching experiment..... 41
S14. Proposed mechanism in the presence of oxygen, photooxidation or photoreduction..... 45
S15. Coordinates of $[1]^{2+}$..... 46
References..... 47

S1. Experimental details

All reagents were commercially available and all inert synthesis reactions were carried out using standard Schlenk-techniques and argon gas. A Bruker DRX 400 spectrometer was used to record nuclear magnetic resonance (NMR) at 298 K. Mestre Nova software was used for the evaluation of the spectra. The mass spectra of the compounds were obtained using matrix-assisted laser desorption ionization (MALDI) Bruker Reflex III mass spectrometer. Trans-2-[3-(4-tert-Butylphenyl)-2-methyl-2-pro-penylidene] malononitrile was used as a matrix. Elemental analysis was performed by Mikroanalytisches Laboratorium Kolbe in Oberhausen, Germany. The elemental content of the molecules was reported as the element's mass fraction percentage. Absorptions were recorded on a spectrometer from JASCO V760. Starna fluorescence quartz cuvettes with a path length of 1 cm and screw caps with an air-tight silicon seal were used. Luminescence was recorded on a FP-8500 Spectrofluorometer. The size distribution of the hydrodynamic diameter (Z_{Avg}) was measured at 20 °C with a Zetasizer Pro from Malvern operating at 633 nm with a scattering angle of 173°. Confocal microscopy images were acquired on a Leica TCS SP8 confocal microscope equipped with a 488 nm laser as excitation source and detected with range of 500-600 nm. Sample wells (μ-Slide 8 Well ibiTreat) were used to characterize giant vesicles. Confocal microscopy images were processed with the LasX software. DC cyclic voltammetry (CV) experiments were performed on a Pine Research Wavedriver 200 electrochemical workstation equipped with a standard three-electrode arrangement: working electrode (WE): glassy carbon electrode (d = 3.0 mm), quasi reference electrode (RE): Ag wire (in a glass frit containing electrolyte solution), counter electrode (CE): Pt wire. All potentials are quoted relative to the ferrocene/ferrocenium internal standard. All experiments were performed in dry dimethylformamide (DMF) and acetonitrile (MeCN), using nBu_4NPF_6 (0.1 M) as supporting electrolyte. The solutions were purged with argon for at least 15 minutes to remove O_2 and kept under a slight positive argon pressure while performing the experiments. Spectroelectrochemical measurements were performed using a Pine honeycomb screen-printed platinum electrode as WE and CE and an Ag wire (in a glass frit containing electrolyte solution) as pseudo-RE. Nanosecond transient absorption experiments were performed on an LP980-K spectrometer from Edinburgh Instruments equipped with an iCCD detector from Andor (DH320T-25F-03-812), a monochromator (STGM325-MA) and a photomultiplier (PMT-LP R928P). The excitation source was an Nd: YAG/YVO4 laser from Ekspla (NT342B-10-AW) equipped with a tunable OPO (410-2600 nm). The sample chamber was tempered to 20 °C using a built-in thermostat. For all spectral measurements, 20 pulses were averaged and the signal was integrated over a 100 ns timespan.

Synthesis route

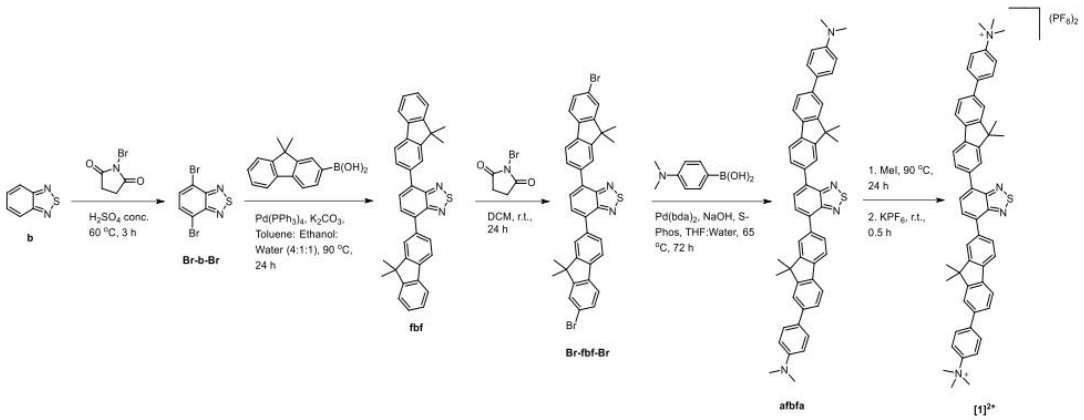

Figure. S1. Synthesis route of molecule **[1]$^{2+}$**.

4,7-Dibromo-2,1,3-benzothiadiazole (Br-b-Br)

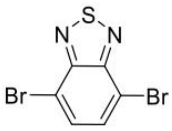

Br-b-Br

In a water bath 2,1,3-benzothiadiazole (1.0 g, 7.34 mmol, 1.00 equivalent (eq.)) and N-bromosuccinimide (3.3 g, 18.4 mmol, 2.52 eq.) were added in a round-bottom flask. Concentrated H_2SO_4 (97%, 10 mL) was added dropwise and the reaction mixture was stirred for 3 h at 60 °C. The reaction cooled to room temperature and placed in an ice bath. To the reaction mixture a 100 ml of distilled water was added dropwise. The product was extracted with 3 x 30 mL of toluene and the combined organic layers were dried with Na_2SO_4 and evaporated under reduced pressure. The reaction gave compound **Br-b-Br** as white-yellow powder (2.10 g, 7.14 mmol) in 97% yield.

^{1}H-NMR (400 MHz, $CDCl_3$): δ = 7.72 (s, 2 H) ppm.

^{13}C-NMR (200 MHz, $CDCl_3$): δ = 152.98, 132.36, 113.93 ppm.

4,7-bis[9,9-dimethylfluoren2-yl]-2,1,3-benzothiadiazole (fbf)

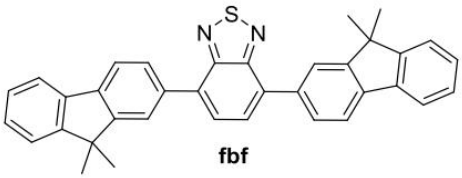

fbf

To a mixture of 4,7-dibromo-2,1,3-benzothiadiazole (0.5 g, 1.70 mmol, 1.00 eq.), 9,9-dimethyl-9H-fluoren-2-yl-2-boronic acid (0.89 g, 3.74 mmol, 2.20 eq.) and K_2CO_3 (1.88 g, 13.6 mmol, 8.00 eq.) in a pressure flask, a degassed solution mixture of 40 mL toluene, 10 mL ethanol and 10 mL water was added. A catalyst $Pd(PPh_3)_4$ (0.17 g, 0.17 mmol, 0.1 eq.) was added under counter flow of argon and the reaction mixture was stirred at 90 °C for 24 h, after the completion of the reaction yellow crystals were forming. The crystals were filtered and washed with water, ethanol, and Et_2O. The crystals were dried under vacuum. Yielding **fbf** as yellow-green powder (0.59 g, 1.13 mmol) in 66% yield.

UV-vis ($CHCl_3$): λ_{max} = 259 nm, 319 nm, and 415 nm.

Luminescence ($CHCl_3$) λ_{ex} at 415 nm: λ_{max} = 550 nm.

^{1}H-NMR (400 MHz, $CDCl_3$): δ = 8.04 - 8.01 (m, 4 H), 7.91 – 7.89 (d, 4 H), 7.82 – 7.80 (m, 2 H), 7.50 – 7.48 (m, 2 H), 7.41 – 7.34 (m, 4 H), 1.60 (s, 12 H) ppm.

^{13}C-NMR (200 MHz, $CDCl_3$): δ = 154.30, 154.11, 154.00, 139.52, 138.82, 136.47, 133.57, 128.42, 128.03, 127.53, 127.10, 123.62, 122.68, 120.30, 120.10, 47.08, 27.25 ppm.

4,7-bis[7-dibromo-9,9-dimethylfluoren-2yl]-2,1,3-benzothiadiazole (Br-fbf-Br)



Br-fbf-Br

In a pressure flask a solution of compound **fbf** (0.35 g, 0.67 mmol, 1.00 eq.) in dichloromethane was degassed with argon and N-bromosuccinimide (0.27 g, 1.55 mmol, 2.26 eq.) was added. The mixture was stirred for 24 h at room temperature. After 24 hours, 10 mL of 6 M HCl was added and the mixture was stirred for an additional 2 hours, resulting in the formation of a yellow solid precipitate. The mixture was passed through a filter to separate the solid from the liquid. Then, the solid was rinsed with water and diethyl ether (Et_2O). The yellow powder of **Br-fbf-Br** (0.23 g, 0.34 mmol) was obtained by drying the solid under vacuum with a 50% yield.

^{1}H-NMR (400 MHz, $CDCl_3$): δ = 8.02 – 7.99 (m, 4 H), 7.88 – 7.86 (m, 4H), 7.67 – 7.65 (m, 2 H), 7.61(d, *J* = 1.7 Hz, 2 H), 7.53 (dd, *J* = 1.8 Hz, 2 H), 1.65 (s, 12 H) ppm.

4,7-bis[7-p-N,N-dimethyl-aniline-9,9-dimethylfluoren-2-yl]-2,1,3-benzothiadiazole (afbfa)

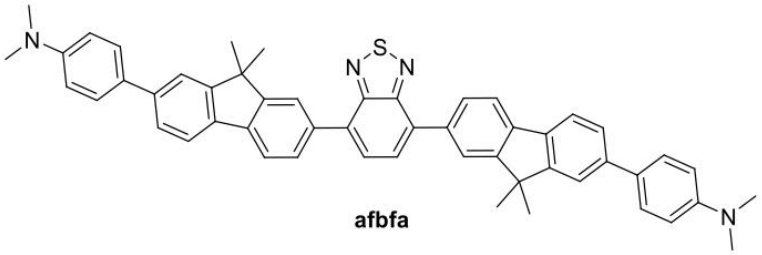

afbfa

Br-fbf-Br (0.3 g, 0.44 mmol, 1.00 eq.), N, N-dimethylaniline boronic acid (0.17 g, 1.02 mmol, 2.31 eq.), NaOH (0.74 g, 18 mmol, 40.9 eq.), and S-Phos (dicyclohexyl(2,6-dimethoxy[1,1-biphenyl]-2-yl) phosphane) (0.04 g, 0.1 mmol, 0.22 eq.) were suspended in a deoxygenated mixture of tetrahydrofuran (130 mL) and water (5 mL). The suspension was degassed with argon for 30 minutes before addition of $Pd_2(dba)_3$ (0.042 g, 0.04 mmol, 0.1 eq.). The mixture was heated and stirred at 65 °C for 3 days. After cooling down to room temperature, some orange precipitate was formed. The precipitate was then filtered off and washed with toluene, water and Et_2O. The powder obtained was dissolved in chloroform and recrystallized with methanol. As a result, orange powder was produced and it gave **afbfa** (0.25 g, 0.33 mmol) in a yield of 74%.

^{1}H-NMR (400 MHz, $CDCl_3$): δ 8.06 – 8.01 (m, 4H), 7.90 (t, *J* = 3.9 Hz, 4H), 7.82 (d, *J* = 7.9 Hz, 2H), 7.61 (m, 8H), 6.86 (d, 2H), 3.03 (s, 12H), 1.64 (s, 12H).

4,7-tris[7-p-N, N, N-trimethyl-aniline-9,9-dimethylfluoren-2-yl]-2,1,3-benzothiadiazole dihexafluorophosphate $[1]^{2+}(PF_6)_2$

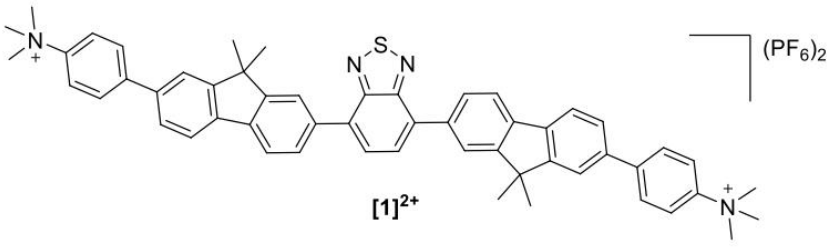

$[1]^{2+}$

In a pressure flask **afbfa** (100 mg, 0.13 mmol, 1.00 eq.) in acetonitrile (15 mL) was degassed with argon and excess methyl iodide (2 mL, 32.1 mmol, 244 eq.) was added. The mixture was heated to 90 °C for 24 h. After 24 h, the mixture turned deep yellow with some precipitate. The solution was filtered and dissolved in ethyl acetate and stirred for 30 min with 10% aqueous solution of ammonium

hexafluorophosphate. The precipitate was filtered and washed with ethyl acetate and dried under a vacuum. To purify the crude product, a silica column was used. The first eluent used was dichloromethane, to remove the first band. Later, the eluent was changed to acetonitrile: 1 M NH_4PF_6 (water) (4:1) to collect the orange band. The orange fraction was dried in rotary evaporator and recrystallized in the mixture of acetonitrile and water. The reaction gave compounds **[1]**$^{2+}(PF_6)_2$ as yellow powder (0.11 g, 0.10 mmol) in 77% yield.

UV-vis (MeCN): λ_{max} = 330 nm and 410 nm.

Luminescence (MeCN) λ_{ex} **at 410 nm:** λ_{max} = 555 nm.

^{1}H NMR (400 MHz, *d*-MeCN) δ 8.20 (d, *J* = 1.1 Hz, 2H), 8.08 (dd, *J* = 7.9, 1.6 Hz, 2H), 8.00 (m, 10H), 7.90 (d, *J* = 1.3 Hz, 2H), 7.89 – 7.85 (m, 4H), 7.76 (dd, *J* = 7.9, 1.7 Hz, 2H), 3.59 (s, 18H), 1.64 (s, 6H).

MALDI-MS: calcd. for $C_{54}H_{52}F_6N_4PS$ (m/z): 933.35, found: 933.35.

Anal. calcd.: $C_{54}H_{52}F_{12}N_4P2S$: C, 60.11; H, 4.86; N, 5.19, found C, 59.90; H, 4.79; N, 5.13.

NMR Spectra

4,7-tris[7-p-N, N, N-trimethyl-aniline-9,9-dimethylfluoren-2-yl]-2,1,3-benzothiadiazole dihexafluorophosphate $[1]^{2+}(PF_6)_2$

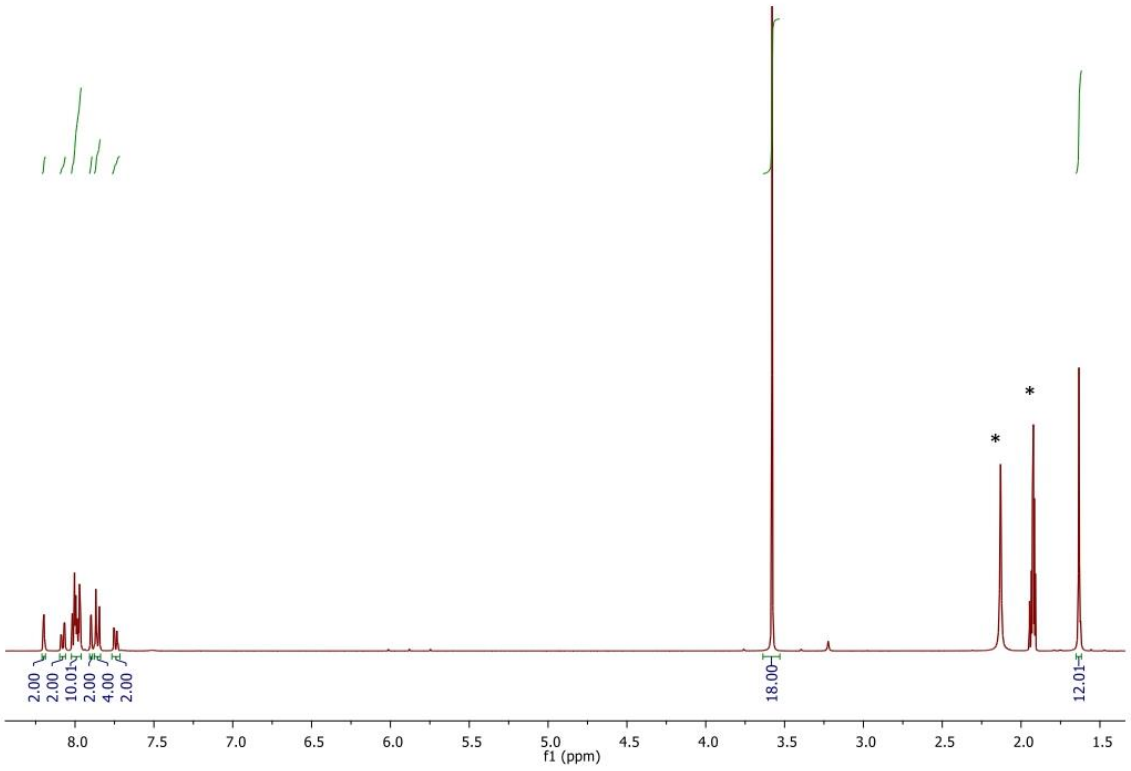

Figure. S2. ^{1}H-NMR spectrum of $[\mathbf{1}]^{2+}(PF_6)_2$ in *d*-MeCN. The asterisk (*) indicates the residual solvent peaks of acetone and water.

4,7-bis[9,9-dimethylfluoren2-yl]-2,1,3-benzothiadiazole (fbf)

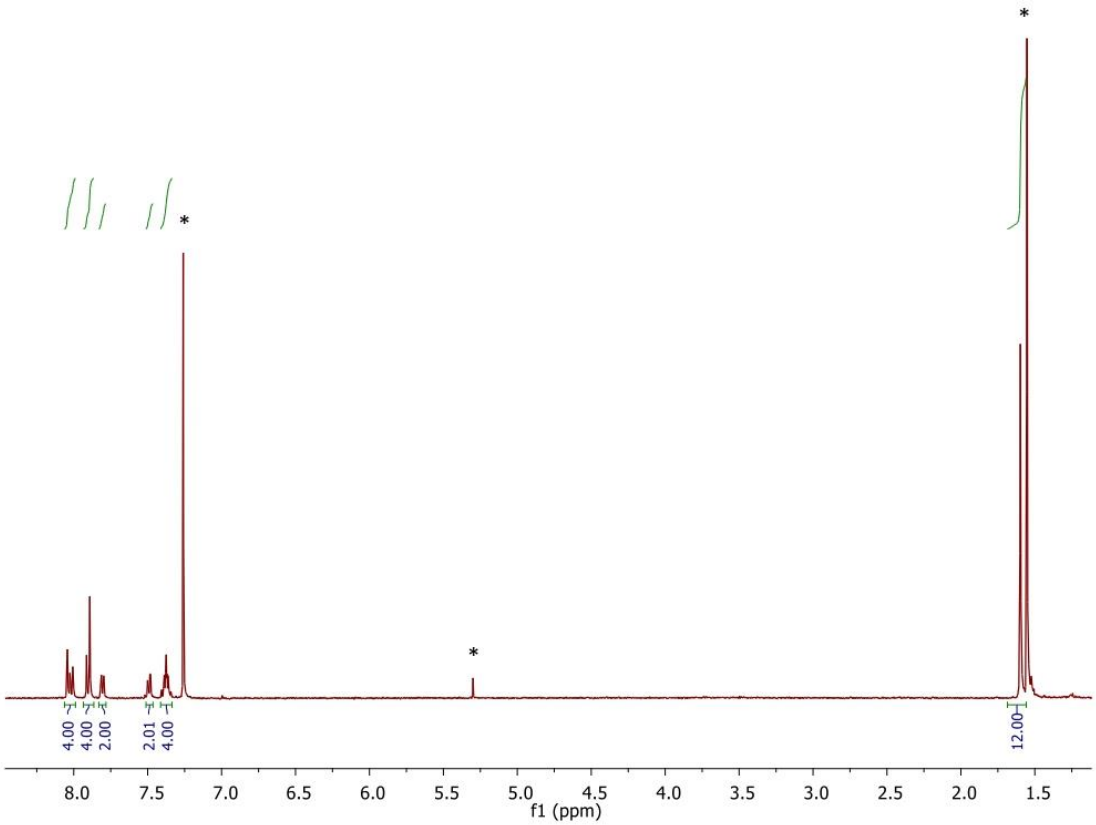

Figure. S3. ^{1}H-NMR spectrum of **fbf** in $CDCl_3$. The asterisk (*) indicates the residual solvent peaks of chloroform, water, and dichloromethane.

Crystal structure of $[1]^{2+}$

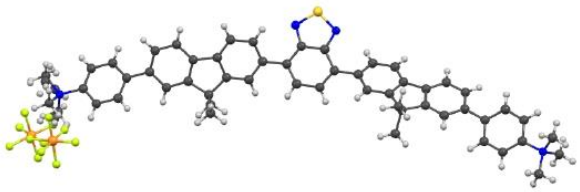

CCDC #2376492

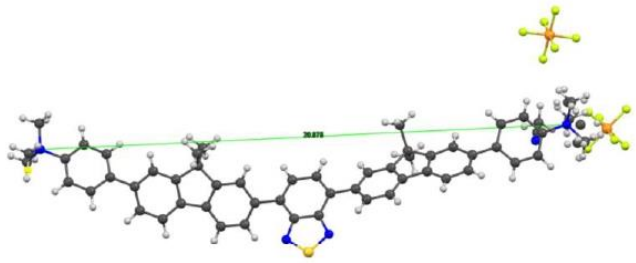

Distance between two terminal nitrogens is 2.99 nm.

Table 1 Crystal data and structure refinement for **[1]**$^{2+}$.

Identification code	NS23032_W7
Empirical formula	$C_{56}H_{55}F_{12}N_5P_2S$
Formula weight	1120.05
Temperature/K	150.0
Crystal system	monoclinic
Space group	C2/c
a/Å	30.244(2)
b/Å	12.2752(7)
c/Å	31.717(2)
α/°	90
β/°	116.043(4)
γ/°	90
Volume/Å^3	10579.5(12)
Z	8
ρ_{calc}g/cm^3	1.406
μ/mm^{-1}	0.208

F(000)	4640.0
Crystal size/mm^3	? × ? × ?
Radiation	MoKα (λ = 0.71073)
2Θ range for data collection/°	3.64 to 55.226
Index ranges	-39 ≤ h ≤ 39, -15 ≤ k ≤ 15, -41 ≤ l ≤ 41
Reflections collected	114845
Independent reflections	12215 [R_{int} = 0.0916, R_{sigma} = 0.0410]
Data/restraints/parameters	12215/0/726
Goodness-of-fit on F^2	1.082
Final R indexes [I>=2σ (I)]	R_1 = 0.0727, wR_2 = 0.1692
Final R indexes [all data]	R_1 = 0.0971, wR_2 = 0.1811
Largest diff. peak/hole / e Å^{-3}	0.39/-0.63

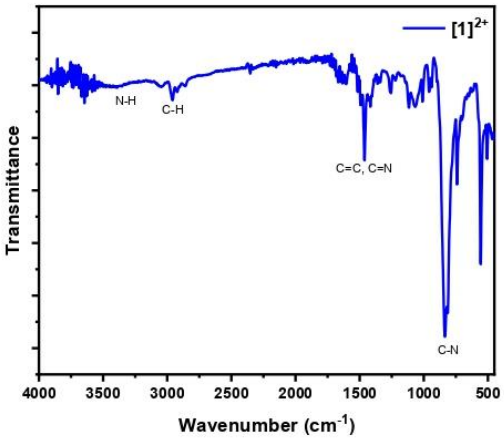

Figure. S4. IR spectrum of **[1]**$^{2+}$

S2. Liposome preparation

Stock solutions. The lipids 1,2-dipalmitoyl-sn-glycero-3-phosphocholine (DPPC) and 1,2-dimyristoyl-sn-glycero-3-phosphoethanolamine-N-[methoxy(polyethylene glycol)-2000] (ammonium salt) (14:0 PEG2000 PE) were prepared as stock solution in $CHCl_3$ with the concentration of 5 mM and 0.05 mM respectively. The chromophore $\mathbf{[1]}^{2+}(PF_6)_2$ salt was prepared with a concentration of 0.05 mM in acetonitrile. Phosphate buffer pH 7.0 was prepared with the mixture of KH_2PO_4 (626 mg, 4.6 mmol), $K_2HPO_4{\cdot}3H_2O$ (1.186 g, 5.2 mmol), and K_2SO_4 (1.70 g, 9.74 mmol) in Milli-Q water (1 L) to reach a final pH of 7.0. The tetrazolium dye XTT (sodium;4-methoxy-5-[3-(2-methoxy-4-nitro-5 sulfonatophenyl)-5-(phenylcarbamoyl)tetrazol-3-ium-2-yl]-2 nitrobenzenesulfonate) and NADH (nicotinamide adenine dinucleotide) were prepared with a concentration of 1 mM in phosphate buffer pH 7.0.

Preparation and characterization of giant vesicles and liposomes. Giant vesicle and liposomes were prepared as follows. To prepare lipid film, in a 5 mL round bottom flask, 1 mL stock solution of DPPC (5.0 mM) and 1 mL 14:0 PEG2000 PE (0.05 mM) in $CHCl_3$ and 1 mL $\mathbf{[1]}^{2+}$ (0.05) in acetonitrile were combined. The organic solvents were evaporated under vacuum leading to deposition of lipid film on the flask wall. The lipid film was dried under high vacuum for at least one hour and hydrated with phosphate buffer pH of 7.0 and 15 mg of NADH. The dispersed lipid film was repeatedly freeze-thawing, using liquid N_2 and a water bath at 52 °C yielding giant vesicles.

Prior to microscopy, and if applicable, giant vesicles were subjected a Sephadex G-25 size exclusion chromatography (SEC) column (6 cm length, 2 cm diameter) using phosphate buffer pH 7.0 as eluent. To prepare the sample for confocal microscopy measurements, a 50-100 μL amount of the giant vesicle sample was loaded into a well at the sample wells. Next, 200 μL of a freshly prepared, air-cooled agarose solution (1 weight-% in water) was added to the well and mixed with the sample. The mixed solution was then allowed to settle at room temperature before confocal microscopy measurements were taken.

To obtain liposomes of uniform size, the dispersion was extruded at 52 °C through 200 nm cellulose membrane filters 11 times with an Avanti Polar Lipids mini-extruder. The mixture of liposomes was treated with an SEC column, with phosphate buffer pH 7.0 as eluent, to separate the unencapsulated NADH. The liposome solution was collected and measured using dynamic light scattering (DLS). The results showed a Z_{Avg}-diameter ranging from 110-140 nm with a polydispersity index of about 0.1.

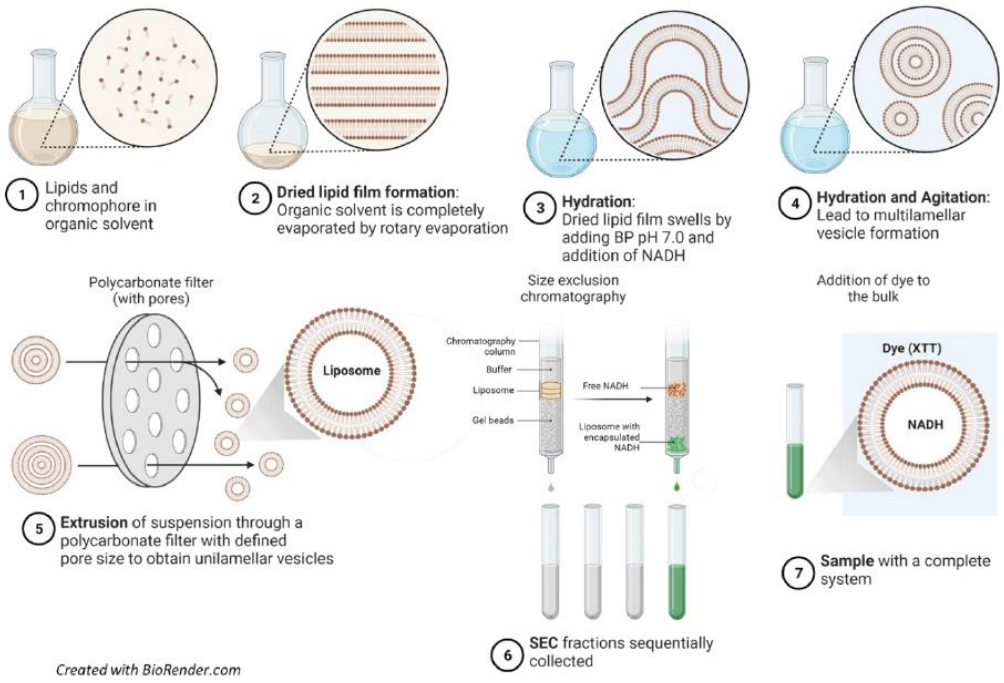

Figure. S5. Liposome preparation via thin film hydration with NADH encapsulated in the inner part of liposomes. Created with Biorender.com.

S3. The typical hydrodynamic diameter of DPPC liposome containing $[1]^{2+}$

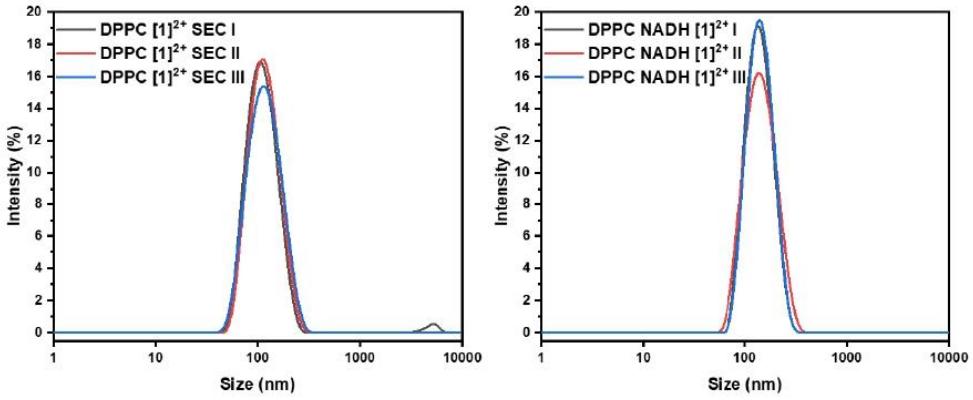

Figure. S6. Typical DLS measurements of DPPC:(14:0 PEG2000 PE):$\mathbf{[1]^{2+}}$= 100:1:1 liposomes without NADH (left) and with encapsulated NADH (right).

Table S1. DLS data: average size and polydispersity index, before and after irradiation of samples.

Parameters	DPPC $[1]^{2+}$		DPPC NADH: $[1]^{2+}$	
	Before	After	Before	After
Z-average (nm)	108	109	134	137
Polydispersity index	0.12	0.13	0.08	0.08

S4. Lifetime of $[1]^{2+}$ in different environments.

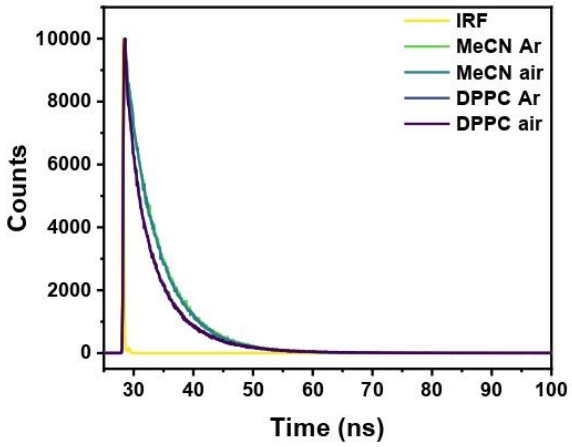

Figure S7. Lifetime measurements of $[1]^{2+}$ in acetonitrile (MeCN) and DPPC liposome under inert and ambient air atmosphere. IRF = instrument response function.

S5. Computational details for the computation of electronic excited states and Fukui functions

All quantum chemical computations were performed with the software Gaussian 16.[1] In order to properly describe the photophysical properties of $[1]^{2+}$, we benchmarked the performance of five functionals against the experimental absorption maxima. These functionals include the popular hybrid functionals B3LYP,[2–4] and PBE0[5–7] (PBE1PBE in Gaussian 16), and, because we expect $[1]^{2+}$ to find delocalized and possibly charge-transfer excitations, three functionals including long-range corrections: CAM-B3LYP,[8] which is based on B3LYP, both the original[9–11] and the revised[12] versions of lc-ωPBE, which use the same exchange-correlation functional as PBE0, and the wB97XD[13] functional by Head-Gordon and coworkers. Based on obtained results, we modified the HF exchange of the two most promising two functionals, PBE0 and CAM-B3LYP, to better reproduce the experimental excitation energies. Specifically, we increased the HF exchange in PBE0 from the default 25% to 30%

and denote this adapted functional as PBE0-30. Additionally, we reduced the μ-parameter in the error function describing the attenuation of CAM-B3LYP from the 0.33 in the default implementation to 0.20 and 0.15, denoted as CAM-B3LYP-20 and CAM-B3LYP-15, respectively. Dispersion was corrected for empirically using Grimme's D3 model with Becke-Johnson damping[14] except for wB97XD, which is already corrected for dispersion effects. These five functionals were tested in combination with a smaller def2-SVP and a larger def2-TZVP basis set,[15,16] but since the larger basis set barely affects the energetic position and intensities of the excitations, we deem the smaller basis set sufficiently accurate. Solvent effects for acetonitrile were included implicitly using a conductor-like polarization continuum model.[17,18] For each functional, **[1]**$^{2+}$ was optimized, and the convergence to a minimum was confirmed by the absence of imaginary frequencies within the harmonic approximation. The xyz-coordinates of the final structure can be found in section S14. Thirty singlet excited states were computed using time-dependent density functional theory for each of the eight functional/basis set combinations. The transition energies and oscillator strengths for the S_1 and S_3 excitations are shown in Figure S8.

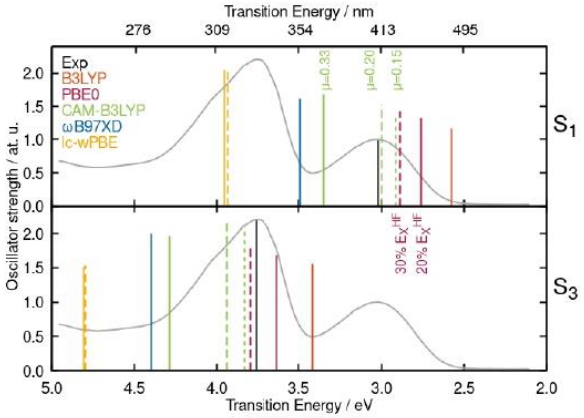

Figure S8. Vertical excitations for the tested functionals (see legend). The solid lines indicate the default implementation of the functionals, while dashed lines represent modified versions of the functionals with labels indicating the differences. For lc-ωPBE, the solid line represents the revised version (also known as lc-ωHPBE), and the dashed line the original implementation. Experimentally recorded band peaks are indicated as black lines, and the experimental spectrum is superimposed in grey.

Both for the S1 and S3 excitations, the excitations are strictly ordered by the HF exchange included in the exchange correlation functional, with increasing HF character correlated to an increased transition energy. This behaviour is well documented in literature.[19,20] One should note that the HF exchange in hybrid functionals and the error function parameters in range-separated functionals are not directly

comparable, but, in general, range separated functionals have a higher HF exchange that their local hybrid counerparts. The default implementations of PBE0 and CAM-B3LYP exhibit the most accurate excitation energies with respect to the experiment of all the traditional implementations, which is why we opted to modify these. Since PBE0 underestimates the excitation energies for both excitations, we increased the HF character; by contrast, CAM-B3LYP overestimates these, which is why we reduced the μ-parameter. The modified versions greatly improve the results, even if all slightly underestimate the excitation energy of the transition to S_1 and overestimate that to the S_3. In order to incorporate the long-range effects included in CAM-B3LYP (and its modified versions), we excluded PBE0-30 from further consideration and computed ensemble absorption spectra using CAM-B3LYP-20 and CAM-B3LYP-15 from Wigner-sampled geometries. We generated these structures with the workflow implemented in the SHARC[21] program package based on a harmonic frequency calculation with each of the functionals. The ensemble was generated at a temperature of 300 K and comprised 20 geometries. To ensure convergence, we limited the sampling to normal modes above 480 cm^{-1}. The convoluted spectra are shown in Figure S9.

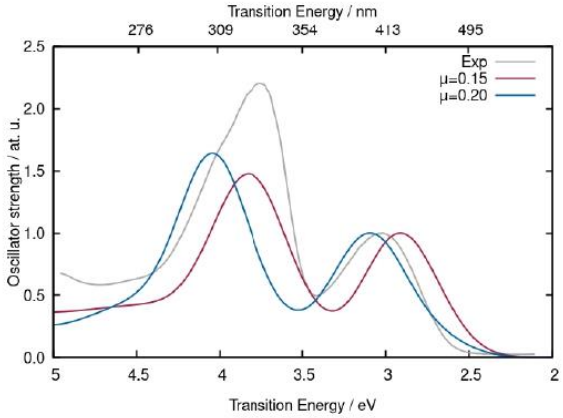

Figure S9. Absorption spectra computed with CAM-B3LYP-20 (blue) and CAM-B3LYP-15 (red) from the Wigner ensemble. The experimental spectrum is superimposed in grey. For comparison, all spectra were normalized at the S_1 peak to 1.

Based on the Wigner sampling, CAM-B3LYP-15 produces two peaks at 324 and 425 nm, and with CAM-B3LYP-20 the bands peak at 306 and 400 nm. While both modified versions of the CAM-B3LYP functional reproduce the experimental spectrum reasonably well, which peaks at 330 and 410 nm, respectively, CAM-B3LYP-20 reproduces best the S_3 energy and CAM-B3LYP-15 the S_1. Hence, we based our decision for what functional to use in the end on Koopmans theorem[22] by comparing the HOMO energies to the ionization energy. According to the theorem, the energy eigenvalue of the HOMO should equal the negative ionization energy, which we compute here as the difference in energy

between **[1]**$^{2+}$ and **[1]**$^{3+}$ (the molecule after ionization) at the same geometry. For CAM-B3LYP-15, the HOMO energy is about half the negative ionization energy (-0.26 vs. 0.50 at. units), while for CAM-B3LYP-20, the energies are in good agreement (-0.26 vs. 0.23 at. units). Therefore, we opted for CAM-B3LYP-20/def2-SVP for all analyses presented in the main manuscript and the following section.

Fukui functions were computed on the optimized geometry of **[1]**$^{2+}$ by performing single point calculations with a total charge of either +1, +2 or +3. As we are interested in the electrochemical properties of **[1]**$^{2+}$ after light absorption, we need to compute the Fukui functions for the relevant excited state. According to Kasha's rule,[23] which says that any excited state populations relax to the lowest excited state of the respective multiplicity within a short period of time, we computed the Fukui functions for the S_1. The Fukui functions in the S_1 can in turn be approximated as the inverse of the ground state Fukui functions.[24] f^- was hence computed as the difference in electron density between charge +2 and +1, which corresponds to f^+ in the ground state. f^+ was analogously computed as the electron density between +2 and +1, corresponding to f^- in the ground state. Δf was computed as the difference between the two Fukui functions.

Visualization of the NTOs, HOMO and LUMO as well as the Fukui functions was done with the molecular viewer Jmol[25] with cutoff values set to 0.04 a.u. for the orbitals, and 0.02 a.u. for the Fukuifunctions. Excited state wave function analysis was performed with the TheoDORE[26] suite.

S6. Characterization of the excited states

Both bright S_1 and S_3 excited states of **[1]**$^{2+}$ are of ππ* character, as evidenced by the natural transition orbitals (NTOs), shown in **Figure 3e-f** in the main manuscript**.** NTOs are orbitals representing the excitations in terms of the excited electron and the ground-state hole and generally provide a better description of the transition compared to standard molecular orbitals. During the excitation to the S_1 (**Figure 3e**), electron density is transferred from the five six-membered rings closest to the center of the molecule to the most central moiety. This leads to a sizeable increase in the static dipole moment to 11.1 Debye for the S_1 compared to 7.5 Debye in the electronic ground state S_0. By contrast, in the S_3 (**Figure 3f**), both the hole and the excited state electron are similarly delocalized over large parts of the molecule, making the S_3 comparable in electronic properties to the ground state, with the dipole moment only moderately increasing to 9.2 Debye.

The transition dipole moments for the excitation to the S_1 and the S_3 are shown in Figure S10. Both are reasonably well aligned along the molecular wire and confirm that a single **[1]**$^{2+}$ absorbs radiation above 300 nm along this axis.

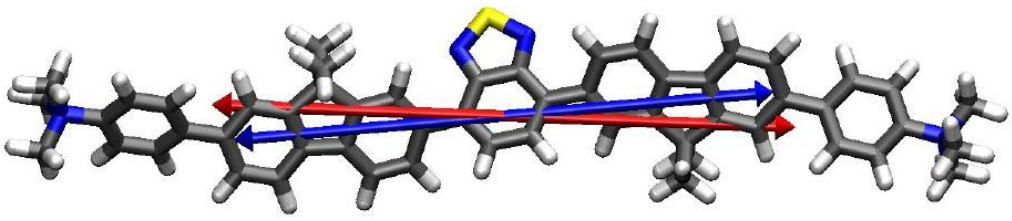

Figure S10. Transition dipole moments for the S_1 (blue) and S_3 (red) excitations.

As stated above, the S_3 exhibits an electronic character that is closer to that of the ground state compared to the S_1, which is of a higher charge transfer character. To support this claim, we divided **[1]**$^{2+}$ into six fragments (see Figure S11a) and computed the charge transfer matrix between these states for the S_1 and S_3 excitations (panels b and c of the same figure).

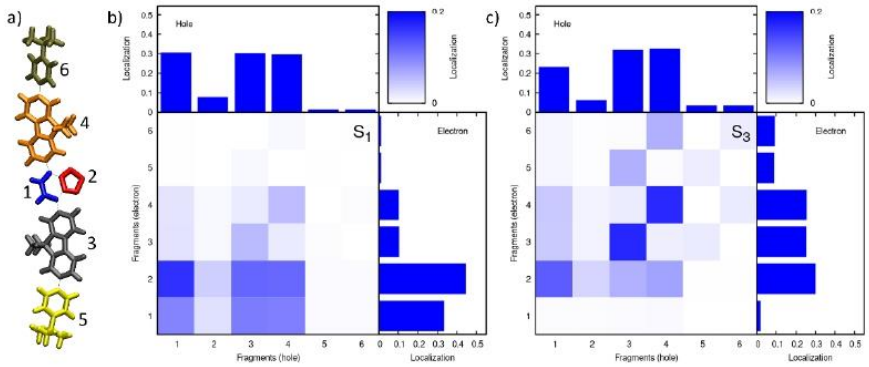

Figure S11. a) Definition of fragments. b) and c) Charge transfer matrix for the excitations to S_1 and S_3., respectively.

The S_1 exhibits multiple charge transfer elements, such as from the six- to the five-membered ring of the central moiety (fragments 1 and 2, respectively), as well as to these two fragments from the adjacent fragments 3 and 4. This means that in the S_1, the five-membered ring hosts significantly more electron density compared to the S_0. In contrast, the excitation to S_3 is more delocalized over the entire molecule, with all fragments except fragment 1 contributing notably. However, the largest weights are on the diagonal and correspond to local excitations on fragments 3 and 4. Since this local character dominates, the resulting electrostatic distribution in the S_3 is more similar to that of the S_0, which can also be seen from the electrostatic potential (ESP) maps in Figure S12.

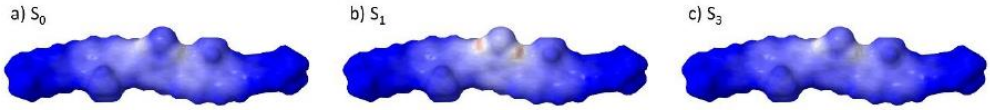

Figure S12. Electrostatic potential of the S_0, S_1 and S_3 states mapped onto a van der Waals surface. Blue areas indicate positive ESPs, white neutral and red negative areas. Blue saturation is where the ESP exceeds a partial charge of +0.15.

In all three states, the ends of **[1]**$^{2+}$ exhibit a mostly positive ESP due to the positive charge on the methylammonium groups. This positive charge extends over the entire molecule, but the central rings are more on the neutral side. Only the S_1 exhibits regions with a net-negative ESP due to the increased electron density on fragment 2. The central moiety of the S_3 is slightly less negative than the S_0, but much less so than the S_1. This similarity in electronic structure between S_0 and S_3, and the fact that the S_1 is quite different from the other two, explains why the excitation to the S_1 is red shifted in DPPC compared to in acetonitrile, while the excitation to S_3 is barely affected.

S7. Confocal microscopy

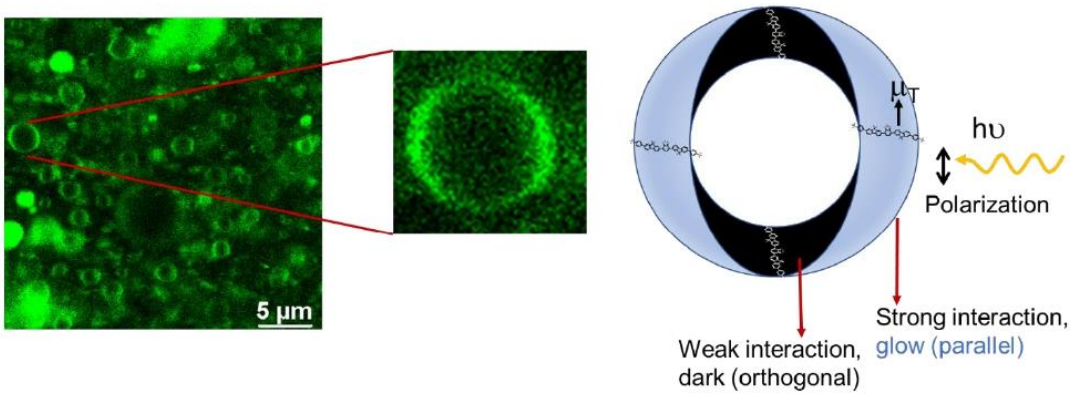

Figure S13. Confocal luminescence microscopy image

The confocal luminescence microscopy image displays a double-half moon shape that results from the interaction of **[1]**$^{2+}$ with the laser beam's incident light. When the laser beam moves parallel to the transition dipole moments of **[1]**$^{2+}$, a strong interaction occurs, leading to high emission intensity. On the other hand, when the laser beam moves orthogonally, a weak interaction happens, leading to less emission. The transition dipole moments of **[1]**$^{2+}$ are aligned along the membrane. The double-half moon effect reveals the preferred orientation of **[1]**$^{2+}$ in the lipid bilayer, but it cannot distinguish between parallel or orthogonal alignment. The preferred arrangement has been unraveled using molecular dynamics (MD) simulations; see below.

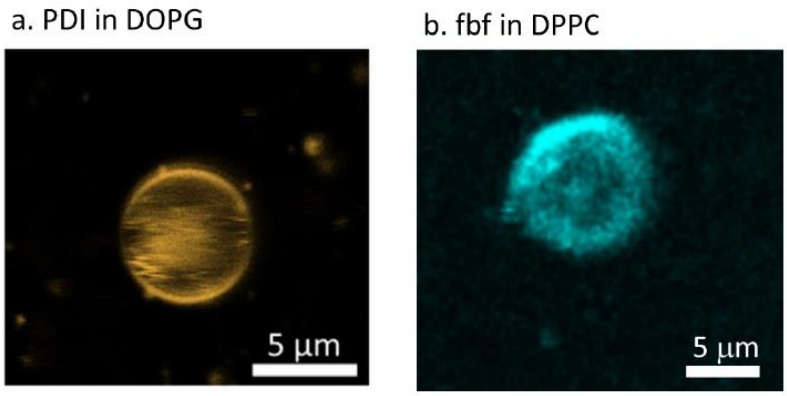

Figure S14. Confocal luminescence microscopy image, a) our previously reported system (reproduced from Ref. 27, with permission from The Royal Society of Chemistry based on a CC BY 3.0 license) with a preferably parallel orientation of the dye,[27] and b) the image of the reference compound fbf in the DPPC liposome.

In another reported work from us, the respective dye aligned alignment mostly parallel to the membrane surface and produced a 90° different half-moon-shape with the same laser alignment (Figure S14a).[27]

Furthermore, the hydrophobic core unit of **[1]**$^{2+}$ was integrated into the DPPC lipid bilayers (Figure S14b) and no half-moon effect was observed, which is concluded to be due to a random orientation within the lipophilic part of the membrane.

S8. Computational details on the membrane assembly simulations

Classical force field MD simulations of the lipid bilayer assembly were carried out to elucidate the orientation and alignment of **[1]**$^{2+}$. To this aim, we randomly distributed 128 DPPC lipids and one molecule of **[1]**$^{2+}$ in a cubic box of 70 Å side length. Due to the low concentration in the experiment, we did not include any 14:0 PEG2000 PE molecules in the simulation. The remaining box volume was then filled with water molecules and KCl ions to ensure charge neutrality and attain a salt concentration of 0.15 mol l^{-1}. The starting systems were assembled with the input generator CHARMM-GUI.[28]

All MD simulations were performed using the program packages Amber22 and Ambertools22.[29] **[1]**$^{2+}$ was described using the generalized Amber force field included in AmberTools22, with ground state point charges computed within the restrained electrostatic potential atomic partial charge (RESP) scheme in antechamber (part of Ambertools22) based on electrostatic potential date

computed in Gaussian16 on the B3LYP/def2-SVP level of theory (see above). The lipids were described using the Lipid21 force field,[30] while water and the atomic ions were described using the "optimal" point charge model[31] implemented in AmberTools22. After a 10.000 step minimization with 5000 steps employing the steepest gradient algorithm and another 5000 steps using a conjugate gradient algorithm, the systems were heated using a Langevin thermostat at a collision frequency of 1.0 ps^{-1} to 100 K in 2500 time steps (5 ps), followed by heating to 300 K in 50 000 steps (100 ps). Finally, the systems were propagated until the membrane was assembled and all water pores had disappeared. The insertion mode of **[1]**$^{2+}$ was then investigated by eye inspection.

For all simulations, a time step of 2 fs was used with the SHAKE algorithm[32] applied to freeze hydrogen bonds at a relative geometric tolerance of $1*10^{-7}$, thus enabling large time steps. Constant pressure periodic boundary conditions were superimposed with anisotropic pressure scaling control with Berendsen[33] at a pressure relaxation time of 1 ps, which was increased to 2 ps for the second heating phase only. The cutoff for non-bonded interaction terms was set to 10 Å. The simulations were performed using the GPU (CUDA) version of pmemd.[34–36] Visualization was done with VMD.[37]

The final points of the eight trajectories are shown in Figure S15. In all eight cases, as noted in the main manuscript, **[1]**$^{2+}$ is arranged in a transmembrane fashion. We note, however, that this configuration impacts the membrane topology, as in five out of the eight simulations, the membrane is visibly distorted where **[1]**$^{2+}$ is embedded (see **Fig. 4 a**, **c**, **f**, **g**, and **h**). It seems like **[1]**$^{2+}$ is slightly too short for an ideal integration into the membrane, causing in the membrane surface to be wavy to reduce its width at this position. This distortion of the membrane is visible in most of the trajectories at some points along the simulation, but in a few cases, the membrane becomes smooth during the simulated timeframe (see the eight trajectory movies as part of this SI). Thus, we believe that the distortion of the membrane is a computational artifact that can be removed when simulating higher time scales.

Our assessment of the possibility of membrane deformation within the context of MD by extending the simulation duration may not yield additional substantive. As such, deformation is a natural aspect of the dynamic process involved; as for the stability of the wires in the membrane, we can observe in our simulations that the orientation only changes as long as there are water pores present in the membrane, which have all evaporated at the end of our trajectories. As the molecular wire orients transmembrane in all simulations, once the pores are gone, we can say that this is the direction the wire will orient.

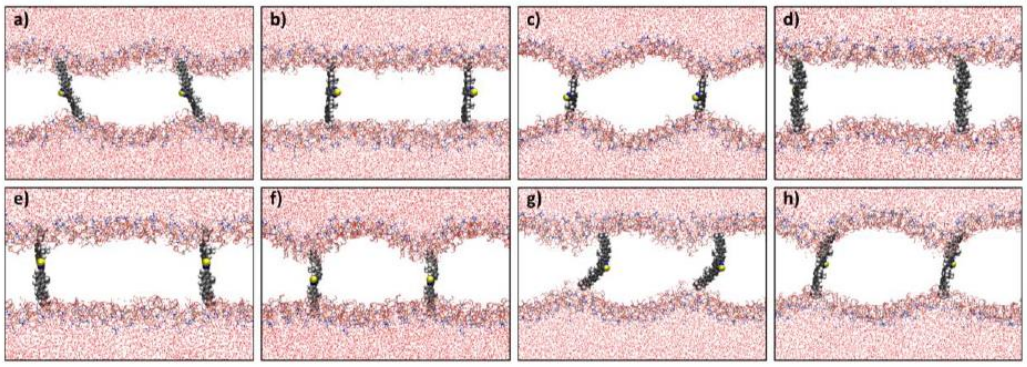

Figure S15. (a-h) Final point of trajectories after 0.5-1 μs, showing how **[1]**$^{2+}$ orients in the membrane. Each graphic shows two periodic images of **[1]**$^{2+}$. Color code: red = oxygen, white = hydrogen, blue = nitrogen, yellow = sulfur, golden = phosphorus, and grey = carbon. The alkyl tails of the lipid bilayer are omitted for clarity.

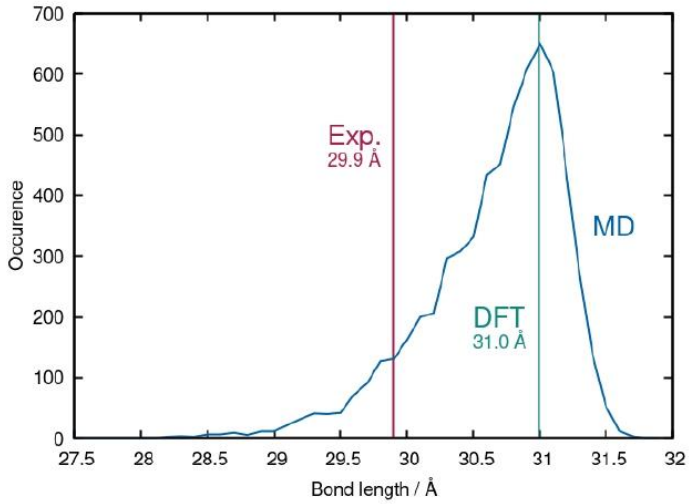

Figure S16. The distance of two $N(CH_3)_3$-groups at **[1]**$^{2+}$. The red line is based on the crystal structure, the green line is from the DFT calculation, and the distribution distance from the MD simulation is from 2.8-3.15 nm.

S9. Calceine-luminescence leakage test

We conducted a calceine test to check the impermeability of the membrane, which is a standard procedure used to assess the potential for membrane disruption during encapsulation with slight modifications.[38,39] We observed the DPPC liposome with and without integration of **[1]**$^{2+}$ and monitored the solution over varying time frames, but did not detect any leakage. To determine if light

could induce membrane disruption, we analyzed the same sample after 2 hours of irradiation with 470 nm LED and still did not observe any calceine leakage.

The calceine test preparation is as follows: in a 5 mL round bottom flask, 1 mL stock solution of DPPC (5.0 mM), 1 mL 14:0 PEG2000 PE (0.05 mM) and 1 mL **[1]**$^{2+}$ (0.05 mM) in acetonitrile were combined. The organic solvents were evaporated under vacuum for at least one hour. Calceine (43.58 mg, 0.07 mmol) was added to the flask and hydrated with 1 mL phosphate buffer (K_2HPO_4/KH_2PO_4) pH 7.7 to yield a calceine concentration of 70 mM. The dispersed lipid film was freeze-thawed for three times, using liquid N_2 and a water bath at 52 °C. The dispersion was extruded at 52 °C through 200 nm cellulose membrane filters 11 times with an Avanti Polar Lipids mini-extruder. The obtained solutions of liposomes were separated from excess Calceine using a SEC with phosphate buffer pH 7.7 as eluent. Luminescence measurements were carried out with 10 μl of liposome solution diluted with 990 μl of phosphate buffer pH 7.7, monitored every 0, 1, 5, 10, 30, 60, 90, and 120 minutes, after the measurements, Triton X-100 (1 mM, 50 μl) was added to the liposome sample. The liposomes are disturbed by the addition of Triton X-100 and release the encapsulated calceine. To check the stability of encapsulation in liposomes, other samples were measured after 2 h irradiation with a 470 nm LED stick. All luminescence spectra were recorded from 495 – 700 nm with excitation at λ_{ex} = 485 nm. Experiments were carried out for 2 days to investigate the stability of membrane.

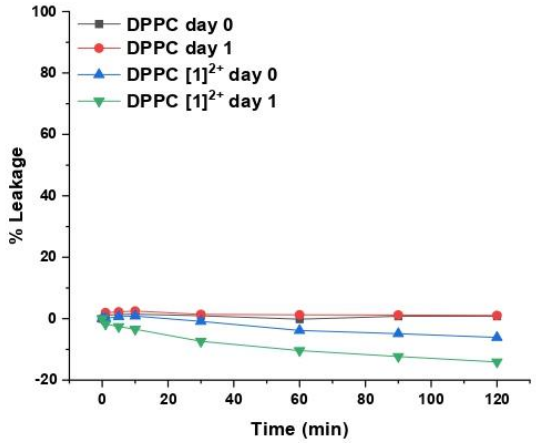

Figure S17. The percentage of calcein leakage is measured by comparing the luminescence before and after the addition of Triton X-100. This measurement is taken at λ_{max} = 518 nm, with and without the presence of **[1]**$^{2+}$.

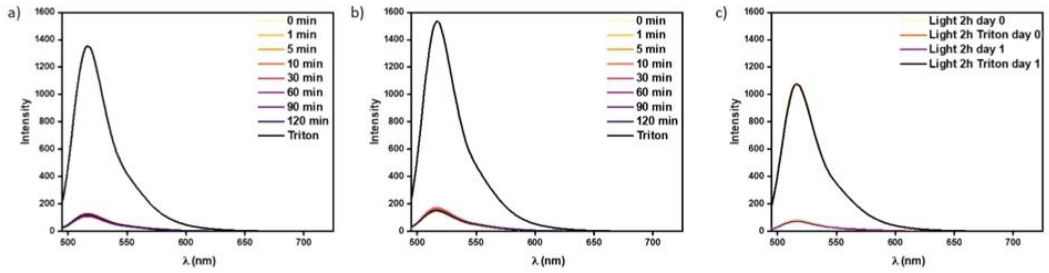

Figure S18. Luminescence spectra of calcein in DPPC liposomes at self-quenching concentration (low intensity) and spectra upon addition of Triton X-100 to disrupt the lipid membrane (high intensity), a) day 0, b) day 1, C) day 0 and 1 after irradiation with 470 nm LED stick for 2 h.

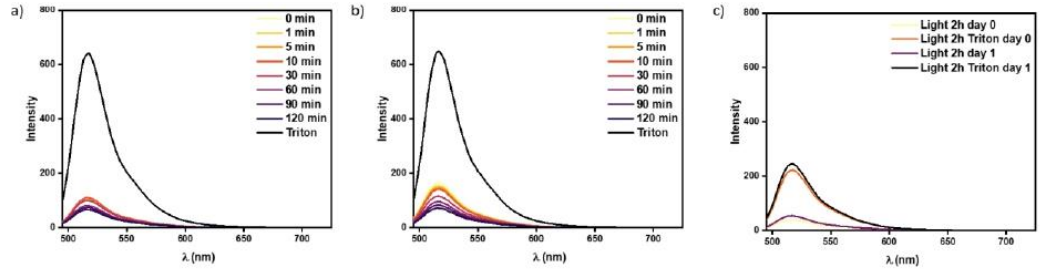

Figure S19. Luminescence spectra of calcein in DPPC liposomes with 1% **[1]**$^{2+}$ at the self-quenching concentration (low intensity) and spectra upon addition of Triton X-100 to disrupt the lipid membrane (high intensity), a) day 0, b) day 1, C) day 0 and 1 after irradiation with 470 nm LED stick for 2 h.

S10. Electrochemical and Spectroelectrochemical characterization

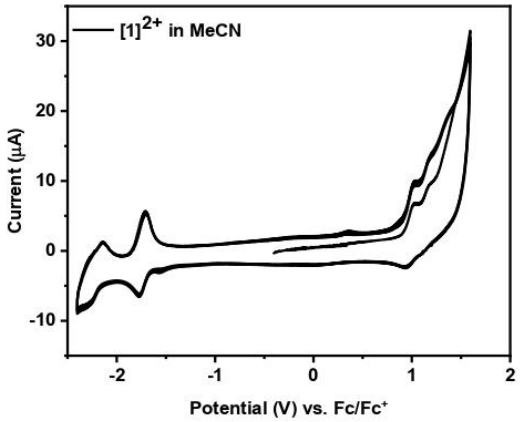

Figure S20. Cyclic voltammograms of **[1]**$^{2+}$ (acetonitrile, 0.1 M nBu_4NPF_6 supporting electrolyte, 0.25 mM analyte, 100 mV s^{-1}, glassy carbon-working electrode, Pt-wire counter electrode, Ag wire (in a glass frit containing electrolyte solution-quasi reference electrode) referenced against Fc/Fc^+.

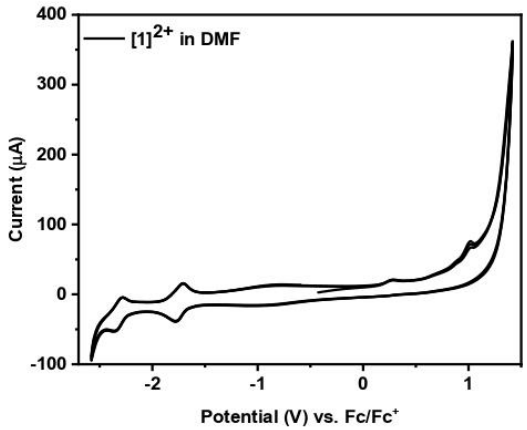

Figure S21. Cyclic voltammograms of **[1]**$^{2+}$ (DMF, 0.1 M nBu_4NPF_6 supporting electrolyte, 0.25 mM analyte, 100 mV s^{-1}, glassy carbon-working electrode, Pt-wire counter electrode, Ag wire (in a glass frit containing electrolyte solution-quasi reference electrode) referenced against Fc/Fc^+.

Table S2. Summarized electrochemical data of **[1]**$^{2+}$ in acetonitrile and DMF referenced against Fc/Fc^+ (potentials are accurate to $\pm$ 0.1 V), (Ox: Oxidation, Red: Reduction).

[1]$^{2+}$	1st Ox	2nd Ox	1st Red	2nd Red
Acetonitrile	1.0	1.2	-1.7	-2.2
DMF	0.3	-	-1.7	-2.3

The spectroelectrochemistry measurements were performed using a pine honeycomb screen-printed platinum electrode as a working electrode and counter electrode and Ag wire (in a glass frit containing electrolyte solution) as a quasi-reference electrode.

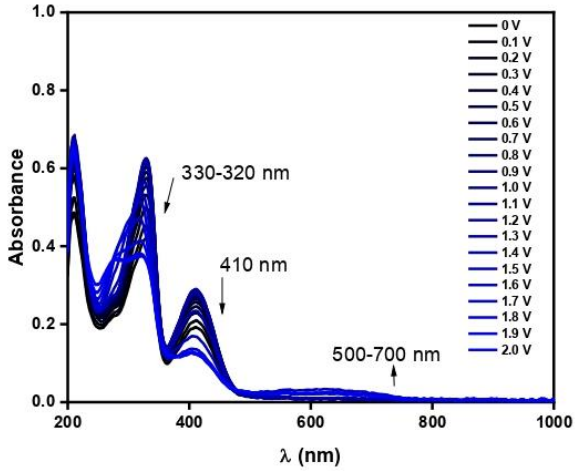

Figure S22. UV-Vis-NIR spectra obtained during spectroelectrochemical oxidation of **[1]**$^{2+}$ in deaerated acetonitrile containing 0.1 M nBu_4PF_6, measured from 0.0 V to 2.0 V, are given in V vs. Fc+ /Fc.

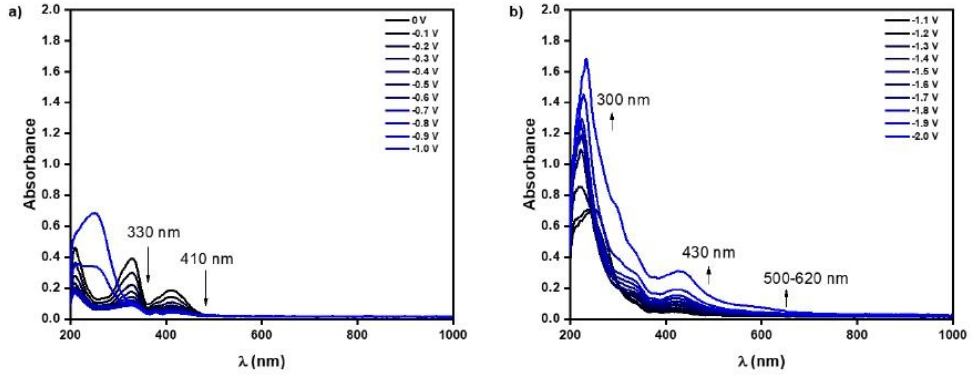

Figure S23. UV-Vis-NIR spectra obtained during spectroelectrochemical reduction of **[1]**$^{2+}$ in deaerated acetonitrile containing 0.1 M nBu_4PF_6, measured from 0.0 V to -2.0 V, are given in V vs. Fc+ /Fc.

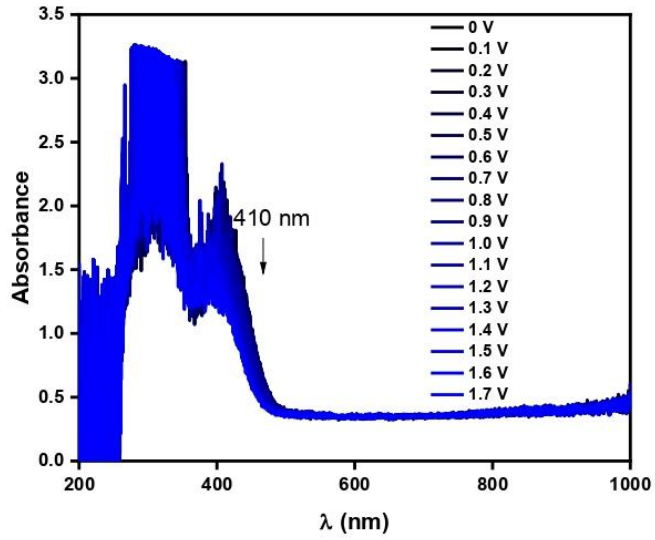

Figure S24. UV-Vis-NIR spectra obtained during spectroelectrochemical oxidation of **[1]**$^{2+}$ in deaerated DMF containing 0.1 M nBu_4PF_6, measured from 0.0 V to 1.7 V, are given in V vs. Fc+ /Fc.

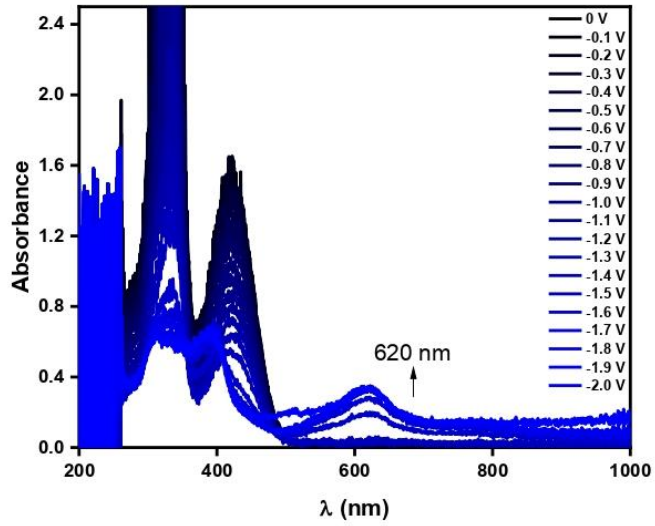

Figure S25. UV-Vis-NIR spectra obtained during spectroelectrochemical reduction of **[1]**$^{2+}$ in deaerated DMF containing 0.1 M nBu_4PF_6, measured from 0.0 V to -2.0 V, are given in V vs. Fc+ /Fc.

Thermochemistry of electron transfer from the photoexcited $[1]^{2+}$ followed by the oxidation of NADH and the reduction of XTT.

The potential energy of every component (vs SCE):

1. $\mathbf{[1]^{2+}}$ (measured in acetonitrile)

Emission: 550 nm (r.t) based on this number, we determined the E_{00} of $\mathbf{[1]^{2+}}$

$E_{00} = 1240/\lambda_{em} = 1240/550 = 2.3$ eV

Electrochemical potential for $\mathbf{[1]^{2+}}$ from Fc^+/Fc to SCE (+0.38 V vs SCE)[40]

$\mathbf{[1]^{3+}/[1]^{2+}}$ = 1.0 V vs Fc^+/Fc → 1.38 V vs SCE

$\mathbf{[1]^{2+}/[1]^{+}}$ = -1.7 V vs Fc^+/Fc → -1.32 V vs SCE

$\mathbf{[1]^{2+*}/*[1]^{2+}}$ = 1.38 V – 2.3 eV = -0.92 V vs SCE

$\mathbf{*[1]^{2+}/[1]^{2+-}}$= -1.32 + 2.3 eV = 0.98 V vs SCE

2. XTT

XTT^-/XTT = -0.19 V vs Ag/AgCl (based on MTT data)[41]

Converted from Ag/AgCl to SCE (-0.044 V vs SCE)[42]

XTT^-/XTT = -0.23 V vs SCE

3. NADH

$NADH^+/NADH$ = 0.65 V vs Ag/AgCl[43]

Converted from Ag/AgCl to SCE (-0.044 V vs SCE)[42]

$NADH^+/NADH$ = 0.61 V vs SCE

4. Driving force for electron transfer from $\mathbf{[1]^{2+}}$ to XTT:

From $\mathbf{*[1]^{2+}}$ (excited state) to XTT

ΔG_{eT} = ($\mathbf{[1]^{2+*}/*[1]^{2+}}$) - ($XTT^-/XTT$) = -0.92 V – (-0.23 V) = **-0.69 V**

From $\mathbf{[1]^{+}}$ (reduced ground state) to XTT

ΔG_{eT} = ($\mathbf{[1]^{2+}/[1]^{+}}$) - ($XTT^-/XTT$) = -1.32 V – (-0.23 V) = **-1.09 V**

From $\mathbf{[1]^{2+}}$ (ground state) to XTT

ΔG_{eT} = ($\mathbf{[1]^{3+}/[1]^{2+}}$) - ($XTT^-/XTT$) = 1.38 V – (-0.23 V) = 1.61 V

5. Driving force for electron transfer from NADH to $\mathbf{[1]^{2+}}$

From NADH to $\mathbf{*[1]^{2+}}$ (excited state)

ΔG_{eT} = ($NADH^+/NADH$) - ($\mathbf{*[1]^{2+}/[1]^{2+-}}$) = 0.61 V - 0.98 V = **-0.37 V**

From NADH to $\mathbf{[1]^{3+}}$ (oxidized ground state)

ΔG_{eT} = ($NADH^+/NADH$) - ($\mathbf{[1]^{3+}/[1]^{2+}}$) = 0.61 V – 1.38 V = **-0.77 V**

From NADH to **[1]**$^{2+}$ (ground state)

ΔG_{eT} = ($NADH^+$/NADH) - (**[1]**$^{2+}$/**[1]**$^{+}$) = 0.61 V – (-1.32 V) = 1.93 V

S11. Photoirradiation

The typical reactions were carried out within quartz cuvettes where 300 μl of liposome solution, 10 μl of 1 mM XTT, and 190 μl phosphate buffer pH 7.0 were added. The mixtures were illuminated within a custom-made reactor equipped with four ventilators to exclude heating of the samples and an LED-stick (Nichia Corporation; NSPB500AS) (λ = 470 ± 10 nm, 15.7 mW measured with a Hioki 3664 optical power meter set to 470 nm).[44] The photon flux (f) was determined using standard ferrioxalate actinometry with a value of $8.2 \cdot 10^{-8}$ Einstein·s^{-1}. The samples were monitored via UV-Vis spectroscopy after 0, 1, 5, 10, 30, 60, 90, and 120 minutes. The number of photons flux absorbed by **[1]**$^{2+}$ was determined by measuring the initial absorption at 470 nm. To calculate the number of photons (n_{photon}) over time, the photon flux from the initial absorption was multiplied by the average of the latest two irradiation times. The number of formazan (n_{fz}) (Fz) was calculated by measuring the increasing absorbance at 470 nm; the increasing absorbance value was converted to the number of Fz formed with the reported extinction coefficient of Fz at 470 nm (21.600 M^{-1} cm^{-1}).[45] The quantum yield (Qy) of Fz formation was calculated by dividing the number of photons absorbed by the number of Fz formed.

$$n_{photon} = f \times (\frac{t_0 + t_1}{2}) \qquad \text{(S1)}$$

$$Qy = \frac{n_{fz}}{n_{photon}} \qquad \text{(S2)}$$

Equation S1 determines the number of photons during irradiation time. Equation S2 is used to calculate the quantum yield of formazan formation.

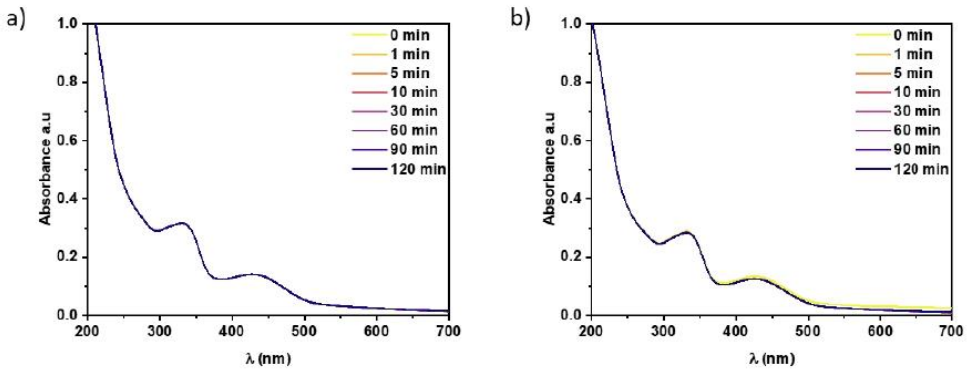

Figure S26. Temporal UV-vis spectra in DPPC:(14:0 PEG2000 PE):$\mathbf{[1]}^{2+}$ = 100:1:1 (/$\mathbf{[1]}^{2+}$/) liposome in phosphate buffer pH 7.0, irradiated with 470 nm LED stick a) ambient air; b) argon atmosphere.

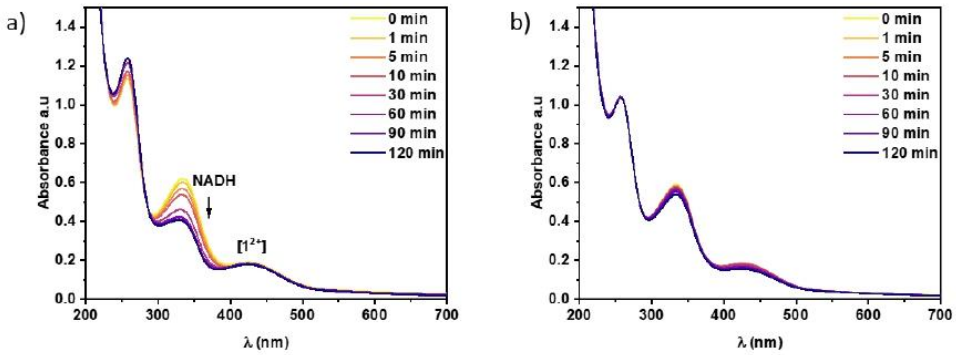

Figure S27. Temporal UV-vis spectra in DPPC:(14:0 PEG2000 PE):$\mathbf{[1]}^{2+}$= 100:1:1 (NADH/$\mathbf{[1]}^{2+}$/) with encapsulation of NADH (0.021 M) in liposome in phosphate buffer pH 7.0, irradiated with 470 nm LED stick a) ambient air; b) argon atmosphere.

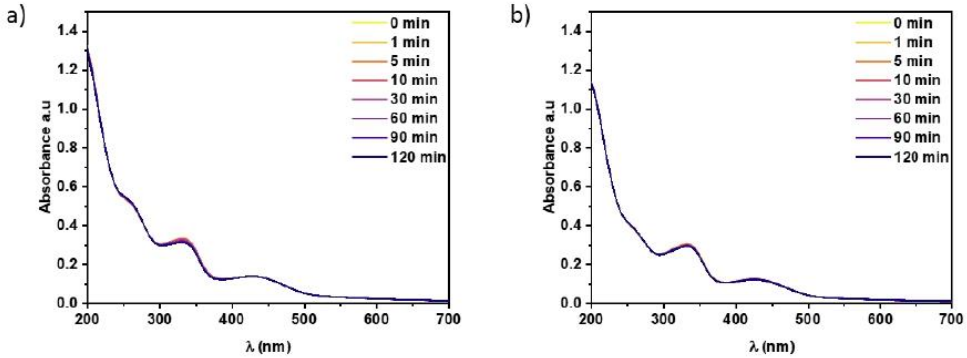

Figure S28. Temporal UV-vis spectra in DPPC:(14:0 PEG2000 PE):$\mathbf{[1]}^{2+}$= 100:1:1 (/$\mathbf{[1]}^{2+}$/NADH) with NADH (2 x 10^{-5} M) at the bulk solution of liposome in phosphate buffer pH 7.0, irradiated with 470 nm LED stick a) ambient air; b) argon atmosphere.

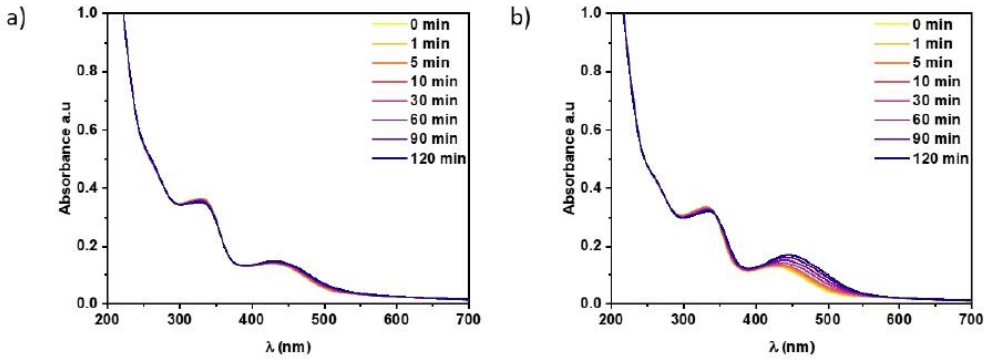

Figure S29. Temporal UV-vis spectra in DPPC:(14:0 PEG2000 PE):$\mathbf{[1]}^{2+}$= 100:1:1 (/$\mathbf{[1]}^{2+}$/NADH, XTT) with NADH (2 x 10^{-5} M) and XTT (2 x 10^{-5} M) (no compartmentalization) at the bulk solution of liposome in phosphate buffer pH 7.0, irradiated with 470 nm LED stick a) ambient air; b) argon atmosphere.

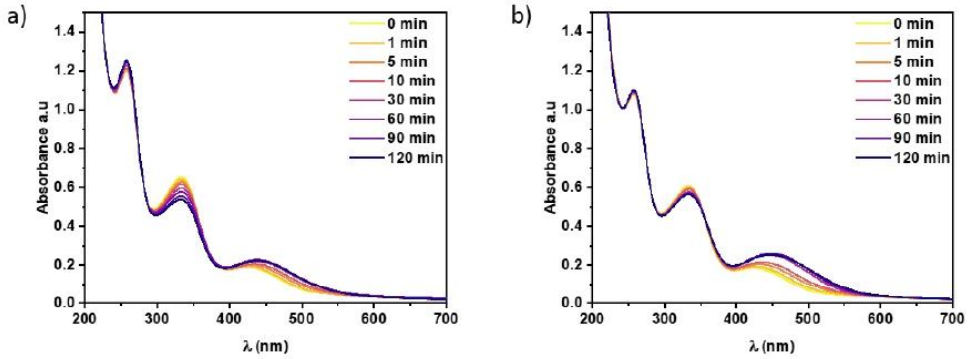

Figure S30. Temporal UV-vis spectra in DPPC:(14:0 PEG2000 PE):$\mathbf{[1]}^{2+}$= 100:1:1 (NADH/$\mathbf{[1]}^{2+}$/XTT) with NADH (0.021 M) encapsulated inside liposome and XTT (2 x 10^{-5} M) (no compartmentalization) at the bulk solution of liposomes in phosphate buffer pH 7.0, irradiated with 470 nm LED stick a) ambient air; b) argon atmosphere.

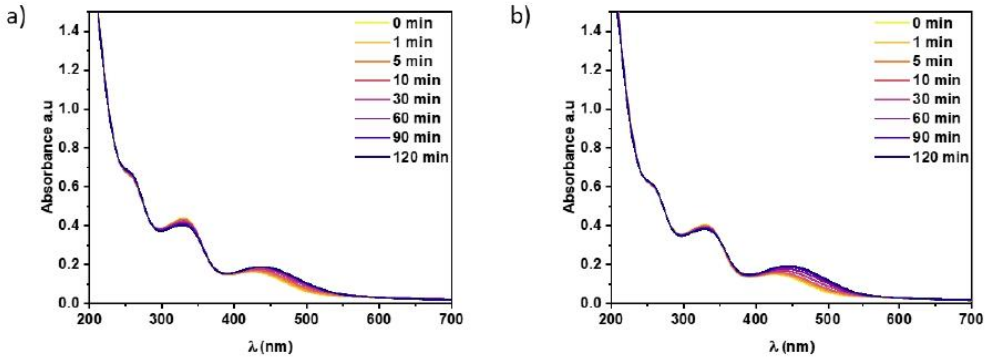

Figure S31. Temporal UV-vis spectra in DPPC:(14:0 PEG2000 PE):**[1]**$^{2+}$:18-Crown-6= 100:1:1:4. (NADH/**[1]**$^{2+}$,4.2%18-crown-6/XTT) with NADH (0.021 M) encapsulated inside liposome and XTT (2 x 10^{-5} M) (no compartmentalization) at the bulk solution of liposomes in phosphate buffer pH 7.0, irradiated with 470 nm LED stick a) ambient air; b) argon atmosphere.

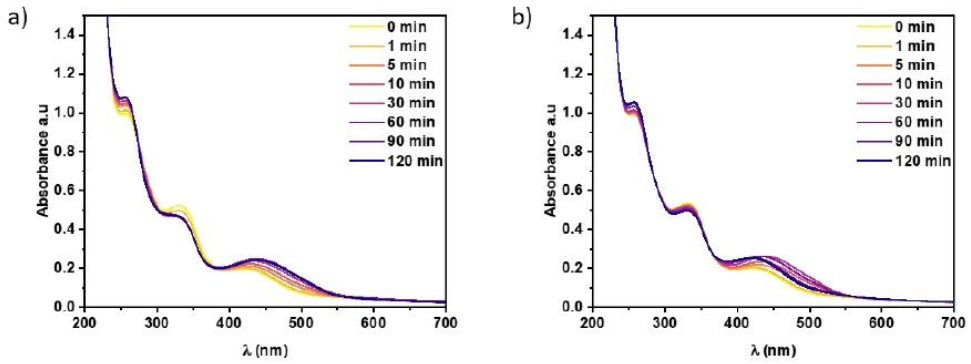

Figure S32. Temporal UV-vis spectra in DPPC:(14:0 PEG2000 PE):**[1]**$^{2+}$:Gramicidin A= 100:1:1:1 (NADH/**[1]**$^{2+}$,1%gramicidinA/XTT) with NADH (0.021 M) encapsulated inside liposome and XTT (2 x 10^{-5} M) (no compartmentalization) at the bulk solution of liposomes in phosphate buffer pH 7.0, irradiated with 470 nm LED stick a) ambient air; b) argon atmosphere.

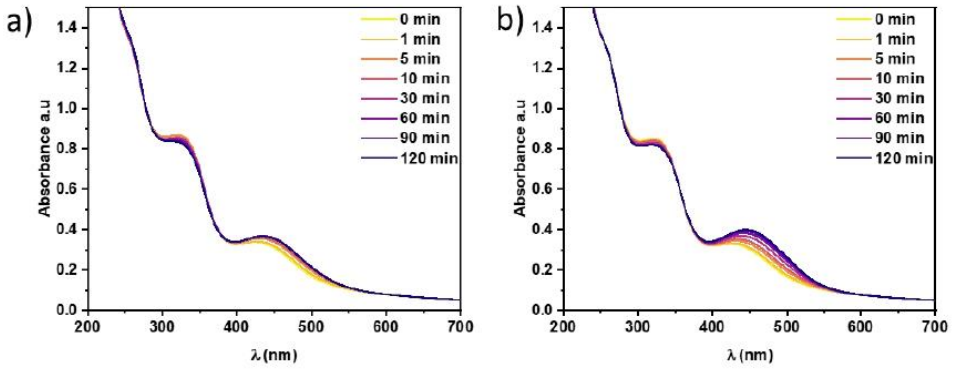

Figure S33. Temporal UV-vis spectra in DPPC:(14:0 PEG2000 PE):**[1]**$^{2+}$= 100:1:1 (XTT/**[1]**$^{2+}$/NADH)with XTT (0.009 M) encapsulated inside liposome and NADH (2 x 10^{-5} M) (no compartmentalization) at the bulk solution of liposome in phosphate buffer pH 7.0, irradiated with 470 nm LED stick a) ambient air; b) argon atmosphere.

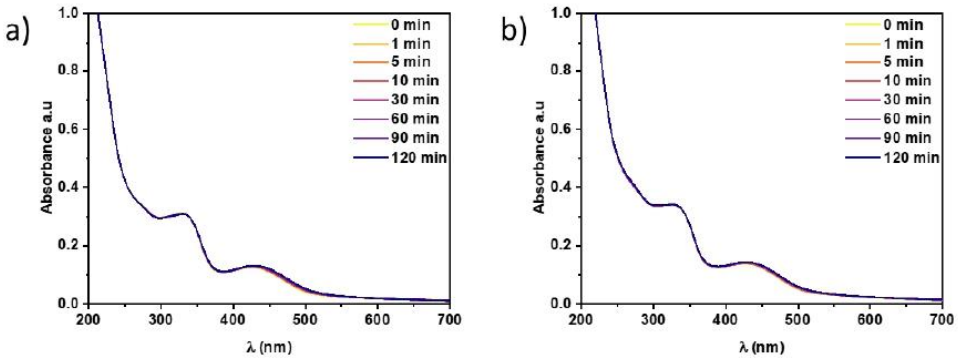

Figure S34. Temporal UV-vis spectra in DPPC:(14:0 PEG2000 PE):**[1]**$^{2+}$ = 100:1:1 (/**[1]**$^{2+}$/XTT) with XTT (2 x 10^{-5} M) (no compartmentalization) at the bulk solution of liposomes in phosphate buffer pH 7.0, irradiated with 470 nm LED stick a) ambient air; b) argon atmosphere.

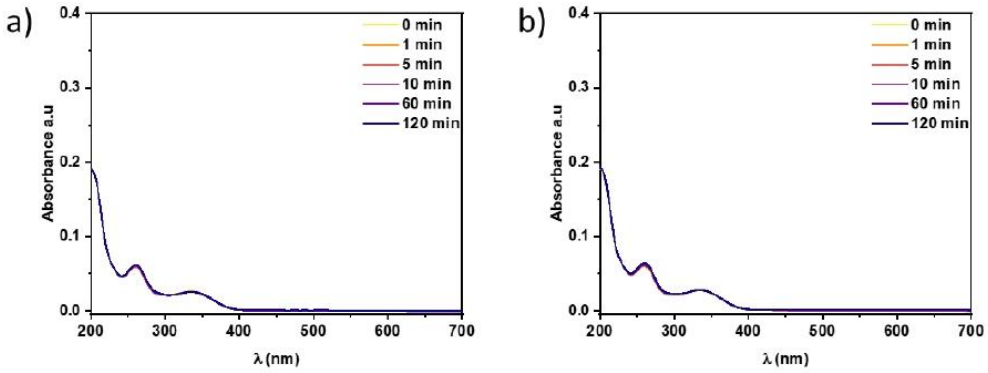

Figure S35. Temporal UV-vis spectra in DPPC:(14:0 PEG2000 PE) = 100:1 (//XTT) with XTT (2 x 10^{-5} M) (no compartmentalization, absence of **[1]**$^{2+}$) at the bulk solution of liposomes in phosphate buffer pH 7.0, irradiated with 470 nm LED stick a) ambient air; b) argon atmosphere.

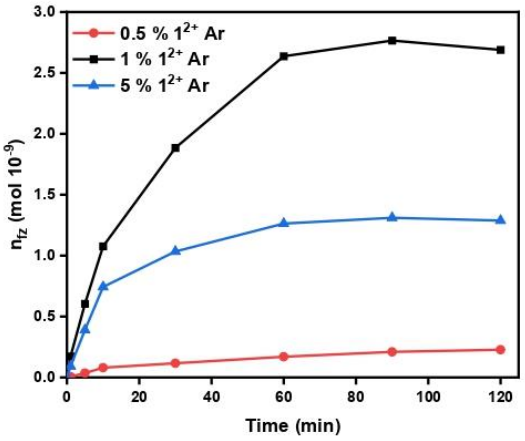

Figure S36. Formation of formazan over time with different loading of **[1]**$^{2+}$ in the DPPC with a composition of NADH/**[1]**$^{2+}$/XTT under inert atmosphere.

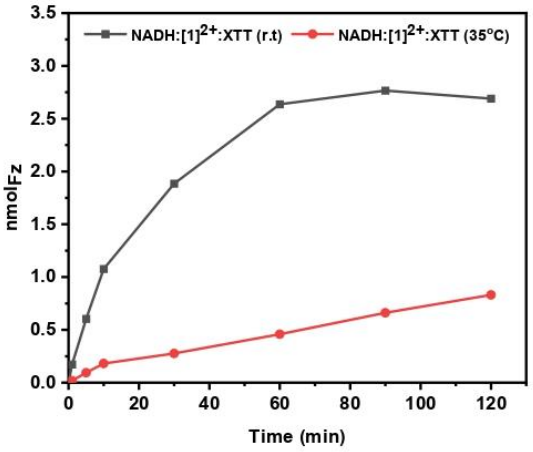

Figure S37. Formation of formazan over time at room temperature (20-25°C) and 35 °C with a composition of NADH/**[1]**$^{2+}$/XTT under an inert atmosphere Electron transfer at room temperature is more efficient. This could be related to the higher temperature, which could give the donor or acceptor electron a higher mobility, which then affects the efficiency of electron transfer, or it could be due to increased permeability around the transitions temperature (40 °C).

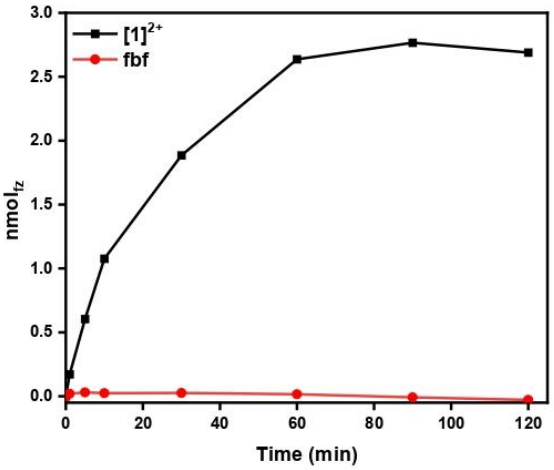

Figure S38. Formation of formazan over time with a composition of NADH/**[1]**$^{2+}$/XTT and NADH/**fbf**/XTT under an inert atmosphere.

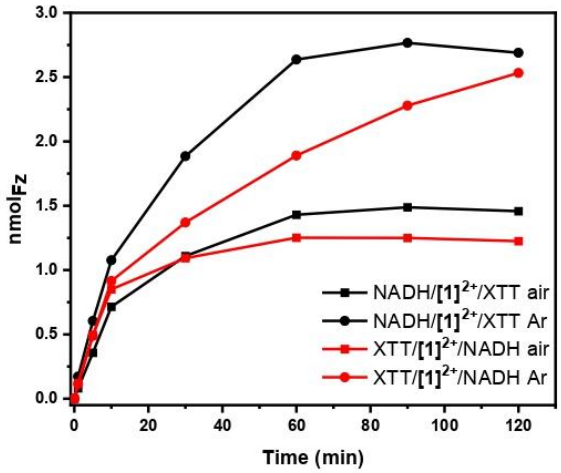

Figure S39. Formation of formazan over time with a composition of NADH/**[1]**$^{2+}$/XTT and XTT/**[1]**$^{2+}$/NADH under an inert and ambient air atmosphere.

S12. Nanosecond transient absorption spectra

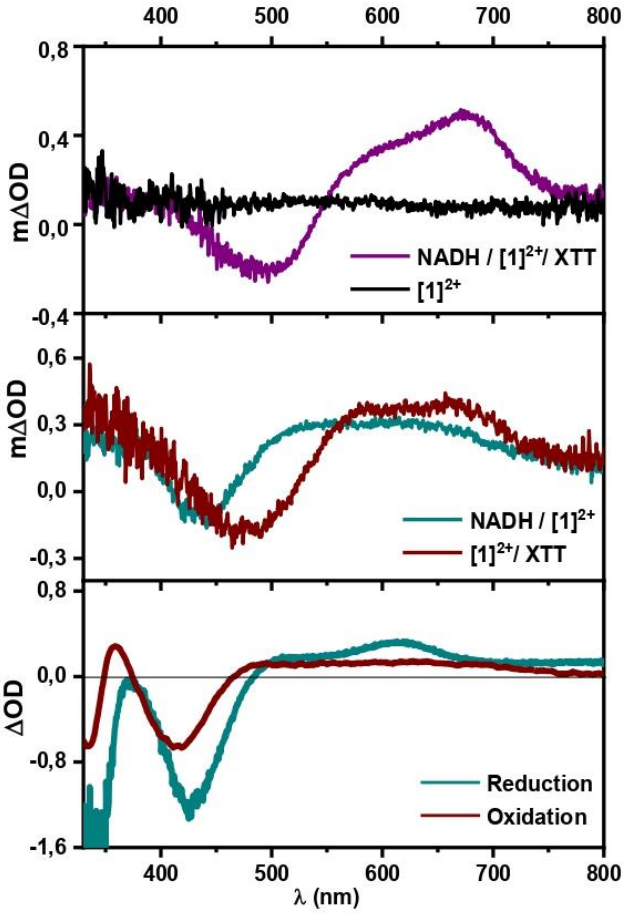

Figure S40. Transient absorption spectrum of 1% **[1]**$^{2+}$ in DPPC (black), spectrum of 1% **[1]**$^{2+}$ in DPPC with encapsulated NADH and XTT in bulk (purple), encapsulated NADH inside DPPC liposome with 1% of **[1]**$^{2+}$ (red), and DPPC liposome with 1% of **[1]**$^{2+}$ XTT at the bulk (blue) after excitation at 420 nm laser pulse of ~10 ns duration after a delay of 1 μs. All measurements were performed in argon atmosphere at 20 °C. (bottom) Spectro-electrochemical UV–vis, the spectrum of **[1]**$^{2+}$ in dry acetonitrile for reduction (red) at an applied potential of -1.8 V vs Fc/Fc^{+} in dry DMF for oxidation (blue) at an applied potential of 2.0 V vs Fc/Fc^{+}, the electrolyte containing 0.1 M tetra-n-butylammonium hexafluorophosphate ($TBAPF_6$).

[1]$^{2+}$ **at DPPC**

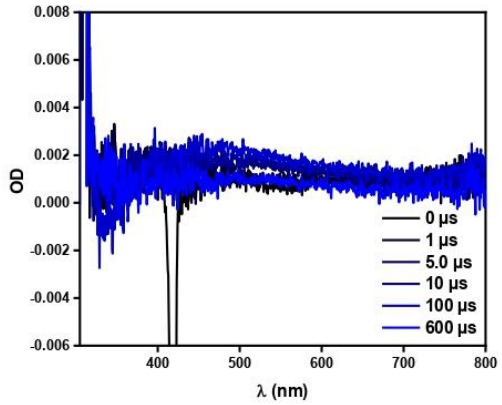

Figure S41. Temporal nanosecond transient absorption spectra of DPPC:(14:0 PEG2000 PE):**[1]**$^{2+}$= 100:1:1 liposomes in phosphate buffer pH 7.0 upon 420 nm pump excitation.

Encapsulated NADH in the liposome

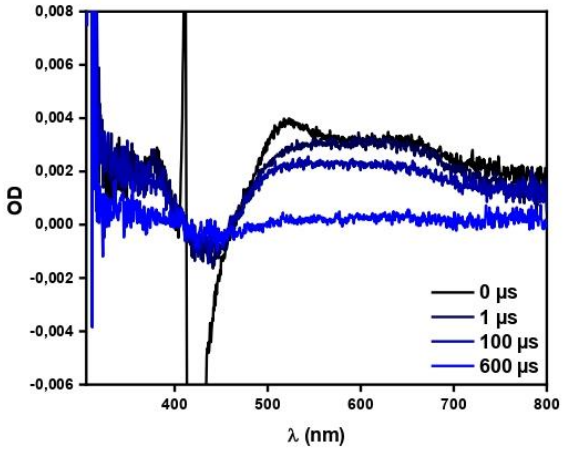

Figure S42. Temporal nanosecond transient absorption spectrum of encapsulated NADH (theoretical value of 22.5 mM) DPPC:(14:0 PEG2000 PE):**[1]**$^{2+}$= 100:1:1 liposomes in phosphate buffer pH 7.0 upon 420 nm pump excitation.

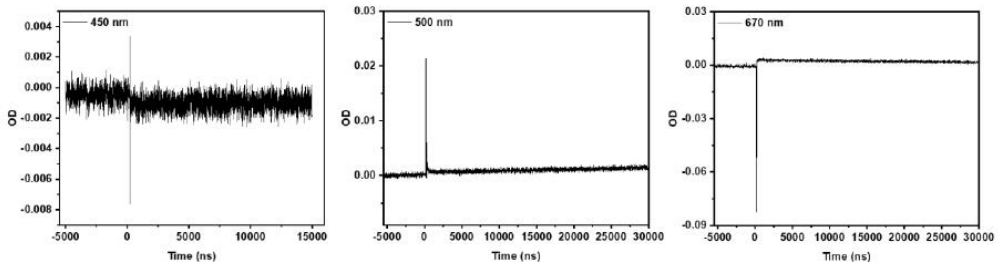

Figure S43. Time traces of the excited states of encapsulated NADH (theoretical value of 22.5 mM) DPPC:(14:0 PEG2000 PE):**[1]**$^{2+}$= 100:1:1 liposomes in phosphate buffer pH 7.0 at 450nm, 500 nm and 670 nm.

XTT at the bulk solution of liposome

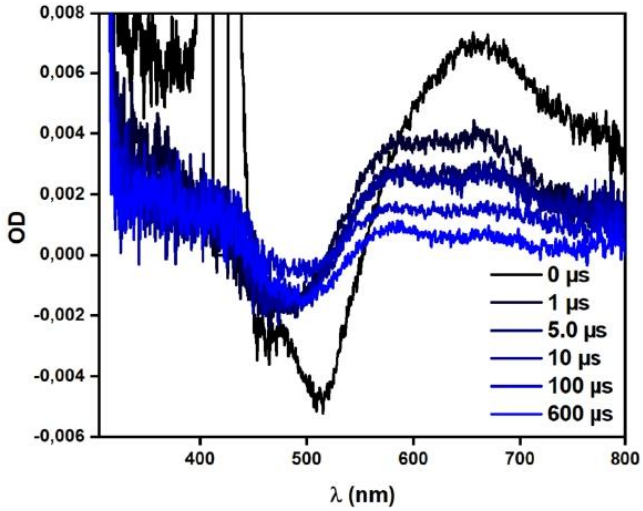

Figure S44. Temporal nanosecond transient absorption spectrum of DPPC:(14:0 PEG2000 PE):**[1]**$^{2+}$= 100:1:1 liposomes in phosphate buffer pH 7.0 with XTT (80 µM) at the bulk solution of liposome upon 420 nm pump excitation.

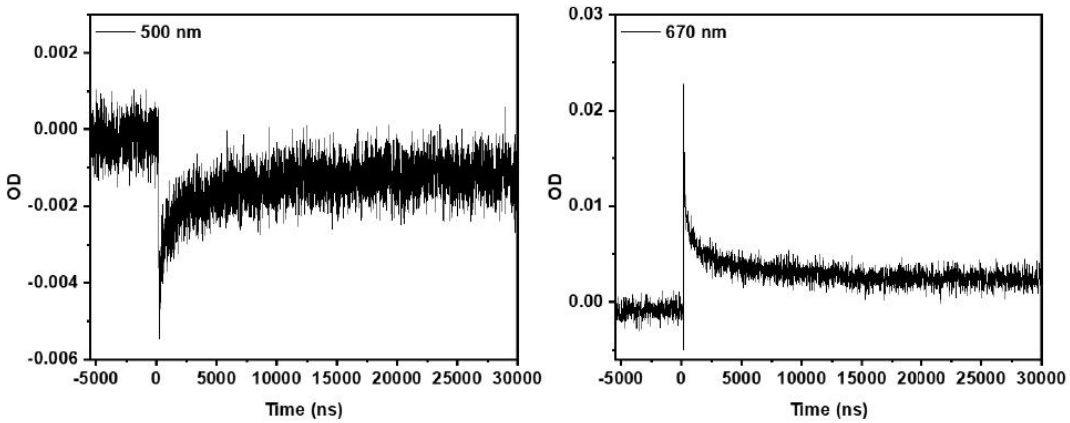

Figure S45. Time traces of the excited states of DPPC:(14:0 PEG2000 PE):**[1]**$^{2+}$= 100:1:1 liposomes in phosphate buffer pH 7.0 with XTT (80 μM) at the bulk solution of liposome at 500 nm and 670 nm.

Encapsulated NADH in the liposome and XTT at the bulk solution

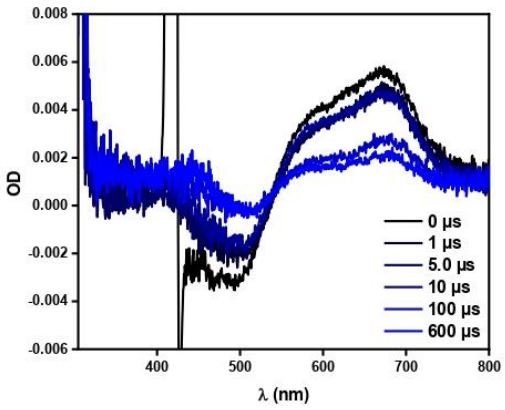

Figure S46.Temporal nanosecond transient absorption spectrum of encapsulated NADH (theoretical value of 22.5 mM) DPPC:(14:0 PEG2000 PE):**[1]**$^{2+}$= 100:1:1 liposomes in phosphate buffer pH 7.0 with XTT (80 μM) at the bulk solution of liposome upon 420 nm pump excitation.

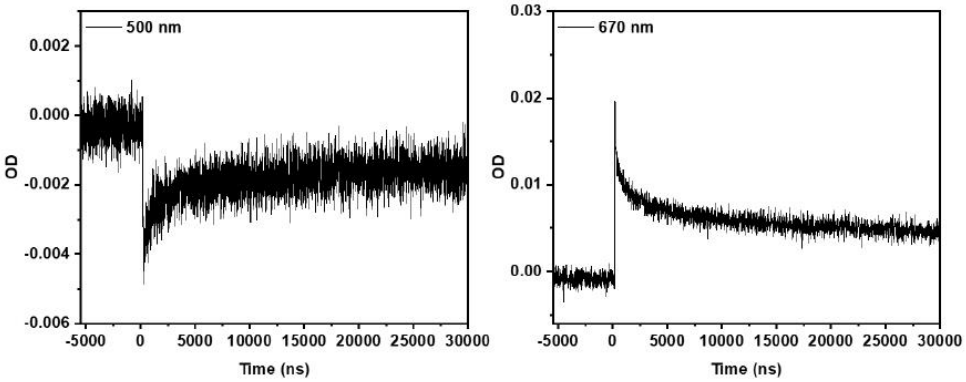

Figure S467. Time traces of the excited states of encapsulated NADH (theoretical value of 22.5 mM) DPPC:(14:0 PEG2000 PE):**[1]**$^{2+}$= 100:1:1 liposomes in phosphate buffer pH 7.0 with XTT (80 μM) at the bulk solution of liposome at 500 nm and 670 nm.

S13. Stern-Volmer quenching experiment

Liposomes were prepared as described in the methods section.

In cuvette:

V = 0.5 mL

[1]$^{2+}$= 10 μM

[DPPC] = 100 μM

[14:0 PEG2000 PE] = 1 μM

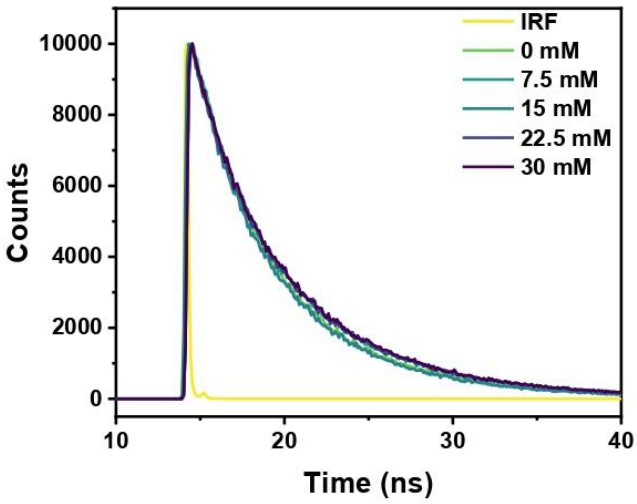

Figure S48. Kinetic traces of luminescence decay upon excitation at 450 nm with various concentrations of encapsulated NADH inside liposome as a quencher.

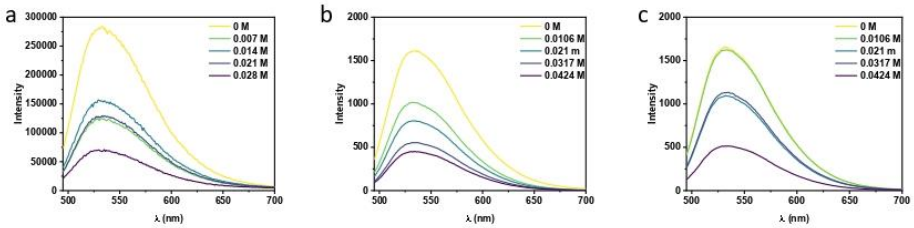

Figure S49. Luminescence quenching upon encapsulation of various concentrations of NADH inside liposome as a quencher (triplicates a, b, and c).

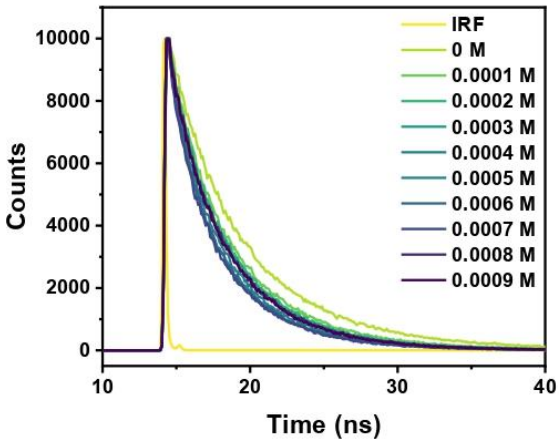

Figure S50. Kinetic traces of luminescence decay upon excitation at 450 nm with various concentrations of XTT as a quencher.

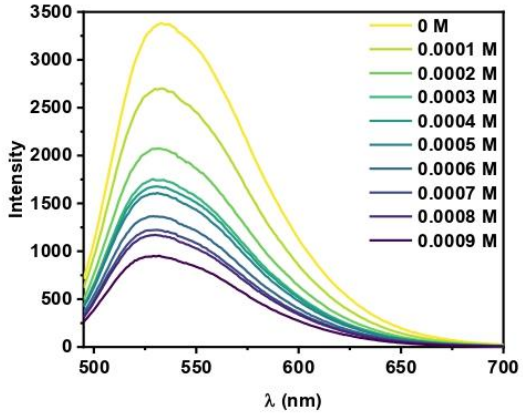

Figure S51. Luminescence quenching upon the addition of various concentrations of XTT as a quencher.

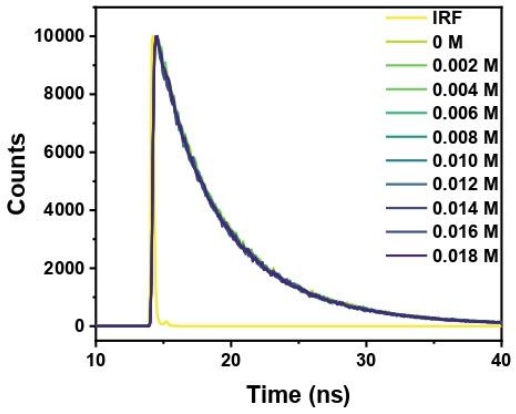

Figure S52. Kinetic traces of luminescence decay upon excitation at 450 nm with various concentrations of NADH as a quencher at the bulk.

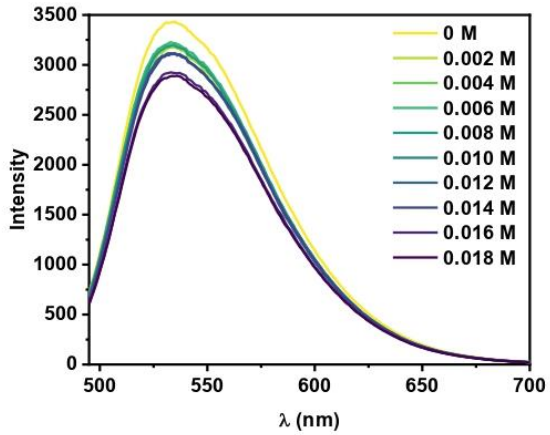

Figure S53. Luminescence quenching upon the addition of various concentrations of NADH as a quencher at the bulk.

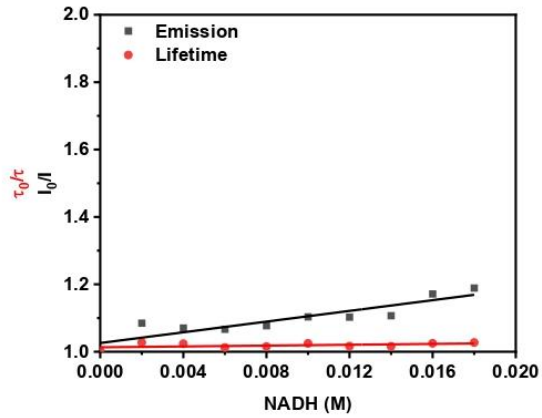

Figure. S54. SV-Plot from the quenching experiment with NADH located at the bulk solution.

S14. Proposed mechanism in the presence of oxygen, photooxidation or photoreduction

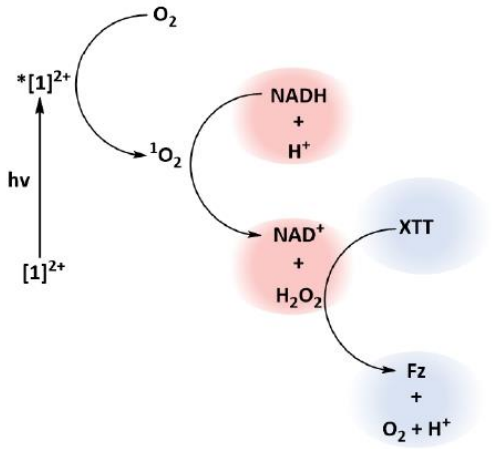

Figure. S55. Proposed mechanism in the presence of oxygen.

S15. Coordinates of $[1]^{2+}$

C	-0.47536	-1.15533	0.26542
C	-1.38655	-0.27254	-0.24406
C	0.91016	-0.86985	0.35754
C	1.45861	0.31269	-0.05600
C	0.54624	1.25715	-0.61697
C	-0.85606	0.96896	-0.70864
C	2.90614	0.58500	0.06655
N	0.86088	2.44842	-1.14024
H	-0.82224	-2.10816	0.64529
H	1.55187	-1.61885	0.80445
N	-1.54591	1.95383	-1.29695
C	-2.82849	-0.58881	-0.31490
S	-0.49723	3.09734	-1.67121
C	3.82969	-0.41352	-0.25370
C	5.17927	-0.17180	-0.10042
C	5.62786	1.06280	0.37112
C	4.72313	2.06427	0.69034
C	3.36877	1.81918	0.53271
H	3.48013	-1.36624	-0.63470
C	6.34203	-1.10380	-0.39003
H	5.06059	3.02444	1.06071
H	2.65515	2.59162	0.78459
C	7.51939	-0.22606	-0.00563
C	8.86388	-0.53094	-0.04787
C	9.80260	0.42682	0.34404
C	9.36077	1.68007	0.77522
C	8.01065	1.98917	0.82275
C	7.09050	1.02970	0.42947
H	9.19538	-1.50038	-0.40214
C	11.24964	0.11585	0.30721
H	10.08444	2.41742	1.09929
H	7.68893	2.96341	1.16930
C	6.39364	-1.48735	-1.87406
C	6.27779	-2.36415	0.48129
H	6.24150	-2.10475	1.54040
H	7.15444	-2.99125	0.30885
H	5.38895	-2.94923	0.23823
H	6.43941	-0.59877	-2.50544
H	5.50697	-2.06140	-2.14907
H	7.27229	-2.10206	-2.07796
C	12.17995	1.06466	-0.10171
C	13.53684	0.78278	-0.13280
C	13.98012	-0.46946	0.24878
C	13.07196	-1.43516	0.65732
C	11.72345	-1.14046	0.68465
H	11.84933	2.04386	-0.42178
H	14.21089	1.55616	-0.46398
N	15.43169	-0.81954	0.23720
H	13.39044	-2.42015	0.96777
H	11.03217	-1.89950	1.02603
C	16.29536	0.31212	-0.21764
C	15.86939	-1.19503	1.62268
H	17.32519	-0.03089	-0.19140
H	16.17351	1.15413	0.45676
H	16.02733	0.58591	-1.23326
H	15.67434	-0.35423	2.28212
H	16.93200	-1.41998	1.59523
H	15.31676	-2.06741	1.95341
C	15.66368	-1.97220	-0.69530
H	15.32844	-1.68155	-1.68683
H	15.10631	-2.83575	-0.34931
H	16.72667	-2.19738	-0.70239
C	-3.24484	-1.84762	-0.75634
C	-3.78694	0.34823	0.07986
C	-5.12389	0.01457	0.03367
C	-5.52782	-1.24649	-0.41002
C	-4.58848	-2.18484	-0.80803
H	-3.47473	1.32432	0.42889
C	-6.31813	0.86970	0.41632
C	-6.98998	-1.30714	-0.35498
H	-2.50230	-2.56648	-1.07960
H	-4.88962	-3.16346	-1.16090
C	-7.46239	-0.08499	0.12826
C	-8.81583	0.13162	0.28137
C	-9.72002	-0.87849	-0.05587
C	-9.23543	-2.09571	-0.54066
C	-7.87578	-2.31956	-0.69049
H	-9.18152	1.08707	0.63977
C	-11.17590	-0.65852	0.09843
H	-9.93285	-2.88727	-0.78488
H	-7.52041	-3.27374	-1.05934
C	-11.68604	0.02265	1.19786
C	-13.04677	0.24092	1.34762
C	-13.92018	-0.22800	0.38446
C	-13.43659	-0.91225	-0.72107
C	-12.07898	-1.12301	-0.85739
H	-11.71834	-1.64141	-1.73587
H	-11.01764	0.38079	1.96967
H	-13.38578	0.77000	2.22373
N	-15.39273	-0.00673	0.49340
H	-14.09598	-1.28173	-1.49355
C	-15.77825	0.70242	1.75090
C	-16.10768	-1.32571	0.48036
H	-15.31401	1.68332	1.77008
H	-15.47169	0.10975	2.60738
H	-16.85849	0.81091	1.74755
H	-15.74193	-1.92125	1.31180
H	-15.91606	-1.83318	-0.45841
H	-17.17237	-1.13640	0.58573
C	-15.85789	0.82901	-0.66280
H	-15.32212	1.77370	-0.63816
H	-16.92685	0.99282	-0.55710
H	-15.65395	0.30595	-1.59082
C	-6.40501	2.12552	-0.45988
C	-6.27586	1.25950	1.89882
H	-6.21394	0.37423	2.53349
H	-7.17325	1.81808	2.17119
H	-5.40885	1.89096	2.10109
H	-6.43806	1.86130	-1.51791
H	-5.53779	2.76658	-0.29127
H	-7.30257	2.69767	-0.21802

References

(1) M. J.Frisch, G. W.Trucks, H. B.Schlegel, G. E.Scuseria, M. A.Robb, J. R.Cheeseman, G.Scalmani, V.Barone, G. A.Petersson, H.Nakatsuji, X.Li, M.Caricato, A. V.Marenich, J.Bloino, B. G.Janesko, R.Gomperts, B.Mennucci, H. P.Hratchian, J. V.Ortiz, A. F.Izmaylov, J. L.Sonnenberg, F. DingWilliams, F.Lipparini, F.Egidi, J.Goings, B.Peng, A.Petrone, T.Henderson, D.Ranasinghe, V. G.Zakrzewski, J.Gao, N.Rega, G.Zheng, W.Liang, M.Hada, M.Ehara, K.Toyota, R.Fukuda, J.Hasegawa, M.Ishida, T.Nakajima, Y.Honda, O.Kitao, H.Nakai, T.Vreven, K.Throssell, J. A.Montgomery Jr., J. E.Peralta, F.Ogliaro, M. J.Bearpark, J. J.Heyd, E. N.Brothers, K. N.Kudin, V. N.Staroverov, T. A.Keith, R.Kobayashi, J.Normand, K.Raghavachari, A. P.Rendell, J. C.Burant, S. S.Iyengar, J.Tomasi, M.Cossi, J. M.Millam, M.Klene, C.Adamo, R.Cammi, J. W.Ochterski, R. L.Martin, K.Morokuma, O.Farkas, J. B.Foresman and D. J.Fox, Gaussian 16, Revision C.01, Gaussian, Inc., Wallingford, CT, 2016. *Citation | Gaussian.com*. https://gaussian.com/citation/ (accessed 2023-12-12).

(2) Perdew, J. P. Density-Functional Approximation for the Correlation Energy of the Inhomogeneous Electron Gas. *Phys. Rev. B* **1986**, *33* (12), 8822–8824. https://doi.org/10.1103/PhysRevB.33.8822.

(3) Lee, C.; Yang, W.; Parr, R. G. Development of the Colle-Salvetti Correlation-Energy Formula into a Functional of the Electron Density. *Phys. Rev. B* **1988**, *37* (2), 785–789. https://doi.org/10.1103/PhysRevB.37.785.

(4) Becke, A. D. Density-functional Thermochemistry. III. The Role of Exact Exchange. *The Journal of Chemical Physics* **1993**, *98* (7), 5648–5652. https://doi.org/10.1063/1.464913.

(5) Adamo, C.; Barone, V. Toward Reliable Density Functional Methods without Adjustable Parameters: The PBE0 Model. *The Journal of Chemical Physics* **1999**, *110* (13), 6158–6170. https://doi.org/10.1063/1.478522.

(6) Perdew, J. P.; Burke, K.; Ernzerhof, M. Generalized Gradient Approximation Made Simple [Phys. Rev. Lett. 77, 3865 (1996)]. *Phys. Rev. Lett.* **1997**, *78* (7), 1396–1396. https://doi.org/10.1103/PhysRevLett.78.1396.

(7) Perdew, J. P.; Burke, K.; Ernzerhof, M. Generalized Gradient Approximation Made Simple. *Phys. Rev. Lett.* **1996**, *77* (18), 3865–3868. https://doi.org/10.1103/PhysRevLett.77.3865.

(8) Yanai, T.; Tew, D. P.; Handy, N. C. A New Hybrid Exchange–Correlation Functional Using the Coulomb-Attenuating Method (CAM-B3LYP). *Chemical Physics Letters* **2004**, *393* (1), 51–57. https://doi.org/10.1016/j.cplett.2004.06.011.

(9) Vydrov, O. A.; Scuseria, G. E. Assessment of a Long-Range Corrected Hybrid Functional. *The Journal of Chemical Physics* **2006**, *125* (23), 234109. https://doi.org/10.1063/1.2409292.

(10) Vreven, T.; Frisch, M. J.; Kudin, K. N.; Schlegel, H. B.; Morokuma, K. Geometry Optimization with QM/MM Methods II: Explicit Quadratic Coupling. *Molecular Physics* **2006**, *104* (5–7), 701–714. https://doi.org/10.1080/00268970500417846.

(11) Vydrov, O. A.; Scuseria, G. E.; Perdew, J. P. Tests of Functionals for Systems with Fractional Electron Number. *The Journal of Chemical Physics* **2007**, *126* (15), 154109. https://doi.org/10.1063/1.2723119.

(12) *Can short-range hybrids describe long-range-dependent properties? | The Journal of Chemical Physics | AIP Publishing*. https://pubs.aip.org/aip/jcp/article/131/4/044108/838663/Can-short-range-hybrids-describe-long-range (accessed 2024-05-14).

(13) Chai, J.-D.; Head-Gordon, M. Long-Range Corrected Hybrid Density Functionals with Damped Atom–Atom Dispersion Corrections. *Phys. Chem. Chem. Phys.* **2008**, *10* (44), 6615–6620. https://doi.org/10.1039/B810189B.

(14) Grimme, S.; Ehrlich, S.; Goerigk, L. Effect of the Damping Function in Dispersion Corrected Density Functional Theory. *Journal of Computational Chemistry* **2011**, *32* (7), 1456–1465. https://doi.org/10.1002/jcc.21759.

(15) Weigend, F. Accurate Coulomb-Fitting Basis Sets for H to Rn. *Phys. Chem. Chem. Phys.* **2006**, *8* (9), 1057–1065. https://doi.org/10.1039/B515623H.

(16) Weigend, F.; Ahlrichs, R. Balanced Basis Sets of Split Valence, Triple Zeta Valence and Quadruple Zeta Valence Quality for H to Rn: Design and Assessment of Accuracy. *Phys. Chem. Chem. Phys.* **2005**, *7* (18), 3297–3305. https://doi.org/10.1039/B508541A.
(17) Cossi, M.; Rega, N.; Scalmani, G.; Barone, V. Energies, Structures, and Electronic Properties of Molecules in Solution with the C-PCM Solvation Model. *Journal of Computational Chemistry* **2003**, *24* (6), 669–681. https://doi.org/10.1002/jcc.10189.
(18) Barone, V.; Cossi, M. Quantum Calculation of Molecular Energies and Energy Gradients in Solution by a Conductor Solvent Model. *J. Phys. Chem. A* **1998**, *102* (11), 1995–2001. https://doi.org/10.1021/jp9716997.
(19) Jacquemin, D.; Mennucci, B.; Adamo, C. Excited-State Calculations with TD-DFT: From Benchmarks to Simulations in Complex Environments. *Phys. Chem. Chem. Phys.* **2011**, *13* (38), 16987–16998. https://doi.org/10.1039/C1CP22144B.
(20) Jacquemin, D.; Wathelet, V.; Perpète, E. A.; Adamo, C. Extensive TD-DFT Benchmark: Singlet-Excited States of Organic Molecules. *J. Chem. Theory Comput.* **2009**, *5* (9), 2420–2435. https://doi.org/10.1021/ct900298e.
(21) Mai, S.; Avagliano, D.; Heindl, M.; Marquetand, P.; Menger, M. F. S. J.; Oppel, M.; Plasser, F.; Polonius, S.; Ruckenbauer, M.; Shu, Y.; Truhlar, D. G.; Zhang, L.; Zobel, P.; González, L. SHARC3.0: Surface Hopping Including Arbitrary Couplings – Program Package for Non-Adiabatic Dynamics, 2023. https://doi.org/10.5281/zenodo.7828641.
(22) Koopmans, T. Über Die Zuordnung von Wellenfunktionen Und Eigenwerten Zu Den Einzelnen Elektronen Eines Atoms. *Physica* **1934**, *1* (1), 104–113. https://doi.org/10.1016/S0031-8914(34)90011-2.
(23) Kasha, M. Characterization of Electronic Transitions in Complex Molecules. *Discuss. Faraday Soc.* **1950**, *9* (0), 14–19. https://doi.org/10.1039/DF9500900014.
(24) Alcoba, D. R.; Lain, L.; Torre, A.; Oña, O. B.; Tiznado, W. Ground and Excited State Similarity Studies by Means of Fukui and Dual-Descriptor Matrices. *Chemical Physics Letters* **2012**, *549*, 103–107. https://doi.org/10.1016/j.cplett.2012.08.030.
(25) *Jmol: an open-source Java viewer for chemical structures in 3D*. https://jmol.sourceforge.net/ (accessed 2023-12-12).
(26) Plasser, F. TheoDORE: A Toolbox for a Detailed and Automated Analysis of Electronic Excited State Computations. *The Journal of Chemical Physics* **2020**, *152* (8), 084108. https://doi.org/10.1063/1.5143076.
(27) Sinambela, N.; Jacobi, R.; Hernández-Castillo, D.; Hofmeister, E.; Hagmeyer, N.; Dietzek, B.; González, L.; Pannwitz, A. Alignment and Photooxidation Dynamics of a Perylene Diimide Chromophore in Lipid Bilayers. *Mol. Syst. Des. Eng.* **2023**, 10.1039.D2ME00243D. https://doi.org/10.1039/D2ME00243D.
(28) Jo, S.; Kim, T.; Iyer, V. G.; Im, W. CHARMM-GUI: A Web-Based Graphical User Interface for CHARMM. *Journal of Computational Chemistry* **2008**, *29* (11), 1859–1865. https://doi.org/10.1002/jcc.20945.
(29) D.A. Case, H.M. Aktulga, K. Belfon, I.Y. Ben-Shalom, J.T. Berryman, S.R. Brozell, D.S. Cerutti, T.E. Cheatham, III, G.A. Cisneros, V.W.D. Cruzeiro, T.A. Darden, N. Forouzesh, G. Giambaşu, T. Giese, M.K. Gilson, H. Gohlke, A.W. Goetz, J. Harris, S. Izadi, S.A. Izmailov, K. Kasavajhala, M.C. Kaymak, E. King, A. Kovalenko, T. Kurtzman, T.S. Lee, P. Li, C. Lin, J. Liu, T. Luchko, R. Luo, M. Machado, V. Man, M. Manathunga, K.M. Merz, Y. Miao, O. Mikhailovskii, G. Monard, H. Nguyen, K.A. O'Hearn, A. Onufriev, F. Pan, S. Pantano, R. Qi, A. Rahnamoun, D.R. Roe, A. Roitberg, C. Sagui, S. Schott-Verdugo, A. Shajan, J. Shen, C.L. Simmerling, N.R. Skrynnikov, J. Smith, J. Swails, R.C. Walker, J. Wang, J. Wang, H. Wei, X. Wu, Y. Wu, Y. Xiong, Y. Xue, D.M. York, S. Zhao, Q. Zhu, and P.A. Kollman (2022), Amber 2022, University of California, San Francisco. Amber.

(30) Dickson, C. J.; Walker, R. C.; Gould, I. R. Lipid21: Complex Lipid Membrane Simulations with AMBER. *J. Chem. Theory Comput.* **2022**, *18* (3), 1726–1736. https://doi.org/10.1021/acs.jctc.1c01217.
(31) Izadi, S.; Anandakrishnan, R.; Onufriev, A. V. Building Water Models: A Different Approach. *J. Phys. Chem. Lett.* **2014**, *5* (21), 3863–3871. https://doi.org/10.1021/jz501780a.
(32) Ryckaert, J.-P.; Ciccotti, G.; Berendsen, H. J. C. Numerical Integration of the Cartesian Equations of Motion of a System with Constraints: Molecular Dynamics of n-Alkanes. *Journal of Computational Physics* **1977**, *23* (3), 327–341. https://doi.org/10.1016/0021-9991(77)90098-5.
(33) Berendsen, H. J. C.; Postma, J. P. M.; van Gunsteren, W. F.; DiNola, A.; Haak, J. R. Molecular Dynamics with Coupling to an External Bath. *The Journal of Chemical Physics* **1984**, *81* (8), 3684–3690. https://doi.org/10.1063/1.448118.
(34) Götz, A. W.; Williamson, M. J.; Xu, D.; Poole, D.; Le Grand, S.; Walker, R. C. Routine Microsecond Molecular Dynamics Simulations with AMBER on GPUs. 1. Generalized Born. *J. Chem. Theory Comput.* **2012**, *8* (5), 1542–1555. https://doi.org/10.1021/ct200909j.
(35) Salomon-Ferrer, R.; Götz, A. W.; Poole, D.; Le Grand, S.; Walker, R. C. Routine Microsecond Molecular Dynamics Simulations with AMBER on GPUs. 2. Explicit Solvent Particle Mesh Ewald. *J. Chem. Theory Comput.* **2013**, *9* (9), 3878–3888. https://doi.org/10.1021/ct400314y.
(36) Le Grand, S.; Götz, A. W.; Walker, R. C. SPFP: Speed without Compromise—A Mixed Precision Model for GPU Accelerated Molecular Dynamics Simulations. *Computer Physics Communications* **2013**, *184* (2), 374–380. https://doi.org/10.1016/j.cpc.2012.09.022.
(37) Humphrey, W.; Dalke, A.; Schulten, K. VMD: Visual Molecular Dynamics. *Journal of Molecular Graphics* **1996**, *14* (1), 33–38. https://doi.org/10.1016/0263-7855(96)00018-5.
(38) Dutta, S.; Watson, B.; Mattoo, S.; Rochet, J.-C. Calcein Release Assay to Measure Membrane Permeabilization by Recombinant Alpha-Synuclein. *BIO-PROTOCOL* **2020**, *10* (14). https://doi.org/10.21769/BioProtoc.3690.
(39) Maherani, B.; Arab-Tehrany, E.; Kheirolomoom, A.; Geny, D.; Linder, M. Calcein Release Behavior from Liposomal Bilayer; Influence of Physicochemical/Mechanical/Structural Properties of Lipids. *Biochimie* **2013**, *95* (11), 2018–2033. https://doi.org/10.1016/j.biochi.2013.07.006.
(40) Pavlishchuk, V. V.; Addison, A. W. Conversion Constants for Redox Potentials Measured versus Different Reference Electrodes in Acetonitrile Solutions at 25°C. *Inorganica Chimica Acta* **2000**, *298* (1), 97–102. https://doi.org/10.1016/S0020-1693(99)00407-7.
(41) Ishiki, K.; Nguyen, D. Q.; Morishita, A.; Shiigi, H.; Nagaoka, T. Electrochemical Detection of Viable Bacterial Cells Using a Tetrazolium Salt. *Anal. Chem.* **2018**, *90* (18), 10903–10909. https://doi.org/10.1021/acs.analchem.8b02404.
(42) Smith, T. J.; Stevenson, K. J. 4 - Reference Electrodes. In *Handbook of Electrochemistry*; Zoski, C. G., Ed.; Elsevier: Amsterdam, 2007; pp 73–110. https://doi.org/10.1016/B978-044451958-0.50005-7.
(43) Lin, K.-C.; Chen, S.-M. Reversible Cyclic Voltammetry of the NADH/NAD+ Redox System on Hybrid Poly(Luminol)/FAD Film Modified Electrodes. *Journal of Electroanalytical Chemistry* **2006**, *589* (1), 52–59. https://doi.org/10.1016/j.jelechem.2006.01.010.
(44) Tschierlei, S.; Karnahl, M.; Presselt, M.; Dietzek, B.; Guthmuller, J.; González, L.; Schmitt, M.; Rau, S.; Popp, J. Photochemisches Schicksal: Der Erste Schritt Bestimmt Die Effizienz Der H2-Bildung Mit Einem Supramolekularen Photokatalysator. *Angewandte Chemie* **2010**, *122* (23), 4073–4076. https://doi.org/10.1002/ange.200906595.
(45) Sutherland, M. W.; Learmonth, B. A. The Tetrazolium Dyes MTS and XTT Provide New Quantitative Assays for Superoxide and Superoxide Dismutase. *Free Radical Research* **1997**, *27* (3), 283–289. https://doi.org/10.3109/10715769709065766.

Chapter 5

Recent Advances in Light Energy Conversion with Biomimetic Vesicle Membranes

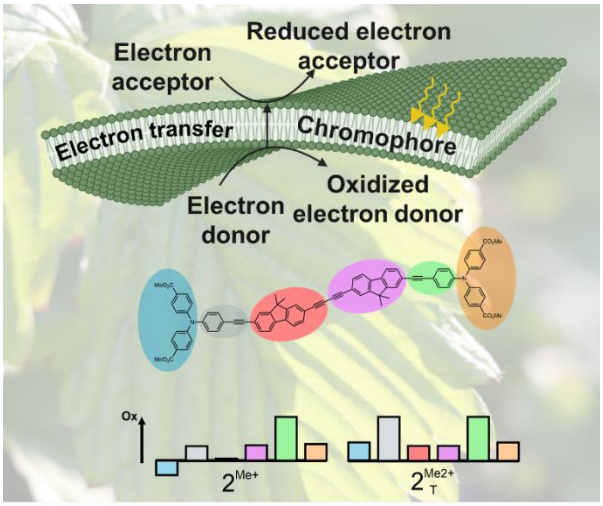

The triarylamines are presented as the charge conduits through a lipid bilayer membrane. Bridged bis(triarylamines) (BTAA) were prepared and studied its redox properties. The cation and dication species were characterized with UV-Vis/NIR and spectroelectrochemistry and showed an intermediate species characteristic for the formation of a first mixed-valent radical, followed by the dication formations. The photo-driven electron transfer with BTAA was tested with the combination of oxidation and reduction reactions in the liposome membrane system. The BTAAs showed an active photo-driven redox reaction by a membrane-mediated mechanism.

Author contributions:
Novitasari Sinambela: Performed the membrane integration, luminescence quenching experiments, confocal imaging measurement, electron transfer experiments, molecular dynamics simulations, paper writing, and manuscript revision.
Moritz Nau: Performed the spectroscopic characterization, cyclic voltammetry (including the simulations), spectroelectrochemistry measurements with data analysis, and all (TD-)DFT calculations on the model compounds, paper writing, and manuscript revision.
Gernot Haug: Conducted most of the chemical syntheses.
Michael Linseis + Rainer F. Winter: Supervision of Moritz Nau.
Philip Koblischek: Conducted one of the chemical syntheses.
Rainer F. Winter + Andrea Pannwitz: Design of the study, paper writing, and manuscript revision.

This chapter has been submitted as a full paper: Novitasari Sinambela,[+] Moritz Nau,[+] Gernot Haug, Michael Linseis, Philip Koblischek, Rainer F. Winter,* and Andrea Pannwitz,* Light-Driven Electron Transfer in a Lipid Bilayer with Mixed Valence Molecular Wires, Sustainable Energy & Fuels, **2025**, 9, 2302-2315. 5. DOI: 10.1039/D4SE01752H. This article is licensed under CC BY 3.0 (https://creativecommons.org/licenses/by/3.0).

Sustainable Energy & Fuels

ROYAL SOCIETY OF CHEMISTRY

PAPER

View Article Online
View Journal | View Issue

Check for updates

Cite this: *Sustainable Energy Fuels*, 2025, **9**, 2302

Light-driven electron transfer in a lipid bilayer with mixed valence molecular wires†

Novitasari Sinambela, ‡[a] Moritz Nau,‡[b] Gernot Haug,[b] Michael Linseis,[b] Philip Koblischek,[a] Rainer F. Winter *[b] and Andrea Pannwitz *[acde]

Received 15th December 2024
Accepted 17th February 2025

DOI: 10.1039/d4se01752h

rsc.li/sustainable-energy

Triarylamines (TAAs) are one of the most important classes of redox-active organic compounds, which are readily available from modular synthesis, thereby offering the possibility to easily adjust their intrinsic redox potentials. We present herein two bis(triarylamines) (BTAAs) with π-extended 2,7-diethynylfluorene or 2,2′-(1,3-butadiyne-1,4-diyl)-bis(7-ethynylfluorene) bridges and two benzoic acid headgroups per TAA and their (formally) mixed-valent radical cations. Owing to their amphiphilic character and favorable redox properties, these BTAAs are designed to serve as charge conduits through membranes. The lipid bilayer/BTAA systems are water-soluble, which allowed us to explore their photoactivity in aqueous solution and utilize their mixed valent form for membrane-mediated photoinduced electron transfer. Our findings will be relevant for constructing artificial nanoreactors for solar light energy conversion and light-driven redox chemistry in water.

Open Access Article. Published on 18 February 2025. Downloaded on 5/22/2025 3:43:42 PM.
This article is licensed under a Creative Commons Attribution 3.0 Unported Licence.

Introduction

Light-driven long-range electron transfer is relevant for solar energy conversion in the natural photosynthesis of plants and photosynthetic bacteria, where photons drive the movement of electrons across biological membranes. Nature uses sophisticated assemblies of transmembrane protein complexes such as photosystem I and II (PSI and PSII) to convert $NADP^+$ into NADPH on one side of the membrane and water into O_2 on the other side of the membrane, as shown in Fig. 1. Previous artificial systems attempting to mimic light-driven transmembrane electron transfer across lipid bilayers employed embedded photosensitizers,[1,2] along with electron carriers, to transfer electrons across membranes *via* diffusion of the photoreduced electron carrier.[3–5] Additionally, there are some studies of light-driven transmembrane electron transfer using either sophisticated and synthetically challenging supramolecular barrels[1] or rigid oligoaromatic molecular wires with varying levels of synthetic complexity.[2,6] In the present study, we explore the concept of mixed valency, *i.e.* electron delocalization over two covalently connected redox centers,[7] in a π-extended molecular wire for transmembrane electron transfer in lipid bilayers. These are multielectron processes that resemble the complexity of multielectron transfer in the photosynthesis system, which later on can be a future model for performing water-splitting and CO_2 reduction.

Triarylamines (TAAs) are one of the most important classes of redox-active organic compounds. One of their key advantages is their ready accessibility *via* modular synthesis, thereby offering the opportunity to attach one aryl substituent at a time and to generate derivatives with two or three different aryl substituents. This allows fine-tuning of their intrinsic redox potentials[8–10] and the deliberate introduction of a broad range of chemical functionalities, *e.g.* for the construction of hybrids with two or more chemically different redox-active constituents[11–21] or for rendering them water soluble.[22–25] Once protected by substituents to prevent oxidatively induced coupling to benzidines[26–29] or cyclization to carbazoles,[30] one-electron oxidized triarylaminium ions are rather stable, even towards water and air.[9,22,31] Bridged bis(triarylamines) (BTAAs), Ar^1Ar^2N-arylene-NAr^1Ar^2, typically undergo two or even more redox processes. Their associated mixed-valent radical cations generated by one-electron oxidation, *i.e.* the removal of an electron from only one of the available redox sites, are outstanding testbeds for probing the effects of the length, the chemical constitution and the conformation of the intervening π-conjugated (poly)arylene bridge and the chemical environment (solvent and counterions)[11,32–35] on the extent of electronic coupling between the terminally appended redox sites.[36–42]

[a]*Institute of Inorganic Chemistry I, Ulm University, Albert-Einstein-Allee 11, 89081 Ulm, Germany*

[b]*Department of Chemistry, University of Konstanz, Universitätsstraße 10, 78464 Konstanz, Germany. E-mail: rainer.winter@uni-konstanz.de*

[c]*Department of Inorganic and Analytical Chemistry, Friedrich Schiller Universität Jena, Humboldtstr. 8, 07743 Jena, Germany. E-mail: andrea.pannwitz@uni-jena.de*

[d]*Center for Energy and Environmental Chemistry Jena (CEEC), Friedrich-Schiller-Universität Jena, Philosophenweg 7a, 07743 Jena, Germany*

[e]*Helmholtz Institute for Polymers in Energy Applications Jena (HIPOLE Jena), Lessingstraße 12–14, 07743 Jena, Germany*

† Electronic supplementary information (ESI) available: Additional references. See DOI: https://doi.org/10.1039/d4se01752h

‡ These authors contributed equally.

This journal is © The Royal Society of Chemistry 2025

Open Access Article. Published on 18 February 2025. Downloaded on 5/22/2025 3:43:42 PM.
This article is licensed under a Creative Commons Attribution 3.0 Unported Licence.

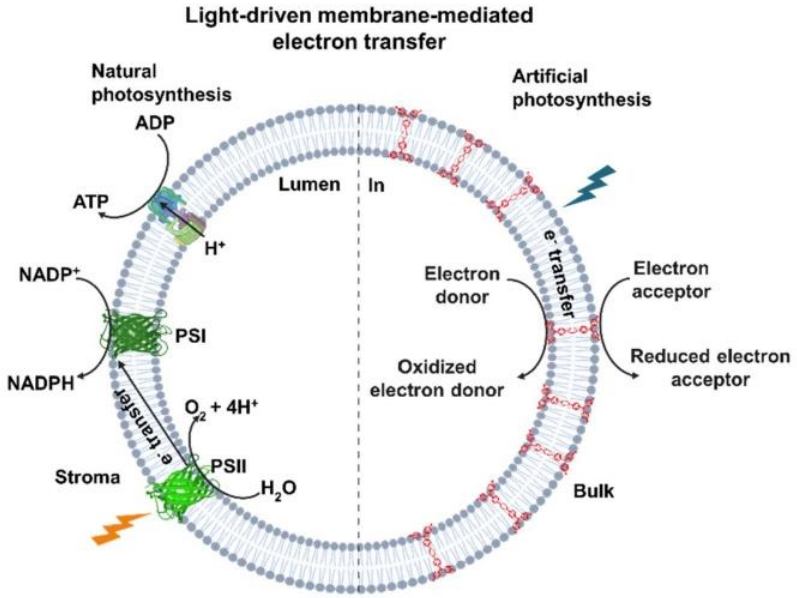

Fig. 1 Comparison of natural and artificial photosynthesis pathways. NADPH = nicotinamide adenine dinucleotide diphosphate, $NADP^+$ = nicotinamide adenine dinucleotide phosphate, PSII = photosystem II, PSI = photosystem I, ATP = adenosine triphosphate, ADP = adenosine diphosphate, and e^- = electron.

Their proven ability to facilitate efficient through-bond charge delocalization over long distances[40,43–46] has also made them attractive for applications as single molecule wires in metal–molecule–metal nanojunctions. Recent studies on anchor group-modified bis(diarylamine)-capped oligophenylenes even revealed negative values of the attenuation factor β up to the terphenylene limit, implying that the electron transfer rate increases with increasing molecular length.[47] The advantageous properties of BTAAs, *i.e.* their redox activity, modularity, and abundance, thus prompted us to utilize them as charge conduits through membranes. We here convey the results of our work on using BTAAs with polar head groups for this purpose.

Results and discussion

Design and synthesis

The molecular wires designed here have hydrophobic cores based on fluorene and alkyne units bridging the BTAA redox centers, which are functionalized with carboxylic acids or esters. The carboxylic acids serve as hydrophilic head groups to anchor the molecular wire on both sides of the lipid bilayer so that they span across the lipid bilayer (Fig. 2a).

Fig. 2b summarizes the synthesis and chemical structures of the target BTAAs. Our synthetic routes afford the methyl esters of the envisioned tetracarboxylic acids and involve cascades of different C–N and C–C cross-coupling reactions, including a Glaser–Hey–Eglinton coupling in the case of $\mathbf{2}^{\mathbf{Me}}$.[48] Ester cleavage subsequently provided free tetracarboxylic acids. Detailed synthetic protocols and methods are provided in the ESI (Schemes S1 and S2†), along with ^{1}H, ^{13}C{^{1}H}, mass spectra, and the absorption spectra and molar extinction coefficients ε of the target BTAAs (ESI, Fig. S16 and S17†). The molecular design with two polar benzoic acid headgroups at each terminus and nonpolar aliphatic hexyl tails at the core segments was conceived to mimic classical lipid bilayer properties. The carboxylic functionalities render BTAAs $\mathbf{1}^{\mathbf{H}}$ and $\mathbf{2}^{\mathbf{H}}$ slightly soluble in aqueous media.

Electrochemistry and spectroscopy

The intended utilization of BTAAs $\mathbf{1}^{\mathbf{H}}$ and $\mathbf{2}^{\mathbf{H}}$ as transmembrane redox mediators puts their redox properties into focus. However, voltammetric characterization of free acids $\mathbf{1}^{\mathbf{H}}$ and $\mathbf{2}^{\mathbf{H}}$ was hindered by the limited solubility of the protonated $\mathbf{1}^{\mathbf{H}}$ and $\mathbf{2}^{\mathbf{H}}$ in aqueous media, while an increase in pH led to poorly reproducible voltammograms with ill-defined redox waves at Pt, Au and glassy carbon electrodes. We therefore resorted to esters $\mathbf{1}^{\mathbf{Me}}$ and $\mathbf{2}^{\mathbf{Me}}$ in the CH_2Cl_2/NBu_4^+ $[BAr^{F24}]^-$ (0.1 M) electrolyte. Fig. 3 displays cyclic voltammograms of $\mathbf{1}^{\mathbf{Me}}$ (panel A) and $\mathbf{2}^{\mathbf{Me}}$ (panel B). The very weakly coordinating $[BAr^{F24}]^-$ anion ($[BAr^{F24}]^- = [B\{C_6H_3(CF_3)_2\text{-}3,5\}_4]^-$) is known for maximizing electrostatic repulsion, thereby maximizing the redox splitting $\Delta E_{1/2}$ between the individual redox couples and hence increasing the thermodynamic stability of the intermediate, mixed-valent radical cation with respect to disproportionation.[49–51] The expected two oxidations of the TAA constituents nevertheless merge into a single composite wave with (average) half-wave potentials of $E_{1/2}(\mathbf{1}^{\mathbf{Me}}) = 675$ mV and $E_{1/2}(\mathbf{2}^{\mathbf{Me}}) = 670$ mV on the ferrocene/ferrocenium scale. Only in the case of the shorter $\mathbf{1}^{\mathbf{Me}}$ can a small splitting into two separate waves be discerned. Computational simulation of the experimental voltammograms yielded a redox splitting of 80 mV in the case of $\mathbf{1}^{\mathbf{Me}}$ and an even smaller value of only 45 mV for

Open Access Article. Published on 18 February 2025. Downloaded on 5/22/2025 3:43:42 PM. This article is licensed under a Creative Commons Attribution 3.0 Unported Licence.

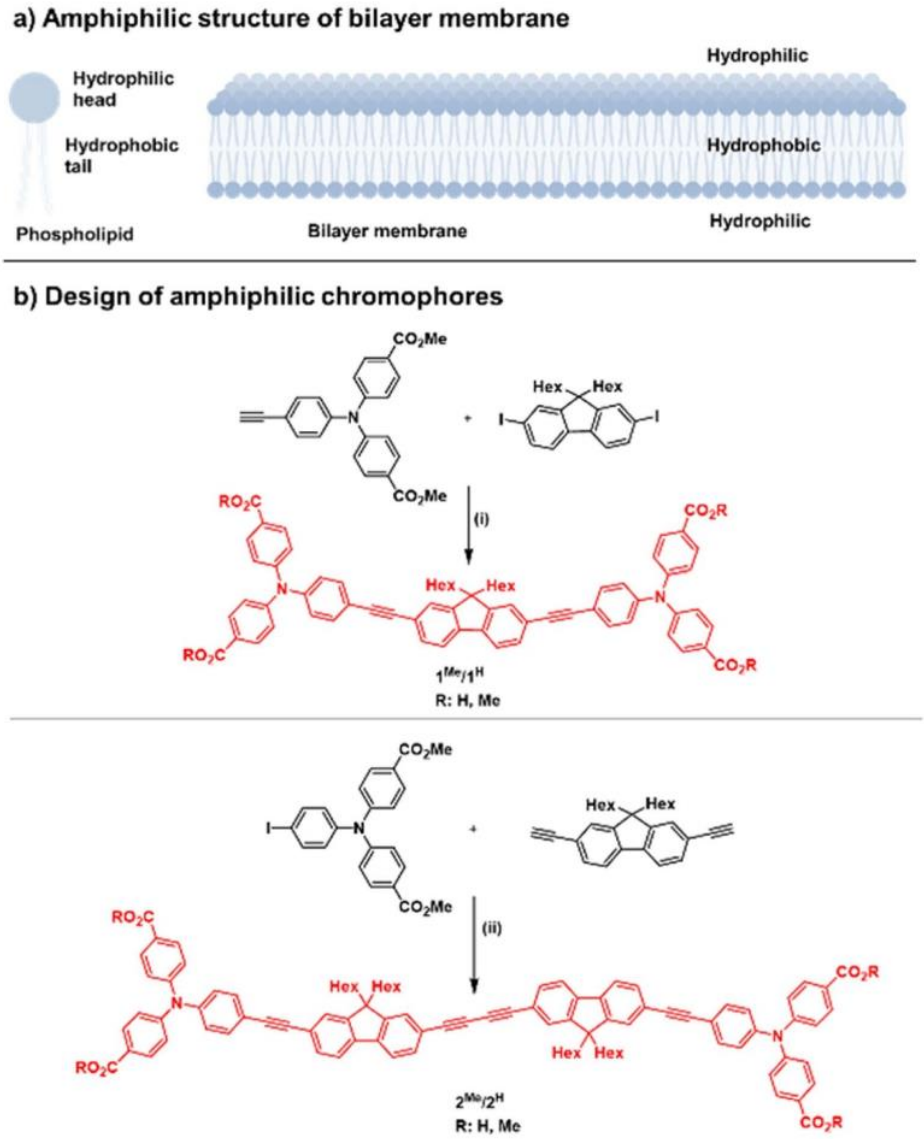

Fig. 2 (a) The structure of a bilayer membrane, built from an amphiphilic phospholipid. (b) Chemical structures and schematic syntheses of target bis(triarylamine) tetracarboxylic acids/methyl esters $\mathbf{1}^{H/Me}$ and $\mathbf{2}^{H/Me}$. (i) $PdCl_2(PPh_3)_2$, NEt_3, CuI, THF, 70 °C, and overnight; $\mathbf{1}^{Me} \rightarrow \mathbf{1}^{H}$: THF/$H_2O$ (2 : 1), LiOH, r.t., and overnight; (ii) $PdCl_2(PPh_3)_2$, NEt_3, CuI, THF, 70 °C, and two days; $\mathbf{2}^{Me} \rightarrow \mathbf{2}^{H}$: THF/$H_2O$ (2 : 1), LiOH, r.t., and overnight.

$\mathbf{2}^{Me}$ with roughly twice the spacer length. Simulated cyclic voltammograms are shown as blue circles in panels A ($\mathbf{1}^{Me}$) and B ($\mathbf{2}^{Me}$) of Fig. 3, superimposed with the experimental data. Details of the used software and the fitting procedures are given in the ESI,† and the parameters obtained by the simulations are provided in Table S4 of the ESI.† The half-wave potential splitting of **2** is barely larger than the statistical contribution of 2 $\ln(2RT/F) = 36$ mV to the free energy change for the stepwise oxidations of two non-interacting redox sites.[52] Similar small half-wave potential separations were also reported for other BTAAs with large spatial extensions of the connecting linker (Table 1).[39,44,53–55]

The close proximity of the two redox waves makes it difficult to access and spectroscopically characterize and discriminate between the one- and two-electron-oxidized radical cations and dications as individual species, which is important in order to elucidate the effective oxidation state when using the present BTAAs as transmembrane redox mediators.

The half-wave potentials of $\mathbf{1}^{Me}$ and $\mathbf{2}^{Me}$ are appreciably more positive than that of the triarylamine-derived mono- and dicarboxylic acids $(4\text{-MeO-}C_6H_4)_2N(C_6H_4\text{-COOH-}4)$ ($E_{1/2} = 170$ mV) and $(4\text{-MeOC}_6H_4)_2N(C_6H_3(COOH)_2\text{-}3,5)$ ($E_{1/2} = 90$ mV) reported by Lahti *et al.*,[22] which we ascribe to the absence of methoxy donor substituents (literature values were recalculated to the ferrocene/ferrocenium scale using the reported half-wave potential of the $Cp_2Fe^{0/+}$ redox couple of 553 mV in $CHCl_3$ on the Ag/AgCl scale,[56] *i.e.* the conditions used by these authors). They are nevertheless *ca.* 150 mV lower than that of the 4-

Open Access Article. Published on 18 February 2025. Downloaded on 5/22/2025 3:43:42 PM.
This article is licensed under a Creative Commons Attribution 3.0 Unported Licence.

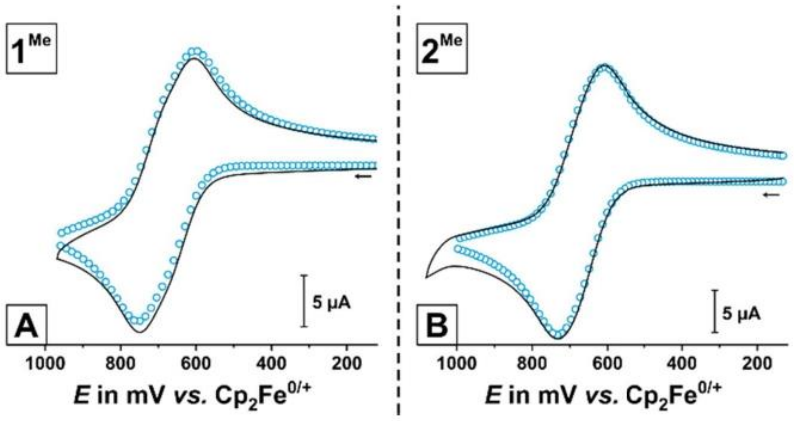

Fig. 3 (A) Overlaid cyclic voltammogram of $\mathbf{1^{Me}}$ in CH_2Cl_2/NBu_4^+ $[BAr^{F24}]^-$ (0.1 M, T = 293 K (±3 K), v = 600 mV s^{-1}, black solid line) and corresponding simulation (blue circles). (B) Overlaid cyclic voltammogram of $\mathbf{2^{Me}}$ in CH_2Cl_2/NBu_4^+ $[BAr^{F24}]^-$ (0.1 M, T = 293 K (±3 K), v = 600 mV s^{-1}, black solid line) and corresponding simulation (blue circles).

Table 1 Electrochemical potentials of the oxidations of $\mathbf{1^{Me}}$ and $\mathbf{2^{Me}}$ obtained from the cyclic voltammograms in CH_2Cl_2/NBu_4^+ $[BAr^{F24}]^-$ (0.1 M, T = 293 K (±3 K)) as well as by digital simulation

	$E_{1/2\ avg}^{0/2+}$ (exp.)	$E_{1/2}^{0/+}$ (simulated)	$E_{1/2}^{+/2+}$ (simulated)	$\Delta E_{1/2}$
$\mathbf{1^{Me}}$	675 mV	635 mV	715 mV	80 mV
$\mathbf{2^{Me}}$	670 mV	640 mV	685 mV	45 mV

ethynylphenyl precursor ($E_{1/2}$ = 820 mV in CH_2Cl_2 *vs.* $Cp_2Fe^{0/+}$), indicating the extent of electron donation from the dihexyl-substituted fluorenyl core unit.

We next turn to the spectroscopic characterization of the oxidized forms of $\mathbf{1^{Me}}$ and $\mathbf{2^{Me}}$ as models of the oxidized BTAA tetracarboxylic acids that one expects to be the active species in transmembrane hole transfer. To generate these species, we applied UV-Vis/NIR spectroelectrochemistry (SEC), *i.e.* spectroscopic monitoring during *in situ* electrochemical oxidation upon incrementally increasing the applied potential to a value 250 mV positive of the convoluted overall two-electron wave. The latter experiments were conducted inside an optically transparent thin-layer electrolysis cell[52] with 1,2-dichloroethane (DCE) as the solvent, using again the NBu_4^+ $[BAr^{F24}]^-$ (0.1 M) supporting electrolyte. The higher boiling point of the DCE solvent as compared to CH_2Cl_2 counteracts solvent evaporation in the vicinity of the working electrode during the experiments. Fig. 4 displays the evolution of the UV-Vis/NIR spectra alongside NIR spectra recorded with an IR/NIR spectrometer (for details, see the ESI, Section S3†) as insets; the latter has a superior sensitivity in the low-energy part of the NIR regime. Panels A and B of Fig. 4 show the results on $\mathbf{1^{Me}}$, while those for $\mathbf{2^{Me}}$ are given in panels C and D.

In both cases, the overall two-electron oxidation proceeds in separate steps *via* an intermediate species (orange lines), which has a characteristic broad NIR band at 1405 nm ($\mathbf{1^{Me\bullet+}}$) or 1400 nm respectively ($\mathbf{2^{Me\bullet+}}$, see panels A and C of Fig. 4 and the corresponding insets). As the oxidation progresses further, the NIR band intensifies and shifts to higher energies (*i.e.* lower wavelengths) of 1250 nm for both $\mathbf{1^{Me2+}}$ and $\mathbf{2^{Me2+}}$. These observations are indicative of the stepwise formation of first the mixed-valent radical cations and then the dications of BTAAs with large, π-extended linkers.[14,39,53,57] Other spectroscopic changes are the gradual and continuous growth of a Vis/NIR band, which is located at 715 nm for $\mathbf{1^{Me}}$ and at 705 nm for $\mathbf{2^{Me}}$. This band corresponds to a π–π* transition of a triarylaminium radical cation and is characteristic of the $TAA^{\bullet+}$ motif. This assignment agrees with the observed rough doubling in intensity upon the second oxidation, which generates an additional triarylaminium chromophore. Also, both oxidized compounds feature one additional band of similar intensity at 550 nm each.

In interpreting the results, one should notice that the close proximity of the individual $E_{1/2}$ values of $\mathbf{1^{Me}}$ and $\mathbf{2^{Me}}$ implies that the intermediate mixed-valent radical cations have only limited stability with respect to disproportionation to the neutral starting compounds and the dioxidized forms, both with isovalent TAA redox sites. This is expressed by the only modest values for the comproportionation equilibrium constant K_c for the comproportionation (*cf.* eqn (1)) of *ca.* 23 ($\mathbf{1^{Me}}$) or only 6 ($\mathbf{2^{Me}}$).

$$K_c = \exp\left(\frac{F}{RT}(\Delta E_{1/2})\right) \quad (1)$$

In eqn (1), R is the universal gas constant, F Faraday's constant, and $\Delta E_{1/2}$ the half-wave potential separation between the two consecutive redox processes. The individual K_c values indicate that a maximum of 70% or 55% of the mixed-valent radical cations are formed as such after the passage of one equivalent of charge, with the remaining 30% or 45% present as equimolar mixtures of the neutral and dioxidized forms. The overlapping NIR bands of the radical cations and the dications in the NIR unfortunately preclude us from deconstructing the spectra and calculating the spectra of the pristine, intermediate radical cations, but it is nevertheless clear that both species

Open Access Article. Published on 18 February 2025. Downloaded on 5/22/2025 3:43:42 PM.
This article is licensed under a Creative Commons Attribution 3.0 Unported Licence.

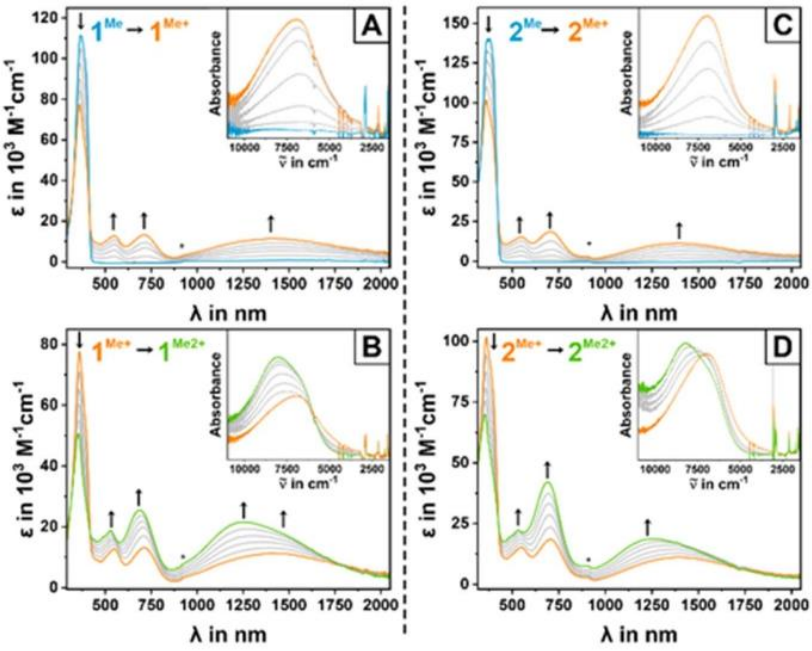

Fig. 4 UV-Vis/NIR spectroelectrochemistry of $\mathbf{1}^{Me}$ (left, panels A and B) and $\mathbf{2}^{Me}$ (right, panels C and D) with the first oxidation shown as blue to orange curves (top, panels A and C) and the second oxidation shown as orange to green curves (bottom, panels B and D), respectively, in CH_2Cl_2 with 0.1 M NBu_4^+ $[BAr^{F24}]^-$ as the supporting electrolyte. IR/NIR spectra are provided in insets in panels A to D. An artifact due to the experimental setup is marked with an asterisk.

have distinct absorptions in the NIR region. The high intensity of the NIR absorption of the radical cations is at first surprising when considering the small half-wave potential splittings and the large N···N distances of 23.15 Å in $\mathbf{1}^{Me\bullet+}$ or 36.65 Å in $\mathbf{2}^{Me\bullet+}$, as obtained from quantum chemical calculations (see below). The intensity gain and the blue-shift upon the second oxidation let us assign the prominent NIR band to charge-transfer (CT) excitation from the respective fluorene linker to the $TAA^{\bullet+}$ acceptor(s) rather than to a pure TAA → $TAA^{\bullet+}$ intervalence charge-transfer (IVCT) excitation, as the latter would be expected to be specific for the mixed-valent radical cations and to vanish as the oxidation proceeds further to the dications.

To shed more light on the electronic structures of one- and two-electron oxidized $\mathbf{1}^{Me+/2+}$ and $\mathbf{2}^{Me+/2+}$, we resorted to density functional quantum-chemical calculations at the B3LYP+35% exact Hartree–Fock exchange def2SVP level of theory. The latter has proven to provide adequate descriptions of the electronic structures of mixed-valent BTAAs by compensating for the inherent tendency of the DFT method to delocalize charges in extended π-conjugated systems.[37,58–60] Our calculations employed slightly truncated models with methyl instead of hexyl substituents, which are henceforth denoted as $\mathbf{1}^{Me'}$ and $\mathbf{2}^{Me'}$. Solvent effects were considered within the framework of the polarizable continuum model, applying the standard parameters for CH_2Cl_2. Further details as well as coordinates of the geometry-optimized structures are provided in Section S11 of the ESI.†

Our calculations indeed provided intense transitions in the NIR for both the one- and the two-electron oxidized forms $\mathbf{1}^{Me'\bullet+/2}$ and $\mathbf{2}^{Me'\bullet+/2+}$, at energies close to the experimental values. Charge density losses on the individual TAA^+ sites and the fluorenyl segments of the linkers were evaluated by natural bond orbital (NBO) analysis (see Fig. 5).[61] According to these results, both radical cations possess localized electronic structures where the unipositive charge is confined to one specific $TAA^{\bullet+}$ entity. In contrast to other BTAAs with electron-rich *para*-anisyl (An) substituents NAn_2, the most electron-rich phenyl group of $\mathbf{1}^{Me}$ and $\mathbf{2}^{Me}$ is the one bonded to the fluorenyl linker. This causes the occupied frontier MOs to spread onto the linker rather than being strictly confined to the periphery.

The calculated NIR transitions in radical cation $\mathbf{2}^{Me'\bullet+}$ are depicted in panel A of Fig. 6, along with graphical representations of the involved molecular orbitals and the corresponding electron density difference maps (EDDMs; blue color = electron density loss and red color = electron density gain). Computational results for its shorter homolog $\mathbf{1}^{Me'\bullet+}$ can be found in Fig. S18 of the ESI.† For both compounds, our calculations predict two separate transitions at low energies as highly intense bands ($\mathbf{1}^{Me\bullet+}$: λ_{calc} = 1036 nm/1675 nm, f = 0.28/1.07; $\mathbf{2}^{Me\bullet+}$: λ_{calc} = 1212 nm/1550 nm, f = 0.46/0.84). They both target β-LUSO, which is localized on the oxidized TAA unit, and emanate from the first three occupied orbitals of the β-manifold, *i.e.* β-HOSO to β-HOSO-2. The latter donor MOs are either localized on the other TAA unit or spread over the entire π-conjugated backbone, including the ester-functionalized diarylamine entities. Both NIR excitations therefore assume bridge-to-TAA^+ CT, augmented with IVCT contributions. The

This journal is © The Royal Society of Chemistry 2025

Open Access Article. Published on 18 February 2025. Downloaded on 5/22/2025 3:43:42 PM.
This article is licensed under a Creative Commons Attribution 3.0 Unported Licence.

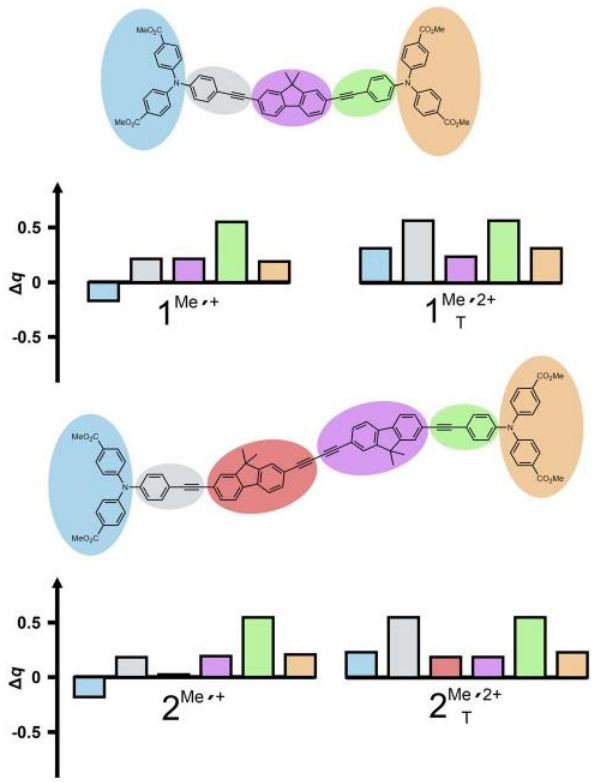

Fig. 5 Calculated electron density losses upon oxidation of model complexes $\mathbf{1}^{Me'}$ and $\mathbf{2}^{Me'}$ to their corresponding one- (left) and two-electron oxidized forms (triplet state), based on natural bond orbital (NBO) analysis. Δq refers to the charge difference of the respective molecular region of the radical monocations (left panels) and the respective dications in their triplet ground state (right panels) relative to the corresponding neutral state. The individual fragments are color-coded according to the graphical representation in the top panels.

absorption bands of one-electron oxidized $\mathbf{1}^{Me\bullet+}$ and $\mathbf{2}^{Me\bullet+}$ generally agree well with the results of investigations on other BTAAs with similarly π-extended linkers.[39,44,54,55]

In contrast to the plethora of BTAAs with shorter linkers, but in line with important bridge-to-TAA$^{\bullet+}$ contributions,[39,54,55] the NIR transitions of $\mathbf{1}^{Me\bullet+}$ and $\mathbf{2}^{Me\bullet+}$ intensify during further oxidation to the dications while experiencing a shift to higher energies and shorter wavelengths respectively, from 1405 nm to 1250 nm for $\mathbf{1}^{Me\bullet+/2+}$ (λ_{calc} = 1183 nm, f = 1.82), and from 1400 nm to 1220 nm for $\mathbf{2}^{Me\bullet+/2+}$ (λ_{calc} = 1345 nm, f = 2.39); see panels A and B of Fig. 6. The dications were computed to prefer the triplet state by 54.0 kJ mol^{-1} ($\mathbf{1}^{Me'2+}$) or 42.5 kJ mol^{-1} ($\mathbf{2}^{Me'2+}$) over the closed and open-shell singlet states, which were calculated to be energetically degenerate. Panels A, B in Fig. 6 and S18 of the ESI† demonstrate the excellent agreement between computed and experimental spectra. A complete collection of all computed electronic absorption bands of $\mathbf{1}^{Me'n+}$ and $\mathbf{2}^{Me'n+}$ (n = 0, 1, 2, the latter in their triplet ground and excited singlet states) along with the corresponding TD-DFT calculated transitions on their methyl-substituted models, contour plots of the contributing orbitals, and computed oscillator strengths are provided in the ESI (see Table S5†). On oxidation of the second TAA entity, the character of the NIR electronic excitation assumes pure bridge-to-TAA$^{\bullet+}$ CT character.

In summary, the highly intense NIR absorptions of one- and two-electron oxidized BTAAs $\mathbf{1}^{Me\bullet+/2+}$ and $\mathbf{2}^{Me\bullet+/2+}$ can be traced to bridge-to-TAA$^{\bullet+}$ CT augmented by TAA-to-TAA$^{\bullet+}$ IVCT excitations in the radical cations. The energetically low-lying bridge-to-TAA$^{\bullet+}$ excitations and the bridge participation in the frontier MOs make $\mathbf{1}^{Me\bullet+}$ and $\mathbf{2}^{Me\bullet+}$ (and by inference the one-electron oxidized free carboxylic acids $\mathbf{1}^{H\bullet+}$ and $\mathbf{2}^{H\bullet+}$) interesting candidates for transmembrane electron transfer when incorporated into a lipid bilayer.

Membrane integration

Incorporation of BTAAs in the lipid membrane bilayers was performed with $\mathbf{1}^{H}$ or $\mathbf{2}^{H}$. At neutral pH, their molecular structures mimic the amphiphilicity of the phospholipid bilayer best by having charged carboxylates at each end of the linear and rigid molecular wire. The charged ends interact with the polar part of the membrane at the water interface, while the entire linker, including the inner phenyl rings, stays inside the hydrophobic part of the membrane. This secures the integration of $\mathbf{1}^{H}$ or $\mathbf{2}^{H}$ into the membrane (Fig. 7) of vesicles. In this study, we used sub-micrometer-sized liposome vesicles for all spectroscopy and electron transfer studies. We also prepared micrometer-sized giant vesicles for microscopic visualization. All vesicles were prepared with lipid bilayers based on 2-dipalmitoyl-*sn*-glycero-3-phosphocholine (DPPC) because DPPC bilayers are known to be impermeable to larger water-soluble molecules at room temperature.[62,63] Along with the main phospholipid DPPC, we added 1 mol% of 14:0 PEG2000 PE to the lipid bilayer membranes to increase the stability of the liposome, as this lipid creates steric bulk and thereby prevents aggregation of the vesicles (see Fig. 7 for the structures of DPPC and 14:0 PEG2000 PE).[5,64,65]

Molecular dynamics (MD) simulations of both molecular wires after 100 ns simulation time are shown in Fig. 7a and b. The MD simulations were done using YASARA and the AMBER force field;[66,67] the details can be found in ESI S4, Fig. S19 and S20.† These MD simulations suggest that both molecular wires $\mathbf{1}^{H}$ and $\mathbf{2}^{H}$ assemble with the lipid bilayer, but $\mathbf{1}^{H}$ assembles at the membrane–water interface, while $\mathbf{2}^{H}$ can align in a transmembrane fashion. We explain these results as follows: in $\mathbf{2}^{H}$, the N···N distance is 33.66 Å in the phospholipid bilayer (similar to the N···N distance of 36.65 Å in $\mathbf{2}^{Me\bullet+}$ determined by DFT, see above). The hydrophilic carboxylate groups are even further apart from each other and can therefore easily span a lipid bilayer membrane, being exposed to the membrane's water interfaces, as can be seen in Fig. 7b. Lipid bilayer membranes typically have a thickness of 30 to 50 Å.[68,69] For the shorter BTAA $\mathbf{1}^{H}$, the N···N distance is 23.48 Å (similar to the N···N distance of 23.15 Å in $\mathbf{1}^{Me\bullet+}$ determined by DFT, see above). The distance of the hydrophilic carboxylic groups in $\mathbf{1}^{H}$ is 28.51 Å, which is too short to span across the membrane and which can lead to the disruption of the membrane by $\mathbf{1}^{H}$.

Open Access Article. Published on 18 February 2025. Downloaded on 5/22/2025 3:43:42 PM.
This article is licensed under a Creative Commons Attribution 3.0 Unported Licence.

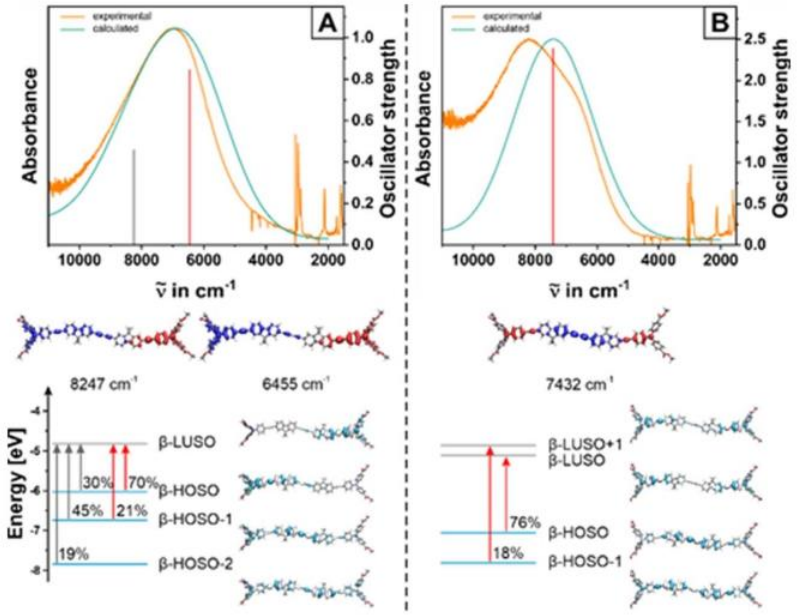

Fig. 6 Top: Comparison between experimental NIR spectra of 2^{Me+} (orange line in panel A) and 2^{Me2+} (green line in panel B) in 1,2-CH_4Cl_2 (0.1 M NBu_4^+ $[BAr^{F24}]^-$ as the supporting electrolyte) and TD-DFT calculated electronic spectra of model compound $2^{Me'+}$ (panel A, turquoise line) and $2^{Me'2+}$ (panel B, violet). Computed transitions are provided as red and grey vertical bars. Bottom: Contour diagrams of the acceptor and donor MOs involved in the NIR transitions together with their contributions to the respective transition and corresponding electron density difference maps (EDDMs). Blue color indicates electron density loss and red color an increase in electron density. Isosurface values for the MO plots are set as ±0.02.

In order to study how the respective molecular wire affects the membrane, we conducted a calcein leakage test using liposomes. In this test, we quantified the amount of calcein, a fluorescent dye, leaked out of the liposomes into the surrounding solution. For detailed information, please refer to ESI S5, Fig. S21.†[70,71] We tested both the modified and unmodified DPPC liposomes for three days with and without irradiation using a 470 nm LED. The measurements with irradiation revealed that the modified DPPC liposome with $\mathbf{1^H}$ released 93% of calcein, while the modified DPPC liposome with $\mathbf{2^H}$ only released 4.5% of calcein. These observations align with our MD simulations, which predicted that the modified liposome with $\mathbf{1^H}$ would disrupt the membrane more effectively than $\mathbf{2^H}$; as $\mathbf{2^H}$ is longer in size, it has a higher possibility of aligning in the transmembrane position in the membrane and would not disrupt the membrane.

UV-Vis absorption and emission spectroscopy were used to characterize the photophysical properties of $\mathbf{1^H}$ and $\mathbf{2^H}$ before and after membrane integration (Fig. 8a and b and Table 2). When measured in a mixture of DCM and MeOH (1 : 1) (Fig. 8a and b, solid black line), $\mathbf{1^H}$ and $\mathbf{2^H}$ showed absorption bands at 366 nm and 385 nm, respectively. This indicates that the respective LUMO of $\mathbf{2^H}$ is lower in energy than that of $\mathbf{1^H}$ due to its extended π-system. The absorption spectra shift to the blue for both structures in the membrane environment as can be seen in Fig. 8a and b and in Table 2. While $\mathbf{1^H}$ experienced only a 4 nm blue shift, the absorbance of $\mathbf{2^H}$ experienced a pronounced blue-shift by ~20 nm. The very minor blue-shift for $\mathbf{1^H}$ might be explained by Tyndall scattering of the liposome suspension, similar to other chromophores in liposomes with minor solvent-dependent absorbance.[75] The very pronounced blue-shift of $\mathbf{2^H}$ is likely due to the lower polarity and rigidity around the compound in a lipid bilayer environment.[72–74] This observation is in line with the MD simulation, which showed that the entire extended π-system of $\mathbf{2^H}$ is located in the lipophilic part of the membrane, which leads to destabilizing the LUMO of $\mathbf{2^H}$, resulting in a more pronounced blue shift in the UV-Vis absorption.

The emission spectra of $\mathbf{1^H}$ and $\mathbf{2^H}$ have their maximum at 422 nm and 430 nm respectively in DCM : CH_2Cl_2 (1 : 1), as indicated by the solid green line in Fig. 8a and b. Both compounds have a shoulder at a higher wavelength in their emission spectra, suggesting the existence of unresolved vibrational energy levels in both compounds. Upon incorporation into the membrane, the maximum is slightly red-shifted by 13 nm and 15 nm for $\mathbf{1^H}$ and $\mathbf{2^H}$ respectively. However, this apparent red shift might also be partly induced by the broadened absorption and respective inner filter effects (Fig. 8a and b, dashed green line).

Furthermore, to show that $\mathbf{2^H}$ is successfully integrated into the lipid membrane, we prepared a giant multilamellar vesicle of $\mathbf{2^H}$ with the same methodology as that used for preparing the liposomes and performed confocal microscopy. We excited the giant multilamellar vesicle with a laser at $\lambda = 405$ nm and detected the fluorescence of the vesicle in the region of 420–650 nm. A double half-moon-shaped emission profile was

Open Access Article. Published on 18 February 2025. Downloaded on 5/22/2025 3:43:42 PM.
This article is licensed under a Creative Commons Attribution 3.0 Unported Licence.

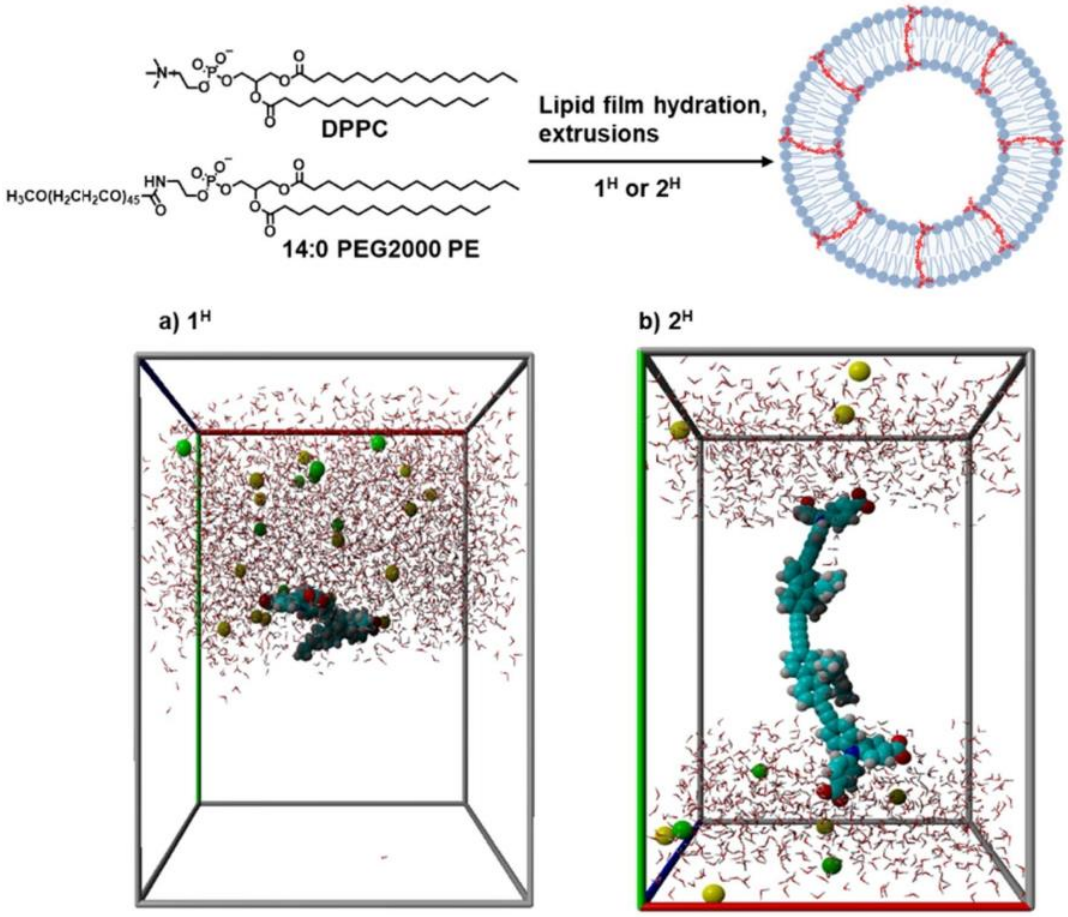

Fig. 7 Integration of $\mathbf{1}^{H}$ or $\mathbf{2}^{H}$ into a DPPC (1,2-dipalmitoyl-*sn*-glycero-3-phosphocholine) liposome and a molecular dynamic simulation snapshot of (a) $\mathbf{1}^{H}$ and (b) $\mathbf{2}^{H}$ in DPPC after 100 ns simulation time. The lipid bilayer membrane is omitted for clarity.

observed in the microscopic image (Fig. 8c), typical for molecules with a preferred alignment in the lipid membrane.[65,72,75] It shall also be noted that, apart from the half-moon effect, the molecules are overall evenly distributed within the membrane and no larger macroscopic phase separation can be observed.[76]

Electron transfer at the membrane

To study the photoactive properties of $\mathbf{1}^{H}$ and $\mathbf{2}^{H}$ toward electron transfer across the lipid bilayer, we started our studies on photoinduced transmembrane electron transfer by preparing a DPPC liposome solution containing 1 mol% of $\mathbf{1}^{H}$ or $\mathbf{2}^{H}$ in the

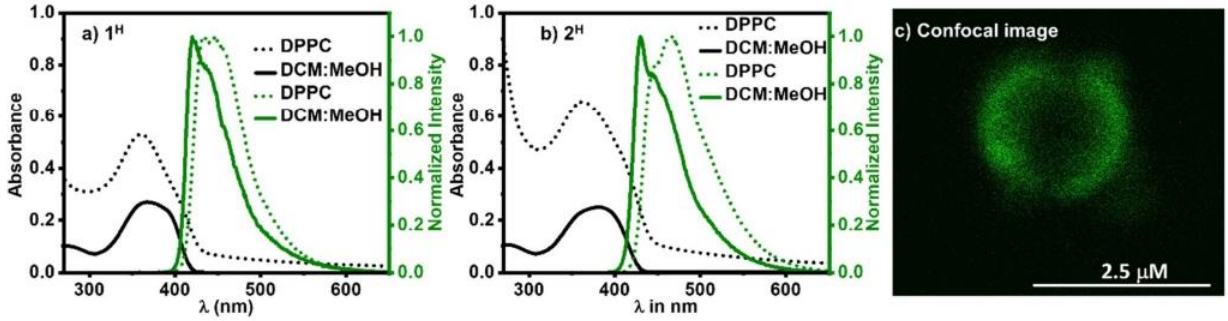

Fig. 8 (a) UV-Vis and emission spectra of $\mathbf{1}^{H}$ and (b) UV-Vis and emission spectra of $\mathbf{2}^{H}$ in a mixture of dichloromethane (DCM) : methanol (MeOH) (1 : 1) and in DPPC liposomes with a composition of DPPC : (14:0 PEG2000 PE) : $\mathbf{1}^{H}$ or $\mathbf{2}^{H}$ = 100 : 1 : 1, in phosphate buffer at pH = 7.0; (c) confocal microscopy image of $\mathbf{2}^{H}$ in a giant vesicle with a composition of 100 : 1 : 1 of DPPC : 14:0 PEG2000PE : $\mathbf{2}^{H}$ in phosphate buffer at pH = 7.0 after size exclusion chromatography, upon fixation in agarose hydrogel.

Open Access Article. Published on 18 February 2025. Downloaded on 5/22/2025 3:43:42 PM.
This article is licensed under a Creative Commons Attribution 3.0 Unported Licence.

Table 2 Spectroscopic data of 1^H and 2^H

	Condition	λ_{Abs} (nm)	λ_{Em} (nm)
1^H	DCM:MeOH	366	422
	DPPC[a]	362	435, 446
2^H	DCM:MeOH	385	430
	DPPC[a]	365	445, 467

[a] UV-Vis and emission spectra of 1^H and 2^H in DPPC liposomes with a composition of DPPC : (14:0 PEG2000 PE) : 1^H or 2^H = 100 : 1 : 1, in phosphate buffer at pH = 7.0.

membrane. The water-soluble electron donor NADH was encapsulated, and the water-soluble electron acceptor (2,3-bis-(2-methoxy-4-nitro-5-sulfophenyl)-2*H*-tetrazolium-5-carboxanilide) (XTT) was added to the bulk solution of the liposome, yielding a composition of NADH/1^H/XTT or NADH/2^H/XTT (Fig. 9a). A similar system was also prepared with encapsulated XTT and NADH at the bulk solution of liposomes, yielding a composition of XTT/2^H/NADH. NADH was chosen due to its water solubility and favorable absorption and emission properties.[77] XTT was selected because it is a well-known compound to quantify intracellular reducing agents in biological assays.[78] The details of sample preparation can be found in

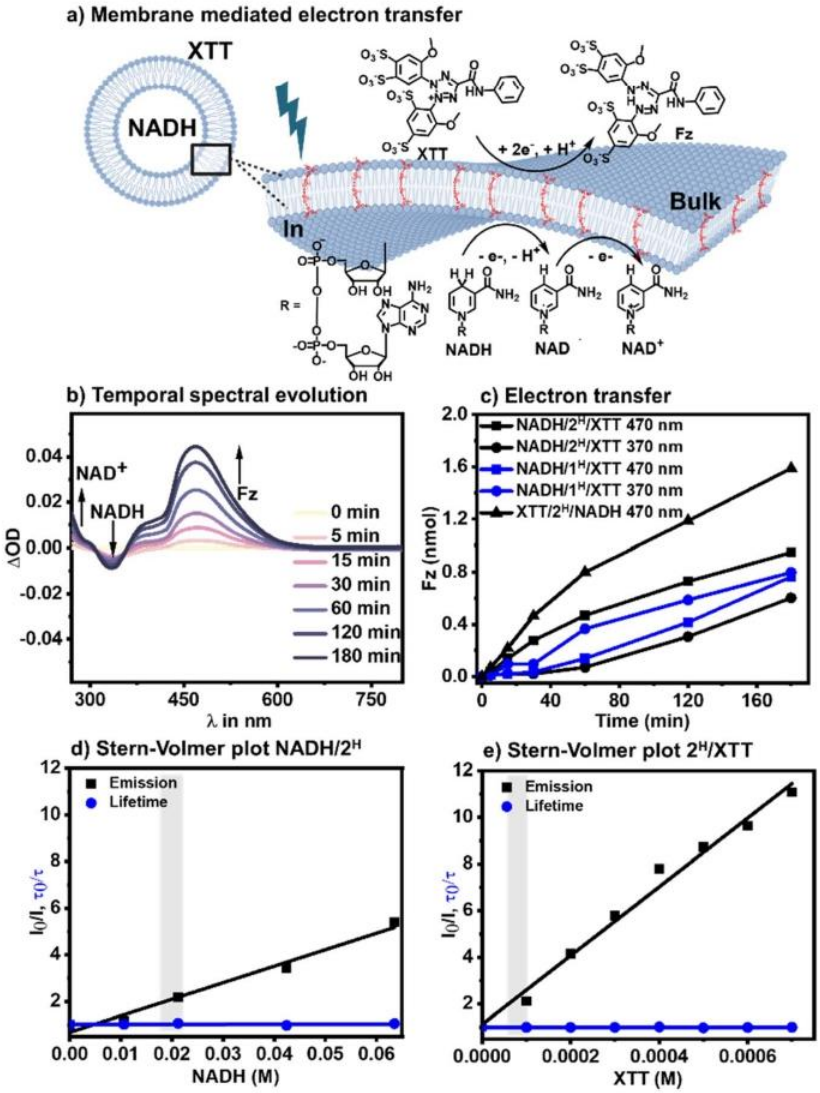

Fig. 9 (a) Schematic illustration of the targeted photoinduced electron transfer at the lipid bilayer with encapsulation of NADH, integration of the chromophore, and presence of XTT in the bulk solution, (b) subtracted temporal evolution of UV-Vis spectra from t = 0 min with sample composition NADH/2^H/XTT, (c) number of Fz molecules formed under irradiation with 460 nm and 370 nm light sources over time for NADH/1^H/XTT, NADH/2^H/XTT, and XTT/2^H/NADH, (d) Stern–Volmer plots of liposome samples with a composition of 100 : 1 : 1 of DPPC : 14:0 PEG2000 PE : 2^H with different concentrations of encapsulated NADH, and (e) Stern–Volmer plots of liposome samples with a composition of 100 : 1 : 1 of DPPC : 14:0 PEG2000 PE : 2^H with different concentrations of XTT in bulk solution. All samples were prepared with 10 mM phosphate buffer at pH 7.0 under ambient conditions. The grey bar corresponds to the used concentration in photoinduced electron transfer experiments.

This journal is © The Royal Society of Chemistry 2025

Open Access Article. Published on 18 February 2025. Downloaded on 5/22/2025 3:43:42 PM.
This article is licensed under a Creative Commons Attribution 3.0 Unported Licence.

the ESI Section S6 and Fig. S22.† Based on dynamic light scattering, the liposomes measure 130–140 nm in diameter for all types of samples (the empty liposome with only $\mathbf{1^H}$ or $\mathbf{2^H}$ integrated and with the encapsulated NADH or XTT; see ESI Section S7 and Fig. S23†).

Upon light irradiation, we observed a gradual increase of the absorption band at $\lambda_{max} = 470$ nm, corresponding to the formation of formazan (Fz), the reduced form of XTT. At the same time, the NAD^+ absorption band at 260 nm increased, the latter corresponding to the oxidized form of NADH and indicating that photoinduced electron transfer had occurred (Fig. 9b). The extent of electron transfer was quantified *via* the intensity of the Fz absorption band (Fig. 9c).

We chose 370 nm and 470 nm LED light sources to irradiate the assembled liposome systems NADH/$\mathbf{1^H}$/XTT and NADH/$\mathbf{2^H}$/XTT. The applied LED light sources have a full-width at half maximum (FWHM) of ±24 nm at $\lambda_{max} = 373$ nm for the 370 nm LED and FWHM ±22 nm at $\lambda_{max} = 464$ nm for the 470 nm LED light source. This leads to the excitation of $\mathbf{1^H}$ and $\mathbf{2^H}$ at either the absorption maximum or in the tail of the absorption (see ESI S8, Fig. S25†). Photoexcitation with the 470 nm LED excited the molecular wire only and excluded the simultaneous excitation of NADH, which has an absorption maximum at 340 nm.[77,79] In the case of the 370 nm LED, both the molecular wire and NADH are simultaneously excited.

Based on the extinction coefficient of Fz, it was calculated in the case of NADH/$\mathbf{2^H}$/XTT that 1.00 nmol of Fz formed after three hours with the 470 nm LED irradiation. This corresponds to 4.4 electron transfers per molecule of $\mathbf{2^H}$. In the case of $\mathbf{2^H}$ with a 370 nm LED, 0.71 nmol of Fz was formed, which is equal to 1.4 nmol of electrons and 3.1 electron transfers per $\mathbf{2^H}$ molecule. This lower performance by the 370 nm light source may be due to the simultaneous absorption of light by both the molecular wire and NADH, as the NADH also absorbs some of the light at 370 nm (see ESI S8, Fig. S25†). In the case of NADH/$\mathbf{1^H}$/XTT and after three hours of irradiation with a 470 nm or 370 nm LED, the Fz yield is 0.77 nmol and 0.78 nmol, respectively. The number of Fz is similarly low with both light sources for $\mathbf{1^H}$, probably due to the lower spectral overlaps of the absorbance of $\mathbf{1^H}$ with the 470 nm LED compared to $\mathbf{2^H}$ (see ESI S8, Fig. S25†). In a previous study, we demonstrated that the light-driven conversion of the water-soluble substrate can be significantly accelerated within the inner aqueous liposome compartment compared to the aqueous bulk.[77] We therefore tested the reverse location of the XTT and NADH and generated XTT/$\mathbf{2^H}$/NADH liposomes. In this system, we observed that by compartmentalization of XTT instead of NADH, we could almost double the production of Fz within three hours, yielding 1.80 nmol, which corresponds to 3.6 nmol electron transfer and 8 electrons transferred per molecule of $\mathbf{2^H}$. This observation indicates that electron transfer from XTT is a limitation that can be minimized through encapsulation of XTT within the inner aqueous compartment (see ESI S9† for absorption growth of Fz over time, Fig. S26–S28†).

To better understand the photoinduced electron transfer dynamics in NADH/$\mathbf{2^H}$/XTT liposomes, we performed a Stern–Volmer luminescence quenching study of $\mathbf{2^H}$ liposomes in the presence of various concentrations of NADH in the inner compartment and XTT in the bulk, respectively. In the Stern–Volmer experiment, the excited state reaction dynamics of $\mathbf{2^H}$ can be resolved by using steady-state and time-resolved emission spectroscopy, by plotting the intensities and the lifetimes as $\frac{I_0}{I}$ and $\frac{\tau_0}{\tau}$ *vs.* quencher concentrations [*Q*],[80] where I_0 and I are the emission intensities in the absence and presence of the quencher, and τ_0 and τ are the excited state lifetimes in the absence and presence of the quencher, respectively.

Table 3 Stern–Volmer quenching constants of $\mathbf{2^H}$ in DPPC membranes with NADH and XTT as quenchers

Quencher	K_{sv} from I_o/I (M^{-1})	k_q (M^{-1} s^{-1})	τ_0 (ns)	Mechanism
NADH/$\mathbf{2^H}$	70.8 ± 6.2	$(8.2 \pm 0.7)10^{10}$	0.86	Static
$\mathbf{2^H}$/XTT	$(14.7 \pm 0.7)10^3$	$(1.7 \pm 0.1)10^{13}$	0.86	Static

$$\frac{I_0}{I} = 1 + K_{sv}[Q] = 1 + k_q\tau_0[Q] \quad (2)$$

The slope from the linear regression of $\frac{I_0}{I}$ *vs.* [*Q*] is the Stern–Volmer constant K_{sv}. By applying eqn (2), the quenching constant k_q can be derived. After the linear fitting of both plots, NADH and XTT showed characteristic static quenching behavior with the lifetime remaining independent of the quencher concentration. Quenching by encapsulated NADH takes place with $k_q = (8.2 \pm 0.7)10^{10}$ M^{-1} s^{-1}. This value is one order of magnitude faster than that in a related study with encapsulated NADH and a positively charged transmembrane molecular wire[6] and might indicate that a stronger ground state encounter complex is formed between the here investigated $\mathbf{2^H}$ and NADH. Similarly, the quenching by XTT from the bulk takes place with $k_q = (1.71 \pm 0.1)10^{13}$ M^{-1} s^{-1} (Table 3). This value is three orders of magnitudes higher than typical collision-based quenching constants, which are on the order of 10^{11} and it is two orders of magnitude higher than in a similar case between XXT and a positively charged chromophore within the DPPC lipid bilayer.[6] Therefore, the k_q values obtained for both quenchers indicate the quenching of $\mathbf{2^H}$ due to a strong association with the quencher already in the ground state.[76,81] We hypothesize that such strong complex formation is partly due to additional hydrogen bond formation by the carboxylate functionality of $\mathbf{2^H}$ with the quencher. The concentrations of NADH and XTT that were applied during the full electron transfer reaction with NADH/$\mathbf{2^H}$/XTT are shown in the highlighted region in the Stern–Volmer quenching plot in Fig. 9d and e. The luminescence and kinetic traces can be found in ESI Section S10 and Fig. S30–S33.†

Conclusion

In summary, we demonstrate that the molecular BTAAs $\mathbf{1^H}$ and $\mathbf{2^H}$ can form mixed-valence species upon one-electron oxidation and that the amphiphilic BTAAs $\mathbf{1^H}$ and $\mathbf{2^H}$ can be integrated into the lipid bilayer of liposomes for light-driven electron transfer from NADH to the acceptor XTT or *vice versa*. While the

Open Access Article. Published on 18 February 2025. Downloaded on 5/22/2025 3:43:42 PM.
This article is licensed under a Creative Commons Attribution 3.0 Unported Licence.

shorter version $\mathbf{1}^{\mathbf{H}}$ disrupts the lipid bilayer significantly, the long molecule $\mathbf{2}^{\mathbf{H}}$ integrates well into the bilayer structure, spanning the membrane. Both compounds are redox-active and generate stable one- and two-electron oxidized cations, thereby enabling transmembrane electron transfer. The mechanism of membrane-mediated electron transfer is likely promoted *via* a mixed valence radical cation state of the one-electron oxidized molecular wire, delocalizing an unpaired electron across the entire molecule. The findings of this study provide a design principle for artificial nanoreactors and are highly relevant for the construction of light-driven redox chemistry systems in water with applications in solar light energy conversion.

Data availability

The data supporting the findings of the article can be found in the ESI.† The raw data of photocatalysis will be made available *via* Chemotion.

Author contributions

N. S. and M. N. contributed equally. N. S. performed the membrane integration, luminescence quenching experiments, transmembrane electron transfer experiments and molecular dynamics simulations. M. N. performed the spectroscopic characterization, cyclic voltammetry (including the simulations), spectroelectrochemistry measurements with data analysis, and all (TD-)DFT calculations on the model compounds, supervised by M. L., R. F. W. and A. P., R. F. W. and A. P. devised the project. P. K. conducted one chemical synthesis. G. H. conducted most chemical syntheses. All authors contributed to scientific discussions and the preparation of the manuscript.

Conflicts of interest

The authors declare no conflict of interest.

Acknowledgements

M. N. thanks the Fonds der Chemischen Industrie for financial support. The authors acknowledge support from the state of Baden-Württemberg and the Deutsche Forschungsgemeinschaft through bwHPC, access to the supercomputing facilities of JUSTUS2 (grant number 40/575-1 FUGG), and the core facilities of the University of Konstanz for NMR spectroscopic and mass spectrometric measurements as well as the platform for mass spectrometry at Friedrich-Schiller-University Jena. A. P. gratefully acknowledges financial support from the Vector Stiftung (project number P2019-0110) as well as the Carl-Zeiss-Foundation and the Deutsche Forschungsgemeinschaft (DFG), project TRR234 "CataLight" project number 364549901, project B8. NMR at Ulm University was recorded on a spectrometer funded by DFG project number 445471845. The confocal images were recorded at the Core Facility for Confocal and Multiphoton Microscopy at Ulm University which is supported by the DFG through project number 91BGG INST 381/39-1.

References

1 S. Bhosale, A. L. Sisson, P. Talukdar, A. Fürstanberg, N. Banetji, E. Vauthey, G. Bollot, J. Mareda, C. Röger, F. Würthner, N. Sakai and S. Matile, Photoproduction of Proton Gradients with π-Stacked Fluorophore Scaffolds in Lipid Bilayers, *Science*, 2006, **313**(5783), 84–86, DOI: **10.1126/science.1126524**.

2 A. Perez-Velasco, V. Gorteau and S. Matile, Rigid Oligoperylenediimide Rods: Anion–π Slides with Photosynthetic Activity, *Angew. Chem., Int. Ed.*, 2008, **47**(5), 921–923, DOI: **10.1002/anie.200703749**.

3 T. A. Moore, D. Gust, P. Mathis, J.-C. Mialocq, C. Chachaty, R. V. Bensasson, E. J. Land, D. Doizi, P. A. Liddell, W. R. Lehman, G. A. Nemeth and A. L. Moore, Photodriven Charge Separation in a Carotenoporphyrin–Quinone Triad, *Nature*, 1984, **307**(5952), 630–632, DOI: **10.1038/307630a0**.

4 P. Seta, E. Bienvenue, A. L. Moore, P. Mathis, R. V. Bensasson, P. Liddell, P. J. Pessiki, A. Joy, T. A. Moore and D. Gust, Photodriven Transmembrane Charge Separation and Electron Transfer by a Carotenoporphyrin–Quinone Triad, *Nature*, 1985, **316**(6029), 653–655, DOI: **10.1038/316653a0**.

5 B. Limburg, J. Wermink, S. S. van Nielen, R. Kortlever, M. T. M. Koper, E. Bouwman and S. Bonnet, Kinetics of Photocatalytic Water Oxidation at Liposomes: Membrane Anchoring Stabilizes the Photosensitizer, *ACS Catal.*, 2016, **6**(9), 5968–5977, DOI: **10.1021/acscatal.6b00151**.

6 N. Sinambela, R. Jacobi, D. Sorsche, L. Gonzalez and A. Pannwitz, Photoinduced Electron Transfer across Phospholipid Bilayers in Anaerobic and Aerobic Atmospheres, *ChemRxiv*, December 3, 2024, preprint, DOI: **10.26434/chemrxiv-2024-x7wgx**.

7 U. Fuerholz, H. B. Buergi, F. E. Wagner, A. Stebler, J. H. Ammeter, E. Krausz, R. J. H. Clark, M. J. Stead and A. Ludi, The Creutz-Taube Complex Revisited, *J. Am. Chem. Soc.*, 1984, **106**(1), 121–123, DOI: **10.1021/ja00313a025**.

8 R. I. Walter, Substituent Effects on the Properties of Stable Aromatic Free Radicals. The Criterion for Non-Hammett Behavior, *J. Am. Chem. Soc.*, 1966, **88**(9), 1923–1930, DOI: **10.1021/ja00961a014**.

9 S. Dapperheld, E. Steckhan, K.-H. G. Brinkhaus and T. Esch, Organic Electron Transfer Systems, II Substituted Triarylamine Cation-Radical Redox Systems – Synthesis, Electrochemical and Spectroscopic Properties, Hammet Behavior, and Suitability as Redox Catalysts, *Chem. Ber.*, 1991, **124**(11), 2557–2567, DOI: **10.1002/cber.19911241127**.

10 S. Amthor, B. Noller and C. Lambert, UV/Vis/NIR Spectral Properties of Triarylamines and Their Corresponding Radical Cations, *Chem. Phys.*, 2005, **316**(1), 141–152, DOI: **10.1016/j.chemphys.2005.05.009**.

11 A. Heckmann, C. Lambert, M. Goebel and R. Wortmann, Synthesis and Photophysics of a Neutral Organic Mixed-Valence Compound, *Angew. Chem., Int. Ed.*, 2004, **43**(43), 5851–5856, DOI: **10.1002/anie.200460495**.

This journal is © The Royal Society of Chemistry 2025

Open Access Article. Published on 18 February 2025. Downloaded on 5/22/2025 3:43:42 PM.
This article is licensed under a Creative Commons Attribution 3.0 Unported Licence.

12 G. Grelaud, M. P. Cifuentes, T. Schwich, G. Argouarch, S. Petrie, R. Stranger, F. Paul and M. G. Humphrey, Multistate Redox-Active Metalated Triarylamines, *Eur. J. Inorg. Chem.*, 2012, **2012**(1), 65–75, DOI: 10.1002/ejic.201100747.

13 W. Polit, T. Exner, E. Wuttke and R. Winter, Vinylruthenium-Triarylamine Conjugates as Electroswitchable Polyelectrochromic NIR Dyes, *BioInorg. React. Mech.*, 2012, **8**, 85–105, DOI: 10.1515/irm-2012-0005.

14 C. Hassenrück and R. F. Winter, Manipulation and Assessment of Charge and Spin Delocalization in Mixed-Valent Triarylamine–Vinylruthenium Conjugates, *Inorg. Chem.*, 2017, **56**(21), 13517–13529, DOI: 10.1021/acs.inorgchem.7b02186.

15 S. Breimaier and R. F. Winter, Electrochemical and Spectroscopic Studies on Triarylamine-Polychlorotriphenylmethyl Dyads with Particularly Strong Triarylamine Donors, *Eur. J. Org Chem.*, 2021, **2021**(33), 4690–4700, DOI: 10.1002/ejoc.202100476.

16 C.-J. Yao, R.-H. Zheng, Q. Shi, Y.-W. Zhong and J. Yao, 1,4-Benzene-Bridged Covalent Hybrid of Triarylamine and Cyclometalated Ruthenium: A New Type of Organic–Inorganic Mixed-Valent System, *Chem. Commun.*, 2012, **48**(45), 5680–5682, DOI: 10.1039/C2CC32471G.

17 J.-H. Tang, J.-Y. Shao, Y.-Q. He, S.-H. Wu, J. Yao and Y.-W. Zhong, Transition from a Metal-Localized Mixed-Valence Compound to a Fully Delocalized and Bridge-Biased Electrophore in a Ruthenium–Amine–Ruthenium Tricenter System, *Chem.–Eur. J.*, 2016, **22**(30), 10341–10345, DOI: 10.1002/chem.201601806.

18 J. Zhang, S.-Z. Guo, Y.-B. Dong, L. Rao, J. Yin, G.-A. Yu, F. Hartl and S. H. Liu, Multistep Oxidation of Diethynyl Oligophenylamine-Bridged Diruthenium and Diiron Complexes, *Inorg. Chem.*, 2017, **56**(2), 1001–1015, DOI: 10.1021/acs.inorgchem.6b02809.

19 K. E. Linton, M. A. Fox, L.-O. Pålsson and M. R. Bryce, Oligo(p-Phenyleneethynylene) (OPE) Molecular Wires: Synthesis and Length Dependence of Photoinduced Charge Transfer in OPEs with Triarylamine and Diaryloxadiazole End Groups, *Chem.–Eur. J.*, 2015, **21**(10), 3997–4007, DOI: 10.1002/chem.201406080.

20 Y.-P. Ou, J. Zhang, A. Wang, A. Yuan, C. Yin and S. H. Liu, Rutheniumethynyl-Triarylamine Organic–Inorganic Mixed-Valence Systems: Regulating Ru-N Electronic Coupling by Different Aryl Bridge Cores, *Chem.–Asian J.*, 2020, **15**(20), 3338–3349, DOI: 10.1002/asia.202000879.

21 Z. Lin, Z. Li, W. Xiao, L. Kong, J. Xu, Y. Xia, X. Zhu, F. Zhang and Y.-P. Ou, Terpyridine Ruthenium–Triarylamine Asymmetrical Mixed-Valence Systems: Syntheses, (Spectro) Electrochemistry and Theoretical Calculations, *J. Organomet. Chem.*, 2023, **993**, 122708, DOI: 10.1016/j.jorganchem.2023.122708.

22 H. Murata and P. M. Lahti, Synthesis and Oxidation of Triarylamine Derivatives Bearing Hydrogen-Bonding Groups, *J. Org. Chem.*, 2007, **72**(13), 4974–4977, DOI: 10.1021/jo070318a.

23 G. Sforazzini, A. Kahnt, M. Wykes, J. K. Sprafke, S. Brovelli, D. Montarnal, F. Meinardi, F. Cacialli, D. Beljonne, B. Albinsson and H. L. Anderson, Synthesis and Photophysics of Coaxial Threaded Molecular Wires: Polyrotaxanes with Triarylamine Jackets, *J. Phys. Chem. C*, 2014, **118**(8), 4553–4566, DOI: 10.1021/jp500624q.

24 P. Thamaraiselvi, N. Duraipandy, M. S. Kiran and S. Easwaramoorthi, Triarylamine Rhodanine Derivatives as Red Emissive Sensor for Discriminative Detection of Ag^{+} and Hg^{2+} Ions in Buffer-Free Aqueous Solutions, *ACS Sustain. Chem. Eng.*, 2019, **7**(11), 9865–9874, DOI: 10.1021/acssuschemeng.9b00417.

25 C. A. Swamy P, A. V. Raveendran, N. Sivakrishna and R. P. Nandi, Triarylborane-Triphenylamine Based Luminophore for the Mitochondria Targeted Live Cell Imaging and Colorimetric Detection of Aqueous Fluoride, *Dalton Trans.*, 2022, **51**(40), 15339–15353, DOI: 10.1039/D2DT01887J.

26 R. R. Nelson and R. N. Adams, Anodic Oxidation Pathways of Substituted Triphenylamines. II. Quantitative Studies of Benzidine Formation, *J. Am. Chem. Soc.*, 1968, **90**(15), 3925–3930, DOI: 10.1021/ja01017a004.

27 R. F. Nelson and R. H. Philp, Electrochemical and Spectroscopic Studies of Cation Radicals. 4. Stopped-Flow Determination of Triarylaminium Radical Coupling Rate Constants, *J. Phys. Chem.*, 1979, **83**(6), 713–716, DOI: 10.1021/j100469a015.

28 K. Sreenath, C. V. Suneesh, V. K. Ratheesh Kumar and K. R. Gopidas, Cu(II)-Mediated Generation of Triarylamine Radical Cations and Their Dimerization. An Easy Route to Tetraarylbenzidines, *J. Org. Chem.*, 2008, **73**(8), 3245–3251, DOI: 10.1021/jo800349n.

29 M. R. Talipov, M. M. Hossain, A. Boddeda, K. Thakur and R. Rathore, A Search for Blues Brothers: X-Ray Crystallographic/Spectroscopic Characterization of the Tetraarylbenzidine Cation Radical as a Product of Aging of Solid Magic Blue, *Org. Biomol. Chem.*, 2016, **14**(10), 2961–2968, DOI: 10.1039/c6ob00140h.

30 R. Reynolds, L. L. Line and R. F. Nelson, Electrochemical Generation of Carbazoles from Aromatic Amines, *J. Am. Chem. Soc.*, 1974, **96**(4), 1087–1092, DOI: 10.1021/ja00811a024.

31 N. G. Connelly and W. E. Geiger, Chemical Redox Agents for Organometallic Chemistry, *Chem. Rev.*, 1996, **96**(2), 877–910, DOI: 10.1021/cr940053x.

32 B. Mladenova, D. R. Kattnig, C. Kaiser, J. Schäfer, C. Lambert and G. Grampp, Investigations of the Degenerate Intramolecular Charge Exchange in Symmetric Organic Mixed Valence Compounds: Solvent Dynamics of Bis(Triarylamine)Paracyclophane Redox Systems, *J. Phys. Chem. C*, 2015, **119**(16), 8547–8553, DOI: 10.1021/acs.jpcc.5b01386.

33 J. Schäfer, M. Holzapfel, B. Mladenova, D. Kattnig, I. Krummenacher, H. Braunschweig, G. Grampp and C. Lambert, Hole Transfer Processes in Meta- and Para-Conjugated Mixed Valence Compounds: Unforeseen Effects of Bridge Substituents and Solvent Dynamics, *J. Am. Chem. Soc.*, 2017, **139**(17), 6200–6209, DOI: 10.1021/jacs.7b01650.

Open Access Article. Published on 18 February 2025. Downloaded on 5/22/2025 3:43:42 PM.
This article is licensed under a Creative Commons Attribution 3.0 Unported Licence.

34 S. Dümmler, W. Roth, I. Fischer, A. Heckmann and C. Lambert, Excited-State Dynamics in a Neutral Organic Mixed-Valence Compound, *Chem. Phys. Lett.*, 2005, **408**(4), 264–268, DOI: 10.1016/j.cplett.2005.04.045.

35 K. Tahara, T. Nakakita, A. A. Starikova, T. Ikeda, M. Abe and J. Kikuchi, Small Anion-Assisted Electrochemical Potential Splitting in a New Series of Bistriarylamine Derivatives: Organic Mixed Valency across a Urea Bridge and Zwitterionization, *Beilstein J. Org. Chem.*, 2019, **15**(1), 2277–2286, DOI: 10.3762/bjoc.15.220.

36 J. Hankache and O. S. Wenger, Organic Mixed Valence, *Chem. Rev.*, 2011, **111**(8), 5138–5178, DOI: 10.1021/cr100441k.

37 M. Kaupp, M. Renz, M. Parthey, M. Stolte, F. Würthner and C. Lambert, Computational and Spectroscopic Studies of Organic Mixed-Valence Compounds: Where Is the Charge?, *Phys. Chem. Chem. Phys.*, 2011, **13**(38), 16973–16986, DOI: 10.1039/C1CP21772K.

38 A. Heckmann and C. Lambert, Organic Mixed-Valence Compounds: A Playground for Electrons and Holes, *Angew. Chem., Int. Ed.*, 2012, **51**(2), 326–392, DOI: 10.1002/anie.201100944.

39 C. Lambert and G. Nöll, The Class II/III Transition in Triarylamine Redox Systems, *J. Am. Chem. Soc.*, 1999, **121**(37), 8434–8442, DOI: 10.1021/ja991264s.

40 K. Lancaster, S. A. Odom, S. C. Jones, S. Thayumanavan, S. R. Marder, J.-L. Brédas, V. Coropceanu and S. Barlow, Intramolecular Electron-Transfer Rates in Mixed-Valence Triarylamines: Measurement by Variable-Temperature ESR Spectroscopy and Comparison with Optical Data, *J. Am. Chem. Soc.*, 2009, **131**(5), 1717–1723, DOI: 10.1021/ja808465c.

41 M. Uebe and A. Ito, Intramolecular Charge Transfer in Kekulé- and Non-Kekulé-Bridged Bis(Triarylamine) Radical Cations: Missing Key Compounds in Organic Mixed-Valence Systems, *Chem.–Asian J.*, 2019, **14**(10), 1692–1696, DOI: 10.1002/asia.201900036.

42 M. Uebe, K. Kaneda, S. Fukuzaki and A. Ito, Bridge-Length-Dependent Intramolecular Charge Transfer in Bis(Dianisylamino)-Terminated Oligo(p-Phenylene)s, *Chem.–Eur. J.*, 2019, **25**(68), 15455–15462, DOI: 10.1002/chem.201903667.

43 K. E. Linton, M. A. Fox, L.-O. Pålsson and M. R. Bryce, Oligo(p-phenyleneethynylene) (OPE) Molecular Wires: Synthesis and Length Dependence of Photoinduced Charge Transfer in OPEs with Triarylamine and Diaryloxadiazole End Groups, *Chem.–Eur. J.*, 2015, **21**(10), 3997–4007, DOI: 10.1002/chem.201406080.

44 A. Heckmann, S. Amthor and C. Lambert, Mulliken–Hush Analysis of a Bis(Triarylamine) Mixed-Valence System with a N···N Distance of 28.7 Å, *Chem. Commun.*, 2006, (28), 2959–2961, DOI: 10.1039/b604603g.

45 C. Lambert and V. Kriegisch, Heterogeneous Electron Transfer Processes in Self-Assembled Monolayers of Amine Terminated Conjugated Molecular Wires, *Langmuir*, 2006, **22**(21), 8807–8812, DOI: 10.1021/la061404t.

46 L. G. Heinz, O. Yushchenko, M. Neuburger, E. Vauthey and O. S. Wenger, Tetramethoxybenzene Is a Good Building Block for Molecular Wires: Insights from Photoinduced Electron Transfer, *J. Phys. Chem. A*, 2015, **119**(22), 5676–5684, DOI: 10.1021/acs.jpca.5b03649.

47 L. Li, J. Z. Low, J. Wilhelm, G. Liao, S. Gunasekaran, C. R. Prindle, R. L. Starr, D. Golze, C. Nuckolls, M. L. Steigerwald, F. Evers, L. M. Campos, X. Yin and L. Venkataraman, Highly Conducting Single-Molecule Topological Insulators Based on Mono- and Di-Radical Cations, *Nat. Chem.*, 2022, **14**(9), 1061–1067, DOI: 10.1038/s41557-022-00978-1.

48 X. Shi, M. Liu, L. Li, J. Zhang, H. Li, Z. Huang, W. Zhang, Z. Zhang, N. Zhou and X. Zhu, Efficient Synthesis of Discrete Oligo(Fluorenediacetylene)s toward Chain-Length-Dependent Optical and Structural Properties, *Polym. Chem.*, 2021, **12**(17), 2598–2605, DOI: 10.1039/D1PY00165E.

49 A. Nafady, T. T. Chin and W. E. Geiger, Manipulating the Electrolyte Medium to Favor Either One-Electron or Two-Electron Oxidation Pathways for (Fulvalendiyl)Dirhodium Complexes, *Organometallics*, 2006, **25**(7), 1654–1663, DOI: 10.1021/om051101e.

50 A. K. Diallo, C. Absalon, J. Ruiz and D. Astruc, Ferrocenyl-Terminated Redox Stars: Synthesis and Electrostatic Effects in Mixed-Valence Stabilization, *J. Am. Chem. Soc.*, 2011, **133**(3), 629–641, DOI: 10.1021/ja109380u.

51 U. Pfaff, A. Hildebrandt, D. Schaarschmidt, T. Hahn, S. Liebing, J. Kortus and H. Lang, Di- and Triferrocenyl (Hetero)Aromatics: Synthesis, Characterization, (Spectro-) Electrochemistry, and Calculations, *Organometallics*, 2012, **31**(19), 6761–6771, DOI: 10.1021/om300511v.

52 R. F. Winter, Half-Wave Potential Splittings $\Delta E_{1/2}$ as a Measure of Electronic Coupling in Mixed-Valent Systems: Triumphs and Defeats, *Organometallics*, 2014, **33**(18), 4517–4536, DOI: 10.1021/om500029x.

53 S. Barlow, C. Risko, S.-J. Chung, N. M. Tucker, V. Coropceanu, S. C. Jones, Z. Levi, J.-L. Brédas and S. R. Marder, Intervalence Transitions in the Mixed-Valence Monocations of Bis(Triarylamines) Linked with Vinylene and Phenylene–Vinylene Bridges, *J. Am. Chem. Soc.*, 2005, **127**(48), 16900–16911, DOI: 10.1021/ja054136e.

54 S. Barlow, C. Risko, S. A. Odom, S. Zheng, V. Coropceanu, L. Beverina, J.-L. Brédas and S. R. Marder, Tuning Delocalization in the Radical Cations of 1,4-Bis[4-(Diarylamino)Styryl]Benzenes, 2,5-Bis[4-(Diarylamino)Styryl] Thiophenes, and 2,5-Bis[4-(Diarylamino)Styryl]Pyrroles through Substituent Effects, *J. Am. Chem. Soc.*, 2012, **134**(24), 10146–10155, DOI: 10.1021/ja3023048.

55 C. Lambert, S. Amthor and J. Schelter, From Valence Trapped to Valence Delocalized by Bridge State Modification in Bis(Triarylamine) Radical Cations: Evaluation of Coupling Matrix Elements in a Three-Level System, *J. Phys. Chem. A*, 2004, **108**(31), 6474–6486, DOI: 10.1021/jp048449s.

56 I. Noviandri, K. N. Brown, D. S. Fleming, P. T. Gulyas, P. A. Lay, A. F. Masters and L. Phillips, The Decamethylferrocenium/Decamethylferrocene Redox Couple: A Superior Redox Standard to the Ferrocenium/Ferrocene Redox Couple for Studying Solvent Effects on

Open Access Article. Published on 18 February 2025. Downloaded on 5/22/2025 3:43:42 PM.
This article is licensed under a Creative Commons Attribution 3.0 Unported Licence.

the Thermodynamics of Electron Transfer, *J. Phys. Chem. B*, 1999, **103**(32), 6713–6722, DOI: **10.1021/jp991381+**.

57 K.-T. Wong, T. Hsi Hung, S. C. Kao, C. Hsien Chou and Y. Oliver Su, Synthesis and Properties of Novel Bis(Triarylamines) Based on a 3,3′-Diphenyl-2,2′-Bithiophene Core, *Chem. Commun.*, 2001, **0**(17), 1628–1629, DOI: **10.1039/B103194P**.

58 M. Renz, K. Theilacker, C. Lambert and M. Kaupp, A Reliable Quantum-Chemical Protocol for the Characterization of Organic Mixed-Valence Compounds, *J. Am. Chem. Soc.*, 2009, **131**(44), 16292–16302, DOI: **10.1021/ja9070859**.

59 M. Renz and M. Kaupp, Predicting the Localized/Delocalized Character of Mixed-Valence Diquinone Radical Anions. Toward the Right Answer for the Right Reason, *J. Phys. Chem. A*, 2012, **116**(43), 10629–10637, DOI: **10.1021/jp308294r**.

60 F. S. Gogesch, S. Schwab, A. Rehse, M. Linseis, A. Baksi, G. H. Clever and R. F. Winter, Diruthenium Complexes with π-Extended Bridging Bis(Alkenyl)Arylene Ligands, A Derived Metallamacrocycle, and Their Oxidized Forms, *Organometallics*, 2023, **42**(21), 3085–3098, DOI: **10.1021/acs.organomet.3c00337**.

61 E. D. Glendening, C. R. Landis and F. Weinhold, Natural Bond Orbital Methods, *Wiley Interdiscip. Rev.: Comput. Mol. Sci.*, 2012, **2**(1), 1–42, DOI: **10.1002/wcms.51**.

62 E. Wu, K. Jacobson and D. Papahadjopoulos, Lateral Diffusion in Phospholipid Multibilayers Measured by Fluorescence Recovery after Photobleaching, *Biochemistry*, 1977, **16**(17), 3936–3941, DOI: **10.1021/bi00636a034**.

63 K. Watanabe, K. Moriya, T. Kouyama, A. Onoda, T. Minatani, S. Y. Takizawa and S. Murata, Photoinduced Transmembrane Electron Transport in DPPC Vesicles: Mechanism and Application to a Hydrogen Generation System, *J. Photochem. Photobiol., A*, 2011, **221**(1), 113–122, DOI: **10.1016/j.jphotochem.2011.04.034**.

64 H. Song, A. Amati, A. Pannwitz, S. Bonnet and L. Hammarström, Mechanistic Insights into the Charge Transfer Dynamics of Photocatalytic Water Oxidation at the Lipid Bilayer–Water Interface, *J. Am. Chem. Soc.*, 2022, **144**(42), 19353–19364, DOI: **10.1021/jacs.2c06842**.

65 N. Sinambela, R. Jacobi, D. Hernández-Castillo, E. Hofmeister, N. Hagmeyer, B. Dietzek, L. González and A. Pannwitz, Alignment and Photooxidation Dynamics of a Perylene Diimide Chromophore in Lipid Bilayers, *Mol. Syst. Des. Eng.*, 2023, **8**(7), 842–852, DOI: **10.1039/D2ME00243D**.

66 E. Krieger, T. Darden, S. B. Nabuurs, A. Finkelstein and G. Vriend, Making Optimal Use of Empirical Energy Functions: Force-Field Parameterization in Crystal Space, *Proteins: Struct., Funct., Genet.*, 2004, **57**(4), 678–683, DOI: **10.1002/prot.20251**.

67 E. Krieger, J. E. Nielsen, C. A. E. M. Spronk and G. Vriend, Fast Empirical pK_a Prediction by Ewald Summation, *J. Mol. Graphics Modell.*, 2006, **25**(4), 481–486, DOI: **10.1016/j.jmgm.2006.02.009**.

68 D. Marsh, *Handbook of Lipid Bilayers*, CRC Press, 2013, DOI: **10.1201/b11712**.

69 D. Drabik, G. Chodaczek, S. Kraszewski and M. Langner, Mechanical Properties Determination of DMPC, DPPC, DSPC, and HSPC Solid-Ordered Bilayers, *Langmuir*, 2020, **36**(14), 3826–3835, DOI: **10.1021/acs.langmuir.0c00475**.

70 S. Dutta, B. Watson, S. Mattoo and J.-C. Rochet, Calcein Release Assay to Measure Membrane Permeabilization by Recombinant Alpha-Synuclein, *Bio-Protoc.*, 2020, **10**(14), e3690, DOI: **10.21769/BioProtoc.3690**.

71 B. Maherani, E. Arab-Tehrany, A. Kheirolomoom, D. Geny and M. Linder, Calcein Release Behavior from Liposomal Bilayer; Influence of Physicochemical/Mechanical/Structural Properties of Lipids, *Biochimie*, 2013, **95**(11), 2018–2033, DOI: **10.1016/j.biochi.2013.07.006**.

72 L. E. Garner, J. Park, S. M. Dyar, A. Chworos, J. J. Sumner and G. C. Bazan, Modification of the Optoelectronic Properties of Membranes via Insertion of Amphiphilic Phenylenevinylene Oligoelectrolytes, *J. Am. Chem. Soc.*, 2010, **132**(29), 10042–10052, DOI: **10.1021/ja1016156**.

73 B. Wang, M. Wang, A. Mikhailovsky, S. Wang and G. C. Bazan, A Membrane-Intercalating Conjugated Oligoelectrolyte with High-Efficiency Photodynamic Antimicrobial Activity, *Angew. Chem., Int. Ed.*, 2017, **56**(18), 5031–5034, DOI: **10.1002/anie.201701146**.

74 C. M. Legaspi, R. E. Stubbs, M. Wahadoszaman, D. J. Yaron, L. A. Peteanu, A. Kemboi, E. Fossum, Y. Lu, Q. Zheng and L. J. Rothberg, Rigidity and Polarity Effects on the Electronic Properties of Two Deep Blue Delayed Fluorescence Emitters, *J. Phys. Chem. C*, 2018, **122**(22), 11961–11972, DOI: **10.1021/acs.jpcc.7b12025**.

75 A. Pannwitz, H. Saaring, N. Beztsinna, X. Li, M. A. Siegler and S. Bonnet, Mimicking Photosystem I with a Transmembrane Light Harvester and Energy Transfer-Induced Photoreduction in Phospholipid Bilayers, *Chem.–Eur. J.*, 2021, **27**(9), 3013–3018, DOI: **10.1002/chem.202003391**.

76 *Principles of Fluorescence Spectroscopy*, ed. J. R. Lakowicz, Springer US, Boston, MA, 2006, DOI: **10.1007/978-0-387-46312-4**.

77 R. E. P. Nau, J. Bösking and A. Pannwitz, Compartmentalization Accelerates Photosensitized NADH to NAD^+ Conversion, *ChemPhotoChem*, 2022, **6**(11), e202200158, DOI: **10.1002/cptc.202200158**.

78 M. W. Sutherland and B. A. Learmonth, The Tetrazolium Dyes MTS and XTT Provide New Quantitative Assays for Superoxide and Superoxide Dismutase, *Free Radical Res.*, 1997, **27**(3), 283–289, DOI: **10.3109/10715769709065766**.

79 S. Fukuzumi, M. Ishikawa and T. Tanaka, Mechanisms of Photo-Oxidation of NADH Model Compounds by Oxygen, *J. Chem. Soc., Perkin Trans. 2*, 1989, (8), 1037–1045, DOI: **10.1039/P29890001037**.

80 V. Balzani, P. Ceroni and A. Juris, *Photochemistry and Photophysics: Concepts, Research, Applications*, John Wiley & Sons, 2014.

81 Y. Rahimi, A. Goulding, S. Shrestha, S. Mirpuri and S. K. Deo, Mechanism of Copper Induced Fluorescence Quenching of Red Fluorescent Protein, DsRed, *Biochem. Biophys. Res. Commun.*, 2008, **370**(1), 57–61, DOI: **10.1016/j.bbrc.2008.03.034**.

Supporting Information for:

Light-Driven Electron Transfer in a Lipid Bilayer with Mixed Valence Molecular Wires

Novitasari Sinambela,[+[a]] Moritz Nau,[+[b]] Gernot Haug,[[b]] Michael Linseis,[[b]] Philip Koblischek,[[a]] Rainer F. Winter,*[[b]] Andrea Pannwitz*[[a,c,d,e]]

Institute of Inorganic Chemistry I, Ulm University, Albert-Einstein-Allee 11, 89081 Ulm (Germany)
Department of Chemistry, University of Konstanz, Universitätsstraße 10, 78464 Konstanz (Germany); E-mail: rainer.winter@uni-konstanz.de
Department of Inorganic and Analytical Chemistry, Friedrich Schiller Universität Jena, Humboldtstr. 8, 07743 Jena (Germany); E-mail: andrea.pannwitz@uni-jena.de
Center for Energy and Environmental Chemistry Jena (CEEC), Friedrich-Schiller-Universität Jena, Philisophenweg 7a, 07743 Jena (Germany)
Helmholtz Institute for Polymers in Energy Applications Jena (HIPOLE Jena), Lessingstraße 12–14, 07743 Jena, (Germany)
+ These authors contributed equally

Table of Contents

General Methods 3
S1 Synthesis and Characterization 5
NMR Spectroscopy 14
Mass Spectrometry 18
S2 Cyclic Voltammetry 20
S3 UV-Vis/NIR Spectroscopy 24
S4 Molecular Dynamics Simulation 28
S5 Calceine-Luminescence Leakage Test 29
S6 Liposome preparation 30
S7 The Typical Hydrodynamic Diameter of DPPC Liposome 32
S8 Spectra of LEDs and DPPC with integrated $\mathbf{1}^{H}$ or $\mathbf{2}^{H}$ 34
S9 Photoinduced electron transfer reactions in the membrane 34
S10 Stern-Volmer Quenching Experiment 37
S11 Atomic Coordinates of DFT Geometry-Optimized Structures 40
References 149

General Methods

NMR Spectroscopy. ^{1}H-NMR (400 MHz) and ^{13}C-NMR (101 MHz) spectra were recorded on a Bruker Avance III 400 spectrometer or on a Bruker Avance Neo 800 spectrometer in the solvent indicated at room temperature (if not stated otherwise). The spectra were referenced to the residual protonated solvent (^{1}H) or the solvent signal (^{13}C).

ESI Mass Spectrometry. Samples were measured on an MS system from Thermo (Bremen, Germany) consisting of an ITQ 900 ion trap mass spectrometer and a DPC direct injection system using the direct insertion probe (DIP) technique. The sample was placed on a rhenium wire and evaporated using a current slope of 100 mA × sec^{-1} (from 0 to 800 mA). The following MS parameters were used: scan range 50-2000 *m/z*. The ion source was set to 200 °C. The damping gas flow was set to 0.3 mL helium. 3 Microscans were used at a maximum ion time of 25 ms.

Cyclic Voltammetry. All voltammetric experiments were performed under argon atmosphere. The voltammograms were recorded using a BASi Epsilon potentiostat and a cell with a platinum electrode (Ø = 1.10 mm, MFC-2012 *BASi*). Prior to each measurement series, the working electrode was freshly polished with diamond pastes with grain sizes of 1 µm and 0.25 µm from *Buehler & Wirtz*. An AgCl and a spiral-shaped Pt wire were used as the reference and counter electrodes. TBA^{+} BAr^{F24-} was used in a concentration of 0.1 mM in CH_2Cl_2 as a supporting electrolyte. All redox potentials were referenced *versus* the FcH/FcH^{+} redox couple after each measurement series by addition of roughly equimolar amounts of ferrocene to the analyte solution. Simulations of cyclic voltammograms were performed using the *DigiSim* program.[1] Therefore, recorded voltammograms at different scan rates (100-2000 mVs^{-1}) were uploaded. Two subsequent one-electron oxidations were used to describe the overall redox process ($A \rightarrow B + e^{-}$; $B \rightarrow C + e^{-}$). The initial parameters were set as follows: c = 0.8 mM (**1**^{Me}), 1.3 mM (**2**^{Me}), electrode surface area = 0.0256 cm^2, *T* = 298 K, CdI = 8×10^{-7} F, planar electrode geometry, α = 0.5, k_s = 0.01 cms^{-1}, diffusion coefficient = 5.32×10^{-6} cm^{2}s^{-1} (1^{Me}), 2.76×10^{-6} cm^{2}s^{-1} (2^{Me}). The program was then allowed to freely change the chosen parameters iteratively to adequately replicate the experimental voltammograms at any scan rate, until the highest level of convergence was reached.

Computational Details. Ground state electronic structures were calculated based on density functional theory (DFT) employing the Gaussian 16 program package.[2] Geometry optimization was followed by vibrational analysis. Open-shell systems were calculated within the unrestricted Kohn-Sham (UKS) approach. Solvent effects were taken into account using the polarizable continuum model, employing the standard parameter for methylene chloride.[3] The double-ξ basis set of Ahlrichs and co-worker with def2-SVP (split-valence-plus-polarization)[4,5] was employed in combination with Becke´s three-parameter hybrid functional, using Lee-Yang-Parr´s non-local correlation (B3LYP).[6] The B3LYP hybrid functional was artificially mixed with 35% exact Hartree-Fock exchange to compensate for the inherent tendency of the DFT method to delocalize charges in extended π-conjugated systems.[7–10] The GaussSum[11], Avogadro[12], GNU Parallel[13] and vmd program packages were used in combination with POV-Ray for data processing, and graphical representations.

UV-Vis/NIR/IR Spectroscopy. UV-Vis/NIR spectra were acquired using a TIDAS fiber optic diode array spectrometer, combining an MCS UV/NIR and a PGS NIR instrument from *j&m Analytic AG* or using a JASCO V760 spectrometer. Extinction coefficients were determined from solutions of the analyte in a quartz cell with an optical path length of 0.2 cm, purchased from *Hellma Analytics*. IR spectra were recorded on a *Tensor II* instrument by *Bruker* equipped with a halogen NIR lamp and an MCT detector.

A Wenking Pos 2 potentiostat from *intelligent controls GmbH* was used for spectroelectrochemical measurements. According to HARTL's design, a custom-made optically transparent electrochemical thin-layer cell (OTTLE) was used,[14] consisting of a working and counter electrode made of Pt grid and a thin silver wire as a *pseudo* reference electrode. The electrodes are sandwiched in between two optically transparent CaF_2 windows. CH_2Cl_2 was used as the solvent. A 0.1 M solution in TBA^+BAr^{F24-} in methylene chloride was used for the spectroelectrochemical studies.

Fluorescence spectroscopy. Luminescence spectra were recorded on an FP-8500 Spectrofluorometer. Starna fluorescence quartz cuvettes with a path length of 1 cm and screw caps with an air-tight silicon seal were used

Confocal microscopy. The images were acquired on a Leica TCS SP8 confocal microscope equipped with a 488 nm laser as an excitation source and detected within a range of 500-600 nm. Sample wells (m-Slide 8 Well ibiTreat) characterized giant vesicles. Confocal microscopy images were processed with the LasX software.

Fluorescence lifetimes. Fluorescence lifetimes were determined with a DeltaPro from Horiba Scientific using a 372 nm pulsed Laser source (Class 3B Laser Product, <0.5 W peak in pulsed and CW mode). The Delta Pro instrumentation consists of a DeltaDiode (Picosecond diode controller), DeltaHub (High throughput TCSPC controller), DPS-1 (Detector Power supply), and a PPD (Picosecond photon detection module). The IRF (Instrument response function) was measured with LUDOX silica nanoparticles. Fits were done with the software EzTime.

S1 Synthesis and Characterization

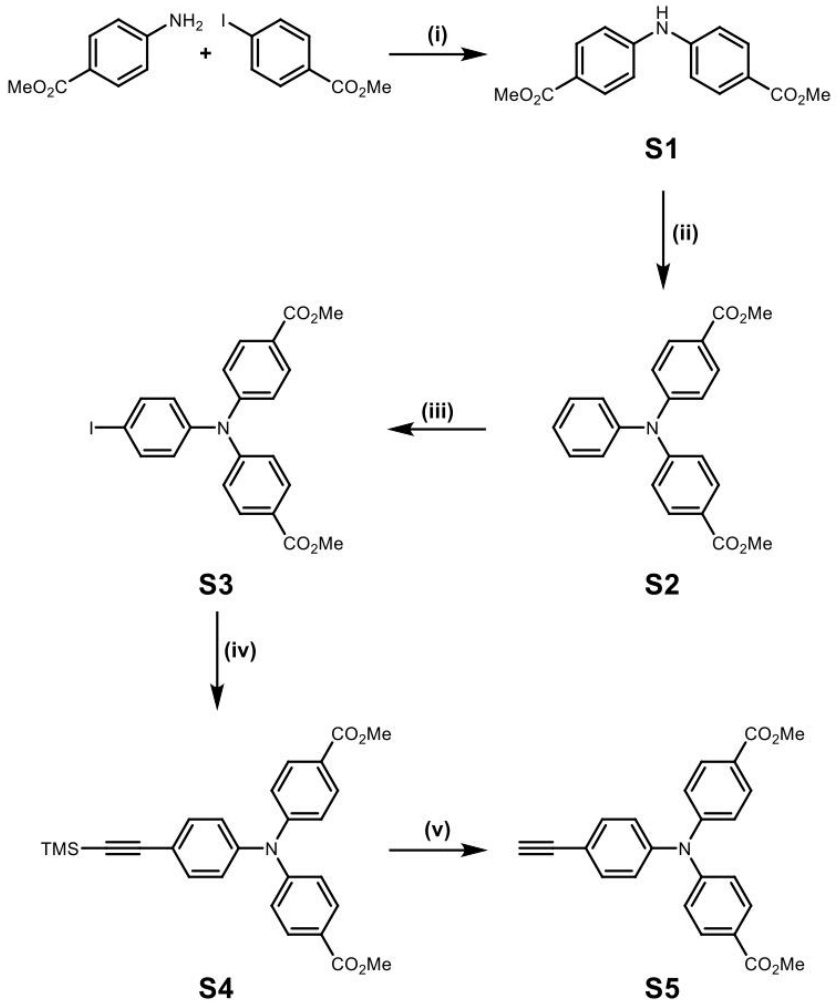

Scheme S1 | Schematic route for the synthesis of intermediates **S1**-**S5**. (i) $Pd(OAC)_2$, *rac*-BINAP, Cs_2CO_3, toluene, 100 °C, overnight; (ii) bromobenzene, $Pd(OAC)_2$, P^tBu_3, Cs_2CO_3, toluene, 100 °C, overnight; (iii) ICl, $Zn(OAc)_2$, 1,4-dioxane, r.t., 2 h; (iv) TMSA, CuI, $PdCl_2(PPh_3)_2$, NEt_3, THF, 70 °C, overnight; (v) K_2CO_3, MeOH/THF (1:1), r.t., 3 h.

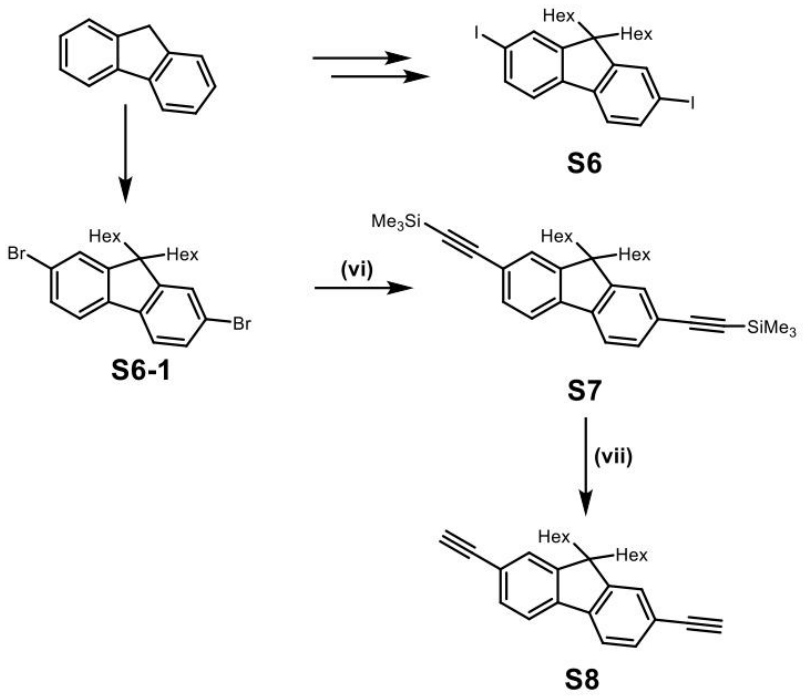

Scheme 2 | Schematic route for the synthesis of intermediates **S6**-**S8**. (vi) TMSA, CuI, $PdCl_2(PPh_3)_2$, NEt_3, THF, 60 °C, overnight; (v) K_2CO_3, MeOH/THF (1:1), r.t., 3 h.

General remarks on the experimental procedures

If not stated otherwise, all syntheses were performed under inert gas conditions using standard SCHLENK techniques. Solvents used under inert atmosphere were predried over common desiccants and subsequently stored in Schlenk flasks over molecular sieves of appropriate pore sizes.[15] Dry toluene was obtained from an *MB-SPS-7* solvent purifier by *M. Braun Inertgas-Systeme GmbH*. All other solvents used were used as purchased in technical grade. Commercially available starting materials used in the syntheses were purchased from commercial suppliers and were used without further purification.

***N*-(Methyl-4-benzoate)-4-carbomethoxyaniline (S1)**

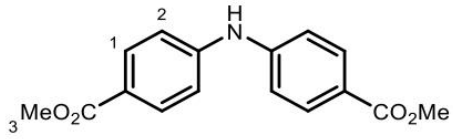

Methyl 4-aminobenzoate (907 mg, 6.00 mmol, 1.20 eq.), methyl 4-iodobenzoate (1.31 g, 5.00 mmol, 1.00 eq.), Cs_2CO_3 (2.28 g, 7.00 mmol, 1.40 eq.), $Pd(OAc)_2$ (56.1 mg, 0.25 mmol, 0.05 eq.), and *rac*-BINAP (249 mg, 0.40 mmol, 0.08 eq.) were dissolved in dry, degassed toluene (50 mL). The resulting mixture was stirred at 100 °C overnight. After allowing the mixture to cool to ambient temperature, it was filtered and the residue was washed with toluene (3 × 15 mL). The organic phases were combined and the solvent was removed under reduced pressure. The crude product was purified *via* column chromatography on silica (hexanes/ethyl acetate; 3:2) to give compound **S1** in 82% yield (1.17 g, 4.10 mmol).

^{1}H-NMR ($CDCl_3$, 400 MHz, 298 K) δ [ppm] = 7.98 (d, $^3J_{HH}$ = 8.7 Hz, 4H, H-1/2), 7.13 (d, $^3J_{HH}$ = 8.7 Hz, 4H, H-1/2), 6.31 (s, 1H, *N*-H), 3.90 (s, 6H, H-3).

***N*,*N*-Di(methyl-4-benzoate)aniline (S2)**

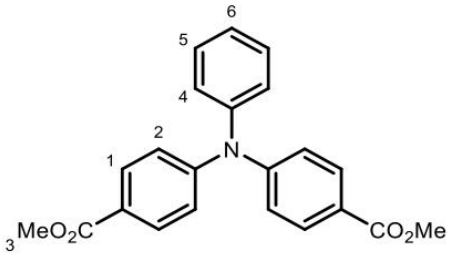

Compound **S1** (600 mg, 2.10 mmol, 1.00 eq.), Cs_2CO_3 (1.03 g, 3.15 mmol, 1.50 eq.), $Pd(OAc)_2$ (29.2 mg, 0.13 mmol, 0.05 eq.), bromobenzene (0.44 mL, 659 mg, 4.20 mmol, 2.00 eq.), and P^tBu_3 (10%wt in hexane, 0.77 mL, 52.6 mg, 0.26 mmol, 0.10 eq.) were dissolved in dry, degassed toluene (50 mL). The resulting mixture was stirred at 100 °C overnight. The reaction was quenched by the addition of water (30 mL) and the phases were separated. The aqueous phase was further extracted with methylene chloride (3 × 30 mL) and the combined organic phases were dried over $MgSO_4$. The solvent was removed under reduced pressure. The crude product was used without further purification. Compound **S2** was obtained in quantitative yield (759 mg, 2.10 mmol).

^{1}H-NMR ($CDCl_3$, 400 MHz, 298 K) δ [ppm] = 7.91 (d, $^3J_{HH}$ = 8.7 Hz, 4H, H-1/2), 7.37-7.11 (m, 5H, H-4/5/6), 7.09 (d, $^3J_{HH}$ = 8.7 Hz, 4H, H-1/2), 3.89 (s, 6H, H-3).

***N*,*N*-Di(methyl-4-benzoate)-4-iodoaniline (S3)**

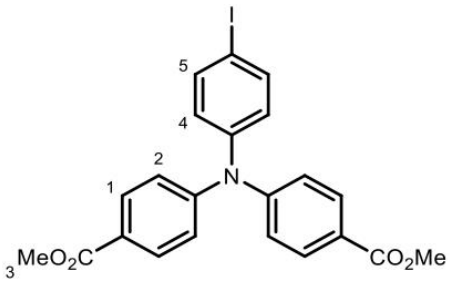

Compound **S2** (820 mg, 2.27 mmol, 1.00 eq.) was dissolved in dry, degassed 1,4-dioxane (5 mL) and subsequently added dropwise to a mixture of $Zn(OAc)_2$ (417 mg, 2.27 mmol, 1.00 eq.) and ICl (0.23 mL, 738 mg, 4.55 mmol, 2.16 eq.) in 1,4-dioxane (5 mL). The mixture was stirred at ambient temperature for two hours. Then, the reaction was quenched by the addition of a saturated aqueous solution of $Na_2S_2O_3$. The product was extracted with CH_2Cl_2 (3 × 30 mL) and the combined extracts were dried over $MgSO_4$. The solution was concentrated under reduced pressure and subsequently filtered over silica. Compound **S3** was obtained as tan solid in 90% yield (995 mg, 2.04 mmol). Recrystallization from EtOH gave colorless crystals.

^{1}H-NMR ($CDCl_3$, 400 MHz, 298 K) δ [ppm] = 7.92 (d, $^3J_{HH}$ = 8.7 Hz, 4H, H-1/2), 7.63 (d, $^3J_{HH}$ = 7.6 Hz, 4H, H-5/4), 7.08 (d, $^3J_{HH}$ = 8.7 Hz, 4H, H-1/2), 6.89 (d, $^3J_{HH}$ = 7.6 Hz, 4H, H-5/4), 3.90 (s, 6H, H-3).

***N*,*N*-Di(methyl-4-benzoate)-4-trimethylsilylaniline (S4)**

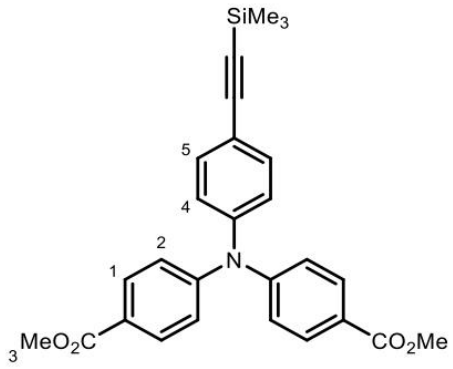

To a solution of compound **S3** (600 mg, 1.23 mmol, 1.00 eq.) in THF/NEt_3 (30 mL, 1:1), CuI (11.8 mg, 0.06 mmol, 0.05 eq.) and $PdCl_2(PPh_3)_2$ (43.5 mg, 0.06 mmol, 0.05 eq.) were added, followed by the addition of ethynyltrimethylsilane (0.26 mL, 182 mg, 1.85 mmol, 1.50 eq.). The mixture was stirred at 70 °C overnight. Then, the reaction was quenched by the addition of a saturated aqeous solution of NH_4Cl. The product was extracted with CH_2Cl_2 (3 × 30 mL) and the combined extracts were dried over $MgSO_4$. The solvent was removed under reduced pressure and the crude product was purified *via* column chromatography on silica (hexanes/ethyl acetate; 9:1) to give compound **S4** in 82% yield (456 mg, 1.00 mmol).

^{1}H-NMR ($CDCl_3$, 400 MHz, 298 K) δ [ppm] = 7.92 (d, $^3J_{HH}$ = 8.7 Hz, 4H, H-1/2), 7.41 (d, $^3J_{HH}$ = 8.5 Hz, 4H, H-5/4), 7.08 (d, $^3J_{HH}$ = 8.7 Hz, 4H, H-1/2), 7.04 (d, $^3J_{HH}$ = 8.5 Hz, 4H, H-5/4), 3.90 (s, 6H, H-3), 0.25 (s, 9H, TMS-H).

***N*,*N*-Di(methyl-4-benzoate)-4-ethynylaniline (S5)**

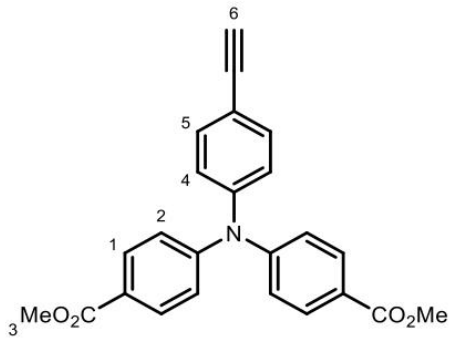

Compound **S4** (456 mg, 1.00 mmol, 1.00 eq.) was dissolved in MeOH/THF (30 mL, 1:1) and K_2CO_3 (275 mg, 2.00 mmol, 2.00 eq.) was added. The mixture was stirred for three hours at ambient temperature. Subsequently, the reaction was quenched with water (20 mL) and the product was extracted with methylene chloride (3 × 30 mL). The combined extracts were dried over $MgSO_4$ and the solvent was removed under reduced pressure. The crude product was further purified *via* column chromatography on silica (hexanes/ethyl acetate; 9:1) to give 294 mg (0.76 mmol) of compound **S5** in 76% yield.

^{1}H-NMR ($CDCl_3$, 400 MHz, 298 K) δ [ppm] = 7.93 (d, $^3J_{HH}$ = 8.8 Hz, 4H, H-1/2), 7.43 (d, $^3J_{HH}$ = 8.7 Hz, 4H, H-5/4), 7.09 (d, $^3J_{HH}$ = 8.8 Hz, 4H, H-1/2), 7.06 (d, $^3J_{HH}$ = 8.7 Hz, 4H, H-5/4), 3.90 (s, 6H, H-3), 3.09 (s, 9H, H-6).

9,9-Dihexyl-2,7-diiodo-9H-fluorene (S6)

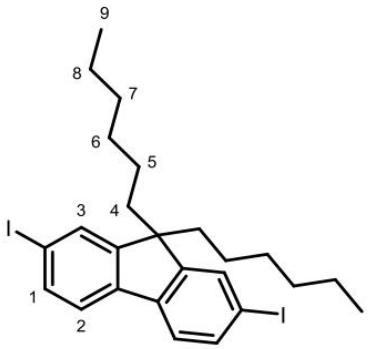

Compound **S6** was prepared according to literature procedures in a two-step protocol starting from fluorene.[16]

^{1}H-NMR ($CDCl_3$, 400 MHz, 298 K) δ [ppm] = 7.64 (dd, $^3J_{HH}$ = 8.7 Hz, $^4J_{HH}$ = 1.6 Hz, 2H, H-1), 7.64 (s, 2H, H-3), 7.64 (d, $^3J_{HH}$ = 8.7 Hz, 2H, H-2), 1.92-1.84 (m, 4H, H-4), 1.16-1.08 (m, 4H, H-5), 1.08-0.98 (m, 8H, H-8/7), 0.78 (t, $^3J_{HH}$ = 7.2 Hz, 6H, H-9), 0.62-0.51 (m, 4H, H-6).

9,9-dihexyl-2,7-dibromo-9H-fluorene (S6-1)

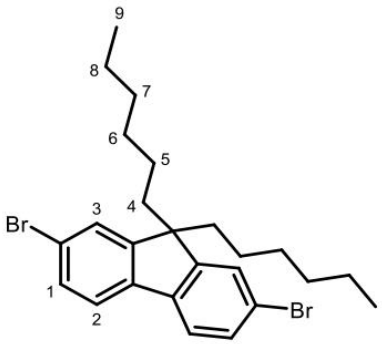

Compound **S6-1** was prepared by stirring a solution of 2,7-dibromo-9H-fluorene (10.0 g, 30.8 mmol, 1.00 eq.), benzyl triethylammonium chloride (355 mg, 1.56 mmol, 0.05 eq.), 1-Bromohexane (11 mL 78.6 mmol, 2.55 eq.) in DMSO (50 mL) and aqueous NaOH (18.24 g, 456 mmol, 40 eq.) solution was added dropwise until the solution turned to blue. The reaction mixture was stirred at room temperature for 3 h. The mixture was extracted once with petroleum ether and the organic phase was washed once with 1 M HCl and three times with water. The organic layer was dried over anhydrous $MgSO_4$. The solvent was removed under reduced pressure. The residual powder was washed with ice-cold ethanol to purify the compound to give the desired product (**S6-1**, 15.2 g, 98%).

^{1}H-NMR ($CDCl_3$, 400 MHz, 298 K) δ [ppm] = 7.52 (d, *J* = 8.0 Hz, 2H), 7.47 – 7.42 (m, 4H), 1.91 (dd, *J* = 8.0, 4.2 Hz, 4H), 1.12 (h, *J* = 7.1 Hz, 12H), 0.78 (t, *J* = 7.3 Hz, 6H), 0.58 (p, *J* = 7.0 Hz, 4H).

2,7-Di(trimethylsilyl)-9,9-dihexylfluorene (S7)

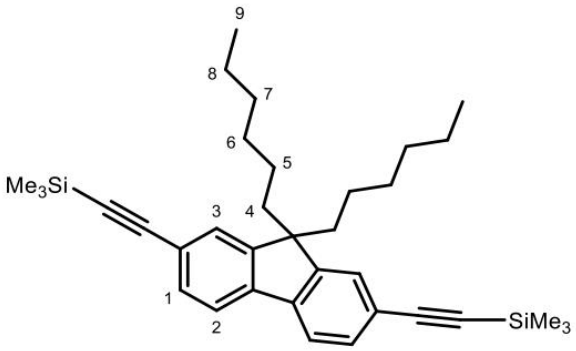

2,7-Dibromo-9,9-dihexylfluorene (492 mg, 1.00 mmol, 1.00 eq.) was dissolved in THF/NEt_3 (10 mL, 7:3). Then, ethynyl(trimethyl)silane (0.43 mL, 295 mg, 3.00 mmol, 3.00 eq.), CuI (19.0 mg, 0.10 mmol, 0.10 eq.) and $PdCl_2(PPh_3)_2$ (70.2 mg, 0.10 mmol, 0.10 eq.) were added. The mixture was stirred at 60 °C overnight. After cooling to room temperature, the reaction was quenched by the addition of ethyl acetate and sat. $NH_4Cl_{(aq.)}$. The phases were separated and the aqueous phase was further extracted with ethyl acetate (2 × 20 mL). The combined organic extracts were dried over $MgSO_4$. The solvent was removed under reduced pressure and the crude product was purified *via* column chromatography on silica (hexanes) to give compound **S7** in 87% yield (456 mg, 0.87 mmol).

^{1}H-NMR ($CDCl_3$, 400 MHz, 298 K) δ [ppm] = 7.59 (d, $^3J_{HH}$ = 7.7 Hz, 2H, H-2), 7.45 (dd, $^3J_{HH}$ = 7.7 Hz, $^4J_{HH}$ = 1.5 Hz, 2H, H-1), 7.42 (d, $^4J_{HH}$ = 1.5 Hz, 2H, H-3), 1.98-1.88 (m, 4H, H-4), 1.15-1.06 (m, 4H, H-5), 1.06-0.94 (m, 8H, H-8/7), 0.77 (t, $^3J_{HH}$ = 7.2 Hz, 6H, H-9), 0.58-0.47 (m, 4H, H-6), 0.29 (s, 18H, TMS-H).

2,7-Di(ethynyl)-9,9-dihexylfluorene (S8)

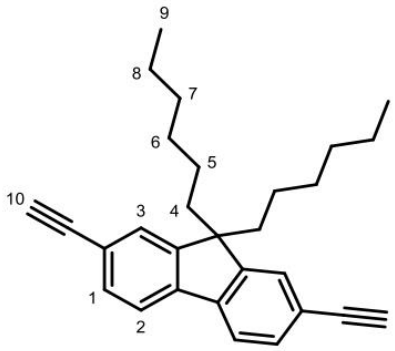

Compound **S7** (457 mg, 0.87 mmol, 1.00 eq.) was dissolved in CH_2Cl_2/MeOH (14 mL, 1:1) and K_2CO_3 (480 mg, 3.47 mmol, 4.00 eq.) was added. The mixture was stirred for three hours at ambient temperature. Subsequently, the reaction was quenched with water (50 mL) and the product was extracted with ethyl acetate (3 × 30 mL). The combined organic phases were dried over $MgSO_4$ and the solvent was removed under reduced pressure. The crude product was further purified *via* column chromatography on silica (hexanes) to give compound **S8** in 80% yield (265 mg, 0.80 mmol).

^{1}H-NMR ($CDCl_3$, 400 MHz, 298 K) δ [ppm] = 7.63 (d, $^3J_{HH}$ = 7.9 Hz, 2H, H-2), 7.48 (dd, $^3J_{HH}$ = 7.9 Hz, $^4J_{HH}$ = 1.4 Hz, 2H, H-1), 7.46 (d, $^4J_{HH}$ = 1.4 Hz, 2H, H-3), 3.15 (s, 2H, H-10), 1.97-1.88 (m, 4H, H-4), 1.16-1.05 (m, 4H, H-5), 1.05-0.95 (m, 8H, H-8/7), 0.77 (t, $^3J_{HH}$ = 7.2 Hz, 6H, H-9), 0.61-0.48 (m, 4H, H-6).

2,7-Bis(N,N-di(methyl-4-benzoate)-4-ethynylaniline]-9,9-dihexylfluorene ($1^{Me/H}$)

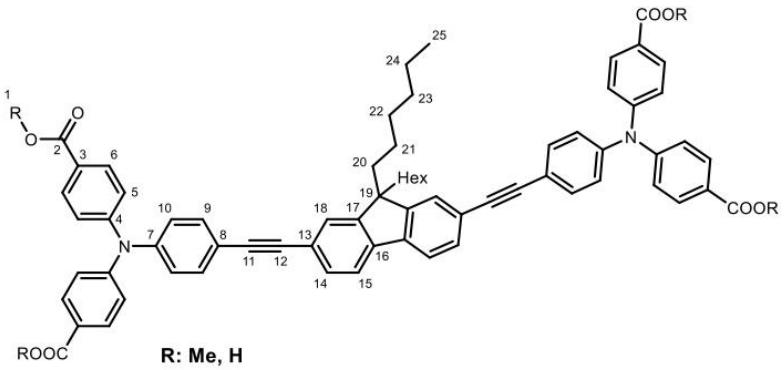

Precursors **S5** (388 mg, 1.01 mmol, 2.20 eq.) and **S6** (270 mg, 0.46 mmol, 1.00 eq.) were dissolved in THF/NEt_3 (8 mL; 1:1). CuI (8.80 mg, 0.46 mmol, 0.10 eq.) and $PdCl_2(PPh_3)_2$ (32.3 mg, 0.46 mmol, 0.10 eq.) were added. The reaction mixture was stirred at 70 °C overnight. Subsequently, the saturated aqueous solution of NH_4Cl. The crude product was extracted with ethyl acetate (3 × 20 mL) and the combined extracts were subsequently dried over $MgSO_4$. The solvent was removed under reduced pressure and the crude product was purified *via* column chromatography on silica (hexanes/ethyl acetate; 4:1). Compound $\mathbf{1^{Me}}$ was obtained in 49% (250 mg, 0.23 mmol).

To deprotect the carboxylic acid functionalities, compound $\mathbf{1^{Me}}$ was dissolved in THF/H_2O (3 mL, 2:1) and LiOH (110 mg, 4.60 mmol, 20.0 eq.) was added. The resulting mixture was stirred at room temperature overnight, then, water was added and the product was extracted with ethyl acetate. The organic phase was dried over $MgSO_4$ and the solvent was removed under reduced pressure. The crude product was washed with methylene chloride and pentane to give compound $\mathbf{1^{H}}$ in quantitative yield (236 mg, 0.23 mmol).

^{1}H-NMR ($CDCl_3$, 800 MHz, 298 K) δ [ppm] = 7.94 (d, c^3J_{HH} = 8.7 Hz, 8H, H-6), 7.66 (d, $^3J_{HH}$ = 8.0 Hz, 2H, H-15), 7.51 (d, $^3J_{HH}$ = 8.7 Hz, 6H, H-9/14), 7.49 (s, 2H, H-18), 7.15-7.09 (m, 12H, H-5/10), 3.91 (s, 12H, H-1), 2.02-1.93 (m, 4H, H-20), 1.15-0.99 (m, 12H, H-21/22/23), 0.77 (t, $^3J_{HH}$ = 8.3 Hz, 6H, H-25), 0.65-0.56 (m, 4H, H-24).

^{13}C{^{1}H}-NMR ($CDCl_3$, 201 MHz, 298 K) δ [ppm] = 166.6, 151.1, 150.6, 146.0, 140.7, 133.0, 131.1, 130.7, 125.9, 125.4, 124.8, 123.1, 121.9, 120.0, 119.6, 90.9, 89.3, 55.3, 52.0, 40.4, 31.6, 29.7, 23.7, 22.6, 14.0.

ESI-MS *calc.* for m/z = 1100.50 (M^-); *found* m/z = 1100.05.

UV-Vis Absorption (CH_2Cl_2) λ_{max} = 366 nm; $\varepsilon_{max} = 112\times10^3$ $M^{-1}cm^{-1}$.

^{1}H-NMR (DMSO-d_6, 400 MHz, 298 K) δ [ppm] = 12.77 (s, 4H, H-1), 7.97-7.79 (m, 10H, H-6/15), 7.63 (s, 2H, H-18), 7.59-7.47 (m, 6H, H-9/14), 7.21-7.09 (m, 12H, H-5/10), 2.02 (bs, 4H, H-20), 1.12-0.84 (m, 12H, H-21/22/23), 0.70 (t, $^3J_{HH}$ = 7.6 Hz, 6H, H-25), 0.45 (bs, 4H, H-24).

^{13}C{^{1}H}-NMR (DMSO-d_6, 101 MHz, 298 K) δ [ppm] = 167.2, 151.3, 150.4, 146.5, 140.8, 133.4, 131.6, 131.1, 126.1, 125.9, 125.6, 123.6, 121.8, 121.1, 118.7, 91.0, 90.1, 55.5, 31.4, 29.4, 23.9, 22.4, 14.3.

ESI-MS *calc.* for m/z = 1044.43 (M^-); *found* m/z = 1044.46.

1,4-Bis(7-[N,N-di(methyl-4-benzoate)-4-ethynylaniline]-9,9-dihexylfluoren-2-yl)buta-1,3-diyne ($2^{Me/H}$)

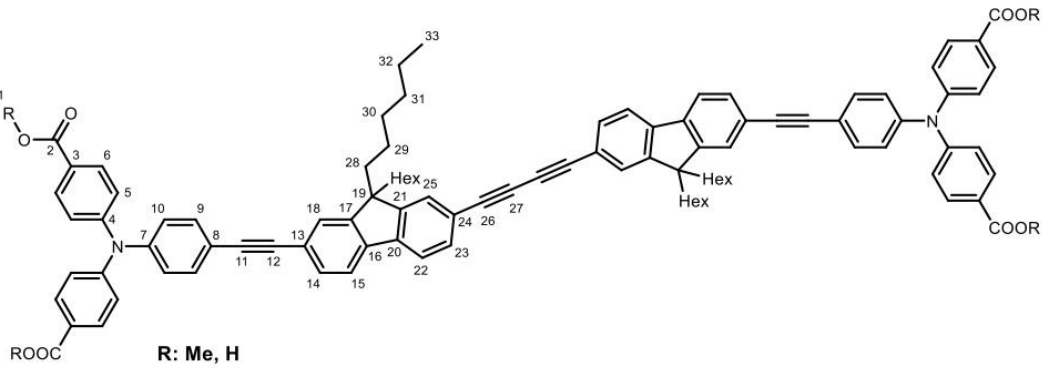

Compounds **S3** (560 mg, 1.15 mmol, 2.20 eq) and **S8** (200 mg, 0.52 mmol, 1.00 eq.) were dissolved in THF/NEt_3 (25 mL; 3:2). CuI (9.90 mg, 0.05 mmol, 0.10 eq.) and $PdCl_2(PPh_3)_2$ (36.5 mg, 0.05 mmol, 0.10 eq.) were added. The reaction mixture was stirred at 70 °C overnight and another portion of the catalyst was added. After additional 24saturated aqueous soluztion of NH_4Cl. The crude product was extracted with ethyl acetate (3 × 30 mL) and the combined extracts were subsequently dried over $MgSO_4$. The solvent was removed under reduced pressure and the crude product was purified *via* column chromatography on silica (hexanes/ethyl acetate; 4:1). Compound $\mathbf{2^{Me}}$ was obtained in 23% yield (90.0 mg, 0.06 mmol).

$\mathbf{2^{Me}}$ was then subjected to an ester-cleavage reaction. Therefore, compound $\mathbf{2^{Me}}$ was dissolved in THF/H_2O (3 mL, 2:1) and LiOH (20.0 eq.) was added. The resulting mixture was stirred at room temperature overnight, then, water was added and the product was extracted with ethyl acetate. The organic phase was dried over $MgSO_4$ and the solvent was removed under reduced pressure. The crude product was washed with methylene chloride and pentane to give compound $\mathbf{2^{H}}$ in quantitative yield (86 mg, 0.06 mmol).

^{1}H-NMR ($CDCl_3$, 800 MHz, 298 K) δ [ppm] = 7.94 (d, $^3J_{HH}$ = 8.7 Hz, 8H, H-6), 7.68-7.64 (m, 4H, H-15/22), 7.54-7.47 (m, 12H, H-9/14/18/23/25), 7.14-7.09 (m, 12H, H-5/10), 3.91 (s, 12H, H-1), 2.01-1.92 (m, 8H, H-28), 1.15-0.98 (m, 24H, H-29/30/31), 0.81-0.74 (m, 12H, H-33), 0.65-0.56 (m, 8H, H-32).

^{13}C{^{1}H}-NMR ($CDCl_3$, 201 MHz, 298 K) δ [ppm] = 166.3, 151.4, 151.2, 150.6, 146.1, 141.7, 140.7, 140.4, 132.9, 131.7, 130.9, 130.6, 127.0, 125.9, 125.5, 125.5, 124.9, 124.9, 123.1, 123.1, 121.9, 120.0, 119.4, 90.6, 89.3, 40.3, 31.6, 31.5, 29.7, 29.7, 23.8, 22.6, 13.8.

ESI-MS *calc.* for m/z = 1481.75 (M^-); *found* m/z = 1481.34.

UV-Vis Absorption (CH_2Cl_2) λ_{max} = 375 nm; $\varepsilon_{max} = 140\times10^3$ $M^{-1}cm^{-1}$.

^{1}H-NMR (Acetone-d_6, 400 MHz, 298 K) δ [ppm] = 11.12 (s, 4H, H-1), 8.00 (d, $^3J_{HH}$ = 8.7 Hz, 8H, H-6), 7.94-7.87 (m, 4H), 7.74-7.64 (m, 4H), 7.64-7.53 (m, 8H), 7.25-7.15 (m, 12H, H-5/10), 2.18-2.09 (m, 8H, H-28), 1.18-0.97 (m, 24H, H-29/30/31), 0.81-0.71 (m, 12H, H-33), 0.68-0.55 (m, 8H, H-32).

^{13}C{^{1}H}-NMR (Acetone-d_6, 101 MHz, 298 K) δ [ppm] = 209.1, 166.2, 151.2, 150.7, 146.4, 140.8, 140.5, 133.0, 133.0, 131.3, 130.8, 126.93 125.9, 125.5, 125.5, 125.2, 125.2, 123.2, 123.2, 122.2, 120.3, 119.3, 90.5, 89.4, 55.4, 55.3, 39.9, 39.8, 31.4, 31.4, 23.7, 22.3, 13.4.

ESI-MS *calc.* for m/z = 1425.69 (M^-); *found* m/z = 1425.45.

13

NMR Spectroscopy

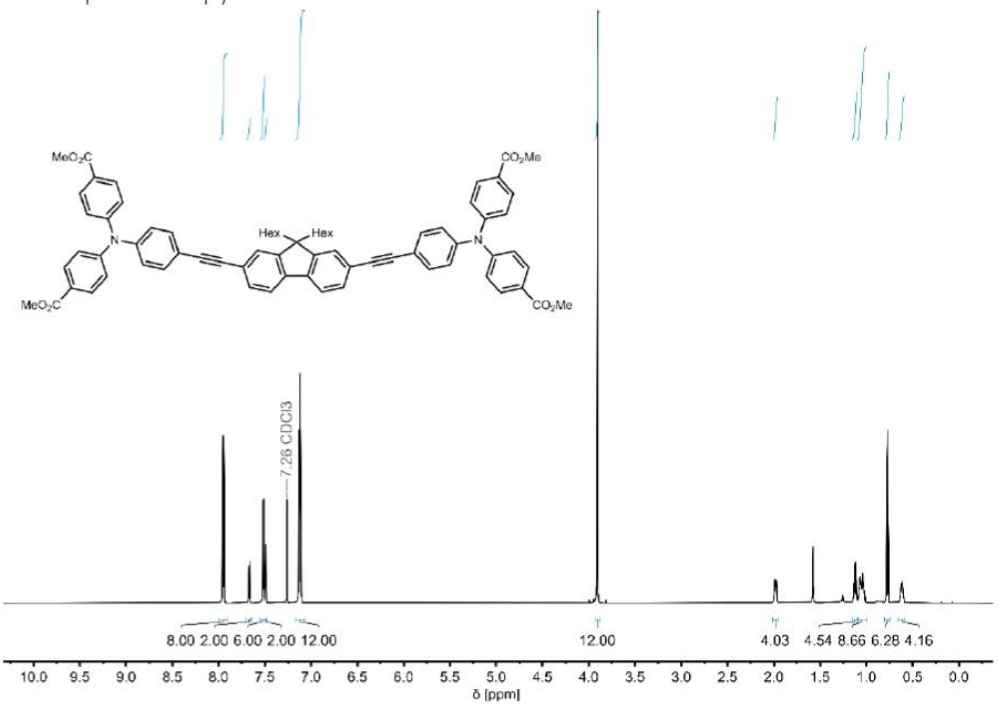

Figure S1. ^{1}H-NMR (800 MHz, 298 K) spectrum of compound **1^{Me}**, measured in $CDCl_3$.

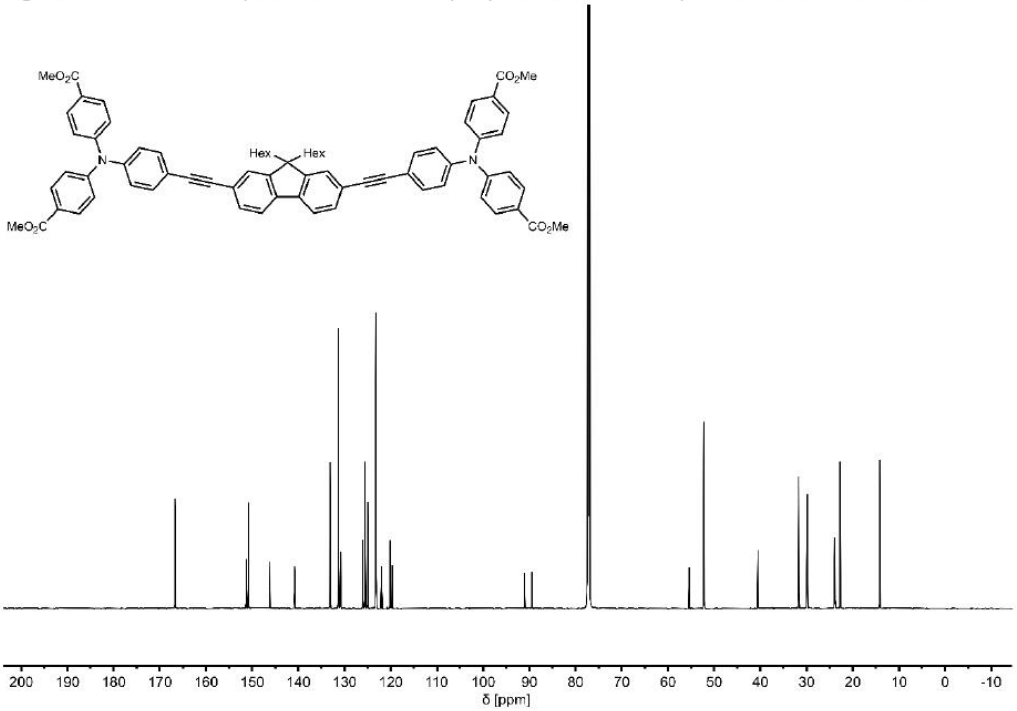

Figure S2. ^{13}C-NMR (202 MHz, 298 K) spectrum of compound **1^{Me}**, measured in $CDCl_3$.

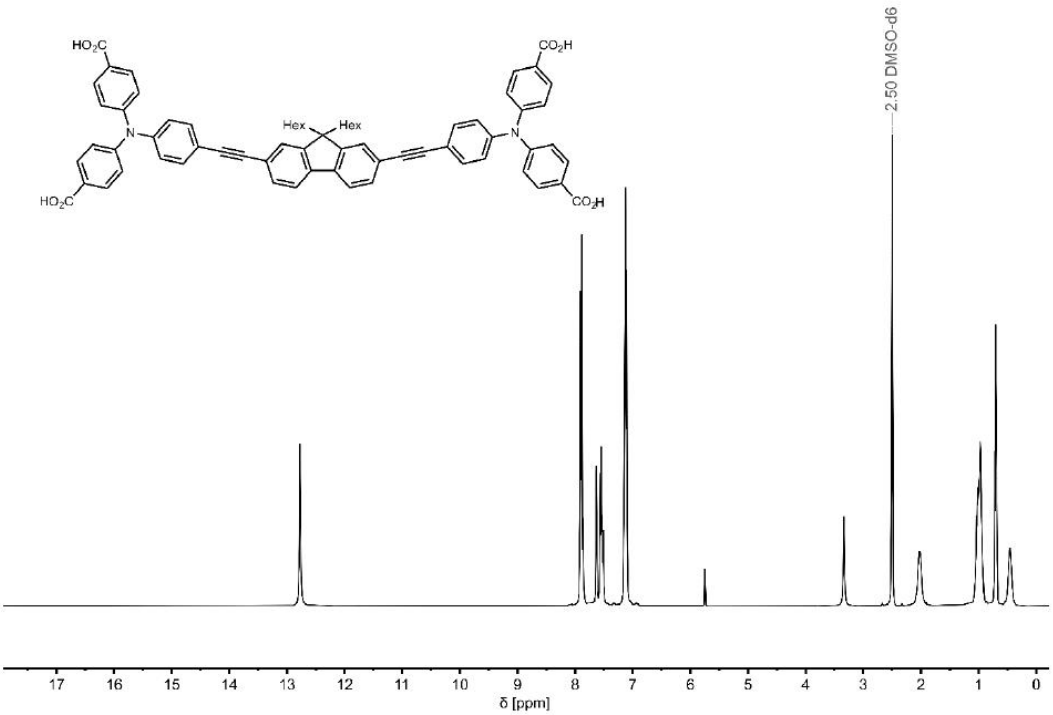

Figure S3. ^{1}H-NMR (400 MHz, 298 K) spectrum of compound **1^{H}**, measured in DMSO-d_6.

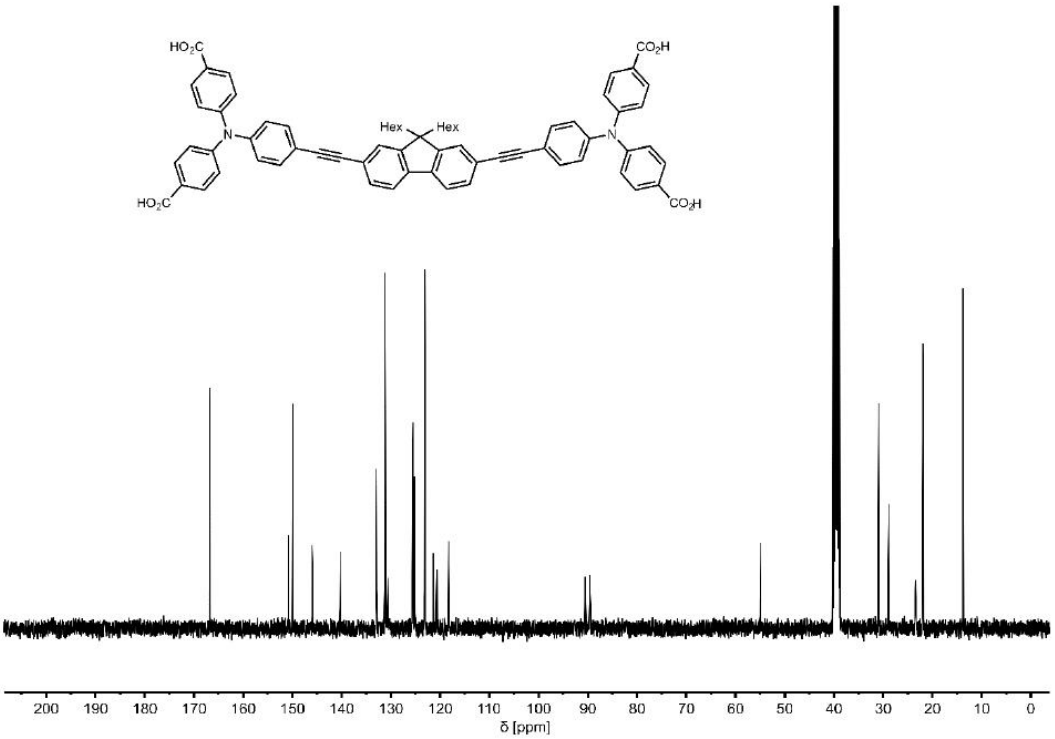

Figure S4. ^{13}C-NMR (400 MHz, 298 K) spectrum of compound **1^{H}**, measured in DMSO-d_6.

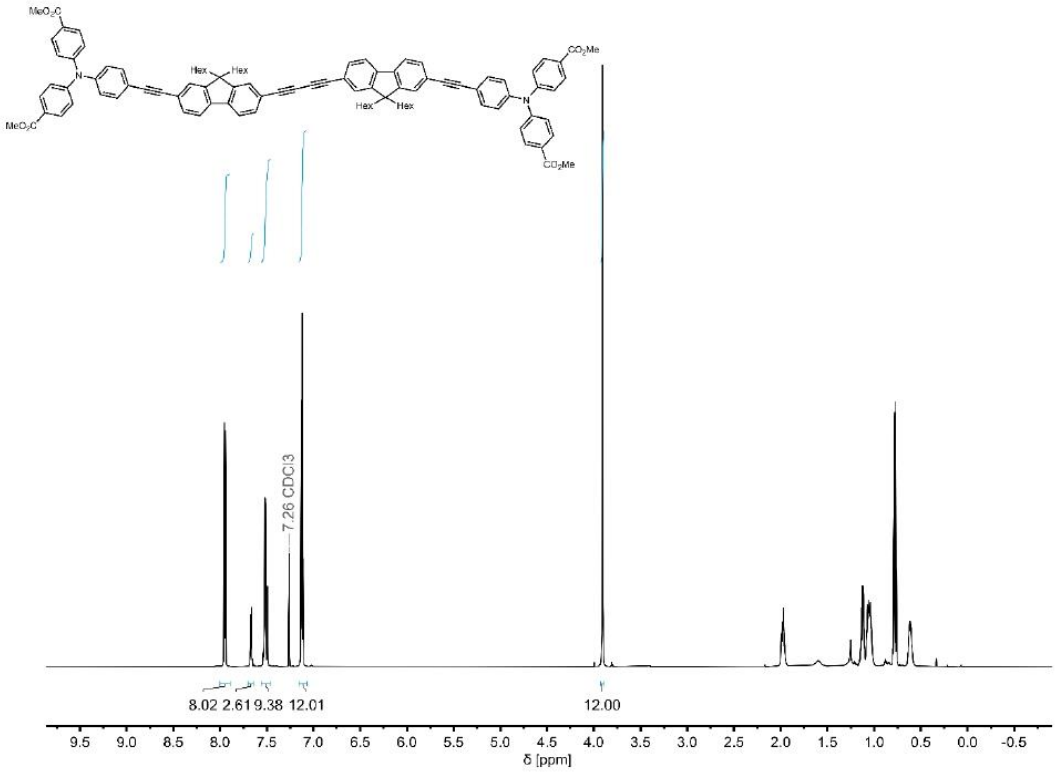

Figure S5. ^{1}H-NMR (800 MHz, 298 K) spectrum of compound **2^{Me}**, measured in $CDCl_3$.

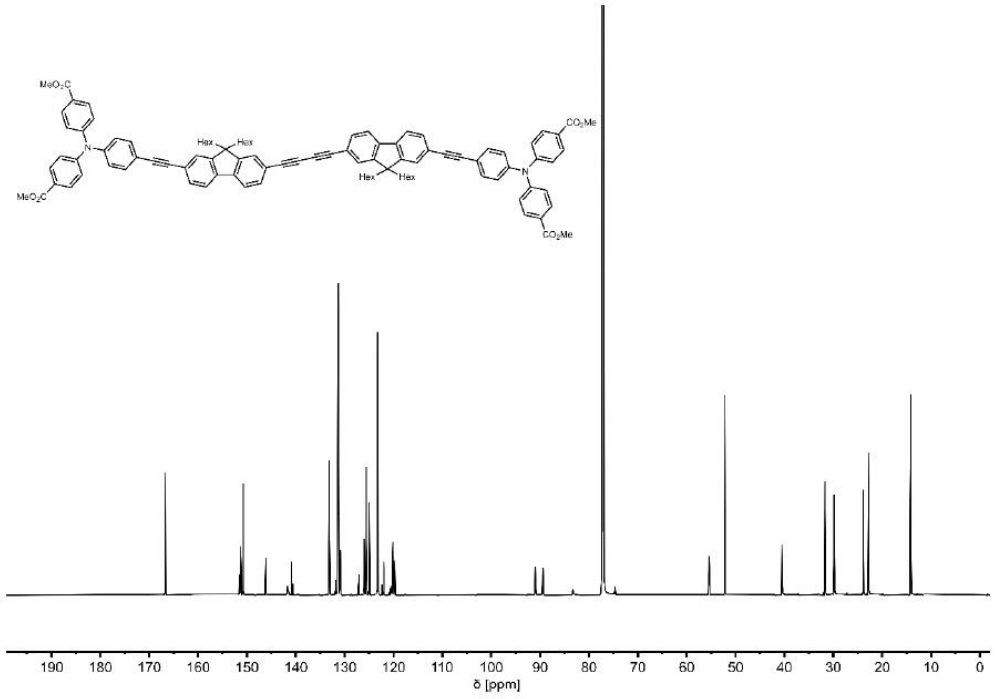

Figure S6. ^{13}C-NMR (800 MHz, 298 K) spectrum of compound **2^{Me}**, measured in $CDCl_3$.

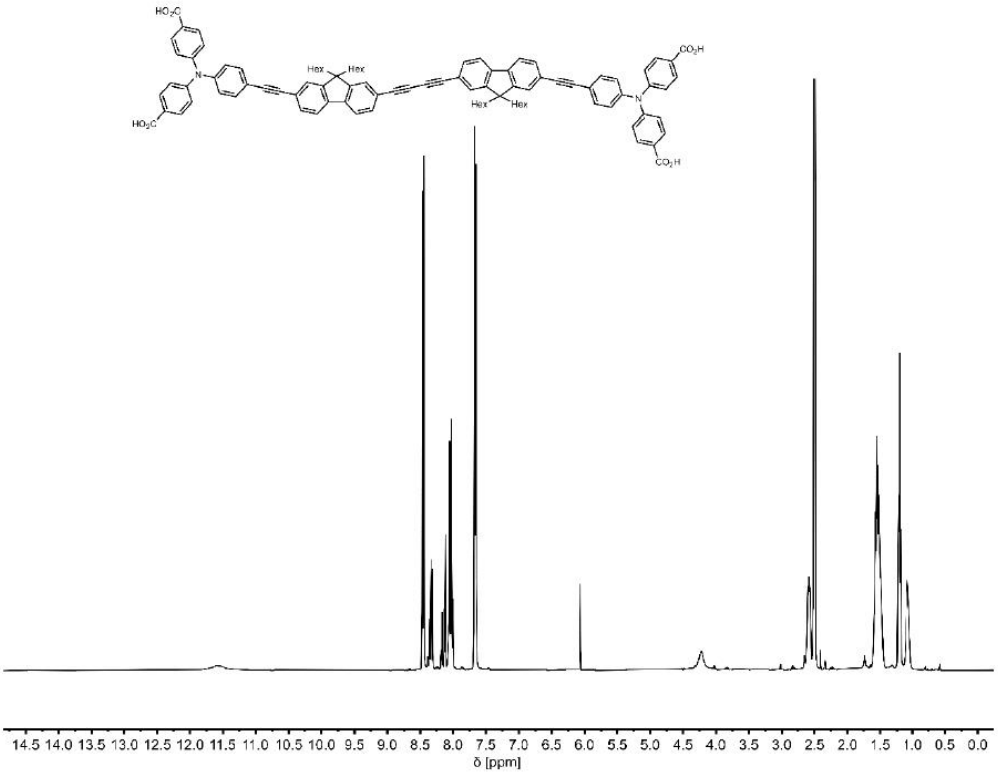

Figure S7. ^{1}H-NMR (400 MHz, 298 K) spectrum of compound **2^{H}**, measured in acetone-d_6.

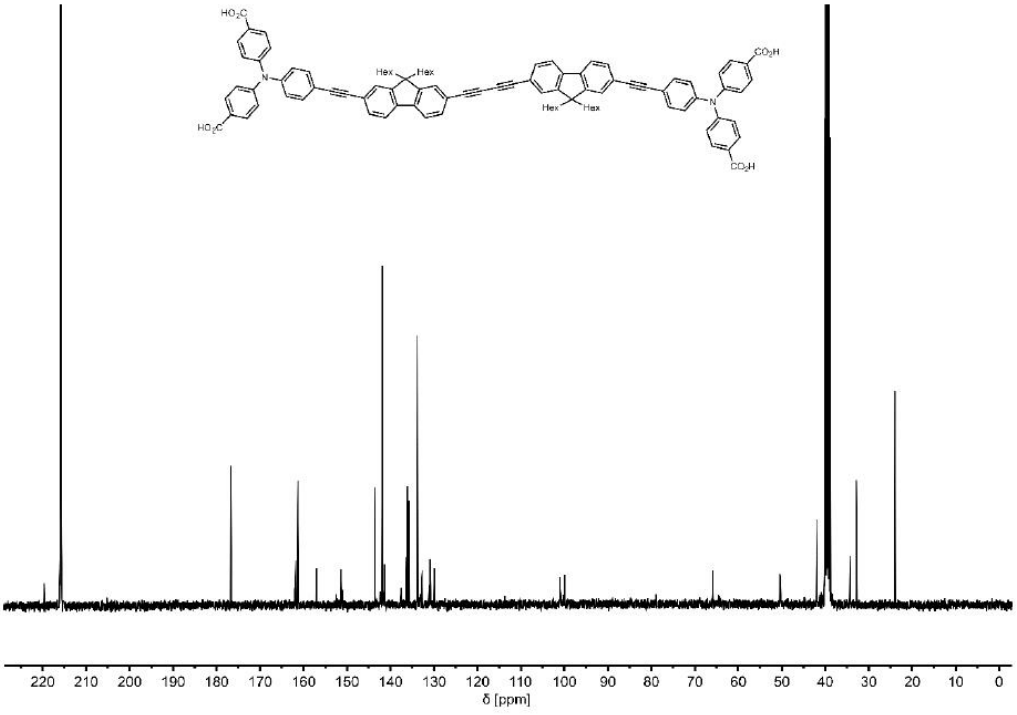

Figure S8. ^{13}C-NMR (400 MHz, 298 K) spectrum of compound **2^{H}**, measured in acetone-d_6.

Mass Spectrometry

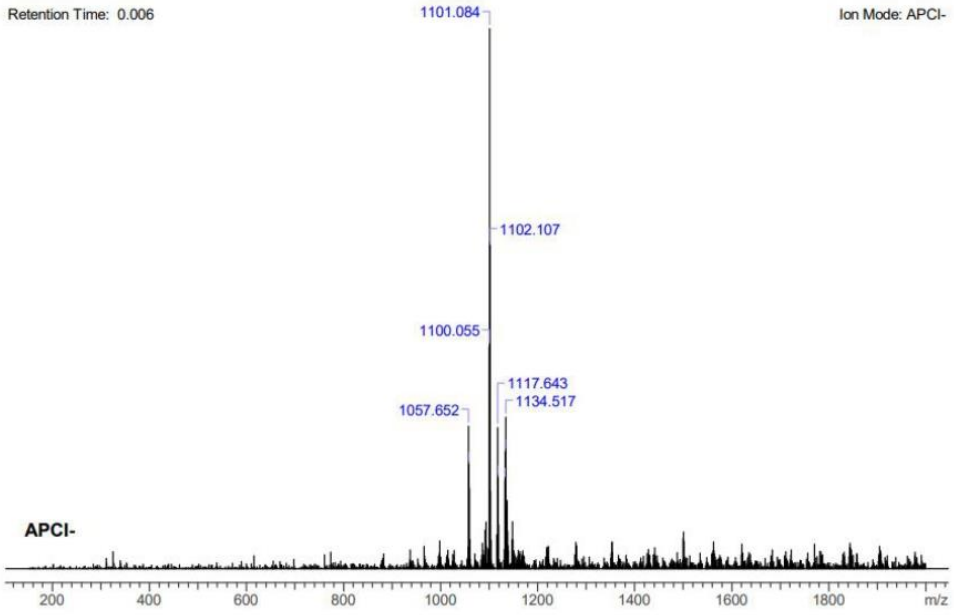

Figure S9. ESI mass spectrum of $\mathbf{1}^{Me}$, recorded in negative ion mode.

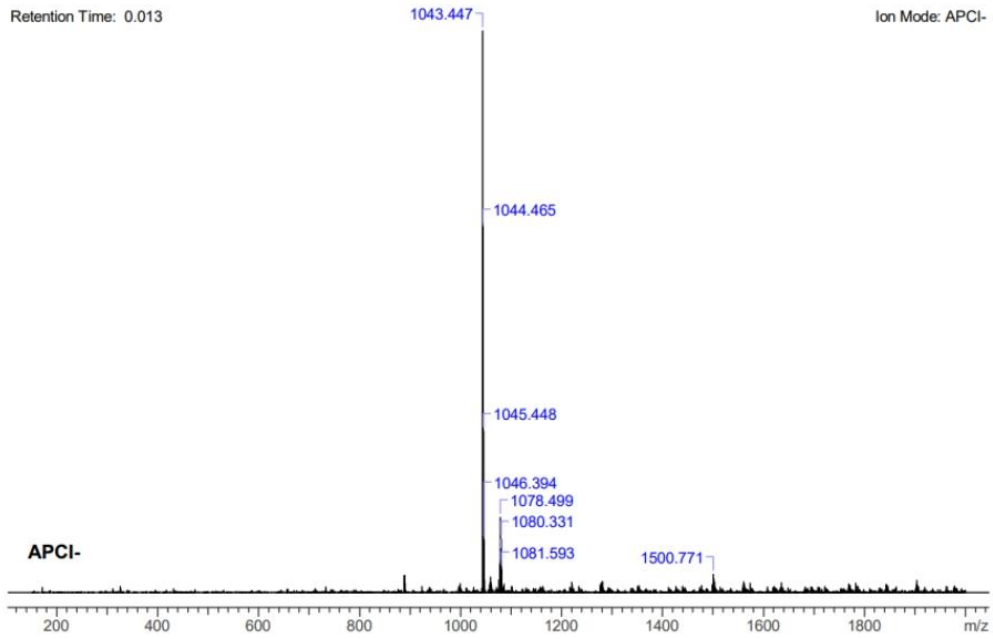

Figure S10. ESI mass spectrum of $\mathbf{1}^{H}$, recorded in negative ion mode.

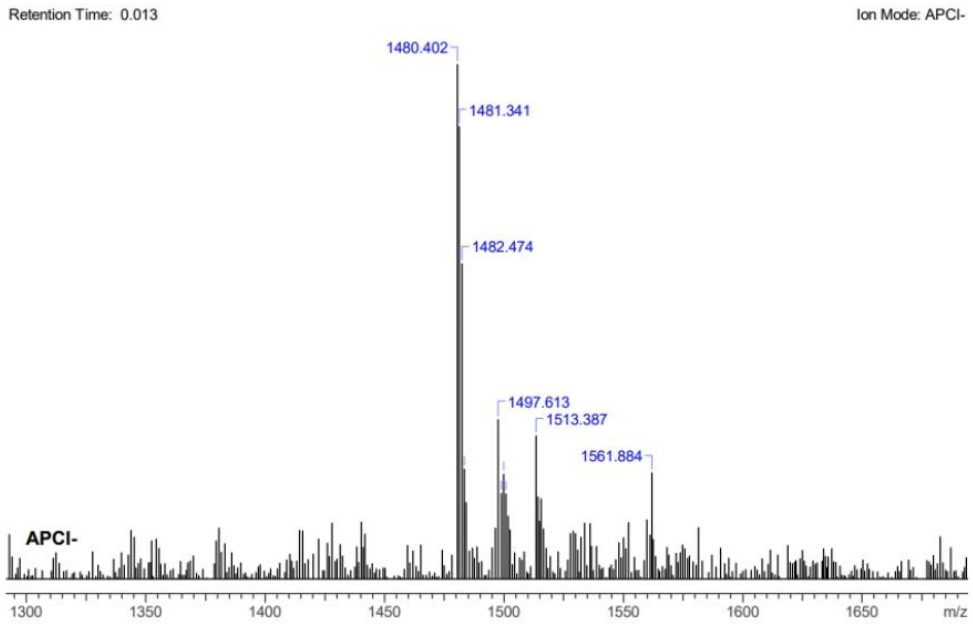

Figure S11. ESI mass spectrum of **2**^{Me}, recorded in negative ion mode.

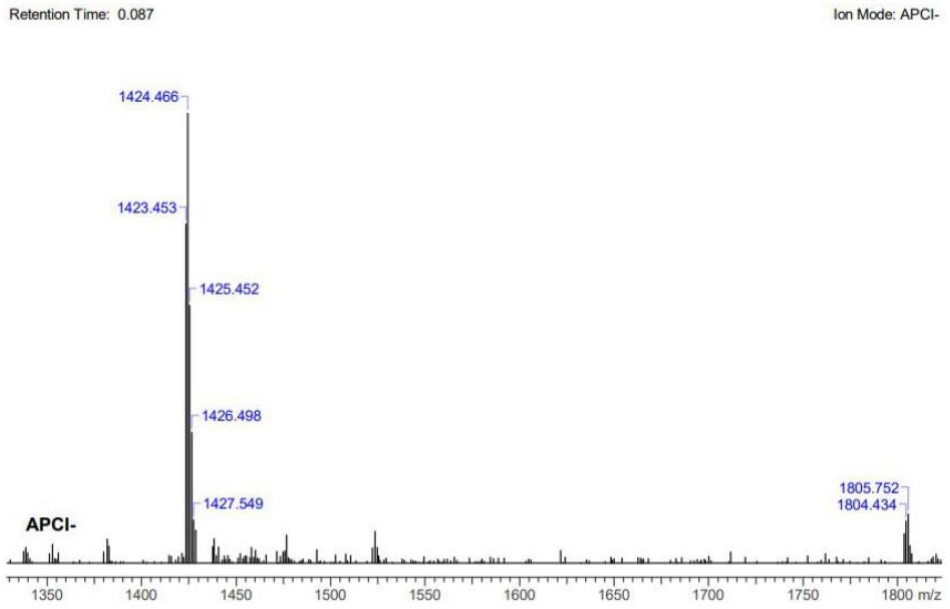

Figure S12. ESI mass spectrum of **2**^{H}, recorded in negative ion mode.

S2 Cyclic Voltammetry

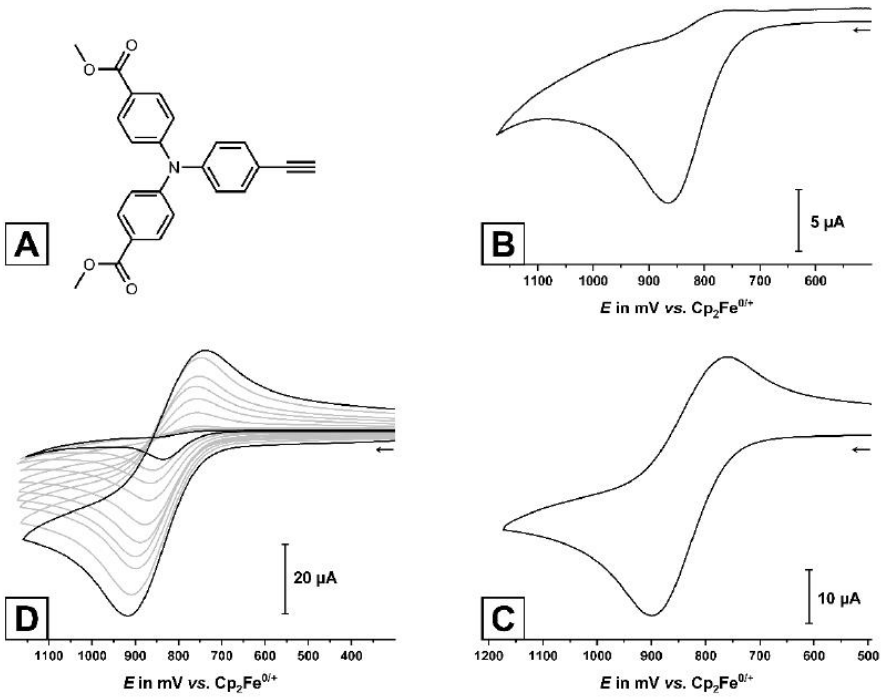

Figure 13. A: Molecular structure of compound **S5**. B. Cyclic voltammogram of S5 at a scan rate of 100 mV/s in 0.1 mM TBA^+ $BAr^{F_{24}-}$ CH_2Cl_2 at r. t. C: Cyclic voltammogram of **S5** at a scan rate of 800 mV/s in 0.1 mM TBA^+ $BAr^{F_{24}-}$ CH_2Cl_2 at r. t. D: Cyclic voltammograms of **S5** (in 0.1 mM TBA^+ $BAr^{F_{24}-}$ CH_2Cl_2 at r. t) at different scan rates ranging from 25 mV/s to 2000 mV/s.

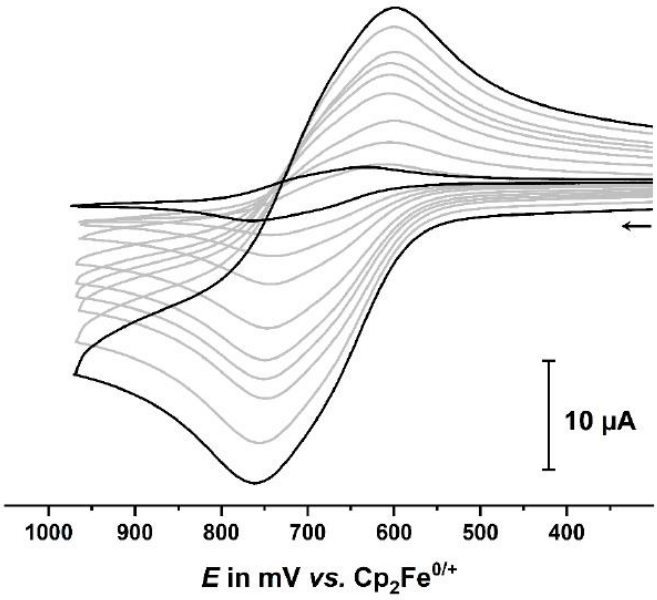

Figure 14. Cyclic voltammograms of $\mathbf{1}^{Me}$ (in 0.1 mM TBA^+ $BAr^{F_{24}-}$ CH_2Cl_2 at r. t.) at different scan rates ranging from 25 mV/s to 2000 mV/s.

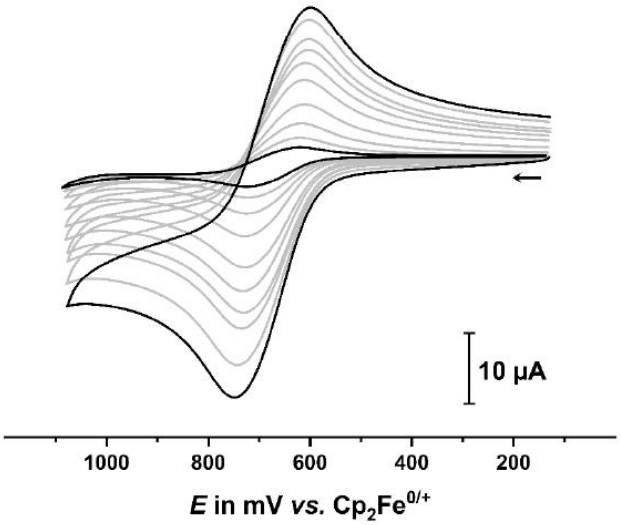

Figure 15. Cyclic voltammograms of $\mathbf{2}^{Me}$ (in 0.1 mM TBA^+ $BAr^{F_{24}-}$ CH_2Cl_2 at r. t.) at different scan rates ranging from 25 mV/s to 2000 mV/s.

Table S1. Electrochemical data of compound **S5** (0.1 mM TBA^+ $BAr^{F_{24}-}$ CH_2Cl_2 at r. t).

Scan rate [mVs^{-1}]	$E_{1/2}^{0/n+}$ [mV]	Δ E_p [mV]
25	790	90
50	810	95
100	815	95
200	810	115
400	815	120
600	825	130
800	830	140
1000	825	140
1500	830	160
2000	830	175

Table S2. Electrochemical data of ester $\mathbf{1}^{Me}$ (0.1 mM TBA^+ $BAr^{F_{24}-}$ CH_2Cl_2 at r. t).

Scan rate [mVs^{-1}]	$E_{1/2}^{0/n+}$ [mV]	Δ E_p [mV]
25	685	110
50	675	130
100	670	130
200	675	140
400	675	140
600	675	145
800	680	145
1000	675	150
1500	680	155
2000	680	160

Table S3. Electrochemical data of ester $\mathbf{2}^{\mathbf{Me}}$ (0.1 mM TBA^+ $BAr^{F_{24}-}$ CH_2Cl_2 at r. t).

Scan rate [mVs^{-1}]	$E_{1/2}^{0/n+}$ [mV]	Δ E_p [mV]
25	675	105
50	670	105
100	670	105
200	670	120
400	670	120
600	670	125
800	670	130
1000	670	135
1500	670	140
2000	675	150

Table S4. Electrochemical data obtained from the digital simulation of the cyclic voltammograms of $\mathbf{1}^{\mathbf{Me}}$ and $\mathbf{2}^{\mathbf{Me}}$ in CH_2Cl_2/NBu_4^+ $[BAr^{F_{24}}]^-$ (0.1 M, T = 293 K (±3 K) v = 600 mV/s).

	$\mathbf{1}^{\mathbf{Me}}$	$\mathbf{2}^{\mathbf{Me}}$
$E_{1/2}^{0/+}$ [mV]	635	640
$E_{1/2}^{+/2+}$ [mV]	715	685
ΔE	80	45
K_c	23	6
$\alpha^{0/+}$ [eV]	0.41	0.55
$\alpha^{+/2+}$ [eV]	0.79	0.55
$k_s^{0/+}$ [cm/s]	0.009	0.005
$k_s^{+/2+}$ [cm/s]	0.011	0.012
D [cm^2/s]	5.32×10^{-6}	2.76×10^{-6}

S3 UV-Vis/NIR Spectroscopy

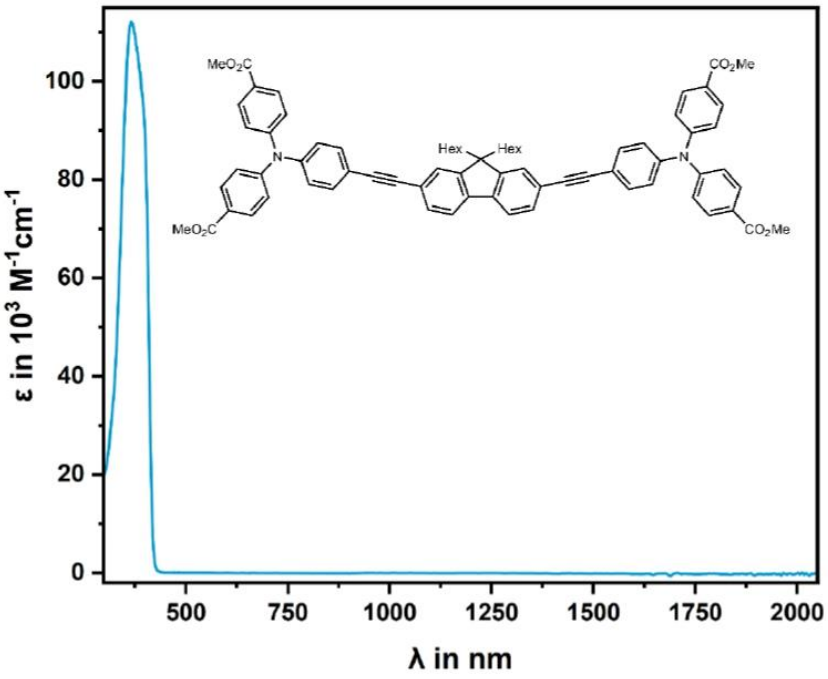

Figure S16. Experimentally determined UV-Vis/NIR spectrum of $\mathbf{1^{Me}}$ in CH_2Cl_2 λ_{max} = 366 nm; ε_{max} = 112×10^3 $M^{-1}cm^{-1}$.

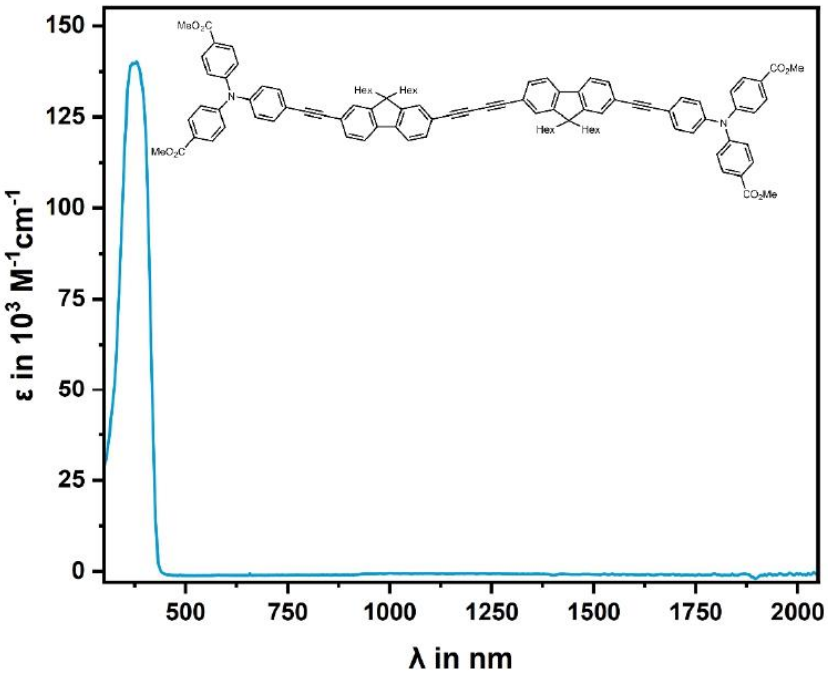

Figure S17. Experimentally determined UV-Vis/NIR spectrum of $\mathbf{2^{Me}}$ in CH_2Cl_2 λ_{max} = 375 nm; ε_{max} = 140×10^3 $M^{-1}cm^{-1}$.

Table S5. Relevant data obtained from UV-Vis/NIR spectroelectrochemistry of compounds $\mathbf{1}^{Me}$ and $\mathbf{2}^{Me}$ in their corresponding oxidation states as well as the TD-DFT calculated wavelengths, oscillator strengths, and corresponding transitions.

Compound		λ_{max} [nm] (ε [10^3 $M^{-1}cm^{-1}$])	TD-DFT calculated transitions	
			λ [nm] (*f*)	contribution
$\mathbf{1}^{Me}$	0	366 (112)	397 (3.47)	H→L (85%)
	1+	360 (77), 547 (13), 712 (13), 1405 (11)	334 (0.57), 465 (0.69), 558 (0.27), 672 (0.03), 1037 (0.28), 1674 (1.08)	βH→βL+4 (45%), αH→αL+3 (45%) αH-1→αL (25%) αH-1→αL (10%), αH→αL (17%), αH→αL+2 (10%) βH-2→βL (72%), βH-1→βL (11%) βH-2→βL (11%), βH-1→βL (73%), βH→βL (15%) βH-1→βL (13%), βH→βL (85%)
	2+	353 (51), 528 (19), 688 (25), 1250 (22)	348 (0.08), 515 (0.30), 517 (0.60), 598 (0.10), 1183 (1.82)	βH-13→βL+1 (15%) αH→αL (15%), βH-3→βL (25%), βH-2→βL+1 (29%) αH→αL (37%), βH-3→βL (18%), βH-2→βL+1 (11%) βH-4→βL (15%), βH-3→βL (15%), βH-1→βL+1 (48%) βH-1→βL+1 (11%), βH→βL (86%)
$\mathbf{2}^{Me}$	0	379 (140)	421 (5.07)	H→L (73%), H-2→L (11%)
	1+	362 (102), 550 (15), 708 (18), 1400 (11)	356 (0.52), 539 (0.19), 865 (0.08), 1213 (0.46), 1549 (0.84)	βH→βL+1 (49%), βH→βL+2 (12%) αH-1→αL (10%) βH-3→βL (19%), βH-2→βL (43%), βH-1→βL (32%) βH-2→βL (19%), βH-1→βL (45%), βH→βL (30%) βH-1→βL (21%), βH→βL (70%)
	2+	355 (70), 533 (22), 690 (42), 1250 (19)	395 (0.71), 586 (0.25), 618 (0.24), 1345 (2.39)	αH→αL (10%), βH-1→βL+3 (12%), βH→βL+2 (26%) αH→αL (19%), βH-2→βL (21%), βH-1→βL+1 (13%), βH→βL+2 (10%) αH→αL (16%), βH-2→βL (19%), βH-1→βL+1 (18%), βH→βL+2 (11%) βH-1→βL+1 (18%), βH→βL (76%)

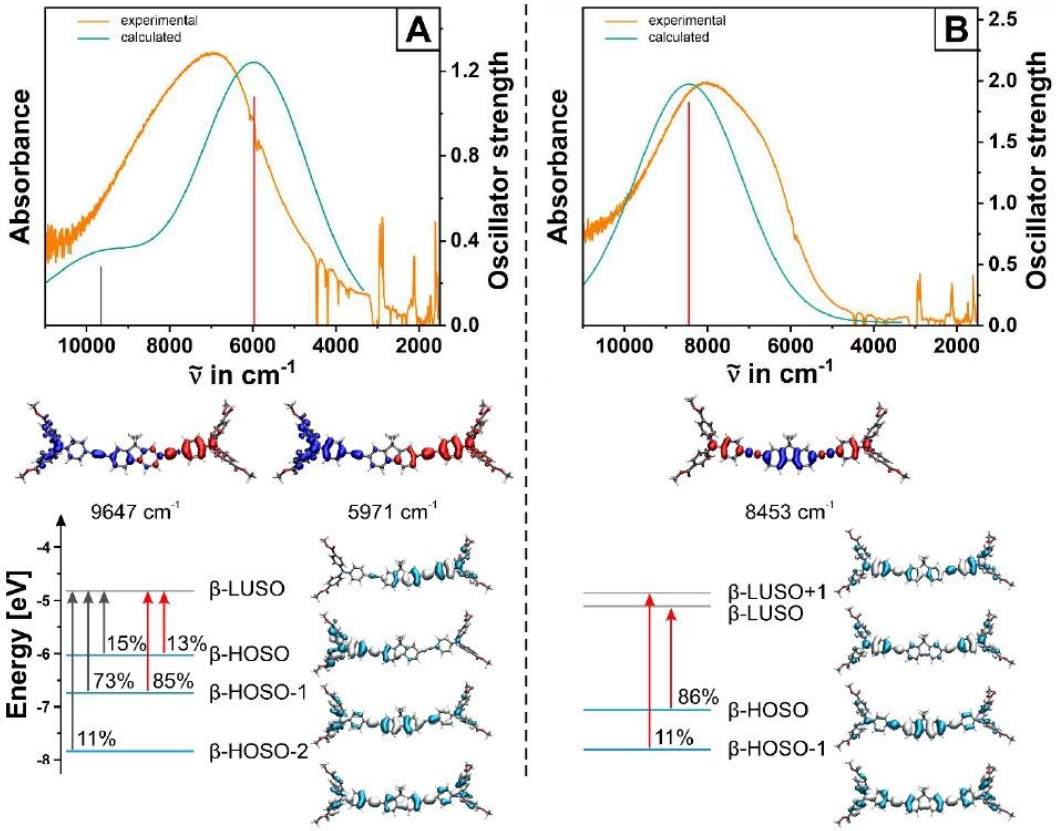

Figure S18. Top: Comparison between experimental NIR spectra of $\mathbf{1}^{Me\,\bullet+}$ (orange line in panel A) and $\mathbf{1Me}^{2+}$ (green line in panel B) in 1,2-CH_4Cl_2 (0.1 M NBu_4^+ $[BAr^{F_{24}}]^-$ as the supporting electrolyte) and TD-DFT calculated electronic spectra of model compound $\mathbf{1}^{Me'\,\bullet+}$ (panel A, turquoise line) and $\mathbf{1}^{Me'\,\bullet2+}$ (panel B, violet). Computed transitions are provided as red and grey vertical bars. Bottom: Contour diagrams of the acceptor and donor MOs involved in the NIR transitions together with their contributions to the respective transition, and corresponding electron density difference maps (EDDMs). Blue colour indicates electron density loss, red colour an increase in electron density. Isosurface values for the MO plots are set as ±0.02.

S4 Molecular Dynamics Simulation

To explore the incorporation of $\mathbf{1}^{H}$ or $\mathbf{2}^{H}$ in the lipid bilayer membrane, MD simulations with the AMBER forcefield were performed using the YASARA v21.6.2 software. The assisted model building was utilized based on the macro for running a molecular dynamics simulation of a membrane protein. This macro sets up and runs a simulation of a membrane protein; in our case, the protein is the chromophore ($\mathbf{1}^{H}$ or $\mathbf{2}^{H}$). It scans the chromophore for secondary structure elements with hydrophobic surface residues, orients it accordingly, and embeds it in a membrane of adjustable lipid composition. Finally, 250 ps restrained equilibration simulations were run, which ensures that the membrane can adapt to the newly embedded chromophore.[17,18] Then, the real simulation starts. The macro can be found at yasara.org/md_runmembrane.mcr.

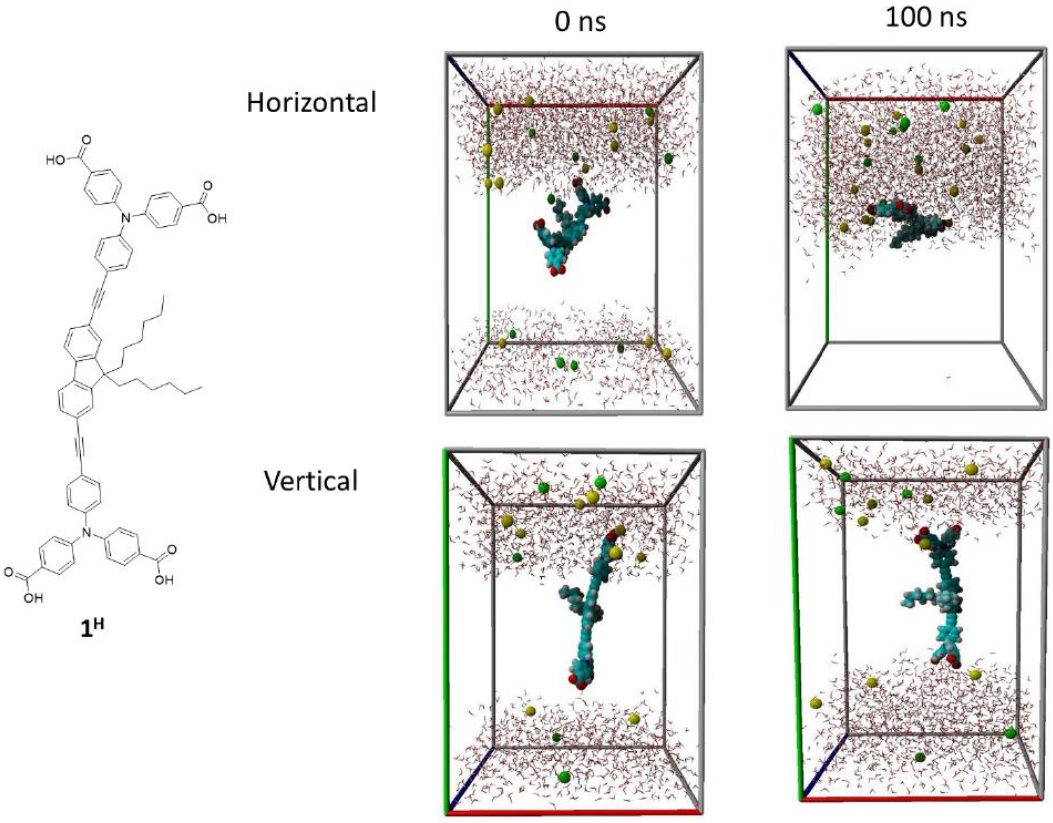

Figure S19. The final point of trajectories shows how $\mathbf{1}^{H}$ orients in the membrane. Top, the simulation started with parallel alignment for 0 ns (left) and after 100 ns (right). Bottom, the simulation started with transmembrane alignment for 0 ns (left) and after 100 ns (right). Red spheres represent water molecules; the membrane was omitted for a clearer view.

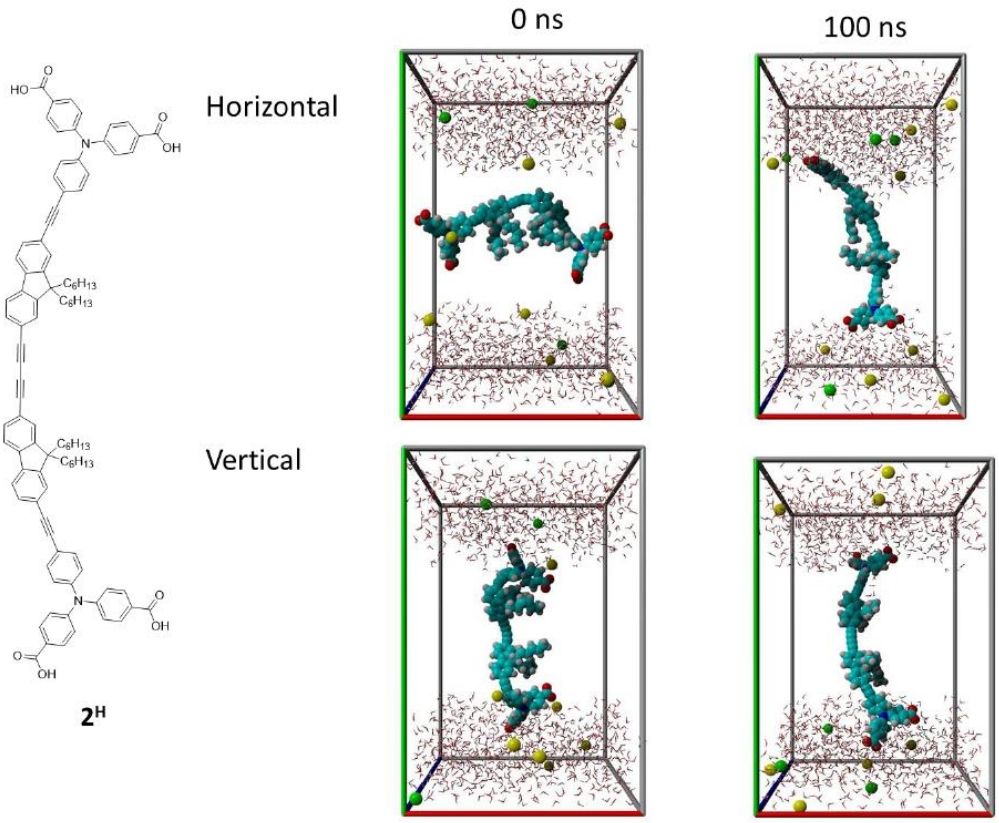

Figure S20. The final point of trajectories shows how $\mathbf{2}^{\mathbf{H}}$ orients in the membrane. Top, the simulation started with parallel alignment for 0 ns (left) and after 100 ns (right). Bottom, the simulation started with transmembrane alignment for 0 ns (left) and after 100 ns (right). Red spheres represent water molecules; the membrane was omitted for a clearer view.

S5 Calceine-Luminescence Leakage Test

We conducted a calceine test to check the impermeability of the membrane, which is a standard procedure used to assess the potential for membrane disruption during encapsulation.[18,19] We examined the DPPC liposome with and without integration of $\mathbf{1}^{\mathbf{H}}$ and $\mathbf{2}^{\mathbf{H}}$ and monitored the solution for 3 days.

The calceine test preparation is as follows: in a 5 mL round bottom flask, 1 mL of a stock solution of DPPC (5.0 mM), 1 mL 14:0 PEG2000 PE (0.05 mM) and 1 mL of $\mathbf{1}^{\mathbf{H}}$ or $\mathbf{2}^{\mathbf{H}}$ (0.05 mM) in acetonitrile were combined. The organic solvents were evaporated under vacuum for at least one hour. Calceine (43.58 mg, 0.07 mmol) was added to the flask and hydrated with 1 mL phosphate buffer (K_2HPO_4/KH_2PO_4, pH 7.7) to yield a calceine concentration of 70 mM. The dispersed lipid film was freeze-thawed three times, using liquid N_2 and a water bath at 52 °C. The dispersion was extruded at 52 °C through 200 nm cellulose membrane filters 11 times with an Avanti Polar Lipids mini-extruder. The obtained solutions of liposomes were separated from excess calceine using an SEC with phosphate buffer pH 7.7 as eluent. Luminescence measurements were carried out with 10 μl of liposome solution diluted with 990 μl of phosphate buffer pH 7.7. After the measurements, Triton X-100 (1 mM, 50 μl) was added to

the liposome sample. The liposomes are disturbed by the addition of Triton X-100 and release the encapsulated calceine. To check the stability of encapsulation in liposomes, other samples were measured after 2 h irradiation with a 470 nm LED stick. All luminescence spectra were recorded from 495 – 700 nm with excitation at λ_{ex} = 485 nm. Experiments were carried out for 3 days to investigate the stability of the membrane.

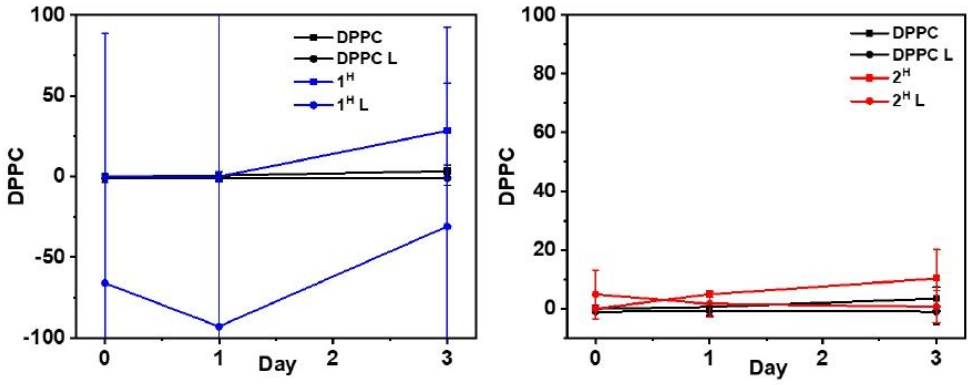

Figure S21. (left) Leakage test with and without **1**^{H}, (right) Leakage test with and without **2**^{H}. The percentage of calcein leakage is measured by comparing the luminescence before and after the addition of Triton X-100. The L symbol means, that the measurements were carried out after 2h irradiation with 470 nm LED.

S6 Liposome preparation

Stock Solutions.

The lipids 1,2-dipalmitoyl-sn-glycero-3-phosphocholine (DPPC) and 1,2-dimyristoyl-sn-glycero-3-phosphoethanolamine-N-[methoxy(polyethylene glycol)-2000] (ammonium salt) (14:0 PEG2000 PE) were prepared as stock solutions in $CHCl_3$ with the concentration of 5 mM and 0.05 mM respectively. The chromophores **1**^{H} or **2**^{H} were prepared with a concentration of 0.05 mM in methanol and $CHCl_3$ (1:1) mixture and for bis(2,2'-bipyridine)-(4,4'-dinonyl-2,2'-bipyridine)-ruthenium(II) hexafluorophosphate (RuC_9) was diluted with the same concentration (0.05 mM) in acetonitrile. Phosphate buffer pH 7.0 was prepared with the mixture of KH_2PO_4 (626 mg, 4.6 mmol), $K_2HPO_4{\cdot}3H_2O$ (1.186 g, 5.2 mmol), and K_2SO_4 (1.70 g, 9.74 mmol) in Milli-Q water (1 L) to reach a final pH of 7.0. The tetrazolium dye XTT (sodium 4-methoxy-5-[3-(2-methoxy-4-nitro-5 sulfonatophenyl)-5-(phenylcarbamoyl)tetrazol-3-ium-2-yl]-2 nitrobenzenesulfonate) was prepared with a concentration of 1 mM in phosphate buffer pH 7.0.

Preparation and characterization of giant vesicles and liposomes.

Giant vesicles and liposomes were prepared as follows. To prepare a lipid film, 1 mL stock solution of DPPC (5.0 mM), 1 mL 14:0 PEG2000 PE (0.05 mM), and 1 mL **1**^{H} or **2**^{H} (0.05 mM) were combined in a 5 mL round bottom flask. The organic solvents were evaporated under vacuum leading to deposition of lipid film on the flask wall. The lipid film was dried under a high vacuum for at least one hour and

hydrated with phosphate buffer pH of 7.0 and 15 mg of NADH or XTT. The dispersed lipid film was repeatedly subjected to freeze-thawing, using liquid N_2 and a water bath at 52 °C, yielding giant vesicles.

Before microscopy, and if applicable, giant vesicles were subjected to a Sephadex G-25 size exclusion chromatography (SEC) column (6 cm length, 2 cm diameter) using phosphate buffer at pH 7.0 as eluent. To prepare the sample for confocal microscopy measurements, a 50-100 μL amount of the giant vesicle sample was loaded into a well of the sample holder. Next, 200 μL of a freshly prepared, air-cooled agarose solution (1 weight-% in water) were added to the well and mixed with the sample. The mixed solution was then allowed to settle at room temperature before confocal microscopy measurements were taken with an excitation laser at λ_{ex}=405 nm and detected emission from 420-650 nm.

To obtain liposomes of uniform size, the dispersion was extruded at 52 °C through 200 nm cellulose membrane filters 11 times with an Avanti Polar Lipids mini-extruder. The mixture of liposomes was treated with an SEC column, with phosphate buffer pH 7.0 as eluent, to separate the unencapsulated NADH. The liposome solution was collected and measured using dynamic light scattering (DLS). The results showed a Z_{Avg}-diameter ranging from 130-150 nm with a polydispersity index of about 0.1.

The procedure of photoirradiation

The typical reactions were carried out within quartz cuvettes where 300 μl of liposome solution, 10 μl of 1 mM XTT or 1 mM NADH, and 190 μl phosphate buffer pH 7.0 were added. The mixtures were illuminated within a custom-made reactor equipped with four ventilators to exclude heating of the samples and an LED stick (λ = 460 $\pm$ 22 nm and λ = 370 $\pm$ 24 nm).[21] The samples were monitored via UV-Vis spectroscopy after 0, 5, 15, 30, 60, 120, and 180 minutes.

Transmembrane electron transfer experiments

To evaluate the photoinduced electron transfer, the number of formazan (n_{fz}) (Fz) was calculated by measuring the increasing absorbance at 470 nm; the increasing absorbance value was converted to the amount of Fz formed with the reported extinction coefficient of Fz at 470 nm (21.600 M^{-1} cm^{-1}).[22]

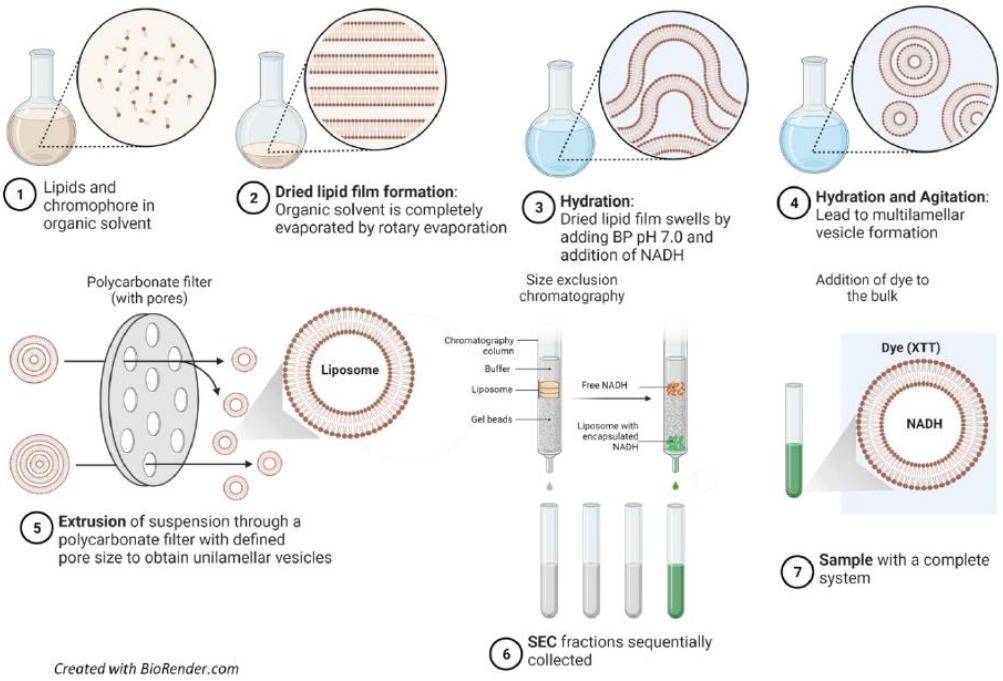

Figure S22. Liposome preparation via thin film hydration with NADH encapsulated in the inner part of liposomes. Created with Biorender.com.

S7 The Typical Hydrodynamic Diameter of DPPC Liposome

The size distribution of the hydrodynamic diameter (Z_{Avg}) was measured at 20 °C with a Zetasizer Pro from Malvern operating at 633 nm with a scattering angle of 173°.

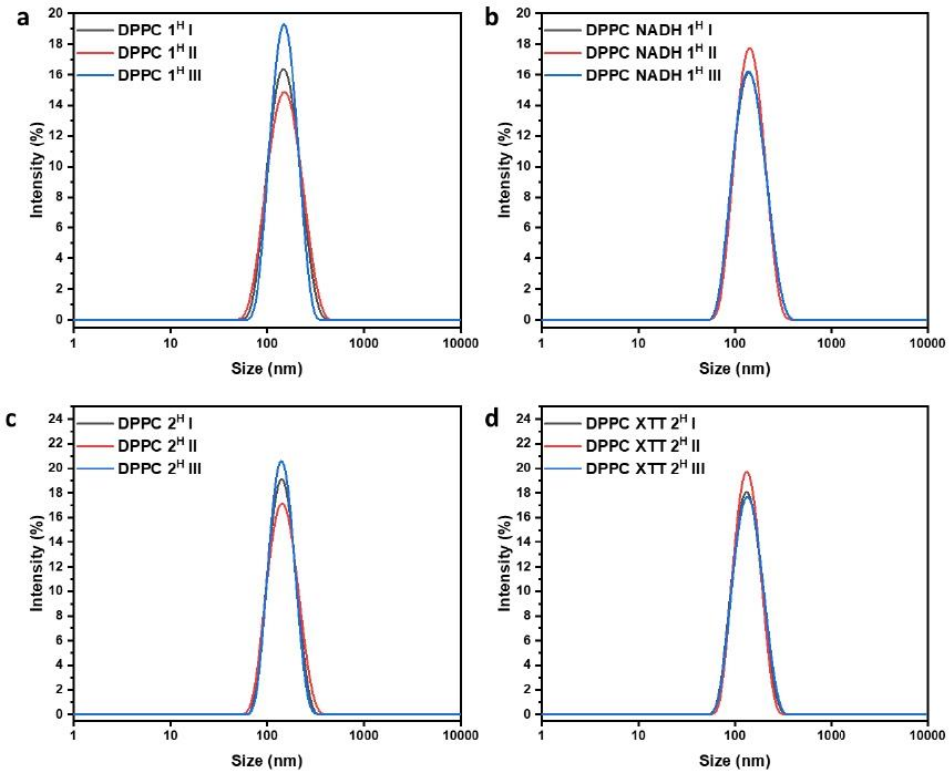

Figure S23. Typical DLS measurements of DPPC:(14:0 PEG2000 PE):$[1]^{2+}$= 100:1:1 liposomes, a) 1 mol% of $\mathbf{1}^{H}$, b) 1 mol% of $\mathbf{1}^{H}$ with encapsulated NADH, c) 1 mol% of $\mathbf{2}^{H}$, and d) 1 mol% of $\mathbf{2}^{H}$ with encapsulated XTT.

S8 Spectra of LEDs and DPPC with integrated $\mathbf{1^H}$ or $\mathbf{2^H}$

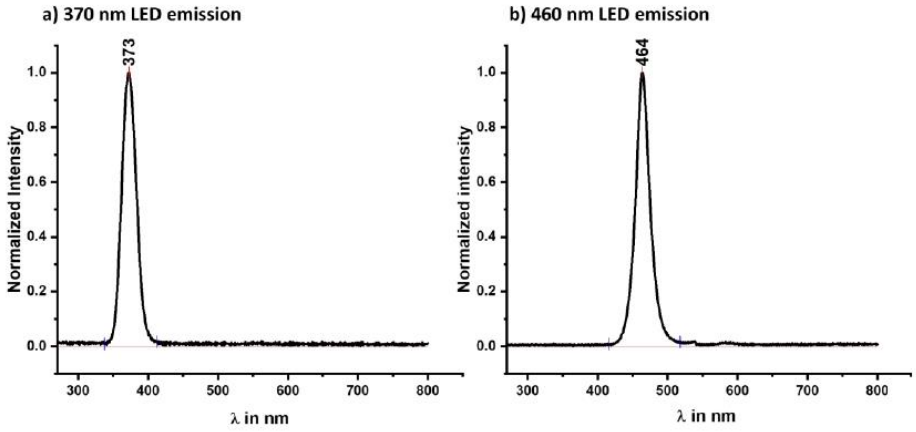

Figure S24. Emission spectra of a) 370 nm LED and b) 460 nm LED.

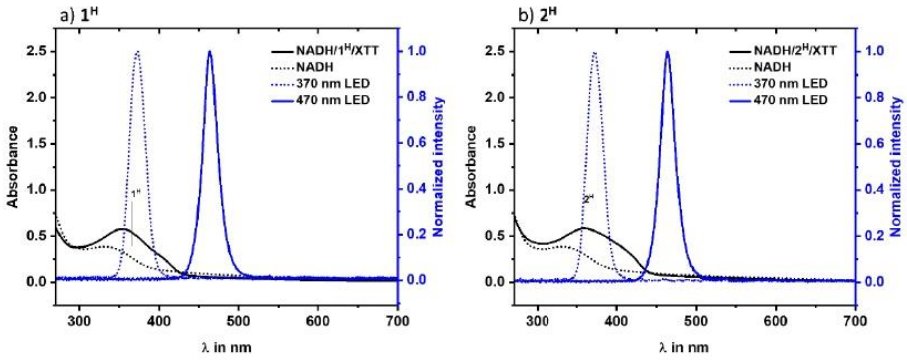

Figure S25. Overlap spectra of a) NADH/$\mathbf{2^H}$/XTT (solid black line) and encapsulated NADH in DPPC liposome (dotted black line) and b) NADH/$\mathbf{1^H}$/XTT (solid black line) and encapsulated NADH in DPPC liposome (dotted black line) before irradiation with the emission spectra of 370 nm (dotted blue line) and 470 nm LEDs (solid blue line).

S9 Photoinduced electron transfer reactions in the membrane

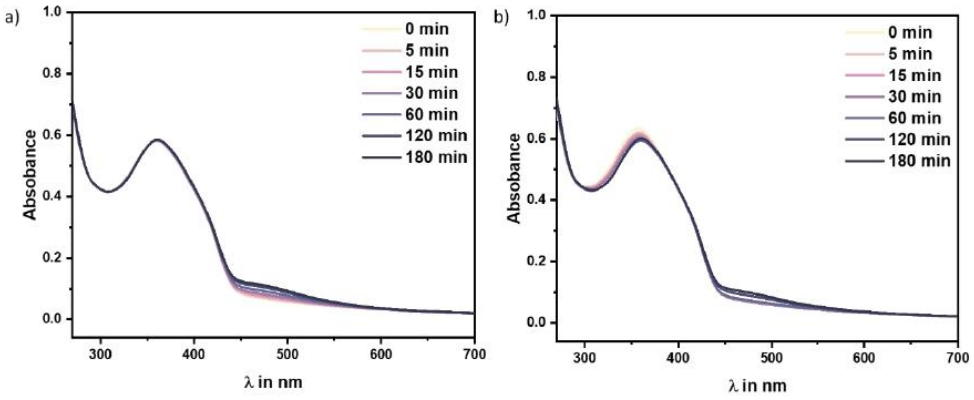

Figure S26. Temporal UV-vis spectra of NADH/**2**^{H}/XTT in phosphate buffer pH 7.0, irradiated with a) 470 nm LED; b) 370 nm LED.

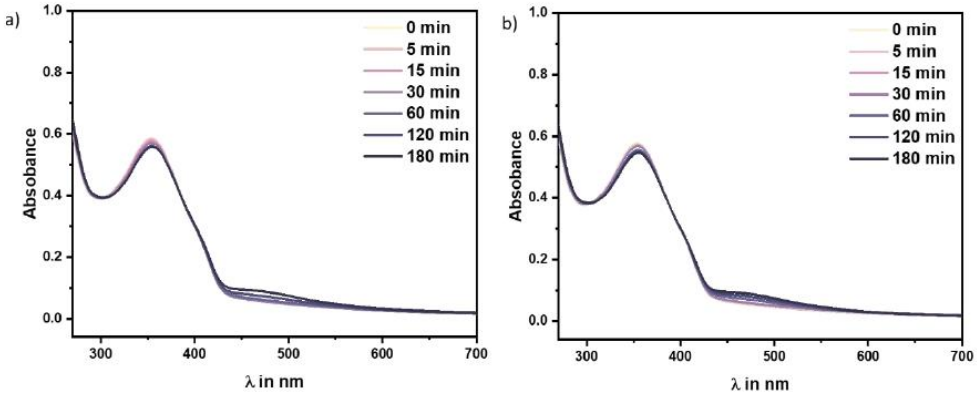

Figure S27. Temporal UV-vis spectra of NADH/**1**^{H}/XTT in phosphate buffer pH 7.0, irradiated with a) 470 nm LED; b) 370 nm LED.

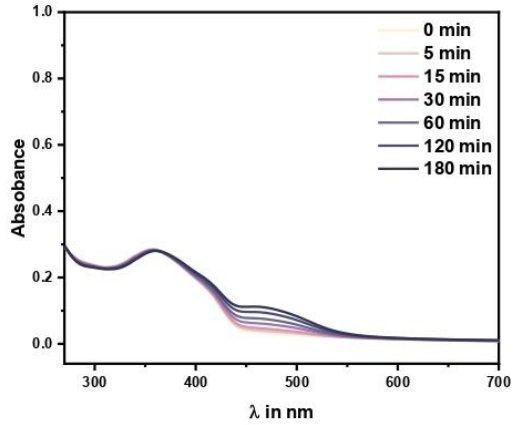

Figure S28. Temporal UV-vis spectra of XTT/**2**^{H}/NADH in phosphate buffer pH 7.0, irradiated with 470 nm LED.

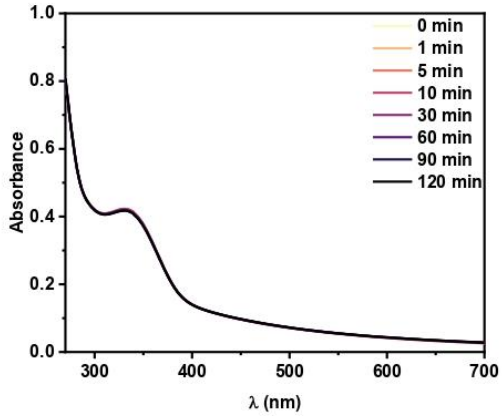

Figure S29. Temporal UV-vis spectra of NADH/-/XTT, NADH encapsulated inside DPPC liposome and XTT at the bulk solution in phosphate buffer pH 7.0, irradiated with 470 nm LED.

S10 Stern-Volmer Quenching Experiment

Liposomes were prepared as described in the methods section.

In cuvette:

V = 0.5 mL

2^{H} = 5 μM

[DPPC] = 500 μM

[14:0 PEG2000 PE] = 5 μM

Encapsulated NADH (NADH/2^{H})

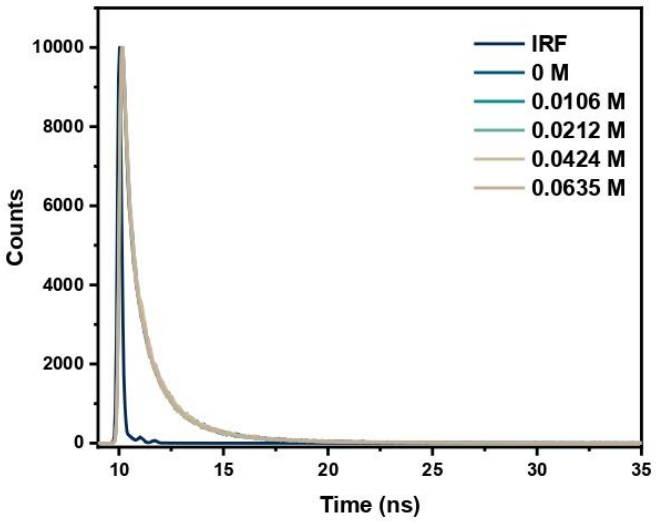

Figure S30. Kinetic traces of luminescence decay upon excitation at 371 nm with various concentrations of encapsulated NADH inside liposome as a quencher.

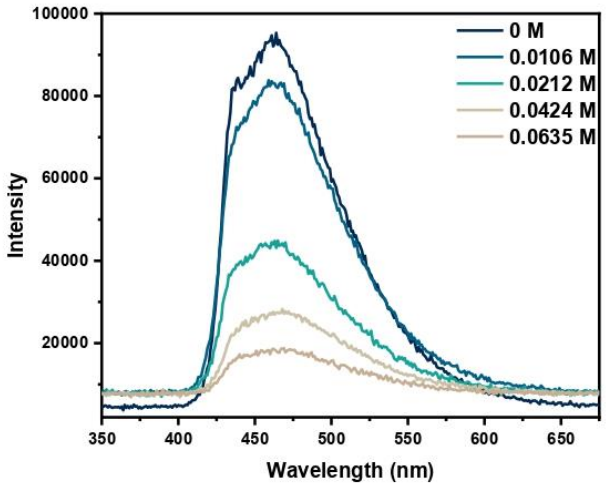

Figure S31. Luminescence quenching upon encapsulation of various concentrations of NADH inside liposome as a quencher.

XTT as quencher at the bulk solution (2^{H}/XTT)

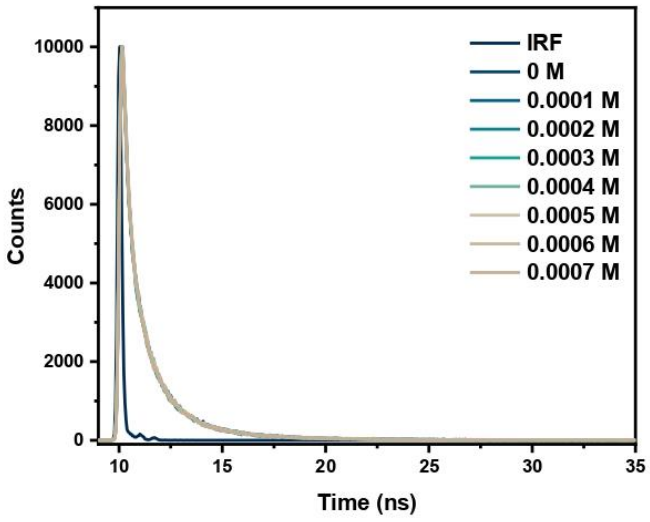

Figure S32. Kinetic traces of luminescence decay upon excitation at 371 nm with various concentrations of XTT as a quencher.

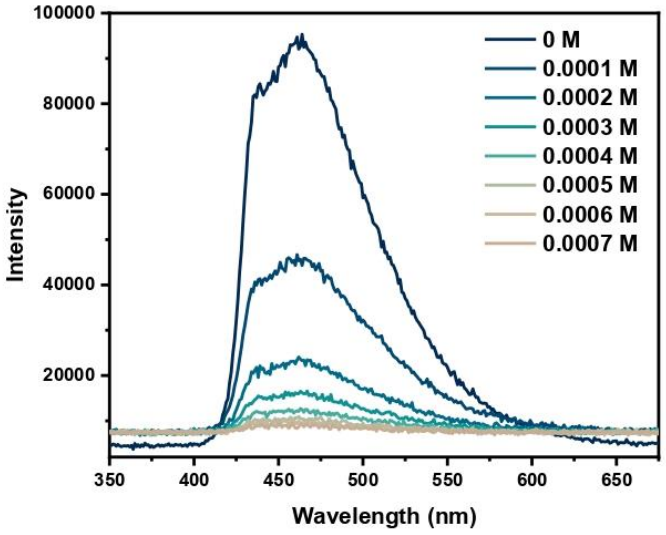

Figure S33. Luminescence quenching upon the addition of various concentrations of XTT as a quencher

S11 Atomic Coordinates of DFT Geometry-Optimized Structures

Table S6. Atomic coordinates of $\mathbf{1}^{Me}$ from its DFT geometry-optimized structure.

Atom	x	y	z
C	-3.52246	0.11964	2.41936
C	-3.12193	0.11601	1.06722
C	-4.10308	0.09554	0.05334
C	-5.44354	0.07973	0.39980
C	-5.83017	0.08295	1.75365
C	-4.86826	0.10304	2.76564
H	-2.76117	0.13558	3.19614
H	-3.79000	0.09292	-0.98897
H	-5.15886	0.10600	3.81463
C	-6.66259	0.05788	-0.51846
C	-7.79627	0.04883	0.50358
C	-9.16196	0.02982	0.27636
C	-10.05028	0.02419	1.37266
C	-9.53254	0.03787	2.68435
C	-8.16153	0.05746	2.91095
C	-7.29223	0.06319	1.81817
H	-9.56536	0.01904	-0.73440
H	-10.22272	0.03329	3.52508
H	-7.77990	0.06816	3.93035
C	-1.73480	0.13351	0.72725
C	-0.55539	0.14909	0.43800
C	-11.46193	0.00523	1.15604
C	-12.66223	-0.01031	0.97176
C	-14.07369	-0.02815	0.75655
C	-14.60629	-0.01112	-0.54583
C	-14.96886	-0.06299	1.84171
C	-15.97774	-0.03523	-0.75383
H	-13.93236	0.00755	-1.39943
C	-16.34027	-0.07279	1.63245
H	-14.57883	-0.06849	2.85709
C	-16.86290	-0.06267	0.33224
H	-16.37038	-0.03550	-1.76793

H	-17.01649	-0.08583	2.48399
C	0.83123	0.16849	0.09783
C	1.81955	0.22633	1.09782
C	1.24547	0.13115	-1.24647
C	3.16670	0.23932	0.76650
H	1.52202	0.24764	2.14387
C	2.59265	0.15834	-1.57677
H	0.49810	0.09447	-2.03595
C	3.57115	0.20949	-0.57489
H	3.91617	0.27065	1.55383
H	2.89286	0.14295	-2.62186
N	-18.26590	-0.08026	0.11900
N	4.94927	0.23112	-0.91325
C	-19.06681	-0.99966	0.82938
C	-20.32685	-0.62335	1.32205
C	-18.61060	-2.30699	1.06496
C	-21.11068	-1.53094	2.01994
H	-20.68833	0.38892	1.16079
C	-19.39385	-3.20583	1.77274
H	-17.64065	-2.61616	0.68422
C	-20.65365	-2.83349	2.25628
H	-22.08137	-1.22442	2.39977
H	-19.04143	-4.21936	1.94867
C	-18.84284	0.82158	-0.80009
C	-19.89396	0.41727	-1.63906
C	-18.36688	2.13942	-0.89844
C	-20.45820	1.30765	-2.54125
H	-20.26430	-0.60319	-1.58580
C	-18.92750	3.02107	-1.80991
H	-17.55873	2.47028	-0.25132
C	-19.98110	2.62064	-2.64011
H	-21.26746	0.97949	-3.18767
H	-18.56154	4.04266	-1.88003
C	5.44732	-0.68355	-1.86545
C	6.41083	-0.28620	-2.80731
C	4.97830	-2.00664	-1.89388

41

C	6.89316	-1.19093	-3.74036
H	6.77458	0.73802	-2.80844
C	5.45708	-2.90456	-2.83745
H	4.23847	-2.33105	-1.16670
C	6.42327	-2.50948	-3.77071
H	7.63491	-0.87996	-4.47218
H	5.08966	-3.92702	-2.84374
C	5.80438	1.16725	-0.29410
C	7.10817	0.80811	0.08451
C	5.36043	2.47462	-0.03604
C	7.94506	1.73198	0.69386
H	7.46243	-0.20361	-0.09518
C	6.19775	3.38978	0.58326
H	4.35674	2.77083	-0.32965
C	7.50012	3.03424	0.95347
H	8.94951	1.43856	0.98624
H	5.85424	4.40324	0.77646
C	-21.45410	-3.83841	3.00156
C	-20.54971	3.60772	-3.59310
C	8.35638	4.05606	1.60805
C	6.97034	-3.43500	-4.79543
O	8.00075	5.18313	1.85749
O	9.57722	3.60159	1.89827
O	6.43617	-4.65626	-4.72970
O	7.80968	-3.13009	-5.60877
O	-21.55411	3.11004	-4.31754
O	-20.15689	4.74379	-3.71145
O	-22.63789	-3.36737	3.39904
O	-21.08730	-4.96615	3.23097
C	-6.68424	-1.21022	-1.39173
H	-7.59811	-1.24587	-1.99840
H	-5.82621	-1.22260	-2.07594
C	-6.71854	1.31455	-1.40662
H	-7.63343	1.31847	-2.01283
H	-5.86156	1.34202	-2.09168
C	-22.16463	3.98188	-5.26208

H	-21.43410	4.32286	-6.00429
H	-22.95209	3.40197	-5.74849
H	-22.59489	4.85641	-4.76120
C	-23.47811	-4.25799	4.12426
H	-22.99084	-4.58372	5.05016
H	-24.38818	-3.69974	4.35470
H	-23.71932	-5.14087	3.52172
C	6.90007	-5.61670	-5.67179
H	7.97829	-5.77840	-5.56207
H	6.35748	-6.54036	-5.45867
H	6.69427	-5.28613	-6.69608
C	10.47181	4.51014	2.53026
H	10.06800	4.84663	3.49178
H	11.40437	3.96292	2.68470
H	10.64860	5.38534	1.89502
H	-6.64534	-2.11678	-0.77566
H	-6.70375	2.22900	-0.80126

Table S7. Atomic coordinates of $\mathbf{1}^{Me+}$ from its DFT geometry-optimized structure.

Atom	x	y	z
C	0.36125	-0.03376	0.04424
C	0.77363	0.00954	-1.31293
C	-0.19875	0.00798	-2.34688
C	-1.53488	-0.03550	-2.01529
C	-1.93260	-0.08093	-0.65747
C	-0.98082	-0.07957	0.37251
H	1.11795	-0.03116	0.82507
H	0.13027	0.04227	-3.38322
H	-1.28683	-0.11329	1.41581

C	-2.74872	-0.04294	-2.93908
C	-3.88354	-0.10021	-1.92163
C	-5.24706	-0.12890	-2.15274
C	-6.13576	-0.18220	-1.05723
C	-5.62183	-0.20630	0.25984
C	-4.25575	-0.17649	0.49119
C	-3.38390	-0.12256	-0.60282
H	-5.64993	-0.11110	-3.16318
H	-6.31585	-0.24793	1.09593
H	-3.87536	-0.19491	1.51058
C	2.14286	0.05408	-1.62943
C	3.33583	0.09284	-1.90407
C	4.69694	0.13761	-2.21696
C	5.68152	0.15292	-1.19019
C	5.13400	0.16945	-3.57044
C	7.01708	0.20453	-1.49411
H	5.36491	0.10640	-0.15134
C	6.46869	0.20728	-3.88043
H	4.39365	0.18047	-4.36628
C	7.45054	0.22988	-2.84987
H	7.75107	0.18934	-0.69467
H	6.77789	0.25724	-4.91967
N	8.78670	0.27498	-3.15669

44

C	9.27671	-0.20677	-4.40727
C	10.14703	0.58790	-5.16240
C	8.91182	-1.48052	-4.85842
C	10.63567	0.11048	-6.36952
H	10.42639	1.57685	-4.80834
C	9.40557	-1.95085	-6.06846
H	8.25820	-2.10519	-4.25465
C	10.26919	-1.15835	-6.83189
H	11.30382	0.71912	-6.97319
H	9.13078	-2.94176	-6.41772
C	9.74088	0.80365	-2.23678
C	10.90148	0.07671	-1.94969
C	9.52791	2.05643	-1.64874
C	11.83787	0.59535	-1.06555
H	11.06071	-0.89560	-2.40861
C	10.46875	2.56731	-0.76598
H	8.63878	2.63101	-1.89630
C	11.62675	1.84258	-0.46665
H	12.73448	0.02916	-0.83131
H	10.32183	3.54130	-0.30654
C	12.60496	2.44144	0.49010
C	10.82877	-1.62138	-8.13701
O	12.45147	3.51267	1.02132

45

O	13.66387	1.66465	0.69399
O	10.41134	-2.83824	-8.47106
O	11.57810	-0.96401	-8.81490
C	-2.75062	-1.28263	-3.85295
H	-3.66284	-1.30878	-4.46193
H	-1.89192	-1.26013	-4.53570
C	-2.81768	1.24295	-3.78402
H	-3.73264	1.25510	-4.38936
H	-1.96166	1.30194	-4.46792
C	10.89223	-3.37553	-9.70118
H	11.98495	-3.45111	-9.68652
H	10.44568	-4.36744	-9.79472
H	10.58927	-2.74217	-10.54203
C	14.65886	2.14513	1.59528
H	14.23242	2.29823	2.59262
H	15.43434	1.37734	1.62921
H	15.07749	3.09176	1.23669
H	-2.70131	-2.20845	-3.26732
H	-2.81372	2.13679	-3.14871
C	-7.54303	-0.21023	-1.27586
C	-8.74368	-0.23218	-1.46222
C	-10.15221	-0.25631	-1.68046
C	-10.68272	-0.18421	-2.98239

C	-11.04884	-0.35176	-0.59946
C	-12.05239	-0.21216	-3.19428
H	-10.00766	-0.11952	-3.83280
C	-12.41868	-0.36756	-0.81157
H	-10.66057	-0.39928	0.41546
C	-12.94088	-0.30091	-2.11207
H	-12.44187	-0.16951	-4.20841
H	-13.09481	-0.42719	0.03770
N	-14.33887	-0.32283	-2.32843
C	-15.14778	-1.22951	-1.60713
C	-16.39607	-0.82987	-1.10517
C	-14.71300	-2.54466	-1.37820
C	-17.19067	-1.72363	-0.40106
H	-16.73998	0.18886	-1.26469
C	-15.50621	-3.42968	-0.66385
H	-13.75277	-2.87112	-1.76928
C	-16.75446	-3.03389	-0.16934
H	-18.15286	-1.40053	-0.01351
H	-15.17166	-4.44988	-0.49184
C	-14.91971	0.56190	-3.26449
C	-15.94747	0.12723	-4.11585
C	-14.47470	1.89007	-3.36007
C	-16.51932	0.99932	-5.03146

47

H	-16.29376	-0.90165	-4.06110
C	-15.04183	2.75348	-4.28508
H	-13.68632	2.24352	-2.70047
C	-16.07177	2.32252	-5.12944
H	-17.31083	0.64924	-5.68822
H	-14.70071	3.78363	-4.35470
C	-17.56693	-4.02531	0.58254
C	-16.64897	3.29144	-6.09699
O	-17.63064	2.76697	-6.83254
O	-16.27957	4.43513	-6.21560
O	-18.73803	-3.53332	0.99019
O	-17.21760	-5.15927	0.80756
C	-18.24752	3.61927	-7.79113
H	-17.51458	3.97096	-8.52589
H	-19.01567	3.01910	-8.28369
H	-18.70298	4.48743	-7.30168
C	-19.58879	-4.40931	1.72148
H	-19.09937	-4.74593	2.64228
H	-20.48588	-3.83417	1.96091
H	-19.85196	-5.28607	1.11927

Table S8. Atomic coordinates of $\mathbf{1}^{Me2+}$ (closed-shell singlet) from its DFT geometry-optimized structure.

Atom	x	y	z
C	-3.58344	0.13832	2.31610
C	-3.16579	0.11762	0.94432
C	-4.13962	0.05867	-0.09852
C	-5.46739	0.02357	0.23037
C	-5.87104	0.04210	1.60162
C	-4.91249	0.10043	2.64339
H	-2.82285	0.18403	3.09109
H	-3.80269	0.04343	-1.13208
H	-5.22427	0.11548	3.68489
C	-6.68068	-0.03767	-0.68871
C	-7.80909	-0.04773	0.33467
C	-9.16070	-0.08785	0.12491
C	-10.03968	-0.08724	1.25028
C	-9.50378	-0.04950	2.57992
C	-8.15102	-0.00729	2.78796
C	-7.28722	-0.00352	1.66481
H	-9.58686	-0.11866	-0.87487
H	-10.19396	-0.05239	3.41944
H	-7.74932	0.02346	3.79789
C	-1.81269	0.15555	0.63832
C	-0.61246	0.18993	0.37133

C	-11.41479	-0.11799	1.06468
C	-12.63390	-0.13726	0.90289
C	-14.01064	-0.15207	0.72145
C	-14.57636	-0.17166	-0.58559
C	-14.89470	-0.14284	1.83825
C	-15.93410	-0.17037	-0.76572
H	-13.91604	-0.20293	-1.44862
C	-16.25297	-0.15508	1.66235
H	-14.47925	-0.10793	2.84226
C	-16.81542	-0.16286	0.35354
H	-16.34221	-0.20678	-1.77056
H	-16.90629	-0.12412	2.52826
C	0.74236	0.22989	0.07012
C	1.71998	0.28690	1.10467
C	1.19198	0.21612	-1.28149
C	3.05645	0.33450	0.80951
H	1.39519	0.27566	2.14211
C	2.52806	0.25125	-1.58047
H	0.45849	0.19447	-2.08365
C	3.50299	0.31539	-0.54340
H	3.78310	0.35448	1.61519
H	2.84530	0.26339	-2.61817
N	-18.17306	-0.16189	0.17493

50

N	4.83866	0.35741	-0.84002
C	-19.05771	-0.63183	1.19240
C	-20.14056	0.15986	1.58919
C	-18.86059	-1.89376	1.76577
C	-21.01474	-0.30393	2.56346
H	-20.28952	1.13905	1.14131
C	-19.73615	-2.34904	2.74133
H	-18.03360	-2.51819	1.43641
C	-20.81714	-1.56011	3.14781
H	-21.85116	0.31250	2.87954
H	-19.59949	-3.32914	3.19097
C	-18.76358	0.31067	-1.03595
C	-19.71440	-0.47476	-1.69622
C	-18.41677	1.56942	-1.54156
C	-20.30495	-0.00844	-2.86341
H	-19.98124	-1.45108	-1.29964
C	-19.00839	2.02725	-2.71021
H	-17.69790	2.18954	-1.01156
C	-19.95411	1.24403	-3.37986
H	-21.03666	-0.62012	-3.38293
H	-18.75333	3.00488	-3.11108
C	5.34092	-0.12913	-2.08506
C	6.19396	0.67471	-2.84940

51

C	5.00903	-1.41691	-2.52104
C	6.69859	0.19309	-4.04863
H	6.45001	1.67412	-2.50700
C	5.51597	-1.89137	-3.72407
H	4.36770	-2.04871	-1.91127
C	6.36329	-1.08944	-4.49613
H	7.35491	0.80923	-4.65774
H	5.26511	-2.89291	-4.06102
C	5.79038	0.88764	0.08323
C	6.93264	0.14597	0.40251
C	5.59673	2.15730	0.64049
C	7.86918	0.66613	1.28613
H	7.07917	-0.83879	-0.03377
C	6.53545	2.66937	1.52491
H	4.72176	2.74320	0.36960
C	7.67557	1.92978	1.85545
H	8.75200	0.08819	1.54324
H	6.40165	3.65596	1.96102
C	-21.72919	-2.10174	4.19838
C	-20.56041	1.78740	-4.63123
C	8.65261	2.53034	2.81132
C	6.93645	-1.55573	-5.79342
O	8.51299	3.61497	3.31918

52

O	9.69512	1.73909	3.04447
O	6.54775	-2.78629	-6.11367
O	7.67228	-0.89053	-6.47873
O	-21.45145	0.96137	-5.17064
O	-20.27425	2.85917	-5.10386
O	-22.72474	-1.27110	4.49184
O	-21.58100	-3.17608	4.72541
C	-6.67761	-1.32625	-1.53358
H	-7.58967	-1.38767	-2.13935
H	-5.81948	-1.33179	-2.21647
C	-6.76045	1.20340	-1.59816
H	-7.67547	1.17510	-2.20207
H	-5.90575	1.22975	-2.28474
C	-22.08943	1.38779	-6.37222
H	-21.34972	1.55107	-7.16355
H	-22.77399	0.58534	-6.65421
H	-22.64366	2.31764	-6.20426
C	-23.65375	-1.69577	5.48642
H	-23.14432	-1.86539	6.44127
H	-24.38332	-0.88950	5.58501
H	-24.15111	-2.62172	5.17779
C	7.04420	-3.32678	-7.33597
H	8.13838	-3.37604	-7.31845

53

H	6.62180	-4.33022	-7.41845
H	6.72826	-2.71124	-8.18529
C	10.68762	2.22063	3.94766
H	10.25200	2.40398	4.93591
H	11.44792	1.43939	4.00852
H	11.12889	3.15099	3.57391
H	-6.62163	-2.21942	-0.90022
H	-6.76171	2.12936	-1.01127
C	-3.58344	0.13832	2.31610
C	-3.16579	0.11762	0.94432
C	-4.13962	0.05867	-0.09852
C	-5.46739	0.02357	0.23037
C	-5.87104	0.04210	1.60162
C	-4.91249	0.10043	2.64339
H	-2.82285	0.18403	3.09109
H	-3.80269	0.04343	-1.13208
H	-5.22427	0.11548	3.68489
C	-6.68068	-0.03767	-0.68871
C	-7.80909	-0.04773	0.33467
C	-9.16070	-0.08785	0.12491
C	-10.03968	-0.08724	1.25028
C	-9.50378	-0.04950	2.57992
C	-8.15102	-0.00729	2.78796

54

C	-7.28722	-0.00352	1.66481
H	-9.58686	-0.11866	-0.87487
H	-10.19396	-0.05239	3.41944
H	-7.74932	0.02346	3.79789
C	-1.81269	0.15555	0.63832
C	-0.61246	0.18993	0.37133
C	-11.41479	-0.11799	1.06468
C	-12.63390	-0.13726	0.90289
C	-14.01064	-0.15207	0.72145
C	-14.57636	-0.17166	-0.58559
C	-14.89470	-0.14284	1.83825
C	-15.93410	-0.17037	-0.76572
H	-13.91604	-0.20293	-1.44862
C	-16.25297	-0.15508	1.66235
H	-14.47925	-0.10793	2.84226
C	-16.81542	-0.16286	0.35354
H	-16.34221	-0.20678	-1.77056
H	-16.90629	-0.12412	2.52826
C	0.74236	0.22989	0.07012
C	1.71998	0.28690	1.10467
C	1.19198	0.21612	-1.28149
C	3.05645	0.33450	0.80951
H	1.39519	0.27566	2.14211

55

C	2.52806	0.25125	-1.58047
H	0.45849	0.19447	-2.08365
C	3.50299	0.31539	-0.54340
H	3.78310	0.35448	1.61519
H	2.84530	0.26339	-2.61817
N	-18.17306	-0.16189	0.17493
N	4.83866	0.35741	-0.84002
C	-19.05771	-0.63183	1.19240
C	-20.14056	0.15986	1.58919
C	-18.86059	-1.89376	1.76577
C	-21.01474	-0.30393	2.56346
H	-20.28952	1.13905	1.14131
C	-19.73615	-2.34904	2.74133
H	-18.03360	-2.51819	1.43641
C	-20.81714	-1.56011	3.14781
H	-21.85116	0.31250	2.87954
H	-19.59949	-3.32914	3.19097
C	-18.76358	0.31067	-1.03595
C	-19.71440	-0.47476	-1.69622
C	-18.41677	1.56942	-1.54156
C	-20.30495	-0.00844	-2.86341
H	-19.98124	-1.45108	-1.29964
C	-19.00839	2.02725	-2.71021

H	-17.69790	2.18954	-1.01156
C	-19.95411	1.24403	-3.37986
H	-21.03666	-0.62012	-3.38293
H	-18.75333	3.00488	-3.11108
C	5.34092	-0.12913	-2.08506
C	6.19396	0.67471	-2.84940
C	5.00903	-1.41691	-2.52104
C	6.69859	0.19309	-4.04863
H	6.45001	1.67412	-2.50700
C	5.51597	-1.89137	-3.72407
H	4.36770	-2.04871	-1.91127
C	6.36329	-1.08944	-4.49613
H	7.35491	0.80923	-4.65774
H	5.26511	-2.89291	-4.06102
C	5.79038	0.88764	0.08323
C	6.93264	0.14597	0.40251
C	5.59673	2.15730	0.64049
C	7.86918	0.66613	1.28613
H	7.07917	-0.83879	-0.03377
C	6.53545	2.66937	1.52491
H	4.72176	2.74320	0.36960
C	7.67557	1.92978	1.85545
H	8.75200	0.08819	1.54324

57

H	6.40165	3.65596	1.96102
C	-21.72919	-2.10174	4.19838
C	-20.56041	1.78740	-4.63123
C	8.65261	2.53034	2.81132
C	6.93645	-1.55573	-5.79342
O	8.51299	3.61497	3.31918
O	9.69512	1.73909	3.04447
O	6.54775	-2.78629	-6.11367
O	7.67228	-0.89053	-6.47873
O	-21.45145	0.96137	-5.17064
O	-20.27425	2.85917	-5.10386
O	-22.72474	-1.27110	4.49184
O	-21.58100	-3.17608	4.72541
C	-6.67761	-1.32625	-1.53358
H	-7.58967	-1.38767	-2.13935
H	-5.81948	-1.33179	-2.21647
C	-6.76045	1.20340	-1.59816
H	-7.67547	1.17510	-2.20207
H	-5.90575	1.22975	-2.28474
C	-22.08943	1.38779	-6.37222
H	-21.34972	1.55107	-7.16355
H	-22.77399	0.58534	-6.65421
H	-22.64366	2.31764	-6.20426

58

C	-23.65375	-1.69577	5.48642
H	-23.14432	-1.86539	6.44127
H	-24.38332	-0.88950	5.58501
H	-24.15111	-2.62172	5.17779
C	7.04420	-3.32678	-7.33597
H	8.13838	-3.37604	-7.31845
H	6.62180	-4.33022	-7.41845
H	6.72826	-2.71124	-8.18529
C	10.68762	2.22063	3.94766
H	10.25200	2.40398	4.93591
H	11.44792	1.43939	4.00852
H	11.12889	3.15099	3.57391
H	-6.62163	-2.21942	-0.90022
H	-6.76171	2.12936	-1.01127

Table S9. Atomic coordinates of $\mathbf{1}^{Me2+}$ (open-shell singlet) from its DFT geometry-optimized structure.

Atom	x	y	z
C	-3.58344	0.13832	2.31610
C	-3.16579	0.11762	0.94432
C	-4.13962	0.05867	-0.09852
C	-5.46739	0.02357	0.23037
C	-5.87104	0.04210	1.60162
C	-4.91249	0.10043	2.64339
H	-2.82285	0.18403	3.09109
H	-3.80269	0.04343	-1.13208
H	-5.22427	0.11548	3.68489
C	-6.68068	-0.03767	-0.68871
C	-7.80909	-0.04773	0.33467
C	-9.16070	-0.08785	0.12491
C	-10.03968	-0.08724	1.25028
C	-9.50378	-0.04950	2.57992
C	-8.15102	-0.00729	2.78796
C	-7.28722	-0.00352	1.66481
H	-9.58686	-0.11866	-0.87487
H	-10.19396	-0.05239	3.41944
H	-7.74932	0.02346	3.79789
C	-1.81269	0.15555	0.63832
C	-0.61246	0.18993	0.37133

C	-11.41479	-0.11799	1.06468
C	-12.63390	-0.13726	0.90289
C	-14.01064	-0.15207	0.72145
C	-14.57636	-0.17166	-0.58559
C	-14.89470	-0.14284	1.83825
C	-15.93410	-0.17037	-0.76572
H	-13.91604	-0.20293	-1.44862
C	-16.25297	-0.15508	1.66235
H	-14.47925	-0.10793	2.84226
C	-16.81542	-0.16286	0.35354
H	-16.34221	-0.20678	-1.77056
H	-16.90629	-0.12412	2.52826
C	0.74236	0.22989	0.07012
C	1.71998	0.28690	1.10467
C	1.19198	0.21612	-1.28149
C	3.05645	0.33450	0.80951
H	1.39519	0.27566	2.14211
C	2.52806	0.25125	-1.58047
H	0.45849	0.19447	-2.08365
C	3.50299	0.31539	-0.54340
H	3.78310	0.35448	1.61519
H	2.84530	0.26339	-2.61817
N	-18.17306	-0.16189	0.17493

N	4.83866	0.35741	-0.84002
C	-19.05771	-0.63183	1.19240
C	-20.14056	0.15986	1.58919
C	-18.86059	-1.89376	1.76577
C	-21.01474	-0.30393	2.56346
H	-20.28952	1.13905	1.14131
C	-19.73615	-2.34904	2.74133
H	-18.03360	-2.51819	1.43641
C	-20.81714	-1.56011	3.14781
H	-21.85116	0.31250	2.87954
H	-19.59949	-3.32914	3.19097
C	-18.76358	0.31067	-1.03595
C	-19.71440	-0.47476	-1.69622
C	-18.41677	1.56942	-1.54156
C	-20.30495	-0.00844	-2.86341
H	-19.98124	-1.45108	-1.29964
C	-19.00839	2.02725	-2.71021
H	-17.69790	2.18954	-1.01156
C	-19.95411	1.24403	-3.37986
H	-21.03666	-0.62012	-3.38293
H	-18.75333	3.00488	-3.11108
C	5.34092	-0.12913	-2.08506
C	6.19396	0.67471	-2.84940

62

C	5.00903	-1.41691	-2.52104
C	6.69859	0.19309	-4.04863
H	6.45001	1.67412	-2.50700
C	5.51597	-1.89137	-3.72407
H	4.36770	-2.04871	-1.91127
C	6.36329	-1.08944	-4.49613
H	7.35491	0.80923	-4.65774
H	5.26511	-2.89291	-4.06102
C	5.79038	0.88764	0.08323
C	6.93264	0.14597	0.40251
C	5.59673	2.15730	0.64049
C	7.86918	0.66613	1.28613
H	7.07917	-0.83879	-0.03377
C	6.53545	2.66937	1.52491
H	4.72176	2.74320	0.36960
C	7.67557	1.92978	1.85545
H	8.75200	0.08819	1.54324
H	6.40165	3.65596	1.96102
C	-21.72919	-2.10174	4.19838
C	-20.56041	1.78740	-4.63123
C	8.65261	2.53034	2.81132
C	6.93645	-1.55573	-5.79342
O	8.51299	3.61497	3.31918

O	9.69512	1.73909	3.04447
O	6.54775	-2.78629	-6.11367
O	7.67228	-0.89053	-6.47873
O	-21.45145	0.96137	-5.17064
O	-20.27425	2.85917	-5.10386
O	-22.72474	-1.27110	4.49184
O	-21.58100	-3.17608	4.72541
C	-6.67761	-1.32625	-1.53358
H	-7.58967	-1.38767	-2.13935
H	-5.81948	-1.33179	-2.21647
C	-6.76045	1.20340	-1.59816
H	-7.67547	1.17510	-2.20207
H	-5.90575	1.22975	-2.28474
C	-22.08943	1.38779	-6.37222
H	-21.34972	1.55107	-7.16355
H	-22.77399	0.58534	-6.65421
H	-22.64366	2.31764	-6.20426
C	-23.65375	-1.69577	5.48642
H	-23.14432	-1.86539	6.44127
H	-24.38332	-0.88950	5.58501
H	-24.15111	-2.62172	5.17779
C	7.04420	-3.32678	-7.33597
H	8.13838	-3.37604	-7.31845

64

H	6.62180	-4.33022	-7.41845
H	6.72826	-2.71124	-8.18529
C	10.68762	2.22063	3.94766
H	10.25200	2.40398	4.93591
H	11.44792	1.43939	4.00852
H	11.12889	3.15099	3.57391
H	-6.62163	-2.21942	-0.90022
H	-6.76171	2.12936	-1.01127
C	-3.58344	0.13832	2.31610
C	-3.16579	0.11762	0.94432
C	-4.13962	0.05867	-0.09852
C	-5.46739	0.02357	0.23037
C	-5.87104	0.04210	1.60162
C	-4.91249	0.10043	2.64339
H	-2.82285	0.18403	3.09109
H	-3.80269	0.04343	-1.13208
H	-5.22427	0.11548	3.68489
C	-6.68068	-0.03767	-0.68871
C	-7.80909	-0.04773	0.33467
C	-9.16070	-0.08785	0.12491
C	-10.03968	-0.08724	1.25028
C	-9.50378	-0.04950	2.57992
C	-8.15102	-0.00729	2.78796

65

C	-7.28722	-0.00352	1.66481
H	-9.58686	-0.11866	-0.87487
H	-10.19396	-0.05239	3.41944
H	-7.74932	0.02346	3.79789
C	-1.81269	0.15555	0.63832
C	-0.61246	0.18993	0.37133
C	-11.41479	-0.11799	1.06468
C	-12.63390	-0.13726	0.90289
C	-14.01064	-0.15207	0.72145
C	-14.57636	-0.17166	-0.58559
C	-14.89470	-0.14284	1.83825
C	-15.93410	-0.17037	-0.76572
H	-13.91604	-0.20293	-1.44862
C	-16.25297	-0.15508	1.66235
H	-14.47925	-0.10793	2.84226
C	-16.81542	-0.16286	0.35354
H	-16.34221	-0.20678	-1.77056
H	-16.90629	-0.12412	2.52826
C	0.74236	0.22989	0.07012
C	1.71998	0.28690	1.10467
C	1.19198	0.21612	-1.28149
C	3.05645	0.33450	0.80951
H	1.39519	0.27566	2.14211

66

C	2.52806	0.25125	-1.58047
H	0.45849	0.19447	-2.08365
C	3.50299	0.31539	-0.54340
H	3.78310	0.35448	1.61519
H	2.84530	0.26339	-2.61817
N	-18.17306	-0.16189	0.17493
N	4.83866	0.35741	-0.84002
C	-19.05771	-0.63183	1.19240
C	-20.14056	0.15986	1.58919
C	-18.86059	-1.89376	1.76577
C	-21.01474	-0.30393	2.56346
H	-20.28952	1.13905	1.14131
C	-19.73615	-2.34904	2.74133
H	-18.03360	-2.51819	1.43641
C	-20.81714	-1.56011	3.14781
H	-21.85116	0.31250	2.87954
H	-19.59949	-3.32914	3.19097
C	-18.76358	0.31067	-1.03595
C	-19.71440	-0.47476	-1.69622
C	-18.41677	1.56942	-1.54156
C	-20.30495	-0.00844	-2.86341
H	-19.98124	-1.45108	-1.29964
C	-19.00839	2.02725	-2.71021

H	-17.69790	2.18954	-1.01156
C	-19.95411	1.24403	-3.37986
H	-21.03666	-0.62012	-3.38293
H	-18.75333	3.00488	-3.11108
C	5.34092	-0.12913	-2.08506
C	6.19396	0.67471	-2.84940
C	5.00903	-1.41691	-2.52104
C	6.69859	0.19309	-4.04863
H	6.45001	1.67412	-2.50700
C	5.51597	-1.89137	-3.72407
H	4.36770	-2.04871	-1.91127
C	6.36329	-1.08944	-4.49613
H	7.35491	0.80923	-4.65774
H	5.26511	-2.89291	-4.06102
C	5.79038	0.88764	0.08323
C	6.93264	0.14597	0.40251
C	5.59673	2.15730	0.64049
C	7.86918	0.66613	1.28613
H	7.07917	-0.83879	-0.03377
C	6.53545	2.66937	1.52491
H	4.72176	2.74320	0.36960
C	7.67557	1.92978	1.85545
H	8.75200	0.08819	1.54324

68

H	6.40165	3.65596	1.96102
C	-21.72919	-2.10174	4.19838
C	-20.56041	1.78740	-4.63123
C	8.65261	2.53034	2.81132
C	6.93645	-1.55573	-5.79342
O	8.51299	3.61497	3.31918
O	9.69512	1.73909	3.04447
O	6.54775	-2.78629	-6.11367
O	7.67228	-0.89053	-6.47873
O	-21.45145	0.96137	-5.17064
O	-20.27425	2.85917	-5.10386
O	-22.72474	-1.27110	4.49184
O	-21.58100	-3.17608	4.72541
C	-6.67761	-1.32625	-1.53358
H	-7.58967	-1.38767	-2.13935
H	-5.81948	-1.33179	-2.21647
C	-6.76045	1.20340	-1.59816
H	-7.67547	1.17510	-2.20207
H	-5.90575	1.22975	-2.28474
C	-22.08943	1.38779	-6.37222
H	-21.34972	1.55107	-7.16355
H	-22.77399	0.58534	-6.65421
H	-22.64366	2.31764	-6.20426

69

C	-23.65375	-1.69577	5.48642
H	-23.14432	-1.86539	6.44127
H	-24.38332	-0.88950	5.58501
H	-24.15111	-2.62172	5.17779
C	7.04420	-3.32678	-7.33597
H	8.13838	-3.37604	-7.31845
H	6.62180	-4.33022	-7.41845
H	6.72826	-2.71124	-8.18529
C	10.68762	2.22063	3.94766
H	10.25200	2.40398	4.93591
H	11.44792	1.43939	4.00852
H	11.12889	3.15099	3.57391
H	-6.62163	-2.21942	-0.90022
H	-6.76171	2.12936	-1.01127

Table S10. Atomic coordinates of $\mathbf{1}^{Me2+}$ (triplet) from its DFT geometry-optimized structure.

Atom	x	y	z
C	-3.54489	0.12345	2.40937
C	-3.14339	0.11350	1.05304
C	-4.11650	0.07684	0.02759
C	-5.45540	0.05240	0.36851
C	-5.84248	0.06208	1.72503
C	-4.88844	0.09745	2.74762
H	-2.78470	0.15196	3.18620
H	-3.79426	0.06917	-1.01137
H	-5.18748	0.10535	3.79351
C	-6.67164	0.01397	-0.55102
C	-7.80343	0.00397	0.47140
C	-9.16688	-0.02530	0.24871
C	-10.04733	-0.02820	1.35533
C	-9.52961	-0.00240	2.67149
C	-8.16173	0.02752	2.89113
C	-7.30007	0.03138	1.78895
H	-9.57814	-0.04546	-0.75819
H	-10.21960	-0.00553	3.51176
H	-7.77298	0.04783	3.90699
C	-1.76641	0.14235	0.72376
C	-0.57922	0.16948	0.44089

C	-11.44780	-0.05483	1.14725
C	-12.65518	-0.07554	0.96839
C	-14.04441	-0.09662	0.76332
C	-14.58410	-0.12299	-0.55053
C	-14.94071	-0.09057	1.86555
C	-15.94081	-0.13400	-0.75439
H	-13.90911	-0.15208	-1.40182
C	-16.29845	-0.11547	1.66965
H	-14.54055	-0.04734	2.87507
C	-16.83472	-0.13354	0.35220
H	-16.33421	-0.18525	-1.76483
H	-16.96747	-0.07848	2.52374
C	0.78645	0.20470	0.11514
C	1.77528	0.24690	1.13432
C	1.20930	0.20107	-1.24112
C	3.10985	0.29276	0.81925
H	1.46624	0.22521	2.17608
C	2.54250	0.23289	-1.56364
H	0.46227	0.19167	-2.03049
C	3.52914	0.28465	-0.54011
H	3.85120	0.29308	1.61224
H	2.84460	0.26213	-2.60593
N	-18.19420	-0.14962	0.15114

N	4.86508	0.32629	-0.85944
C	-19.07508	-0.70259	1.12321
C	-20.22875	0.00150	1.49123
C	-18.79761	-1.95584	1.68606
C	-21.09246	-0.54118	2.43174
H	-20.43466	0.97534	1.05504
C	-19.66934	-2.49075	2.62274
H	-17.91882	-2.51342	1.37242
C	-20.81792	-1.78926	3.00344
H	-21.98110	0.00615	2.73154
H	-19.47610	-3.46584	3.06199
C	-18.76730	0.38729	-1.03653
C	-19.74448	-0.34297	-1.72477
C	-18.37006	1.65079	-1.49478
C	-20.30946	0.18455	-2.87704
H	-20.04379	-1.32456	-1.36702
C	-18.94370	2.17043	-2.64559
H	-17.63576	2.22767	-0.93848
C	-19.91244	1.44301	-3.34458
H	-21.05736	-0.38258	-3.42304
H	-18.65572	3.15308	-3.00975
C	5.34661	-0.22865	-2.07927
C	6.23758	0.50827	-2.87060

C	4.94858	-1.51471	-2.46688
C	6.71184	-0.03929	-4.05245
H	6.53827	1.50757	-2.56725
C	5.43281	-2.05548	-3.65028
H	4.28338	-2.09448	-1.83213
C	6.31428	-1.32089	-4.45056
H	7.39253	0.52279	-4.68635
H	5.13668	-3.05620	-3.95026
C	5.81276	0.92662	0.01703
C	7.01250	0.26088	0.29908
C	5.55286	2.18779	0.57059
C	7.94104	0.85001	1.14515
H	7.20491	-0.71932	-0.12884
C	6.48905	2.76907	1.41261
H	4.63555	2.71528	0.32199
C	7.68502	2.10638	1.70719
H	8.86690	0.33288	1.37857
H	6.30938	3.75082	1.84267
C	-21.72054	-2.41504	4.01798
C	-20.49576	2.05282	-4.57886
C	8.65711	2.78205	2.62048
C	6.86191	-1.86128	-5.73260
O	8.46096	3.85974	3.12278

O	9.75755	2.06554	2.81623
O	6.41575	-3.08201	-6.00462
O	7.62462	-1.25353	-6.44036
O	-21.40826	1.27600	-5.15033
O	-20.17119	3.13170	-5.00654
O	-22.78012	-1.66352	4.29217
O	-21.50719	-3.48490	4.52993
C	-6.68237	-1.26240	-1.41318
H	-7.59504	-1.30888	-2.02027
H	-5.82427	-1.27161	-2.09681
C	-6.73752	1.26467	-1.44766
H	-7.65197	1.25522	-2.05385
H	-5.88136	1.29243	-2.13317
C	-22.02856	1.76529	-6.33817
H	-21.28003	1.93642	-7.11929
H	-22.73411	0.99363	-6.65205
H	-22.55661	2.70351	-6.13641
C	-23.70674	-2.16986	5.25146
H	-23.21541	-2.31539	6.21955
H	-24.49592	-1.42031	5.33609
H	-24.12403	-3.12491	4.91457
C	6.88076	-3.69212	-7.20737
H	7.97115	-3.79448	-7.18880

75

H	6.40881	-4.67558	-7.25093
H	6.59214	-3.09317	-8.07784
C	10.75284	2.62202	3.67358
H	10.34744	2.78235	4.67844
H	11.56696	1.89538	3.70505
H	11.11122	3.57743	3.27541
H	-6.63640	-2.16378	-0.79034
H	-6.73006	2.18379	-0.84964
C	-3.54489	0.12345	2.40937
C	-3.14339	0.11350	1.05304
C	-4.11650	0.07684	0.02759
C	-5.45540	0.05240	0.36851
C	-5.84248	0.06208	1.72503
C	-4.88844	0.09745	2.74762
H	-2.78470	0.15196	3.18620
H	-3.79426	0.06917	-1.01137
H	-5.18748	0.10535	3.79351
C	-6.67164	0.01397	-0.55102
C	-7.80343	0.00397	0.47140
C	-9.16688	-0.02530	0.24871
C	-10.04733	-0.02820	1.35533
C	-9.52961	-0.00240	2.67149
C	-8.16173	0.02752	2.89113

C	-7.30007	0.03138	1.78895
H	-9.57814	-0.04546	-0.75819
H	-10.21960	-0.00553	3.51176
H	-7.77298	0.04783	3.90699
C	-1.76641	0.14235	0.72376
C	-0.57922	0.16948	0.44089
C	-11.44780	-0.05483	1.14725
C	-12.65518	-0.07554	0.96839
C	-14.04441	-0.09662	0.76332
C	-14.58410	-0.12299	-0.55053
C	-14.94071	-0.09057	1.86555
C	-15.94081	-0.13400	-0.75439
H	-13.90911	-0.15208	-1.40182
C	-16.29845	-0.11547	1.66965
H	-14.54055	-0.04734	2.87507
C	-16.83472	-0.13354	0.35220
H	-16.33421	-0.18525	-1.76483
H	-16.96747	-0.07848	2.52374
C	0.78645	0.20470	0.11514
C	1.77528	0.24690	1.13432
C	1.20930	0.20107	-1.24112
C	3.10985	0.29276	0.81925
H	1.46624	0.22521	2.17608

C	2.54250	0.23289	-1.56364
H	0.46227	0.19167	-2.03049
C	3.52914	0.28465	-0.54011
H	3.85120	0.29308	1.61224
H	2.84460	0.26213	-2.60593
N	-18.19420	-0.14962	0.15114
N	4.86508	0.32629	-0.85944
C	-19.07508	-0.70259	1.12321
C	-20.22875	0.00150	1.49123
C	-18.79761	-1.95584	1.68606
C	-21.09246	-0.54118	2.43174
H	-20.43466	0.97534	1.05504
C	-19.66934	-2.49075	2.62274
H	-17.91882	-2.51342	1.37242
C	-20.81792	-1.78926	3.00344
H	-21.98110	0.00615	2.73154
H	-19.47610	-3.46584	3.06199
C	-18.76730	0.38729	-1.03653
C	-19.74448	-0.34297	-1.72477
C	-18.37006	1.65079	-1.49478
C	-20.30946	0.18455	-2.87704
H	-20.04379	-1.32456	-1.36702
C	-18.94370	2.17043	-2.64559

78

H	-17.63576	2.22767	-0.93848
C	-19.91244	1.44301	-3.34458
H	-21.05736	-0.38258	-3.42304
H	-18.65572	3.15308	-3.00975
C	5.34661	-0.22865	-2.07927
C	6.23758	0.50827	-2.87060
C	4.94858	-1.51471	-2.46688
C	6.71184	-0.03929	-4.05245
H	6.53827	1.50757	-2.56725
C	5.43281	-2.05548	-3.65028
H	4.28338	-2.09448	-1.83213
C	6.31428	-1.32089	-4.45056
H	7.39253	0.52279	-4.68635
H	5.13668	-3.05620	-3.95026
C	5.81276	0.92662	0.01703
C	7.01250	0.26088	0.29908
C	5.55286	2.18779	0.57059
C	7.94104	0.85001	1.14515
H	7.20491	-0.71932	-0.12884
C	6.48905	2.76907	1.41261
H	4.63555	2.71528	0.32199
C	7.68502	2.10638	1.70719
H	8.86690	0.33288	1.37857

H	6.30938	3.75082	1.84267
C	-21.72054	-2.41504	4.01798
C	-20.49576	2.05282	-4.57886
C	8.65711	2.78205	2.62048
C	6.86191	-1.86128	-5.73260
O	8.46096	3.85974	3.12278
O	9.75755	2.06554	2.81623
O	6.41575	-3.08201	-6.00462
O	7.62462	-1.25353	-6.44036
O	-21.40826	1.27600	-5.15033
O	-20.17119	3.13170	-5.00654
O	-22.78012	-1.66352	4.29217
O	-21.50719	-3.48490	4.52993
C	-6.68237	-1.26240	-1.41318
H	-7.59504	-1.30888	-2.02027
H	-5.82427	-1.27161	-2.09681
C	-6.73752	1.26467	-1.44766
H	-7.65197	1.25522	-2.05385
H	-5.88136	1.29243	-2.13317
C	-22.02856	1.76529	-6.33817
H	-21.28003	1.93642	-7.11929
H	-22.73411	0.99363	-6.65205
H	-22.55661	2.70351	-6.13641

80

C	-23.70674	-2.16986	5.25146
H	-23.21541	-2.31539	6.21955
H	-24.49592	-1.42031	5.33609
H	-24.12403	-3.12491	4.91457
C	6.88076	-3.69212	-7.20737
H	7.97115	-3.79448	-7.18880
H	6.40881	-4.67558	-7.25093
H	6.59214	-3.09317	-8.07784
C	10.75284	2.62202	3.67358
H	10.34744	2.78235	4.67844
H	11.56696	1.89538	3.70505
H	11.11122	3.57743	3.27541
H	-6.63640	-2.16378	-0.79034
H	-6.73006	2.18379	-0.84964

Table S11. Atomic coordinates of **2**^{Me} from its DFT geometry-optimized structure.

Atom	x	y	z
C	-2.28356	-0.56735	1.29178
C	-2.65838	0.78184	1.46330
C	-1.66265	1.76214	1.66461
C	-0.33134	1.38465	1.69084
C	0.03036	0.03454	1.51814
C	-0.94645	-0.94334	1.31832
H	-3.05710	-1.31617	1.13735
H	-1.95773	2.80126	1.79628
H	-0.67374	-1.98846	1.18424
C	0.90173	2.26119	1.89251
C	2.01465	1.22023	1.80828
C	3.38214	1.40934	1.91574
C	4.24864	0.30132	1.80581
C	3.70817	-0.98328	1.58871
C	2.33570	-1.17159	1.48115
C	1.48821	-0.06721	1.59085
H	3.80292	2.39895	2.08298
H	4.38211	-1.83294	1.50514
H	1.93584	-2.16996	1.31327
C	-4.03418	1.15155	1.43342
C	-5.21170	1.46540	1.40749

C	-6.53369	1.81559	1.37772
C	-9.09036	2.48613	1.31732
C	-10.07674	1.49924	1.10255
C	-9.47750	3.83058	1.49803
C	-11.41094	1.86568	1.07190
H	-9.77219	0.46377	0.96387
C	-10.81768	4.19549	1.46714
H	-8.71124	4.58464	1.66291
C	-12.63504	0.98022	0.85579
C	-11.78516	3.21122	1.25358
H	-11.09991	5.23714	1.60833
C	-13.75724	2.01094	0.94106
C	-13.24346	3.30107	1.17258
C	-15.12216	1.81088	0.82255
C	-14.10148	4.39698	1.28572
C	-15.99918	2.91030	0.93553
H	-15.53306	0.81909	0.64407
C	-15.47157	4.19763	1.16720
H	-13.71161	5.39742	1.46450
H	-16.15344	5.04072	1.25309
C	-7.71210	2.12596	1.35052
C	5.66192	0.47791	1.91203
C	-17.40974	2.72041	0.81683

C	6.86396	0.62654	2.00077
C	-18.60877	2.55608	0.71605
C	8.27771	0.79777	2.10362
C	8.83748	2.06789	2.33491
C	9.14837	-0.30027	1.97564
C	10.21105	2.23129	2.44111
H	8.18259	2.92934	2.44535
C	10.52243	-0.13316	2.06740
H	8.73756	-1.28987	1.78835
C	11.07223	1.13395	2.30496
H	10.62390	3.21860	2.63424
H	11.17951	-0.99180	1.95143
C	-20.01829	2.36131	0.59763
C	-20.55131	1.08395	0.34398
C	-20.91080	3.44095	0.73152
C	-21.92123	0.89354	0.23611
H	-19.87990	0.23391	0.24501
C	-22.27969	3.25143	0.60941
H	-20.51976	4.43840	0.91950
C	-22.80335	1.97495	0.36379
H	-22.31524	-0.10340	0.05342
H	-22.95291	4.10038	0.70210
N	12.47731	1.30254	2.40616

N	-24.20411	1.78034	0.24578
C	13.23116	0.41050	3.19866
C	14.49009	-0.04088	2.77081
C	12.72795	-0.04961	4.42649
C	15.22672	-0.91965	3.55215
H	14.88759	0.29535	1.81667
C	13.46407	-0.93613	5.19756
H	11.75851	0.29663	4.77535
C	14.72214	-1.38087	4.77440
H	16.19682	-1.26539	3.20593
H	13.07553	-1.28680	6.15071
C	13.10576	2.35867	1.71261
C	14.15551	3.08034	2.30353
C	12.68393	2.71266	0.42054
C	14.77025	4.11879	1.61872
H	14.48461	2.82771	3.30814
C	13.29478	3.75865	-0.25406
H	11.87810	2.15890	-0.05415
C	14.34616	4.47333	0.33197
H	15.57752	4.67216	2.09054
H	12.97085	4.02734	-1.25670
C	-25.07067	2.35291	1.20088
C	-26.30096	2.90866	0.81231

C	-24.71145	2.38629	2.55784
C	-27.14531	3.47093	1.75715
H	-26.58865	2.90386	-0.23581
C	-25.55622	2.96039	3.49722
H	-23.76624	1.95352	2.87509
C	-26.78571	3.50712	3.10982
H	-28.09470	3.90558	1.45354
H	-25.26773	2.97376	4.54462
C	-24.71280	1.01404	-0.82454
C	-25.78777	0.13193	-0.62905
C	-24.14268	1.11363	-2.10428
C	-26.28266	-0.62092	-1.68435
H	-26.23132	0.03294	0.35828
C	-24.63465	0.35056	-3.15209
H	-23.31508	1.79751	-2.27382
C	-25.71093	-0.52348	-2.95905
H	-27.11122	-1.30363	-1.51739
H	-24.19576	0.43361	-4.14348
C	15.46962	-2.32691	5.64180
C	14.96795	5.58091	-0.43784
C	-26.20118	-1.31332	-4.11746
C	-27.72535	4.12721	4.07859
O	-25.72609	-1.26081	-5.22672

O	-27.23454	-2.09966	-3.80919
O	-27.26549	4.10893	5.33138
O	-28.79520	4.60202	3.78031
O	15.96730	6.17263	0.21971
O	14.61823	5.92172	-1.54259
O	16.65661	-2.66776	5.13587
O	15.06047	-2.75185	6.69580
C	0.88007	2.94964	3.26979
H	1.80180	3.52370	3.42875
H	0.03433	3.64552	3.34016
C	1.03216	3.31290	0.77544
H	1.95821	3.88955	0.89530
H	0.19118	4.01726	0.80779
C	-12.59895	0.30234	-0.52640
H	-11.74689	-0.38579	-0.59667
H	-13.51471	-0.27837	-0.69540
C	-12.76330	-0.08094	1.96418
H	-13.68342	-0.66481	1.83408
H	-11.91588	-0.77754	1.93202
C	16.62532	7.25006	-0.43703
H	15.92116	8.06178	-0.65167
H	17.40159	7.59718	0.24846
H	17.07548	6.91405	-1.37787

C	17.44646	-3.57548	5.89570
H	16.92102	-4.52756	6.03083
H	18.36583	-3.73063	5.32680
H	17.67866	-3.15653	6.88125
C	-28.09751	4.68024	6.33456
H	-29.05998	4.15872	6.38382
H	-27.55959	4.56706	7.27838
H	-28.27991	5.74110	6.12936
C	-27.77358	-2.89907	-4.85589
H	-27.01462	-3.58339	-5.25150
H	-28.59716	-3.46492	-4.41490
H	-28.14317	-2.26989	-5.67336
H	0.78886	2.21498	4.07899
H	-12.50903	1.04376	-1.32954
H	-12.78883	0.38383	2.95724
H	1.04721	2.84057	-0.21426
C	-2.28356	-0.56735	1.29178
C	-2.65838	0.78184	1.46330
C	-1.66265	1.76214	1.66461
C	-0.33134	1.38465	1.69084
C	0.03036	0.03454	1.51814
C	-0.94645	-0.94334	1.31832
H	-3.05710	-1.31617	1.13735

H	-1.95773	2.80126	1.79628
H	-0.67374	-1.98846	1.18424
C	0.90173	2.26119	1.89251
C	2.01465	1.22023	1.80828
C	3.38214	1.40934	1.91574
C	4.24864	0.30132	1.80581
C	3.70817	-0.98328	1.58871
C	2.33570	-1.17159	1.48115
C	1.48821	-0.06721	1.59085
H	3.80292	2.39895	2.08298
H	4.38211	-1.83294	1.50514
H	1.93584	-2.16996	1.31327
C	-4.03418	1.15155	1.43342
C	-5.21170	1.46540	1.40749
C	-6.53369	1.81559	1.37772
C	-9.09036	2.48613	1.31732
C	-10.07674	1.49924	1.10255
C	-9.47750	3.83058	1.49803
C	-11.41094	1.86568	1.07190
H	-9.77219	0.46377	0.96387
C	-10.81768	4.19549	1.46714
H	-8.71124	4.58464	1.66291
C	-12.63504	0.98022	0.85579

89

C	-11.78516	3.21122	1.25358
H	-11.09991	5.23714	1.60833
C	-13.75724	2.01094	0.94106
C	-13.24346	3.30107	1.17258
C	-15.12216	1.81088	0.82255
C	-14.10148	4.39698	1.28572
C	-15.99918	2.91030	0.93553
H	-15.53306	0.81909	0.64407
C	-15.47157	4.19763	1.16720
H	-13.71161	5.39742	1.46450
H	-16.15344	5.04072	1.25309
C	-7.71210	2.12596	1.35052
C	5.66192	0.47791	1.91203
C	-17.40974	2.72041	0.81683
C	6.86396	0.62654	2.00077
C	-18.60877	2.55608	0.71605
C	8.27771	0.79777	2.10362
C	8.83748	2.06789	2.33491
C	9.14837	-0.30027	1.97564
C	10.21105	2.23129	2.44111
H	8.18259	2.92934	2.44535
C	10.52243	-0.13316	2.06740
H	8.73756	-1.28987	1.78835

90

C	11.07223	1.13395	2.30496
H	10.62390	3.21860	2.63424
H	11.17951	-0.99180	1.95143
C	-20.01829	2.36131	0.59763
C	-20.55131	1.08395	0.34398
C	-20.91080	3.44095	0.73152
C	-21.92123	0.89354	0.23611
H	-19.87990	0.23391	0.24501
C	-22.27969	3.25143	0.60941
H	-20.51976	4.43840	0.91950
C	-22.80335	1.97495	0.36379
H	-22.31524	-0.10340	0.05342
H	-22.95291	4.10038	0.70210
N	12.47731	1.30254	2.40616
N	-24.20411	1.78034	0.24578
C	13.23116	0.41050	3.19866
C	14.49009	-0.04088	2.77081
C	12.72795	-0.04961	4.42649
C	15.22672	-0.91965	3.55215
H	14.88759	0.29535	1.81667
C	13.46407	-0.93613	5.19756
H	11.75851	0.29663	4.77535
C	14.72214	-1.38087	4.77440

91

H	16.19682	-1.26539	3.20593
H	13.07553	-1.28680	6.15071
C	13.10576	2.35867	1.71261
C	14.15551	3.08034	2.30353
C	12.68393	2.71266	0.42054
C	14.77025	4.11879	1.61872
H	14.48461	2.82771	3.30814
C	13.29478	3.75865	-0.25406
H	11.87810	2.15890	-0.05415
C	14.34616	4.47333	0.33197
H	15.57752	4.67216	2.09054
H	12.97085	4.02734	-1.25670
C	-25.07067	2.35291	1.20088
C	-26.30096	2.90866	0.81231
C	-24.71145	2.38629	2.55784
C	-27.14531	3.47093	1.75715
H	-26.58865	2.90386	-0.23581
C	-25.55622	2.96039	3.49722
H	-23.76624	1.95352	2.87509
C	-26.78571	3.50712	3.10982
H	-28.09470	3.90558	1.45354
H	-25.26773	2.97376	4.54462
C	-24.71280	1.01404	-0.82454

C	-25.78777	0.13193	-0.62905
C	-24.14268	1.11363	-2.10428
C	-26.28266	-0.62092	-1.68435
H	-26.23132	0.03294	0.35828
C	-24.63465	0.35056	-3.15209
H	-23.31508	1.79751	-2.27382
C	-25.71093	-0.52348	-2.95905
H	-27.11122	-1.30363	-1.51739
H	-24.19576	0.43361	-4.14348
C	15.46962	-2.32691	5.64180
C	14.96795	5.58091	-0.43784
C	-26.20118	-1.31332	-4.11746
C	-27.72535	4.12721	4.07859
O	-25.72609	-1.26081	-5.22672
O	-27.23454	-2.09966	-3.80919
O	-27.26549	4.10893	5.33138
O	-28.79520	4.60202	3.78031
O	15.96730	6.17263	0.21971
O	14.61823	5.92172	-1.54259
O	16.65661	-2.66776	5.13587
O	15.06047	-2.75185	6.69580
C	0.88007	2.94964	3.26979
H	1.80180	3.52370	3.42875

H	0.03433	3.64552	3.34016
C	1.03216	3.31290	0.77544
H	1.95821	3.88955	0.89530
H	0.19118	4.01726	0.80779
C	-12.59895	0.30234	-0.52640
H	-11.74689	-0.38579	-0.59667
H	-13.51471	-0.27837	-0.69540
C	-12.76330	-0.08094	1.96418
H	-13.68342	-0.66481	1.83408
H	-11.91588	-0.77754	1.93202
C	16.62532	7.25006	-0.43703
H	15.92116	8.06178	-0.65167
H	17.40159	7.59718	0.24846
H	17.07548	6.91405	-1.37787
C	17.44646	-3.57548	5.89570
H	16.92102	-4.52756	6.03083
H	18.36583	-3.73063	5.32680
H	17.67866	-3.15653	6.88125
C	-28.09751	4.68024	6.33456
H	-29.05998	4.15872	6.38382
H	-27.55959	4.56706	7.27838
H	-28.27991	5.74110	6.12936
C	-27.77358	-2.89907	-4.85589

H	-27.01462	-3.58339	-5.25150
H	-28.59716	-3.46492	-4.41490
H	-28.14317	-2.26989	-5.67336
H	0.78886	2.21498	4.07899
H	-12.50903	1.04376	-1.32954
H	-12.78883	0.38383	2.95724
H	1.04721	2.84057	-0.21426

Table S12. Atomic coordinates of $\mathbf{2}^{Me+}$ from its DFT geometry-optimized structure.

Atom	x	y	z
C	8.51725	15.94718	0.17346
C	5.95748	16.60217	0.10907
C	4.97787	15.60921	-0.11066
C	5.56259	17.94393	0.29435
C	3.64183	15.96747	-0.14120
H	5.28928	14.57625	-0.25265
C	4.22047	18.30043	0.26343
H	6.32418	18.70185	0.46291
C	2.42313	15.07570	-0.36117
C	3.25951	17.31046	0.04533
H	3.93130	19.33960	0.40831
C	1.29510	16.09959	-0.27218
C	1.80107	17.39189	-0.03583

C	-0.06866	15.89188	-0.39124
C	0.93678	18.48255	0.08148
C	-0.95193	16.98571	-0.27374
H	-0.47386	14.89844	-0.57330
C	-0.43194	18.27550	-0.03743
H	1.32076	19.48459	0.26387
H	-1.11887	19.11409	0.05179
C	7.33678	16.25062	0.14373
C	-2.36130	16.78788	-0.39215
C	-3.55941	16.61661	-0.49229
C	-4.96775	16.41340	-0.60979
C	-5.49239	15.13504	-0.87557
C	-5.86740	17.48537	-0.46272
C	-6.86111	14.93621	-0.98259
H	-4.81533	14.29074	-0.98473
C	-7.23516	17.28758	-0.58375
H	-5.48293	18.48355	-0.26524
C	-7.75060	16.01006	-0.84171
H	-7.24847	13.93847	-1.17481
H	-7.91397	18.13085	-0.48074
N	-9.14987	15.80702	-0.95878
C	-10.01910	16.36841	0.00082
C	-11.25197	16.92109	-0.38364

C	-9.66006	16.39284	1.35795
C	-12.09909	17.47196	0.56547
H	-11.53957	16.92281	-1.43181
C	-10.50758	16.95566	2.30171
H	-8.71285	15.96197	1.67187
C	-11.73961	17.49947	1.91835
H	-13.05060	17.90428	0.26521
H	-10.21930	16.96229	3.34923
C	-9.65572	15.04375	-2.03279
C	-10.72400	14.15304	-1.84013
C	-9.08970	15.15568	-3.31329
C	-11.21641	13.40352	-2.89899
H	-11.16434	14.04482	-0.85233
C	-9.57898	14.39582	-4.36469
H	-8.26751	15.84662	-3.48059
C	-10.64858	13.51304	-4.17443
H	-12.03987	12.71410	-2.73436
H	-9.14337	14.48827	-5.35669
C	-11.13621	12.72713	-5.33671
C	-12.68223	18.10775	2.89186
O	-10.66363	12.78959	-6.44652
O	-12.16380	11.93236	-5.03119
O	-12.22218	18.08226	4.14440

O	-13.75427	18.57967	2.59708
C	2.46363	14.40353	-1.74606
H	3.31944	13.72030	-1.81867
H	1.55115	13.81848	-1.91752
C	2.30084	14.00956	0.74313
H	1.38409	13.42107	0.61043
H	3.15214	13.31784	0.70835
C	-13.05679	18.64224	5.15187
H	-14.01667	18.11568	5.19752
H	-12.51812	18.52486	6.09476
H	-13.24442	19.70364	4.95432
C	-12.70012	11.13609	-6.08172
H	-11.93775	10.45903	-6.48319
H	-13.51918	10.56237	-5.64249
H	-13.07543	11.76806	-6.89442
H	2.54962	15.14855	-2.54628
H	2.27237	14.47027	1.73799
C	12.77646	13.58858	0.08597
C	12.39472	14.93601	0.27768
C	13.38135	15.91882	0.50886
C	14.71334	15.54676	0.54586
C	15.08141	14.19936	0.35394
C	14.11167	13.21758	0.12286

H	12.00683	12.84127	-0.09141
H	13.07832	16.95337	0.65501
H	14.39174	12.17674	-0.02611
C	15.93854	16.42449	0.77964
C	17.05448	15.38820	0.69414
C	18.41411	15.57214	0.82461
C	19.27955	14.45457	0.70617
C	18.74037	13.16681	0.45642
C	17.37513	12.98687	0.32645
C	16.52996	14.09852	0.44500
H	18.83965	16.55489	1.01585
H	19.41671	12.32002	0.36848
H	16.97080	11.99525	0.13523
C	11.01928	15.29807	0.23911
C	9.83983	15.60505	0.20770
C	20.67140	14.61983	0.83604
C	21.88224	14.76126	0.94924
C	23.26487	14.91980	1.07960
C	23.83089	16.19598	1.35415
C	24.14197	13.80798	0.94180
C	25.18640	16.35430	1.47927
H	23.17239	17.05105	1.48341
C	25.49738	13.95787	1.07703

99

H	23.72644	12.83099	0.70873
C	26.06048	15.23754	1.34828
H	25.59376	17.33179	1.71706
H	26.14935	13.10108	0.94000
N	27.41611	15.39092	1.48093
C	28.25260	14.29883	1.86090
C	29.41195	14.02766	1.12575
C	27.92797	13.52474	2.98168
C	30.23535	12.97556	1.50311
H	29.65792	14.63096	0.25578
C	28.75666	12.47511	3.35163
H	27.04203	13.75692	3.56740
C	29.91239	12.19197	2.61693
H	31.13011	12.75436	0.92887
H	28.52303	11.86947	4.22335
C	28.04661	16.64951	1.24535
C	28.94889	17.15777	2.18635
C	27.78416	17.35352	0.06387
C	29.57516	18.37426	1.95124
H	29.14715	16.60746	3.10243
C	28.41491	18.56845	-0.16312
H	27.10445	16.94089	-0.67744
C	29.31133	19.08764	0.77632

100

H	30.26763	18.77828	2.68373
H	28.22820	19.12372	-1.07860
C	30.76841	11.05149	3.06234
C	29.96295	20.39864	0.47862
O	30.79611	20.78632	1.43838
O	29.75583	21.03622	-0.52321
O	31.84199	10.88713	2.29684
O	30.51362	10.35560	4.01309
C	15.89510	17.08949	2.16813
H	16.81070	17.66678	2.34806
H	15.04448	17.77909	2.23641
C	16.08226	17.49353	-0.31961
H	17.00280	18.07298	-0.17506
H	15.23704	18.19228	-0.28824
C	31.47112	22.02843	1.25115
H	30.75003	22.84826	1.16256
H	32.09800	22.16958	2.13381
H	32.08950	21.99719	0.34751
C	32.72729	9.82261	2.63819
H	32.20668	8.85993	2.59180
H	33.53481	9.85177	1.90400
H	33.12710	9.96442	3.64814
H	15.79658	16.34177	2.96417

H	16.11492	17.03717	-1.31619
C	8.51725	15.94718	0.17346
C	5.95748	16.60217	0.10907
C	4.97787	15.60921	-0.11066
C	5.56259	17.94393	0.29435
C	3.64183	15.96747	-0.14120
H	5.28928	14.57625	-0.25265
C	4.22047	18.30043	0.26343
H	6.32418	18.70185	0.46291
C	2.42313	15.07570	-0.36117
C	3.25951	17.31046	0.04533
H	3.93130	19.33960	0.40831
C	1.29510	16.09959	-0.27218
C	1.80107	17.39189	-0.03583
C	-0.06866	15.89188	-0.39124
C	0.93678	18.48255	0.08148
C	-0.95193	16.98571	-0.27374
H	-0.47386	14.89844	-0.57330
C	-0.43194	18.27550	-0.03743
H	1.32076	19.48459	0.26387
H	-1.11887	19.11409	0.05179
C	7.33678	16.25062	0.14373
C	-2.36130	16.78788	-0.39215

C	-3.55941	16.61661	-0.49229
C	-4.96775	16.41340	-0.60979
C	-5.49239	15.13504	-0.87557
C	-5.86740	17.48537	-0.46272
C	-6.86111	14.93621	-0.98259
H	-4.81533	14.29074	-0.98473
C	-7.23516	17.28758	-0.58375
H	-5.48293	18.48355	-0.26524
C	-7.75060	16.01006	-0.84171
H	-7.24847	13.93847	-1.17481
H	-7.91397	18.13085	-0.48074
N	-9.14987	15.80702	-0.95878
C	-10.01910	16.36841	0.00082
C	-11.25197	16.92109	-0.38364
C	-9.66006	16.39284	1.35795
C	-12.09909	17.47196	0.56547
H	-11.53957	16.92281	-1.43181
C	-10.50758	16.95566	2.30171
H	-8.71285	15.96197	1.67187
C	-11.73961	17.49947	1.91835
H	-13.05060	17.90428	0.26521
H	-10.21930	16.96229	3.34923
C	-9.65572	15.04375	-2.03279

C	-10.72400	14.15304	-1.84013
C	-9.08970	15.15568	-3.31329
C	-11.21641	13.40352	-2.89899
H	-11.16434	14.04482	-0.85233
C	-9.57898	14.39582	-4.36469
H	-8.26751	15.84662	-3.48059
C	-10.64858	13.51304	-4.17443
H	-12.03987	12.71410	-2.73436
H	-9.14337	14.48827	-5.35669
C	-11.13621	12.72713	-5.33671
C	-12.68223	18.10775	2.89186
O	-10.66363	12.78959	-6.44652
O	-12.16380	11.93236	-5.03119
O	-12.22218	18.08226	4.14440
O	-13.75427	18.57967	2.59708
C	2.46363	14.40353	-1.74606
H	3.31944	13.72030	-1.81867
H	1.55115	13.81848	-1.91752
C	2.30084	14.00956	0.74313
H	1.38409	13.42107	0.61043
H	3.15214	13.31784	0.70835
C	-13.05679	18.64224	5.15187
H	-14.01667	18.11568	5.19752

104

H	-12.51812	18.52486	6.09476
H	-13.24442	19.70364	4.95432
C	-12.70012	11.13609	-6.08172
H	-11.93775	10.45903	-6.48319
H	-13.51918	10.56237	-5.64249
H	-13.07543	11.76806	-6.89442
H	2.54962	15.14855	-2.54628
H	2.27237	14.47027	1.73799
C	12.77646	13.58858	0.08597
C	12.39472	14.93601	0.27768
C	13.38135	15.91882	0.50886
C	14.71334	15.54676	0.54586
C	15.08141	14.19936	0.35394
C	14.11167	13.21758	0.12286
H	12.00683	12.84127	-0.09141
H	13.07832	16.95337	0.65501
H	14.39174	12.17674	-0.02611
C	15.93854	16.42449	0.77964
C	17.05448	15.38820	0.69414
C	18.41411	15.57214	0.82461
C	19.27955	14.45457	0.70617
C	18.74037	13.16681	0.45642
C	17.37513	12.98687	0.32645

105

C	16.52996	14.09852	0.44500
H	18.83965	16.55489	1.01585
H	19.41671	12.32002	0.36848
H	16.97080	11.99525	0.13523
C	11.01928	15.29807	0.23911
C	9.83983	15.60505	0.20770
C	20.67140	14.61983	0.83604
C	21.88224	14.76126	0.94924
C	23.26487	14.91980	1.07960
C	23.83089	16.19598	1.35415
C	24.14197	13.80798	0.94180
C	25.18640	16.35430	1.47927
H	23.17239	17.05105	1.48341
C	25.49738	13.95787	1.07703
H	23.72644	12.83099	0.70873
C	26.06048	15.23754	1.34828
H	25.59376	17.33179	1.71706
H	26.14935	13.10108	0.94000
N	27.41611	15.39092	1.48093
C	28.25260	14.29883	1.86090
C	29.41195	14.02766	1.12575
C	27.92797	13.52474	2.98168
C	30.23535	12.97556	1.50311

H	29.65792	14.63096	0.25578
C	28.75666	12.47511	3.35163
H	27.04203	13.75692	3.56740
C	29.91239	12.19197	2.61693
H	31.13011	12.75436	0.92887
H	28.52303	11.86947	4.22335
C	28.04661	16.64951	1.24535
C	28.94889	17.15777	2.18635
C	27.78416	17.35352	0.06387
C	29.57516	18.37426	1.95124
H	29.14715	16.60746	3.10243
C	28.41491	18.56845	-0.16312
H	27.10445	16.94089	-0.67744
C	29.31133	19.08764	0.77632
H	30.26763	18.77828	2.68373
H	28.22820	19.12372	-1.07860
C	30.76841	11.05149	3.06234
C	29.96295	20.39864	0.47862
O	30.79611	20.78632	1.43838
O	29.75583	21.03622	-0.52321
O	31.84199	10.88713	2.29684
O	30.51362	10.35560	4.01309
C	15.89510	17.08949	2.16813

107

H	16.81070	17.66678	2.34806
H	15.04448	17.77909	2.23641
C	16.08226	17.49353	-0.31961
H	17.00280	18.07298	-0.17506
H	15.23704	18.19228	-0.28824
C	31.47112	22.02843	1.25115
H	30.75003	22.84826	1.16256
H	32.09800	22.16958	2.13381
H	32.08950	21.99719	0.34751
C	32.72729	9.82261	2.63819
H	32.20668	8.85993	2.59180
H	33.53481	9.85177	1.90400
H	33.12710	9.96442	3.64814
H	15.79658	16.34177	2.96417
H	16.11492	17.03717	-1.31619

Table S13. Atomic coordinates of $\mathbf{2}^{Me2+}$ (closed-shell singlet) from its DFT geometry-optimized structure.

Atom	x	y	z
C	-2.25032	-0.58261	1.16649
C	-2.64751	0.77278	1.35089
C	-1.66785	1.77780	1.57327
C	-0.34041	1.42281	1.60921
C	0.04383	0.06765	1.42410

C	-0.91963	-0.93513	1.20133
H	-3.01563	-1.33580	0.99756
H	-1.98769	2.80796	1.71159
H	-0.62354	-1.97184	1.05916
C	0.87916	2.30881	1.83310
C	1.99811	1.27766	1.74885
C	3.35415	1.46696	1.87086
C	4.22454	0.34995	1.75262
C	3.68655	-0.94761	1.51207
C	2.32799	-1.13532	1.39185
C	1.47459	-0.02092	1.50887
H	3.77876	2.45122	2.05414
H	4.36870	-1.78948	1.42536
H	1.92576	-2.12917	1.20926
C	-4.00656	1.11030	1.31367
C	-5.19840	1.40412	1.28249
C	-6.50618	1.72683	1.24930
C	-9.05742	2.35815	1.18576
C	-10.03825	1.35163	0.97631
C	-9.45369	3.71452	1.36195
C	-11.36613	1.70616	0.94626
H	-9.71922	0.32040	0.84414
C	-10.78493	4.06671	1.33146

109

H	-8.68769	4.46919	1.52100
C	-12.58711	0.81797	0.73871
C	-11.74935	3.06239	1.12273
H	-11.08022	5.10454	1.46705
C	-13.70599	1.84918	0.82408
C	-13.18179	3.14967	1.04752
C	-15.06352	1.65738	0.71657
C	-14.03501	4.26388	1.16056
C	-15.93370	2.77393	0.83210
H	-15.48840	0.67079	0.54682
C	-15.39496	4.07367	1.05388
H	-13.63252	5.25999	1.33001
H	-16.07687	4.91597	1.13844
C	-7.69802	2.02065	1.21955
C	5.61134	0.51873	1.87106
C	-17.32305	2.60190	0.73088
C	6.82269	0.66366	1.97349
C	-18.53472	2.45420	0.64604
C	8.20941	0.82785	2.09062
C	8.77247	2.10062	2.36473
C	9.08845	-0.27500	1.93838
C	10.13291	2.26288	2.47929
H	8.11404	2.95470	2.50308

C	10.44909	-0.11687	2.05536
H	8.67719	-1.25492	1.70873
C	11.00847	1.15736	2.32893
H	10.53752	3.24274	2.71313
H	11.10194	-0.97213	1.91118
C	-19.92451	2.28650	0.55103
C	-20.49081	1.00507	0.33448
C	-20.80056	3.39464	0.67046
C	-21.85335	0.84007	0.24020
H	-19.83640	0.14009	0.25870
C	-22.16372	3.23212	0.58213
H	-20.38437	4.38821	0.81807
C	-22.72575	1.94988	0.36324
H	-22.26413	-0.15450	0.09576
H	-22.81277	4.09936	0.65551
N	12.37593	1.31774	2.44664
N	-24.09720	1.78529	0.27203
C	13.21059	0.23843	2.85193
C	14.37643	-0.04880	2.13147
C	12.88447	-0.52120	3.98345
C	15.20247	-1.08961	2.53386
H	14.62730	0.53841	1.25178
C	13.71129	-1.56335	4.37652

H	11.99253	-0.28415	4.55814
C	14.87509	-1.85701	3.65766
H	16.10204	-1.31689	1.96928
H	13.47150	-2.15490	5.25640
C	12.99687	2.56748	2.16716
C	13.92758	3.09944	3.06807
C	12.70072	3.25489	0.98245
C	14.54881	4.30966	2.79076
H	14.15459	2.56742	3.98840
C	13.32105	4.46631	0.71431
H	11.99668	2.83137	0.27047
C	14.24846	5.00417	1.61328
H	15.26426	4.72535	3.49429
H	13.10393	5.00478	-0.20469
C	-24.98734	2.67253	0.93807
C	-26.08144	3.21141	0.24871
C	-24.78865	2.99143	2.28776
C	-26.95786	4.06414	0.90337
H	-26.23429	2.96746	-0.79948
C	-25.66670	3.84996	2.93549
H	-23.95360	2.55518	2.83029
C	-26.75835	4.39341	2.24876
H	-27.80495	4.49468	0.37547

H	-25.51503	4.09044	3.98374
C	-24.65925	0.72499	-0.49109
C	-25.68120	-0.06199	0.05461
C	-24.21240	0.47938	-1.79664
C	-26.24443	-1.08634	-0.69428
H	-26.02513	0.12568	1.06856
C	-24.77512	-0.54977	-2.53696
H	-23.43600	1.10434	-2.23089
C	-25.79414	-1.34068	-1.99494
H	-27.03140	-1.70072	-0.26669
H	-24.44073	-0.74411	-3.55286
C	15.72912	-2.98591	4.12755
C	14.88805	6.30772	1.27234
C	-26.36617	-2.43013	-2.83730
C	-27.72984	5.31735	2.90164
O	-25.99265	-2.68133	-3.95643
O	-27.33746	-3.09996	-2.22222
O	-27.43261	5.55981	4.17593
O	-28.68348	5.79704	2.34013
O	15.75804	6.71056	2.19466
O	14.64608	6.93320	0.26980
O	16.81332	-3.15797	3.37613
O	15.46928	-3.67174	5.08513

C	0.83659	2.97990	3.21904
H	1.75099	3.56069	3.39136
H	-0.01571	3.66729	3.28523
C	1.01264	3.37154	0.72611
H	1.93197	3.95376	0.86432
H	0.16563	4.06767	0.75925
C	-12.55541	0.13694	-0.64270
H	-11.70332	-0.55053	-0.71103
H	-13.47096	-0.44537	-0.80348
C	-12.71109	-0.23693	1.85418
H	-13.63142	-0.82030	1.72783
H	-11.86430	-0.93328	1.81908
C	16.42459	7.94861	1.96200
H	15.70117	8.76809	1.88924
H	17.08601	8.10342	2.81687
H	17.00720	7.90420	1.03531
C	17.69669	-4.21448	3.74299
H	17.18010	-5.17977	3.70398
H	18.51339	-4.19365	3.01855
H	18.08428	-4.05832	4.75568
C	-28.30306	6.43282	4.89079
H	-29.32050	6.02743	4.91569
H	-27.89962	6.50303	5.90302

H	-28.32560	7.42292	4.42240
C	-27.95106	-4.16403	-2.94482
H	-27.21194	-4.92945	-3.20566
H	-28.71115	-4.58315	-2.28236
H	-28.41465	-3.78868	-3.86372
H	0.74354	2.23623	4.01928
H	-12.46927	0.87499	-1.44892
H	-12.73256	0.23166	2.84519
H	1.04223	2.91003	-0.26799
C	-2.25032	-0.58261	1.16649
C	-2.64751	0.77278	1.35089
C	-1.66785	1.77780	1.57327
C	-0.34041	1.42281	1.60921
C	0.04383	0.06765	1.42410
C	-0.91963	-0.93513	1.20133
H	-3.01563	-1.33580	0.99756
H	-1.98769	2.80796	1.71159
H	-0.62354	-1.97184	1.05916
C	0.87916	2.30881	1.83310
C	1.99811	1.27766	1.74885
C	3.35415	1.46696	1.87086
C	4.22454	0.34995	1.75262
C	3.68655	-0.94761	1.51207

115

C	2.32799	-1.13532	1.39185
C	1.47459	-0.02092	1.50887
H	3.77876	2.45122	2.05414
H	4.36870	-1.78948	1.42536
H	1.92576	-2.12917	1.20926
C	-4.00656	1.11030	1.31367
C	-5.19840	1.40412	1.28249
C	-6.50618	1.72683	1.24930
C	-9.05742	2.35815	1.18576
C	-10.03825	1.35163	0.97631
C	-9.45369	3.71452	1.36195
C	-11.36613	1.70616	0.94626
H	-9.71922	0.32040	0.84414
C	-10.78493	4.06671	1.33146
H	-8.68769	4.46919	1.52100
C	-12.58711	0.81797	0.73871
C	-11.74935	3.06239	1.12273
H	-11.08022	5.10454	1.46705
C	-13.70599	1.84918	0.82408
C	-13.18179	3.14967	1.04752
C	-15.06352	1.65738	0.71657
C	-14.03501	4.26388	1.16056
C	-15.93370	2.77393	0.83210

H	-15.48840	0.67079	0.54682
C	-15.39496	4.07367	1.05388
H	-13.63252	5.25999	1.33001
H	-16.07687	4.91597	1.13844
C	-7.69802	2.02065	1.21955
C	5.61134	0.51873	1.87106
C	-17.32305	2.60190	0.73088
C	6.82269	0.66366	1.97349
C	-18.53472	2.45420	0.64604
C	8.20941	0.82785	2.09062
C	8.77247	2.10062	2.36473
C	9.08845	-0.27500	1.93838
C	10.13291	2.26288	2.47929
H	8.11404	2.95470	2.50308
C	10.44909	-0.11687	2.05536
H	8.67719	-1.25492	1.70873
C	11.00847	1.15736	2.32893
H	10.53752	3.24274	2.71313
H	11.10194	-0.97213	1.91118
C	-19.92451	2.28650	0.55103
C	-20.49081	1.00507	0.33448
C	-20.80056	3.39464	0.67046
C	-21.85335	0.84007	0.24020

H	-19.83640	0.14009	0.25870
C	-22.16372	3.23212	0.58213
H	-20.38437	4.38821	0.81807
C	-22.72575	1.94988	0.36324
H	-22.26413	-0.15450	0.09576
H	-22.81277	4.09936	0.65551
N	12.37593	1.31774	2.44664
N	-24.09720	1.78529	0.27203
C	13.21059	0.23843	2.85193
C	14.37643	-0.04880	2.13147
C	12.88447	-0.52120	3.98345
C	15.20247	-1.08961	2.53386
H	14.62730	0.53841	1.25178
C	13.71129	-1.56335	4.37652
H	11.99253	-0.28415	4.55814
C	14.87509	-1.85701	3.65766
H	16.10204	-1.31689	1.96928
H	13.47150	-2.15490	5.25640
C	12.99687	2.56748	2.16716
C	13.92758	3.09944	3.06807
C	12.70072	3.25489	0.98245
C	14.54881	4.30966	2.79076
H	14.15459	2.56742	3.98840

C	13.32105	4.46631	0.71431
H	11.99668	2.83137	0.27047
C	14.24846	5.00417	1.61328
H	15.26426	4.72535	3.49429
H	13.10393	5.00478	-0.20469
C	-24.98734	2.67253	0.93807
C	-26.08144	3.21141	0.24871
C	-24.78865	2.99143	2.28776
C	-26.95786	4.06414	0.90337
H	-26.23429	2.96746	-0.79948
C	-25.66670	3.84996	2.93549
H	-23.95360	2.55518	2.83029
C	-26.75835	4.39341	2.24876
H	-27.80495	4.49468	0.37547
H	-25.51503	4.09044	3.98374
C	-24.65925	0.72499	-0.49109
C	-25.68120	-0.06199	0.05461
C	-24.21240	0.47938	-1.79664
C	-26.24443	-1.08634	-0.69428
H	-26.02513	0.12568	1.06856
C	-24.77512	-0.54977	-2.53696
H	-23.43600	1.10434	-2.23089
C	-25.79414	-1.34068	-1.99494

H	-27.03140	-1.70072	-0.26669
H	-24.44073	-0.74411	-3.55286
C	15.72912	-2.98591	4.12755
C	14.88805	6.30772	1.27234
C	-26.36617	-2.43013	-2.83730
C	-27.72984	5.31735	2.90164
O	-25.99265	-2.68133	-3.95643
O	-27.33746	-3.09996	-2.22222
O	-27.43261	5.55981	4.17593
O	-28.68348	5.79704	2.34013
O	15.75804	6.71056	2.19466
O	14.64608	6.93320	0.26980
O	16.81332	-3.15797	3.37613
O	15.46928	-3.67174	5.08513
C	0.83659	2.97990	3.21904
H	1.75099	3.56069	3.39136
H	-0.01571	3.66729	3.28523
C	1.01264	3.37154	0.72611
H	1.93197	3.95376	0.86432
H	0.16563	4.06767	0.75925
C	-12.55541	0.13694	-0.64270
H	-11.70332	-0.55053	-0.71103
H	-13.47096	-0.44537	-0.80348

C	-12.71109	-0.23693	1.85418
H	-13.63142	-0.82030	1.72783
H	-11.86430	-0.93328	1.81908
C	16.42459	7.94861	1.96200
H	15.70117	8.76809	1.88924
H	17.08601	8.10342	2.81687
H	17.00720	7.90420	1.03531
C	17.69669	-4.21448	3.74299
H	17.18010	-5.17977	3.70398
H	18.51339	-4.19365	3.01855
H	18.08428	-4.05832	4.75568
C	-28.30306	6.43282	4.89079
H	-29.32050	6.02743	4.91569
H	-27.89962	6.50303	5.90302
H	-28.32560	7.42292	4.42240
C	-27.95106	-4.16403	-2.94482
H	-27.21194	-4.92945	-3.20566
H	-28.71115	-4.58315	-2.28236
H	-28.41465	-3.78868	-3.86372
H	0.74354	2.23623	4.01928
H	-12.46927	0.87499	-1.44892
H	-12.73256	0.23166	2.84519
H	1.04223	2.91003	-0.26799

Table S14. Atomic coordinates of $\mathbf{2}^{Me2+}$ (open-shell singlet) from its DFT geometry-optimized structure.

Atom	x	y	z
C	-2.25031	-0.58258	1.16699
C	-2.64748	0.77286	1.35113
C	-1.66782	1.77793	1.57330
C	-0.34038	1.42293	1.60930
C	0.04385	0.06771	1.42447
C	-0.91964	-0.93511	1.20190
H	-3.01564	-1.33580	0.99822
H	-1.98765	2.80811	1.71142
H	-0.62356	-1.97185	1.05994
C	0.87920	2.30896	1.83300
C	1.99813	1.27777	1.74896
C	3.35416	1.46706	1.87091
C	4.22452	0.34996	1.75293
C	3.68647	-0.94767	1.51267
C	2.32793	-1.13535	1.39249
C	1.47456	-0.02086	1.50926
H	3.77881	2.45134	2.05396
H	4.36860	-1.78956	1.42615
H	1.92566	-2.12922	1.21012
C	-4.00653	1.11038	1.31387

C	-5.19836	1.40421	1.28267
C	-6.50614	1.72693	1.24947
C	-9.05738	2.35826	1.18592
C	-10.03823	1.35173	0.97659
C	-9.45364	3.71463	1.36200
C	-11.36611	1.70627	0.94655
H	-9.71921	0.32048	0.84450
C	-10.78489	4.06683	1.33152
H	-8.68764	4.46932	1.52096
C	-12.58711	0.81806	0.73911
C	-11.74932	3.06251	1.12292
H	-11.08017	5.10467	1.46703
C	-13.70598	1.84929	0.82443
C	-13.18180	3.14978	1.04774
C	-15.06354	1.65747	0.71696
C	-14.03501	4.26397	1.16071
C	-15.93371	2.77399	0.83240
H	-15.48840	0.67086	0.54729
C	-15.39499	4.07372	1.05407
H	-13.63254	5.26009	1.33008
H	-16.07689	4.91604	1.13858
C	-7.69799	2.02074	1.21971
C	5.61127	0.51872	1.87131

123

C	-17.32311	2.60194	0.73118
C	6.82265	0.66364	1.97368
C	-18.53475	2.45422	0.64633
C	8.20932	0.82782	2.09074
C	8.77242	2.10069	2.36442
C	9.08834	-0.27513	1.93887
C	10.13285	2.26296	2.47888
H	8.11401	2.95483	2.50249
C	10.44896	-0.11701	2.05580
H	8.67703	-1.25512	1.70955
C	11.00839	1.15732	2.32892
H	10.53749	3.24288	2.71238
H	11.10178	-0.97234	1.91192
C	-19.92460	2.28649	0.55129
C	-20.49088	1.00507	0.33482
C	-20.80065	3.39461	0.67060
C	-21.85344	0.84006	0.24049
H	-19.83647	0.14008	0.25912
C	-22.16383	3.23207	0.58218
H	-20.38448	4.38819	0.81818
C	-22.72583	1.94985	0.36336
H	-22.26421	-0.15453	0.09608
H	-22.81289	4.09932	0.65548

N	12.37579	1.31769	2.44656
N	-24.09734	1.78525	0.27203
C	13.21047	0.23842	2.85199
C	14.37617	-0.04904	2.13140
C	12.88449	-0.52087	3.98378
C	15.20222	-1.08978	2.53395
H	14.62691	0.53791	1.25150
C	13.71134	-1.56293	4.37701
H	11.99267	-0.28360	4.55856
C	14.87501	-1.85683	3.65802
H	16.10169	-1.31727	1.96928
H	13.47168	-2.15422	5.25709
C	12.99680	2.56737	2.16685
C	13.92748	3.09946	3.06771
C	12.70073	3.25453	0.98198
C	14.54877	4.30960	2.79018
H	14.15442	2.56761	3.98815
C	13.32113	4.46586	0.71361
H	11.99672	2.83087	0.27005
C	14.24851	5.00386	1.61252
H	15.26420	4.72542	3.49365
H	13.10410	5.00414	-0.20551
C	-24.98750	2.67230	0.93825

C	-26.08178	3.21107	0.24909
C	-24.78867	2.99119	2.28793
C	-26.95823	4.06365	0.90392
H	-26.23476	2.96715	-0.79909
C	-25.66673	3.84958	2.93582
H	-23.95347	2.55505	2.83032
C	-26.75857	4.39291	2.24928
H	-27.80546	4.49409	0.37616
H	-25.51492	4.09005	3.98405
C	-24.65926	0.72512	-0.49138
C	-25.68137	-0.06193	0.05393
C	-24.21213	0.47970	-1.79688
C	-26.24446	-1.08613	-0.69527
H	-26.02553	0.12557	1.06784
C	-24.77470	-0.54930	-2.53750
H	-23.43559	1.10469	-2.23083
C	-25.79388	-1.34027	-1.99587
H	-27.03156	-1.70055	-0.26796
H	-24.44007	-0.74348	-3.55335
C	15.72908	-2.98562	4.12811
C	14.88818	6.30732	1.27134
C	-26.36575	-2.42955	-2.83854
C	-27.73008	5.31669	2.90234

O	-25.99203	-2.68051	-3.95767
O	-27.33713	-3.09954	-2.22378
O	-27.43267	5.55919	4.17658
O	-28.68388	5.79626	2.34101
O	15.75821	6.71026	2.19356
O	14.64623	6.93262	0.26869
O	16.81318	-3.15791	3.37659
O	15.46935	-3.67119	5.08592
C	0.83663	2.98032	3.21881
H	1.75103	3.56115	3.39100
H	-0.01567	3.66771	3.28487
C	1.01269	3.37146	0.72579
H	1.93203	3.95368	0.86387
H	0.16570	4.06762	0.75880
C	-12.55544	0.13691	-0.64222
H	-11.70336	-0.55056	-0.71053
H	-13.47100	-0.44542	-0.80294
C	-12.71106	-0.23673	1.85468
H	-13.63141	-0.82009	1.72843
H	-11.86429	-0.93311	1.81962
C	16.42484	7.94823	1.96067
H	15.70148	8.76776	1.88787
H	17.08635	8.10310	2.81546

H	17.00735	7.90365	1.03393
C	17.69658	-4.21434	3.74362
H	17.17996	-5.17963	3.70493
H	18.51319	-4.19371	3.01907
H	18.08429	-4.05791	4.75622
C	-28.30311	6.43209	4.89158
H	-29.32052	6.02662	4.91655
H	-27.89957	6.50228	5.90377
H	-28.32578	7.42222	4.42325
C	-27.95056	-4.16348	-2.94672
H	-27.21137	-4.92884	-3.20754
H	-28.71078	-4.58274	-2.28449
H	-28.41396	-3.78796	-3.86564
H	0.74360	2.23680	4.01920
H	-12.46933	0.87489	-1.44852
H	-12.73248	0.23195	2.84565
H	1.04227	2.90974	-0.26822
C	-2.25031	-0.58258	1.16699
C	-2.64748	0.77286	1.35113
C	-1.66782	1.77793	1.57330
C	-0.34038	1.42293	1.60930
C	0.04385	0.06771	1.42447
C	-0.91964	-0.93511	1.20190

H	-3.01564	-1.33580	0.99822
H	-1.98765	2.80811	1.71142
H	-0.62356	-1.97185	1.05994
C	0.87920	2.30896	1.83300
C	1.99813	1.27777	1.74896
C	3.35416	1.46706	1.87091
C	4.22452	0.34996	1.75293
C	3.68647	-0.94767	1.51267
C	2.32793	-1.13535	1.39249
C	1.47456	-0.02086	1.50926
H	3.77881	2.45134	2.05396
H	4.36860	-1.78956	1.42615
H	1.92566	-2.12922	1.21012
C	-4.00653	1.11038	1.31387
C	-5.19836	1.40421	1.28267
C	-6.50614	1.72693	1.24947
C	-9.05738	2.35826	1.18592
C	-10.03823	1.35173	0.97659
C	-9.45364	3.71463	1.36200
C	-11.36611	1.70627	0.94655
H	-9.71921	0.32048	0.84450
C	-10.78489	4.06683	1.33152
H	-8.68764	4.46932	1.52096

129

C	-12.58711	0.81806	0.73911
C	-11.74932	3.06251	1.12292
H	-11.08017	5.10467	1.46703
C	-13.70598	1.84929	0.82443
C	-13.18180	3.14978	1.04774
C	-15.06354	1.65747	0.71696
C	-14.03501	4.26397	1.16071
C	-15.93371	2.77399	0.83240
H	-15.48840	0.67086	0.54729
C	-15.39499	4.07372	1.05407
H	-13.63254	5.26009	1.33008
H	-16.07689	4.91604	1.13858
C	-7.69799	2.02074	1.21971
C	5.61127	0.51872	1.87131
C	-17.32311	2.60194	0.73118
C	6.82265	0.66364	1.97368
C	-18.53475	2.45422	0.64633
C	8.20932	0.82782	2.09074
C	8.77242	2.10069	2.36442
C	9.08834	-0.27513	1.93887
C	10.13285	2.26296	2.47888
H	8.11401	2.95483	2.50249
C	10.44896	-0.11701	2.05580

H	8.67703	-1.25512	1.70955
C	11.00839	1.15732	2.32892
H	10.53749	3.24288	2.71238
H	11.10178	-0.97234	1.91192
C	-19.92460	2.28649	0.55129
C	-20.49088	1.00507	0.33482
C	-20.80065	3.39461	0.67060
C	-21.85344	0.84006	0.24049
H	-19.83647	0.14008	0.25912
C	-22.16383	3.23207	0.58218
H	-20.38448	4.38819	0.81818
C	-22.72583	1.94985	0.36336
H	-22.26421	-0.15453	0.09608
H	-22.81289	4.09932	0.65548
N	12.37579	1.31769	2.44656
N	-24.09734	1.78525	0.27203
C	13.21047	0.23842	2.85199
C	14.37617	-0.04904	2.13140
C	12.88449	-0.52087	3.98378
C	15.20222	-1.08978	2.53395
H	14.62691	0.53791	1.25150
C	13.71134	-1.56293	4.37701
H	11.99267	-0.28360	4.55856

131

C	14.87501	-1.85683	3.65802
H	16.10169	-1.31727	1.96928
H	13.47168	-2.15422	5.25709
C	12.99680	2.56737	2.16685
C	13.92748	3.09946	3.06771
C	12.70073	3.25453	0.98198
C	14.54877	4.30960	2.79018
H	14.15442	2.56761	3.98815
C	13.32113	4.46586	0.71361
H	11.99672	2.83087	0.27005
C	14.24851	5.00386	1.61252
H	15.26420	4.72542	3.49365
H	13.10410	5.00414	-0.20551
C	-24.98750	2.67230	0.93825
C	-26.08178	3.21107	0.24909
C	-24.78867	2.99119	2.28793
C	-26.95823	4.06365	0.90392
H	-26.23476	2.96715	-0.79909
C	-25.66673	3.84958	2.93582
H	-23.95347	2.55505	2.83032
C	-26.75857	4.39291	2.24928
H	-27.80546	4.49409	0.37616
H	-25.51492	4.09005	3.98405

C	-24.65926	0.72512	-0.49138
C	-25.68137	-0.06193	0.05393
C	-24.21213	0.47970	-1.79688
C	-26.24446	-1.08613	-0.69527
H	-26.02553	0.12557	1.06784
C	-24.77470	-0.54930	-2.53750
H	-23.43559	1.10469	-2.23083
C	-25.79388	-1.34027	-1.99587
H	-27.03156	-1.70055	-0.26796
H	-24.44007	-0.74348	-3.55335
C	15.72908	-2.98562	4.12811
C	14.88818	6.30732	1.27134
C	-26.36575	-2.42955	-2.83854
C	-27.73008	5.31669	2.90234
O	-25.99203	-2.68051	-3.95767
O	-27.33713	-3.09954	-2.22378
O	-27.43267	5.55919	4.17658
O	-28.68388	5.79626	2.34101
O	15.75821	6.71026	2.19356
O	14.64623	6.93262	0.26869
O	16.81318	-3.15791	3.37659
O	15.46935	-3.67119	5.08592
C	0.83663	2.98032	3.21881

H	1.75103	3.56115	3.39100
H	-0.01567	3.66771	3.28487
C	1.01269	3.37146	0.72579
H	1.93203	3.95368	0.86387
H	0.16570	4.06762	0.75880
C	-12.55544	0.13691	-0.64222
H	-11.70336	-0.55056	-0.71053
H	-13.47100	-0.44542	-0.80294
C	-12.71106	-0.23673	1.85468
H	-13.63141	-0.82009	1.72843
H	-11.86429	-0.93311	1.81962
C	16.42484	7.94823	1.96067
H	15.70148	8.76776	1.88787
H	17.08635	8.10310	2.81546
H	17.00735	7.90365	1.03393
C	17.69658	-4.21434	3.74362
H	17.17996	-5.17963	3.70493
H	18.51319	-4.19371	3.01907
H	18.08429	-4.05791	4.75622
C	-28.30311	6.43209	4.89158
H	-29.32052	6.02662	4.91655
H	-27.89957	6.50228	5.90377
H	-28.32578	7.42222	4.42325

C	-27.95056	-4.16348	-2.94672
H	-27.21137	-4.92884	-3.20754
H	-28.71078	-4.58274	-2.28449
H	-28.41396	-3.78796	-3.86564
H	0.74360	2.23680	4.01920
H	-12.46933	0.87489	-1.44852
H	-12.73248	0.23195	2.84565
H	1.04227	2.90974	-0.26822

Table S15. Atomic coordinates of $\mathbf{2}^{Me2+}$ (triplet) from its DFT geometry-optimized structure.

Atom	x	y	z
C	-2.23359	-0.59597	1.05136
C	-2.62449	0.74645	1.25421
C	-1.64561	1.73502	1.49196
C	-0.31058	1.37266	1.52469
C	0.06695	0.02998	1.32183
C	-0.89497	-0.95702	1.08392
H	-2.99758	-1.34785	0.86890
H	-1.95620	2.76610	1.64665
H	-0.60718	-1.99447	0.92634
C	0.90822	2.25777	1.76421
C	2.03182	1.23047	1.67047
C	3.39076	1.42431	1.80261

C	4.26443	0.31532	1.67528
C	3.73618	-0.97382	1.41516
C	2.37160	-1.16376	1.28384
C	1.51811	-0.06050	1.41140
H	3.80812	2.40898	2.00185
H	4.41897	-1.81468	1.32030
H	1.97558	-2.15722	1.08478
C	-4.00300	1.09932	1.22081
C	-5.18390	1.40014	1.19460
C	-6.50787	1.73740	1.16713
C	-9.06754	2.39105	1.11879
C	-10.04970	1.39808	0.91542
C	-9.45549	3.73762	1.29828
C	-11.38513	1.75996	0.89495
H	-9.74134	0.36385	0.77842
C	-10.79447	4.09825	1.27761
H	-8.68899	4.49296	1.45400
C	-12.60733	0.87006	0.69352
C	-11.75978	3.10661	1.07553
H	-11.07991	5.13885	1.41767
C	-13.72984	1.89850	0.78771
C	-13.21244	3.19485	1.00956
C	-15.09104	1.70095	0.68743

C	-14.06437	4.30008	1.13001
C	-15.96322	2.81152	0.81016
H	-15.51117	0.71192	0.51783
C	-15.43120	4.10634	1.03097
H	-13.66564	5.29790	1.29970
H	-16.11286	4.94849	1.12243
C	-7.68885	2.03817	1.14414
C	5.65660	0.49136	1.80741
C	-17.35809	2.63101	0.71594
C	6.86542	0.64225	1.92287
C	-18.56925	2.47610	0.63731
C	8.24742	0.81203	2.05662
C	8.80080	2.09020	2.34657
C	9.13439	-0.29024	1.90713
C	10.15463	2.25971	2.47554
H	8.13416	2.93743	2.48507
C	10.48822	-0.12970	2.04626
H	8.72804	-1.26805	1.66181
C	11.03876	1.15214	2.33321
H	10.55277	3.23776	2.72644
H	11.14852	-0.97844	1.89932
C	-19.95469	2.30144	0.55078
C	-20.51547	1.01204	0.33496

C	-20.83726	3.40981	0.67824
C	-21.87223	0.83942	0.24539
H	-19.85464	0.15250	0.25827
C	-22.19543	3.24178	0.60366
H	-20.42212	4.40428	0.81983
C	-22.75259	1.95028	0.38163
H	-22.28034	-0.15703	0.10904
H	-22.84934	4.10510	0.67537
N	12.39257	1.31616	2.47028
N	-24.11080	1.77994	0.30109
C	13.23660	0.22864	2.84550
C	14.40420	-0.02353	2.11634
C	12.91017	-0.55993	3.95581
C	15.23403	-1.07206	2.48906
H	14.65092	0.59071	1.25430
C	13.74606	-1.60524	4.32141
H	12.01813	-0.34148	4.53748
C	14.90976	-1.86988	3.59242
H	16.13501	-1.27938	1.91942
H	13.51185	-2.22182	5.18525
C	13.01226	2.58172	2.24550
C	13.91323	3.08750	3.18936
C	12.73993	3.29536	1.07187

C	14.52785	4.31181	2.96508
H	14.11853	2.52980	4.09937
C	13.35991	4.51766	0.85564
H	12.06219	2.88428	0.32794
C	14.25431	5.03471	1.79817
H	15.21869	4.71454	3.69978
H	13.16621	5.08066	-0.05361
C	-25.00897	2.69194	0.93068
C	-26.09177	3.20650	0.20759
C	-24.82113	3.04448	2.27245
C	-26.97079	4.08291	0.82589
H	-26.23100	2.93084	-0.83445
C	-25.70748	3.92166	2.88372
H	-23.99619	2.61818	2.83767
C	-26.78560	4.44756	2.16422
H	-27.80960	4.50170	0.27617
H	-25.57088	4.19133	3.92673
C	-24.67881	0.68565	-0.41591
C	-25.68538	-0.08333	0.17948
C	-24.25022	0.40514	-1.71944
C	-26.25002	-1.13899	-0.52296
H	-26.01194	0.13802	1.19220
C	-24.82082	-0.65168	-2.41400

H	-23.49003	1.02412	-2.18926
C	-25.82063	-1.43058	-1.82287
H	-27.02312	-1.74583	-0.06114
H	-24.50609	-0.87779	-3.42939
C	15.77321	-3.00715	4.03282
C	14.89356	6.35478	1.51229
C	-26.40063	-2.55448	-2.61877
C	-27.76492	5.39452	2.77840
O	-26.04573	-2.83472	-3.73607
O	-27.35007	-3.21083	-1.96110
O	-27.48535	5.66792	4.04814
O	-28.70554	5.86037	2.18605
O	15.72570	6.73960	2.47370
O	14.67746	7.00042	0.51766
O	16.85385	-3.15332	3.27410
O	15.51709	-3.71478	4.97437
C	0.86068	2.91265	3.15735
H	1.77226	3.49514	3.34088
H	0.00530	3.59580	3.23108
C	1.04319	3.33568	0.67249
H	1.95953	3.92085	0.82058
H	0.19288	4.02801	0.70929
C	-12.58388	0.19017	-0.68830

H	-11.72923	-0.49357	-0.76492
H	-13.49808	-0.39605	-0.84502
C	-12.72234	-0.18799	1.80663
H	-13.64083	-0.77598	1.68540
H	-11.87257	-0.88085	1.76728
C	16.38930	7.98970	2.29804
H	15.66066	8.80395	2.22067
H	17.01764	8.12661	3.18029
H	17.00502	7.97363	1.39221
C	17.74703	-4.21282	3.61121
H	17.23602	-5.17985	3.55116
H	18.55953	-4.16829	2.88334
H	18.13793	-4.07730	4.62548
C	-28.36128	6.56438	4.72867
H	-29.38089	6.16459	4.74805
H	-27.97169	6.65723	5.74432
H	-28.36995	7.54191	4.23445
C	-27.97084	-4.30436	-2.63403
H	-27.22994	-5.07068	-2.88636
H	-28.71097	-4.70737	-1.93998
H	-28.45883	-3.96242	-3.55317
H	0.76805	2.15867	3.94819
H	-12.50608	0.92990	-1.49405

H	-12.74029	0.27894	2.79868
H	1.07864	2.88668	-0.32733
C	-2.23359	-0.59597	1.05136
C	-2.62449	0.74645	1.25421
C	-1.64561	1.73502	1.49196
C	-0.31058	1.37266	1.52469
C	0.06695	0.02998	1.32183
C	-0.89497	-0.95702	1.08392
H	-2.99758	-1.34785	0.86890
H	-1.95620	2.76610	1.64665
H	-0.60718	-1.99447	0.92634
C	0.90822	2.25777	1.76421
C	2.03182	1.23047	1.67047
C	3.39076	1.42431	1.80261
C	4.26443	0.31532	1.67528
C	3.73618	-0.97382	1.41516
C	2.37160	-1.16376	1.28384
C	1.51811	-0.06050	1.41140
H	3.80812	2.40898	2.00185
H	4.41897	-1.81468	1.32030
H	1.97558	-2.15722	1.08478
C	-4.00300	1.09932	1.22081
C	-5.18390	1.40014	1.19460

142

C	-6.50787	1.73740	1.16713
C	-9.06754	2.39105	1.11879
C	-10.04970	1.39808	0.91542
C	-9.45549	3.73762	1.29828
C	-11.38513	1.75996	0.89495
H	-9.74134	0.36385	0.77842
C	-10.79447	4.09825	1.27761
H	-8.68899	4.49296	1.45400
C	-12.60733	0.87006	0.69352
C	-11.75978	3.10661	1.07553
H	-11.07991	5.13885	1.41767
C	-13.72984	1.89850	0.78771
C	-13.21244	3.19485	1.00956
C	-15.09104	1.70095	0.68743
C	-14.06437	4.30008	1.13001
C	-15.96322	2.81152	0.81016
H	-15.51117	0.71192	0.51783
C	-15.43120	4.10634	1.03097
H	-13.66564	5.29790	1.29970
H	-16.11286	4.94849	1.12243
C	-7.68885	2.03817	1.14414
C	5.65660	0.49136	1.80741
C	-17.35809	2.63101	0.71594

143

C	6.86542	0.64225	1.92287
C	-18.56925	2.47610	0.63731
C	8.24742	0.81203	2.05662
C	8.80080	2.09020	2.34657
C	9.13439	-0.29024	1.90713
C	10.15463	2.25971	2.47554
H	8.13416	2.93743	2.48507
C	10.48822	-0.12970	2.04626
H	8.72804	-1.26805	1.66181
C	11.03876	1.15214	2.33321
H	10.55277	3.23776	2.72644
H	11.14852	-0.97844	1.89932
C	-19.95469	2.30144	0.55078
C	-20.51547	1.01204	0.33496
C	-20.83726	3.40981	0.67824
C	-21.87223	0.83942	0.24539
H	-19.85464	0.15250	0.25827
C	-22.19543	3.24178	0.60366
H	-20.42212	4.40428	0.81983
C	-22.75259	1.95028	0.38163
H	-22.28034	-0.15703	0.10904
H	-22.84934	4.10510	0.67537
N	12.39257	1.31616	2.47028

144

N	-24.11080	1.77994	0.30109
C	13.23660	0.22864	2.84550
C	14.40420	-0.02353	2.11634
C	12.91017	-0.55993	3.95581
C	15.23403	-1.07206	2.48906
H	14.65092	0.59071	1.25430
C	13.74606	-1.60524	4.32141
H	12.01813	-0.34148	4.53748
C	14.90976	-1.86988	3.59242
H	16.13501	-1.27938	1.91942
H	13.51185	-2.22182	5.18525
C	13.01226	2.58172	2.24550
C	13.91323	3.08750	3.18936
C	12.73993	3.29536	1.07187
C	14.52785	4.31181	2.96508
H	14.11853	2.52980	4.09937
C	13.35991	4.51766	0.85564
H	12.06219	2.88428	0.32794
C	14.25431	5.03471	1.79817
H	15.21869	4.71454	3.69978
H	13.16621	5.08066	-0.05361
C	-25.00897	2.69194	0.93068
C	-26.09177	3.20650	0.20759

C	-24.82113	3.04448	2.27245
C	-26.97079	4.08291	0.82589
H	-26.23100	2.93084	-0.83445
C	-25.70748	3.92166	2.88372
H	-23.99619	2.61818	2.83767
C	-26.78560	4.44756	2.16422
H	-27.80960	4.50170	0.27617
H	-25.57088	4.19133	3.92673
C	-24.67881	0.68565	-0.41591
C	-25.68538	-0.08333	0.17948
C	-24.25022	0.40514	-1.71944
C	-26.25002	-1.13899	-0.52296
H	-26.01194	0.13802	1.19220
C	-24.82082	-0.65168	-2.41400
H	-23.49003	1.02412	-2.18926
C	-25.82063	-1.43058	-1.82287
H	-27.02312	-1.74583	-0.06114
H	-24.50609	-0.87779	-3.42939
C	15.77321	-3.00715	4.03282
C	14.89356	6.35478	1.51229
C	-26.40063	-2.55448	-2.61877
C	-27.76492	5.39452	2.77840
O	-26.04573	-2.83472	-3.73607

O	-27.35007	-3.21083	-1.96110
O	-27.48535	5.66792	4.04814
O	-28.70554	5.86037	2.18605
O	15.72570	6.73960	2.47370
O	14.67746	7.00042	0.51766
O	16.85385	-3.15332	3.27410
O	15.51709	-3.71478	4.97437
C	0.86068	2.91265	3.15735
H	1.77226	3.49514	3.34088
H	0.00530	3.59580	3.23108
C	1.04319	3.33568	0.67249
H	1.95953	3.92085	0.82058
H	0.19288	4.02801	0.70929
C	-12.58388	0.19017	-0.68830
H	-11.72923	-0.49357	-0.76492
H	-13.49808	-0.39605	-0.84502
C	-12.72234	-0.18799	1.80663
H	-13.64083	-0.77598	1.68540
H	-11.87257	-0.88085	1.76728
C	16.38930	7.98970	2.29804
H	15.66066	8.80395	2.22067
H	17.01764	8.12661	3.18029
H	17.00502	7.97363	1.39221

C	17.74703	-4.21282	3.61121
H	17.23602	-5.17985	3.55116
H	18.55953	-4.16829	2.88334
H	18.13793	-4.07730	4.62548
C	-28.36128	6.56438	4.72867
H	-29.38089	6.16459	4.74805
H	-27.97169	6.65723	5.74432
H	-28.36995	7.54191	4.23445
C	-27.97084	-4.30436	-2.63403
H	-27.22994	-5.07068	-2.88636
H	-28.71097	-4.70737	-1.93998
H	-28.45883	-3.96242	-3.55317
H	0.76805	2.15867	3.94819
H	-12.50608	0.92990	-1.49405
H	-12.74029	0.27894	2.79868
H	1.07864	2.88668	-0.32733

References

(1) Rudolph, M.; Feldberg, S. Digisim3, Version 3.03. *Bioanal. Syst. Inc* **1994**.

(2) *Gaussian 16, Revision B.01, Frisch, M.J., Trucks, G.W., Schlegel, H.B., Scuseria, G.E., Robb, M.A., Cheeseman, J.R.; Scalmani, G.; Barone, V.; Petersson, G.A.; Nakatsuji, H.; Li, X.; Caricato, M.; Marenich, A.V.; Bloino, J., Janesko, B.G., Gomperts, R., Mennucci, B., Hratchian, H.P., Ortiz, J.V., Izmaylov, A.F., Sonnenberg, J.L., Williams-Young, D., Ding, F., Lipparini, F., Egidi, F., Goings, J., Peng, B., Petrone, A., Henderson, T., Ranasinghe, D., Zakrzewski, V.G., Gao, J., Rega, N., Zheng, G., Liang, W., Hada, M., Ehara, M., Toyota, K., Fukuda, R., Hasegawa, J., Ishida, M., Nakajima, T., Honda, Y., Kitao, O., Nakai, H., Vreven, T., Throssell, K., Montgomery Jr., J.A., Peralta, J.E., Ogliaro, F., Bearpark, M.J., Heyd, J.J., Brothers, E.N., Kudin, K.N., Staroverov, V.N., Keith, T.A., Kobayashi, R., Normand, J., Raghavachari, K., Rendell, A.P., Burant, J.C., Iyengar, S.S., Tomasi, J., Cossi, M., Millam, J.M., Klene, M., Adamo, C., Cammi, R., Ochterski, J.W., Martin, R.L., Morokuma, K., Farkas, O., Foresman, J.B., Fox, D.J. Gaussian, Inc., Wallingford CT (2016) GaussView 5.0. Wallingford, E.U.A. - References - Scientific Research Publishing*. https://www.scirp.org/reference/referencespapers?referenceid=2418053 (accessed 2024-12-03).

(3) Cossi, M.; Rega, N.; Scalmani, G.; Barone, V. Energies, Structures, and Electronic Properties of Molecules in Solution with the C-PCM Solvation Model. *J. Comput. Chem.* **2003**, *24* (6), 669–681. https://doi.org/10.1002/jcc.10189.

(4) Weigend, F. Accurate Coulomb-Fitting Basis Sets for H to Rn. *Phys. Chem. Chem. Phys.* **2006**, *8* (9), 1057–1065. https://doi.org/10.1039/B515623H.

(5) Weigend, F.; Ahlrichs, R. Balanced Basis Sets of Split Valence, Triple Zeta Valence and Quadruple Zeta Valence Quality for H to Rn: Design and Assessment of Accuracy. *Phys. Chem. Chem. Phys.* **2005**, *7* (18), 3297–3305. https://doi.org/10.1039/B508541A.

(6) Becke, A. D. Density-functional Thermochemistry. III. The Role of Exact Exchange. *J. Chem. Phys.* **1993**, *98* (7), 5648–5652. https://doi.org/10.1063/1.464913.

(7) Renz, M.; Kaupp, M. Predicting the Localized/Delocalized Character of Mixed-Valence Diquinone Radical Anions. Toward the Right Answer for the Right Reason. *J Phys Chem A* **2012**, *116* (43), 10629–10637. https://doi.org/10.1021/jp308294r.

(8) Renz, M.; Theilacker, K.; Lambert, C.; Kaupp, M. A Reliable Quantum-Chemical Protocol for the Characterization of Organic Mixed-Valence Compounds. *J Am Chem Soc* **2009**, *131* (44), 16292–16302. https://doi.org/10.1021/ja9070859.

(9) Kaupp, M.; Renz, M.; Parthey, M.; Stolte, M.; Würthner, F.; Lambert, C. Computational and Spectroscopic Studies of Organic Mixed-Valence Compounds: Where Is the Charge? *Phys. Chem. Chem. Phys.* **2011**, *13* (38), 16973–16986. https://doi.org/10.1039/C1CP21772K.

(10) Gogesch, F. S.; Schwab, S.; Rehse, A.; Linseis, M.; Baksi, A.; Clever, G. H.; Winter, R. F. Diruthenium Complexes with π-Extended Bridging Bis(Alkenyl)Arylene Ligands, A Derived Metallamacrocycle, and Their Oxidized Forms. *Organometallics* **2023**, *42* (21), 3085–3098. https://doi.org/10.1021/acs.organomet.3c00337.

(11) O'Boyle, N. M.; Tenderholt, A. L.; Langner, K. M. Cclib: A Library for Package-Independent Computational Chemistry Algorithms. *J. Comput. Chem.* **2008**, *29* (5), 839–845. https://doi.org/10.1002/jcc.20823.

(12) Hanwell, M. D.; Curtis, D. E.; Lonie, D. C.; Vandermeersch, T.; Zurek, E.; Hutchison, G. R. Avogadro: An Advanced Semantic Chemical Editor, Visualization, and Analysis Platform. *J. Cheminformatics* **2012**, *4* (1), 17. https://doi.org/10.1186/1758-2946-4-17.

(13) Tange, O. GNU Parallel: The Command-Line Power Tool. *USENIX Mag.* **2011**, 42–47.

(14) Krejčik, M.; Daněk, M.; Hartl, F. Simple Construction of an Infrared Optically Transparent Thin-Layer Electrochemical Cell. *J Electroanal Chem* **1991**, *317* (1–2), 179–187. https://doi.org/10.1016/0022-0728(91)85012-e.

(15) Casey, M.; Leonard, J.; Lygo, B. *Advanced practical organic chemistry*; Blackie: Glasgow, 1990.

(16) Hempe, M.; Schnellbächer, L.; Wiesner, T.; Reggelin, M. Meta- and Para-Functionalized Thermally Crosslinkable OLED-Materials through Selective Transition-Metal-Catalyzed Cross-Coupling Reactions. *Synthesis* **2017**, *49*, 4489–4499. https://doi.org/10.1055/s-0036-1590824.

(17) Krieger, E.; Darden, T.; Nabuurs, S. B.; Finkelstein, A.; Vriend, G. Making Optimal Use of Empirical Energy Functions: Force-Field Parameterization in Crystal Space. *Proteins Struct. Funct. Genet.* **2004**, *57* (4), 678–683. https://doi.org/10.1002/prot.20251.

(18) Krieger, E.; Nielsen, J. E.; Spronk, C. A. E. M.; Vriend, G. Fast Empirical pKa Prediction by Ewald Summation. *J. Mol. Graph. Model.* **2006**, *25* (4), 481–486. https://doi.org/10.1016/j.jmgm.2006.02.009.

(19) Dutta, S.; Watson, B.; Mattoo, S.; Rochet, J.-C. Calcein Release Assay to Measure Membrane Permeabilization by Recombinant Alpha-Synuclein. *BIO-Protoc.* **2020**, *10* (14). https://doi.org/10.21769/BioProtoc.3690.

(20) Maherani, B.; Arab-Tehrany, E.; Kheirolomoom, A.; Geny, D.; Linder, M. Calcein Release Behavior from Liposomal Bilayer; Influence of Physicochemical/Mechanical/Structural Properties of Lipids. *Biochimie* **2013**, *95* (11), 2018–2033. https://doi.org/10.1016/j.biochi.2013.07.006.

(21) Tschierlei, S.; Karnahl, M.; Presselt, M.; Dietzek, B.; Guthmuller, J.; González, L.; Schmitt, M.; Rau, S.; Popp, J. Photochemical Fate: The First Step Determines Efficiency of H2 Formation with a Supramolecular Photocatalyst. *Angew. Chem. Int. Ed.* **2010**, *49* (23), 3981–3984. https://doi.org/10.1002/anie.200906595.

(22) Sutherland, M. W.; Learmonth, B. A. The Tetrazolium Dyes MTS and XTT Provide New Quantitative Assays for Superoxide and Superoxide Dismutase. *Free Radic. Res.* **1997**, *27* (3), 283–289. https://doi.org/10.3109/10715769709065766.

Chapter 6

Summary, Conclusions, and Outlook

6.1 Summary

Inspired by the natural photosynthesis, the approach used in this thesis is biomimetic phospholipid bilayer membranes. Using a spherical lipid membrane was a key to addressing the challenges of facilitating insoluble organic compounds in water, achieving compartmentalization, and enabling photo-redox reactions in a completely aqueous system.

In Chapter 3, the reported study involved the preparation of an organic chromophore based on perylene diimide that has been modified to render its solubility in an aqueous system. The photophysical properties of the organic molecule remained nearly unchanged compared to those in organic solvents. To characterize the placement of the dye within the membrane, molecular dynamics simulations and confocal microscopy were conducted. Both sets of data indicated that the dye tended to align in a parallel position within the membrane, with some probability of adopting a transmembrane orientation. The photoactivity of the dye was demonstrated through its photooxidation in the presence of sodium peroxydisulfate as an oxidant. The rate of photooxidation in a mixture of acetonitrile and water was found to be two times faster than that in the membrane. Although the photooxidation within the membrane occurred at a slower rate, the experiment demonstrated the potential for conducting photooxidation of organic chromophores in a completely aqueous system.

In Chapter 4, the reported study focused on the preparation of a molecular wire designed for photoinduced electron transfer across lipid bilayer membranes. The molecular wire was engineered to match the thickness of the membrane and to align with a transmembrane orientation. The transmembrane alignment of the molecular wire within the membrane was later confirmed through confocal microscopy images and molecular dynamics simulations. The photo-driven transmembrane electron transfer was demonstrated by the complementary redox reaction involving compartmentalization of NADH inside liposome and XTT placed in the bulk solution of the membrane and the reverse combination. The quenching constant for the oxidative quenching of the molecular wire by XTT was found to be faster than that for the reductive quenching by NADH. This observation led to the proposed mechanism that the redox reaction preferred to first oxidize the molecular wire rather than reduce the molecular wire. The system was active both in inert and in ambient air.

In Chapter 5, the same reactants, NADH and XTT, were used to explore the other possibility of electron transfer in the lipid bilayer system with organic molecules. The triarylamine compounds, known as redox-active organic compounds, can be modified allowing the adjustment of their redox potential. Two different organic bridged bis(triarylamines) dyes were

reported, differing in length from their N-N terminals. These dyes exhibited photo-driven electron transfer within the membrane. In the system, either NADH or XTT was placed inside the liposome, while the complementary redox pair (NADH/XTT) was introduced in the bulk solution. The results indicated that placing the reactant inside the liposome accelerated the respective reaction, likely due to the confined space within the liposome. The proposed mechanisms for both dyes involved the photooxidation and photoreduction of NADH and XTT through a membrane-mediated process.

6.2 General conclusions and outlook

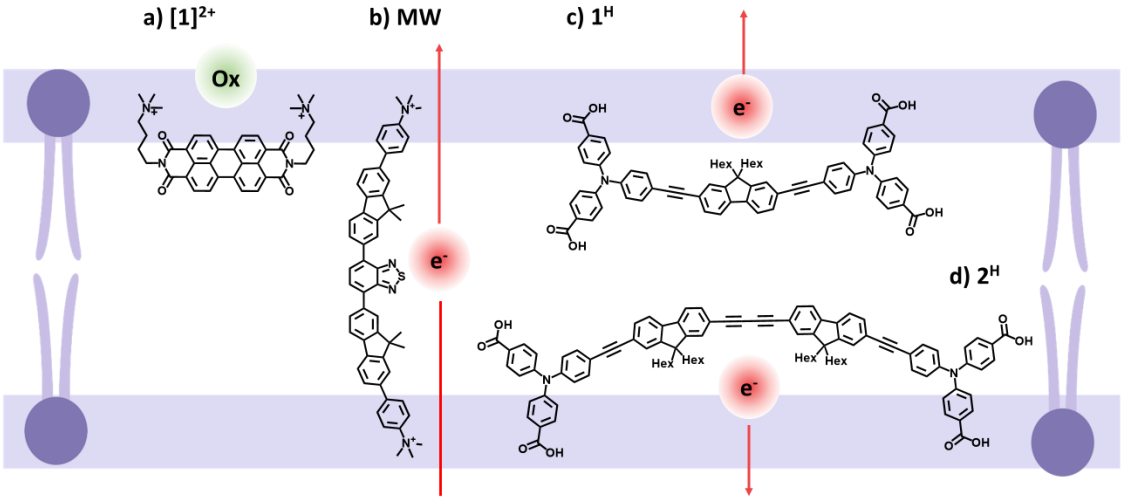

Figure 6. 1 Organic chromophore studied in this thesis: a) PDI-based chromophore for photooxidation reaction, b) molecular wire (MW) for transmembrane electron transfer across the lipid bilayer, c, and d) brigaded triarylamine compounds with mixed valence character for membrane-mediated electron transfer. The lipid bilayers were created with BioRender.com.

Based on the work described in this thesis, it is possible to run light-driven reactions in the lipid bilayer membrane. The design of the chromophore will determine the placement of the chromophore in the membrane (Figure 6. 1). Designing a chromophore that can be integrated into a membrane can be achieved through several approaches.

The first approach, discussed in Chapter 3, involves electrostatic interactions. In this case, the chromophore **[1]**$^{2+}$ is positively charged, while the membrane is negatively charged. This electrostatic interaction allows for the photooxidation of **[1]**$^{2+}$ to occur, even though it is known to be insoluble in water. Chapter 4 introduces another key principle for transmembrane electron transfer across lipid bilayers, focusing on the synthesis of a molecular wire (MW) that matches the thickness of the membrane. The initial screening of the alignment of MW within the membrane laid the foundation for verifying transmembrane electron transfer. Chapter 5 explores additional strategies for functionalizing the membrane, with an emphasis on membrane-mediated electron transfer via a mixed valence chromophore. The length of the dyes is crucial for facilitating efficient electron transfer. Although it might be expected that shorter dyes would enable faster electron transfer, the case of the bridged bis(triarylamines) chromophore reveals the opposite trend: longer wires perform better. This improved performance is attributed to the population of electron density after oxidation at the dyes, which is influenced by the bridging structure of the chromophores.

The hesitation among many researchers regarding the use of liposomes as biomimetic reactors may no longer be warranted, as this thesis explored various reactions and approaches to assess the viability of the liposome system as a reliable medium for photo-driven reactions. In all cases, it was found that the lipid bilayer system did not diminish the photoactive properties of the organic compounds employed. While there may have been shifts in absorbance or slower reaction rates compared to purely organic solvents, it was demonstrated that the liposome system remained active throughout the photoreaction. The attempt to mimic the stroma and lumen systems of natural photosynthesis was successfully achieved within the liposomal framework. The compartmentalization properties of liposomes effectively separated two reactions using the lipid bilayer membrane, and the integration of a molecular wire facilitated the connection between these reactions.

To move beyond the compartmentalization in the liposome, the lipid planar membrane can be an alternative for transforming two complementary redox reactions in a more controlled fashion (Figure 6. 2).[1,2] In the planar membrane, the control over placing the reaction at two sides of the membrane is easier compared to the liposome system. In the liposome system, we have to encapsulate the first reactant, wash the leftover unencapsulated reactant, and then introduce the second reactant to the bulk solution of the liposome. In the planar lipid bilayer, the sample preparation will only consist of placing the first reactant, building the membrane, and finally adding the second reactant.

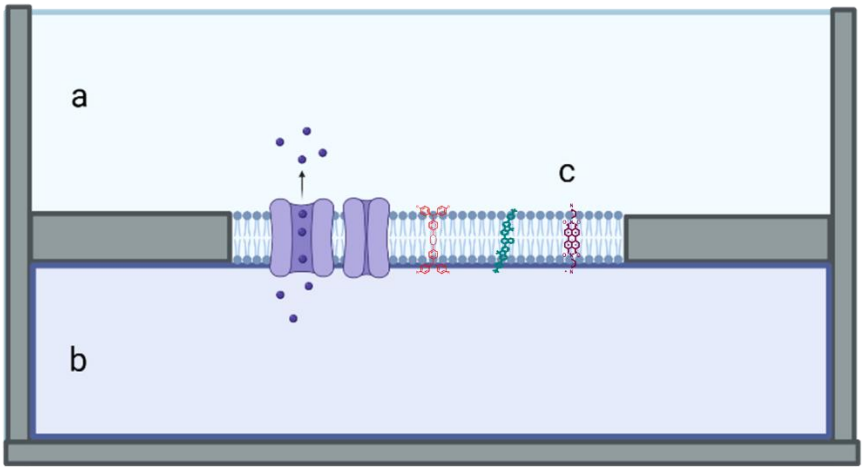

Figure 6. 2 Illustration of planer lipid bilayer stations a and b have different types of solution and c is the membrane which divided the compartments a and b. Created with BioRender.com.

The prototype instrument of a planar membrane bilayer is already commercially available.[3] This instrument was mostly used for the characterization of electrophysiological study of channels[4] and pores[5] in cell membranes. The resistive current of the membrane can be

measured under the condition of constant potential, which subtracts the conductance due to the presence of pores or channels. This conductivity measure can be related to the voltage-dependent gating, ligand binding, and channel block.[3] The practical procedure in the case of transmembrane electron transfer is that the synthetic membrane solution should be mixed with molecular wire before forming an interface of molecular dimensions between two electrolyte-filled compartments. The electron transfer can be proven by monitoring the current changes in the electrolytes.

Finally, the development of an artificial photosynthesis system, by placing two different reactions on two sides of the membrane, and integration of active chromophores in a membrane-type system is possible. To build upon this concept and create an artificial photosynthesis system capable of water-splitting reactions or CO_2 reduction with a membrane basis, several key considerations are essential: 1) confining the catalyst to a specific reaction site, 2) designing a water-soluble catalyst, 3) achieving a net reaction with no by-products, and 4) the collection of the products. The fundamental knowledge gained from the studied cases in this thesis can serve as a foundation for upgrading the model to achieve a total water splitting reaction or CO_2 reduction in a fully aqueous system, ultimately contributing to the development of a more efficient artificial photosynthesis system.

6.3 References

1. Wang, H. *et al.* Determining the Physical Properties of Molecules with Nanometer-Scale Pores. *ACS Sens.* **3**, 251–263 (2018).
2. Tancrède, P., Paquin, P., Houle, A. & Leblanc, R. M. Formation of asymmetrical planar lipid bilayer membranes from characterized monolayers. *Journal of Biochemical and Biophysical Methods* **7**, 299–310 (1983).
3. Zaitseva, E. *et al.* Electrophysiology on Channel-Forming Proteins in Artificial Lipid Bilayers: Next-Generation Instrumentation for Multiple Recordings in Parallel. in *Patch Clamp Electrophysiology* (eds. Dallas, M. & Bell, D.) vol. 2188 67–92 (Springer US, New York, NY, 2021).
4. Burden, D. L. *et al.* Confirming Silent Translocation through Nanopores with Simultaneous Single-Molecule Fluorescence and Single-Channel Electrical Recordings. *Anal. Chem.* **95**, 18020–18028 (2023).
5. Roesel, T., Cao, C., Bada Juarez, J. F., Dal Peraro, M. & Roke, S. Dissecting the Membrane Association Mechanism of Aerolysin Pores at Femtomolar Concentrations Using Water as a Probe. *Nano Lett.* **24**, 13888–13894 (2024).

List of Publications

1. Recent Advances in Light Energy Conversion with Biomimetic Vesicle Membranes

Authors: Novitasari Sinambela, Julian Bösking, Amir Abbas, and Andrea Pannwitz*

*Corresponding author

Published in: ChemBioChem 2021, 22, 3140–3147

DOI: 10.1002/cbic.2021002203140

Reprint Permission: This article is licensed under Creative Commons Attribution 4.0 International (CC BY 4.0). Published by Wiley-VCH GmbH.

Type of article: Review

Author contributions:

Novitasari Sinambela: Outline and literature research on the chapter electron transfer at and across lipid bilayers, drawing of all illustrations, and manuscript revision.

Julian Bösking: Outline and literature research on the chapter energy transfer in the lipid bilayers part and manuscript revision.

Amir Abbas: Outline and literature research on the chapter light-energy conversion with the polymersomes part and manuscript revision.

Andrea Pannwitz: Paper writing and manuscript revision.

Abstract: Lipid bilayer membranes are ubiquitous in natural chemical conversions. They enable for self-assembly and compartmentalization of reaction partners and it becomes increasingly evident that a thorough fundamental understanding of these concepts is highly desirable for chemical reactions and solar energy conversion with artificial systems. This minireview focusses on selected case studies from recent years, most of which were inspired by either membrane-facilitated light harvesting or respective charge transfer. The main focus is on highly biomimetic liposomes with artificial chromophores, and some cases for polymer membranes will be made. Furthermore, we categorized these studies into energy transfer and electron transfer, with phospholipid vesicles, and polymer membranes for light-driven reactions.

2. Alignment and Photooxidation Dynamics of a Perylene Diimide Chromophore in Lipid Bilayers

Authors: Novitasari Sinambela, Richard Jacobi, David Hernández-Castillo, Elisabeth Hofmeister, Nina Hagmeyer, Benjamin Dietzek-Ivanšić, Leticia González, and Andrea Pannwitz*

*Corresponding author

Published in: Mol. Syst. Des. Eng., 2023, 8, 842-852

DOI: 10.1039/D2ME00243D

Reprint Permission: This article is licensed under a Creative Commons Attribution 3.0 International (CC BY 3.0). Published by Royal Society of Chemistry.

Type of article: Research Article

Author contributions:

Novitasari Sinambela: Performed the chemical synthesis and liposome assemblies, steady-state and time-resolved spectroscopy characterization, confocal imaging measurement, photooxidation experiments, paper writing, and manuscript revision.

Richard Jacobi + David Hernández-Castillo + Leticia González: Design of the computational protocols, and analysis of all calculations, paper writing, and manuscript revision.

Elisabeth Hofmeister + Nina Hagmeyer + Benjamin Dietzek-Ivanšić: EPR spectroscopy investigations.

Benjamin Dietzek-Ivanšić + Andrea Pannwitz: Design of the study.

Andrea Pannwitz: Paper writing and manuscript revision.

Abstract: We present a method of enabling photochemical reactions in water by using biomimetic, water-soluble liposomes and a specifically functionalized perylene diimide chromophore. Linking two flexible saturated C4-alkyl chains with terminal positively charged trimethylammonium groups to the rigid perylene diimide core yielded $[1]^{2+}$ allowing for its co-assembly at the lipid bilayer interface of DOPG liposomes (DOPG = 1,2-dioleoyl-*sn-glycero*-3-phospho-(1′-*rac*-glycerol)) with a preferred orientation and in close proximity to the water interface. According to molecular dynamics simulations the chromophore aligns preferably parallel to the membrane surface which is supported by confocal microscopy. Irradiation experiments with visible light and in the presence of a negatively charged, water-soluble oxidant were slower in the DOPG-membrane than under acetonitrile–water reaction conditions. The generated radical species was characterized by EPR spectroscopy in an acetonitrile–water mixture and associated to the DOPG-membrane. Time-resolved emission studies revealed a static quenching process for the initial electron transfer from photoexcited $[1]^{2+}$ to the water-soluble oxidant. The findings presented in this study yield design principles for the functionalization of lipid bilayer membranes which will be relevant for the molecular engineering of artificial cellular organelles and nano-reactors based on biomimetic vesicles and membranes.

3. Photoinduced Electron Transfer Across Phospholipid Bilayers in Anaerobic and Aerobic Atmospheres

Authors: Novitasari Sinambela,+ Richard Jacobi,+ Dieter Sorsche, Leticia González,* and Andrea Pannwitz*

+These authors contributed equally

*Corresponding author

Published in: Angew. Chem. Int. Ed. 2025, e202423393

DOI: 10.1002/anie.202423393

Reprint Permission: This article is licensed under Creative Commons Attribution 4.0 International (CC BY 4.0). Published by Wiley-VCH GmbH.

Type of article: Research Article

Author contributions:

Novitasari Sinambela: Performed the chemical synthesis and liposome assemblies, steady-state and time-resolved spectroscopy characterization, confocal imaging measurement, spectroelectrochemistry measurements with data analysis, transmembrane electron transfer experiments, paper writing, and manuscript revision.

Richard Jacobi + Leticia González: Design of the computational protocols, and analysis of all calculations, paper writing, and manuscript revision.

Dieter Sorsche: Structure determination with single crystal X-ray diffraction.

Andrea Pannwitz: Paper writing and manuscript revision.

Abstract: In natural photosynthesis, light-driven electron transfer across the thylakoid membrane enables efficient charge separation and the confinement of reaction spaces for generating NADPH and CO_2 and oxidation of water. These reactions are complementary redox reactions and require different reaction conditions for optimal performance. However, current artificial photosynthesis studies only take place in the bulk and are sensitive towards oxygen and air, which limits their applicability under aerated and water-splitting conditions. Herein, we report light-driven electron transfer across a lipid bilayer membrane of liposome vesicles via a rigid oligoaromatic molecular wire that allows to electronically connect an oxidation and reduction reaction which are spatially separated by the membrane. The molecular wire has a simple, symmetric, easy-to-synthesize design based on benzothiadiazole and fluorene units and absorbs in the visible spectrum which makes it suitable for solar energy conversion. The model reactions in this study are light-driven NADH oxidation on one side of the membrane and light-driven reduction of an organic water-soluble dye in the bulk phase of liposomes. Additionally, the system is active in both aerobic and anaerobic atmospheres, rendering it ideal for aerobic conditions or reactions that produce oxygen such as solar-driven water splitting and artificial photosynthesis applications.

4. Light-Driven Electron Transfer in a Lipid Bilayer with Mixed Valence Molecular Wires

Authors: Novitasari Sinambela,[+] Moritz Nau,[+] Gernot Haug, Michael Linseis, Philip Koblischek, Rainer F. Winter,* and Andrea Pannwitz*

+These authors contributed equally

*Corresponding author

Published in: Sustainable Energy & Fuels, 2025, 9, 2302–2315

DOI: 10.1039/D4SE01752H

Reprint Permission: This article is licensed under a Creative Commons Attribution 3.0 International (CC BY 3.0). Published by Royal Society of Chemistry.

Type of article: Research Article

Author contributions:

Novitasari Sinambela: Performed the membrane integration, luminescence quenching experiments, confocal imaging measurement, electron transfer experiments, molecular dynamics simulations, paper writing, and manuscript revision.

Moritz Nau: Performed the spectroscopic characterization, cyclic voltammetry (including the simulations), spectroelectrochemistry measurements with data analysis, and all (TD-)DFT calculations on the model compounds, paper writing, and manuscript revision.

Gernot Haug: Conducted most of the chemical syntheses.

Michael Linseis + Rainer F. Winter: Supervision of Moritz Nau.

Philip Koblischek: Conducted one of the chemical syntheses.

Rainer F. Winter + Andrea Pannwitz: Design of the study, paper writing, and manuscript revision.

Abstract: Triarylamines (TAA) are one of the most important classes of redox-active organic compounds, which are readily available from modular synthesis, thereby offering the possibility to easily adjust their intrinsic redox potentials. We present herein two bis(triarylamines) (BTAAs) with π-extended 2,7-diethynylfluorene or 2,2'-(1,3-butadiyne-1,4-diyl)-bis(7-ethynylfluorene) bridges and two benzoic acid headgroups per TAA and their (formally) mixed-valent radical cations. Owing to their amphiphilic character and favorable redox properties, these BTAAs are designed to serve as charge conduits through membranes. The lipid bilayer / BTAA systems are water-soluble, which allowed us to explore their photoactivity in aqueous solution as well as to utilize their mixed valent forms membrane-mediated photoinduced electron transfer. Our findings will be relevant for constructing artificial nanoreactors for solar light energy conversion and light-driven redox chemistry in water.

Curriculum Vitae

Personal Information

Name : Novitasari Sinambela

Birth : 1995, in Indonesia

ORCID : 0000-0003-3568-250X

Education

05/2020- Present	PhD candidate in the group of Jun. Prof. Dr. Andrea Pannwitz, Chemistry Department University of Ulm (DE)
08/2017-04/2019	Master thesis in Inorganic Chemistry at Institute of Technology Bandung (ID)
08/2013-07/2017	Bachelor studies in Chemistry, Institute of Technology Bandung (ID) (B.Sc)

Acknowledgments

I would like to express my gratitude to Jun.-Prof. Dr. Andrea Pannwitz for her guidance throughout my PhD. I appreciate the challenges and opportunities she presented to me, as well as the freedom I was given to explore my research.

I am grateful to several collaborators and would like to acknowledge the following individuals for their productive and inspiring contributions:

- Prof. Dr. Leticia González and Richard Jacobi and Dr. David Hernández-Castillo. I enjoyed working with you and appreciated your support with the calculations and simulations of my large membrane system.
- Prof. Dr. Benjamin Dietzek-Ivanšić, and Nina Hagmeyer, and Elisabeth Hofmeister. Thank you for letting me use your EPR machine for measurements.
- Prof. Dr. Rainer F. Winter, Moritz Nau, Gernot Haug, Dr. Michael Linseis and Dr. Philip Koblischek. I am thankful for the special mixed valence compounds you provided.
- Prof. Dr. Dirk Ziegenbalg, Dr. Daniel Kowalczyk, and Benedikt Wiedemann. I am thankful for all the photoreactors and LEDs you provided.
- Dr. Giada Caniglia, I am thankful for working with you on the planar lipid bilayer station setup.
- Dr. Dieter Sorsche, I am thankful for all the XRD-single crystal that you have done and solved.
- For Amir Abbas and Julian Bösking, thank you for all your support in preparing the minireview.

I would also like to thank all current and former members of the Pannwitz, Rau, Streb, Anjass, and Tschierlei groups for fostering a stimulating and educational research environment. I appreciated our lively scientific discussions in the lab, hallways, during lunch, and coffee breaks. Additionally, I am thankful to everyone in AC I. Beyond those I worked with directly, many individuals at the institute contributed to a positive working atmosphere at Ulm University. I value the good communication among research groups and the cooperation among the members, including the generous sharing of chemicals, instruments, and scientific ideas.

Finally, I want to express my thanks to my family and friends. I am grateful for your support, motivation, humor, and wise insights throughout this journey. Thank you all for being there for me.

Declaration of Honesty in Academic Work

The present work was carried out from May 2020 to February 2025 at the Institute of Inorganic Chemistry I at the University of Ulm in the research group of Jun.-Prof. Dr. Andrea Pannwitz.

I hereby declare that I have completed this work independently and have not used any sources or aids other than those specified. I have indicated any passages that have been quoted verbatim or paraphrased and have adhered to the current version of the University of Ulm's regulations for ensuring good scientific practice.

Furthermore, I declare that I have not submitted the dissertation I am presenting here in this or a similar form in any other doctoral procedure, either in Germany or abroad. I have not applied for admission to a doctoral program at the University of Ulm or any other university with the right to confer doctoral degrees, nor have I already obtained the doctoral degree Dr. rer. nat., or have I definitively failed in a previous doctoral procedure for the doctoral degree Dr. rer. nat. at the University of Ulm or any other university with the right to confer doctoral degrees.

I am familiar with the valid framework doctoral regulations of the University of Ulm and the doctoral regulations of the Faculty of Natural Sciences for obtaining the Dr. rer. nat. degree.

Ulm,

Novitasari Sinambela